Remote Sensing and Volcanic Emissions

View of the east side of Augustine Island on January 24, 2006, with a strong steam and gas plume rising from the summit. Upper parts of the volcanic edifice are lightly coated with ash and minor lahar deposits can be seen in some drainages. Alaska Volcano Observatory photo by Cyrus Read.

The 2006 Eruption of Augustine Volcano, Alaska
Power, J.A., Coombs, M.L., and Freymueller, J.T., editors
U.S. Geological Survey Professional Paper 1769

Chapter 20

Integrated Satellite Observations of the 2006 Eruption of Augustine Volcano

By John E. Bailey[1,2], Kenneson G. Dean[1], Jonathan Dehn[1], and Peter W. Webley[1]

Abstract

Satellite observations played an important role in monitoring the 2006 eruption of Augustine Volcano. It represented the first opportunity for observers to use, in an operational setting, new Web-based tools and techniques developed by the Alaska Volcano Observatory remote sensing group. The "Okmok Algorithm" was used to analyze thermal infrared satellite data and highlight changes in the style and phases of activity. Temperature measurements were used to estimate ash cloud heights, which compared favorably to radar and ground-based observations, although larger discrepancies were seen when compared to pilot reports. Brightness temperature difference techniques were used to locate and track the 14 ash clouds produced during the explosive phase of the eruption. Stacking of these analyses allowed the creation of composite maps showing the distribution of airborne ash. The data from these maps were further combined with information from local reports and samples of ashfall to create a prototype of a concentration map that could be used to assess the potential hazard an eruption represents to aircraft, infrastructure and human health.

Introduction

The Alaska Volcano Observatory (AVO) monitors volcanoes in Alaska using a combination of geophysical, geological, and remote sensing data. AVO is responsible for providing both government authorities and the general public with information concerning hazards related to volcanoes that are currently in or showing increased potential for eruption. In particular, the detection of volcanic ash plumes and clouds is critical because of the potential of ash to damage machinery, adversely affect human health, and disrupt transportation infrastructure. AVO issues reports in conjunction with the National Weather Service (NWS) through the Anchorage Volcanic Ash Advisory Center (VAAC) and Federal Aviation Administration (FAA) to alert aircraft to the presence of potentially hazardous volcanic ash clouds.

The need for a volcanic hazards monitoring program in Alaska was highlighted during the December 1989 eruption of Redoubt Volcano (Dean and others, 1994; Miller and Chouet, 1994), when a Boeing 747 flew into the Redoubt ash cloud, causing all four engines to fail (Casadevall, 1994). A catastrophic loss of life was averted by the pilot restarting engines less than 2 minutes before impact. Damage to the aircraft was estimated at $80 million. Using a combination of satellite datasets and analysis methods, AVO is now able to track ash clouds similar to those from Redoubt and predict their probable dispersion patterns (Webley and others, this volume). In addition, other techniques using satellite data aid evaluation of precursory activity and assessment of the evolution in an eruption by considering the thermal output at the edifice.

Augustine Volcano is a small dome complex that forms an island near the mouth of Cook Inlet, Alaska (fig. 1). It erupted in January 2006 after a 20-year period of repose (Power and others, 2006). Seismic activity began increasing during May 2005, the first gas emissions began in September 2005, and steam plumes were first observed in satellite data on December 12, 2005. Between January 11 and 17, 2006, the volcano erupted explosively 13 times and then produced a continuous output of ash and gas from January 28 until February 2. After a hiatus, the volcano went into a two-week period of effusive eruption, which ended in mid-March. Located 280 km southeast of Anchorage International Airport, the volcano sits along the path of several local and international air traffic

[1]Alaska Volcano Observatory, Geophysical Institute, University of Alaska Fairbanks, 903 Koyukuk Drive, Fairbanks, AK 99775.

[2]Now at Scenarios Network for Alaska Planning, University of Alaska Geography Program, Fairbanks, AK 99775.

corridors (Power and others, 2006). To help prevent aircraft encounters with ash clouds, regional air traffic patterns were altered during the explosive phase of the eruption. Several nearby communities were affected by ashfall over this same period (Wallace and others, this volume).

Prior to 2006, there had been five known major historical eruptions (1883, 1935, 1963–64, 1976, 1986) of Augustine Volcano. Typically these events involved explosive eruptions followed by a period of lava effusion. Due to the relative repeatability of eruptions, the volcano was already well instrumented prior to the identification of precursory activity. As evidence increased that an eruption was likely to occur, the original instrumentation was greatly supplemented (Power and Lalla, this volume). The 2006 eruption of Augustine was the most intensely monitored eruption in AVO history, resulting in a multitude of datasets and providing an excellent opportunity to calibrate and validate satellite datasets. The range of activity displayed by the volcano provided a rich diversity of signals, with both explosive (of phreatic and magmatic origins) and effusive events occurring, and thus provided a robust test of AVO Remote Sensing (AVORS) group's operational capabilities.

This paper provides an overview of the observations made by AVORS using satellite data for all phases of the eruption. It highlights two areas of observation and analysis that are the primary capabilities of satellite-based volcano monitoring—thermal anomaly detection and ash cloud detection and tracking. On the basis of these datasets, we present discussions of the trends in the volcano's thermal output, discrepancies in the measurements of eruption cloud heights, and maps of the concentration and distribution of ash detected.

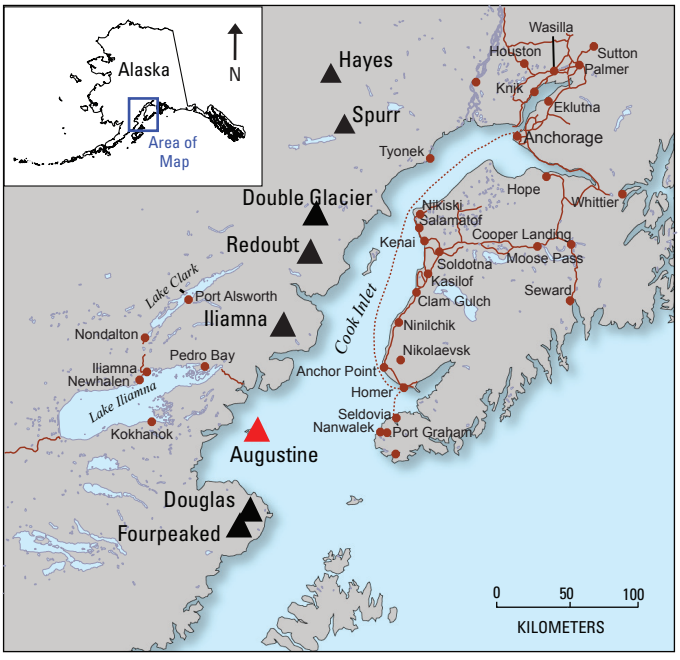

Figure 1. Map showing location of Augustine Volcano in Cook Inlet, Alaska. The area shown represents the Augustine sector that the Alaska Volcano Observatory remote sensing group creates from satellite data swaths to make large datasets more manageable during monitoring. Triangles indicate the location of volcanoes. Red lines show roads.

Background and Methodology

Satellite data provide quantitative information on volcanic clouds (Dean and others, 2002; Schneider and others, 2000) and elevated surface temperatures at volcanic edifices (Dehn and others, 2000; Harris and others, 1997, 2000). In recent years, new developments in satellite analysis have been implemented at AVO to harvest this information and make it available for operational monitoring purposes. These developments include systematic observation reporting using a dynamic database; Web-based imagery viewers; thermal anomaly detection and alarms; automated ash detection and compositing. Other tools, such as interfaces showing the detection of SO_2 using the Ozone Monitoring Instrument (OMI) and Atmospheric Infrared Sounder (AIRS) data have been developed through collaborations with other researchers. Satellite observations are supported by ground-based and airborne measurements (for example, use of a forward-looking infrared camera [FLIR]; Wessels and others, this volume); use of the Puff particle dispersion model (Searcy and others, 1998; Webley, this volume), ground-based aerosol samplers and LIDAR (Sasson and others, 2007; Webley and others, 2008), radar measurements (Schneider and others, 2006); webcam and pilot observations of activity. The operations of AVO combine all these measurements with those provided by seismology, geodesy and geology to create its best understanding of a volcanic event.

Satellite Datasets

The 2006 eruption of Augustine Volcano was the first operational test for many of the new remote sensing tools. They primarily analyze three satellite datasets: Advanced Very High Resolution Radiometer (AVHRR) data from the National Oceanic and Atmospheric Administration's (NOAA) Polar Orbiting Environmental Satellites (POES), Moderate Resolution Imaging Spectroradiometer (MODIS) data from the National Aeronautics and Space Administration's (NASA) Terra and Aqua satellites, and NOAA's Geostationary Operational Environmental Satellites (GOES) data. AVHRR and MODIS data are collected by receiving stations operated by the Geographic Information Network of Alaska (GINA) at the University of Alaska's Geophysical Institute. An additional AVHRR data feed is supplied by NOAA's Gilmore Creek satellite tracking station. GOES data are provided by the Naval Research Laboratory (NRL), Monterey Bay.

Data from these satellites/sensors are recorded in visible, mid-infrared, and thermal infrared wavelengths (table 1). AVHRR represents the "workhorse" for thermal anomaly and

Table 1. List of satellite data, wavelengths, and spatial and temporal resolution used to monitor volcanoes in Alaska.

[GOES, Geostationary Operational Environmental Satellites; NOAA, National Ocean and Atmospheric Administration; AVHRR, Advanced Very High Resolution Radiometer; MODIS, Moderate Resolution Imaging Spectroradiometer]

Satellite and Sensor[1]	Bands (B)	Wavelengths (μm)	Spatial Resolution (km)	Temporal Resolution (Repeat Coverage)
GOES Imager	1	0.52–0.72	8.0 at 60° N	0.5 hr
	4	10.5–11.5		
	5	11.5–12.5		
NOAA AVHRR (v3)	1	0.58–0.68	1.1 at nadir	Approx. every 1–2 hours at 60° N., due to large swath width and overlap
	2	0.73–1.00		
	3A (day)	1.58–1.64		
	3B (night)	3.55–3.93		
	4	10.3–11.3		
	5	11.5–12.5		
MODIS Terra/Aqua	28	7.175–7.475	1.0 at nadir	Approx. 2–4 passes per day
	29	8.4–8.7		
	31	10.78–11.28		
	32	11.77–12.27		

[1]All polar orbit except GOES (Geostationary).

ash detection. GOES is useful for tracking ash clouds because of its high temporal resolution. MODIS supplements the AVHRR thermal data and provides additional visible wavelength data allowing the creation of true color composites. Other data of opportunity (Landsat, Advanced Spaceborne Thermal Emission and Reflection Radiometer [ASTER]), which have high spatial resolution (<20 m/pixel) but infrequent repeat coverage (16+ days), can be used to corroborate observations made with AVHRR, MODIS, and GOES.

Detection Methodology

Dehn and others (2000) define a thermal anomaly (TA) as an unexpected increase in the radiant temperature value of a pixel in relation to its neighbors. For monitoring purposes, AVORS generally requires this difference (ΔT) to be >5°C to be of significance in any given dataset (AVHRR, MODIS, or GOES). However, in the early stages of activity at Augustine, observers were sensitive to smaller variations, especially when the anomalous pixels were located at the volcano's summit. Detection of thermal anomalies can be done either manually or using an automated algorithm. AVORS employs both methods, as there are a number of volcanological, environmental and technical explanations for TAs identified at a volcano, and not all are an indicator of volcanic activity. However, past history has shown that elevated radiant temperatures can often be a precursor to, or earlier indicators of, volcanic activity at Alaskan volcanoes, for example, Pavlof, 1996 (Roach and others, 2001), Okmok, 1997 (Patrick and others, 2003), Shishaldin, 1999 (Dehn and others, 2002), Cleveland, 2001 (Dean and others, 2004).

The 1996 eruption of Pavlof Volcano led to the creation of an algorithm that automatically processed images and identified thermal anomalies assessed to be of volcanic origin. This algorithm was successfully implemented during the 1997 eruption of Okmok and henceforth was known as the "Okmok Algorithm" (Dehn and others, 2000; Schneider and others, 2000; Dean and others, 2002). It has subsequently been updated (Okmok2) and augmented with a Web-based user interface that gives analysts access to a 15-year archive (1993+) of AVHRR images and Okmok Algorithm calculations for the North Pacific Region (fig. 2*A*). Additionally, if a thermal anomaly identified by the Okmok Algorithm meets certain criteria it generates warning emails and phone text messages that are sent to AVORS analysts. These alerts can also trigger a request for the acquisition of ASTER imagery at the volcano in question (Ramsey and Dehn, 2004).

Unfortunately it is difficult to create an algorithm that is 100 percent accurate in its identification of volcanic TAs, making manual checks an equally important part of regular monitoring activities. AVORS makes twice-daily manual checks of all acquisitions of AVHRR, MODIS, and GOES data and enters metrics for all identified thermal anomalies into a database using a Web-based interface. Reports that use a systematic template are then automatically generated and electronically distributed. The same database and electronic reports also include observations that are made of volcanic plumes and clouds.

The height and prediction of the movement of volcanic clouds are critical parameters required to assess their impact.

Satellite images offer a means to make these assessments, which would be difficult using only ground-based instruments and observations. Detection of these phenomena is complicated by the fact they might be composed of ash (of various size components), gas (of different species), or both. They might also assume different morphologies, related to atmospheric conditions, and whether they are a plume (generally used when the feature is still attached to the volcano) or a cloud (generally used when detached; that is, their volume is no longer being added to by the volcano). Although plumes will often have an elongated shape (due to regional wind effects) and higher ash density or steam content, volcanic clouds assume morphologies that can be hard to discriminate from surrounding meteoric clouds. Indeed all of these phenomena might not be seen on images if they are below higher altitude weather clouds.

As atmospheric winds carry volcanic clouds away from a volcano, diffusion and mixing cause them to spread, larger ash particles fall out, and their density is reduced. Thus an opaque cloud evolves into a translucent cloud. This evolution of volcanic clouds from opaque to translucent and the structure of the atmosphere both complicate and improve analyses (Schneider and others, 1995, 1999; Dean and others, 2004; Tupper and others, 2004). The identification of opaque versus translucent clouds requires the use of different bands in the satellite data. Opaque clouds appear as solid features, are colder than translucent clouds, and are usually visible in all bands. Translucent clouds by definition are less "solid" and often require a combination bands to be made visible.

Opaque clouds are needed to estimate height (table 2), where cloud-top temperatures measured from thermal IR band 4 (B4) satellite data are compared to atmosphere temperature profiles measured by sounders. This is referred to as the cloud temperature method. However, a major obstacle to the cloud temperature method is the tropopause, a position in the atmosphere where temperature does not decrease with height but stays about the same or, if above the tropopause, increases with height. An unambiguous height estimate can be derived only for clouds below the tropopause or larger umbrella clouds that reach into the stratosphere (Holasek and others, 1996; Tupper and others, 2007). For the 2006 Augustine eruption the lower tropopause boundary was at an altitude of approximately 8 km and upper boundary was at an altitude of approximately 16 km. Several of the 2006 Augustine eruptions were above the 8 km height.

Once a volcanic cloud becomes translucent valid cloud-top temperatures cannot be measured. However, a technique has been developed to detect translucent clouds that contain ash by subtracting long-wave thermal-infrared bands. This is referred to as the brightness temperature difference (BTD) or the split-window technique (Prata, 1989; Holasek and Rose, 1991). BTD values associated with volcanic ash have a negative signal between, 0 to −10 or lower, with the lowest value having the highest mass and presumably ash concentration for specific grain sizes (fig. 2*B*). Ash retrieval models have been developed to estimate ash particle size and total mass using BTD data (Wen and Rose, 1994; Schneider and others, 1999; Rose and Mayberry, 2000; Rose and others, 2001). Meteoric clouds can also exhibit negative BTD values, but the majority of these will not be more negative than −1.5. However, caution must be used when employing this technique, as volcanic clouds with ice-coated ash will not show a negative BTD signal (Prata 1989; Rose and others, 1995).

Ash Concentrations

One of the lessons learned from identifying and tracking the ash clouds produced by the Augustine eruptions was that it was easy to create a bottleneck in the flow of information being reported. This problem was caused by several factors: (1) six discrete eruptions occurred every few hours over a 20-hour period; (2) these events produced seven independently drifting ash clouds, visible in multiple datasets; (3) AVO reporting of ash clouds customarily involved text describing the position, direction of movement, and signal strength for each cloud on each image, a time consuming activity. In response to the bottleneck, a technique to produce composites of time-sequential BTD images was developed during post-eruption analysis. This method can act as a rapid visual summary of the previously cumbersome written descriptions.

There are three steps in the generation of the ash composites: (1) pixel values are extracted from selected images and compiled in a table, (2) BTD values are computed, and (3) values are displayed as an image. Three types of images are generated using the Most-Negative BTD values (Tupper and others, 2004), the Sum of BTD values, and Average BTD values. The Most-Negative image is generated such that the strongest BTD signal at each location is displayed and presumably includes the highest ash concentrations at that place. The Average image calculates average pixel values at each location and appears to identify signals that are related to the meteorological background, so it can be used to determine thresholds to differentiate weather from ash or other particulate signals. The Sum image is a simple summation of values at every location, but its usefulness is yet to be determined. Presently the Most-Negative images are automatically generated for each monitoring sector every 12 hours, with plans to implement updates in as near real-time as processing delays will allow. The images can viewed using a Web-based application, allowing multiple analysts to view the information simultaneously. These data have already proved to be a useful passive monitoring technique for small events at Cleveland (Alaska) and Bezymianny (Russia) volcanoes in 2007. However, as noted by Tupper and others (2004) some caution must be employed due to the failings of this technique for ice-coated ash.

Eruption Observations

The multitude of datasets collected during the eruption of Augustine permitted a detailed analysis of the events that

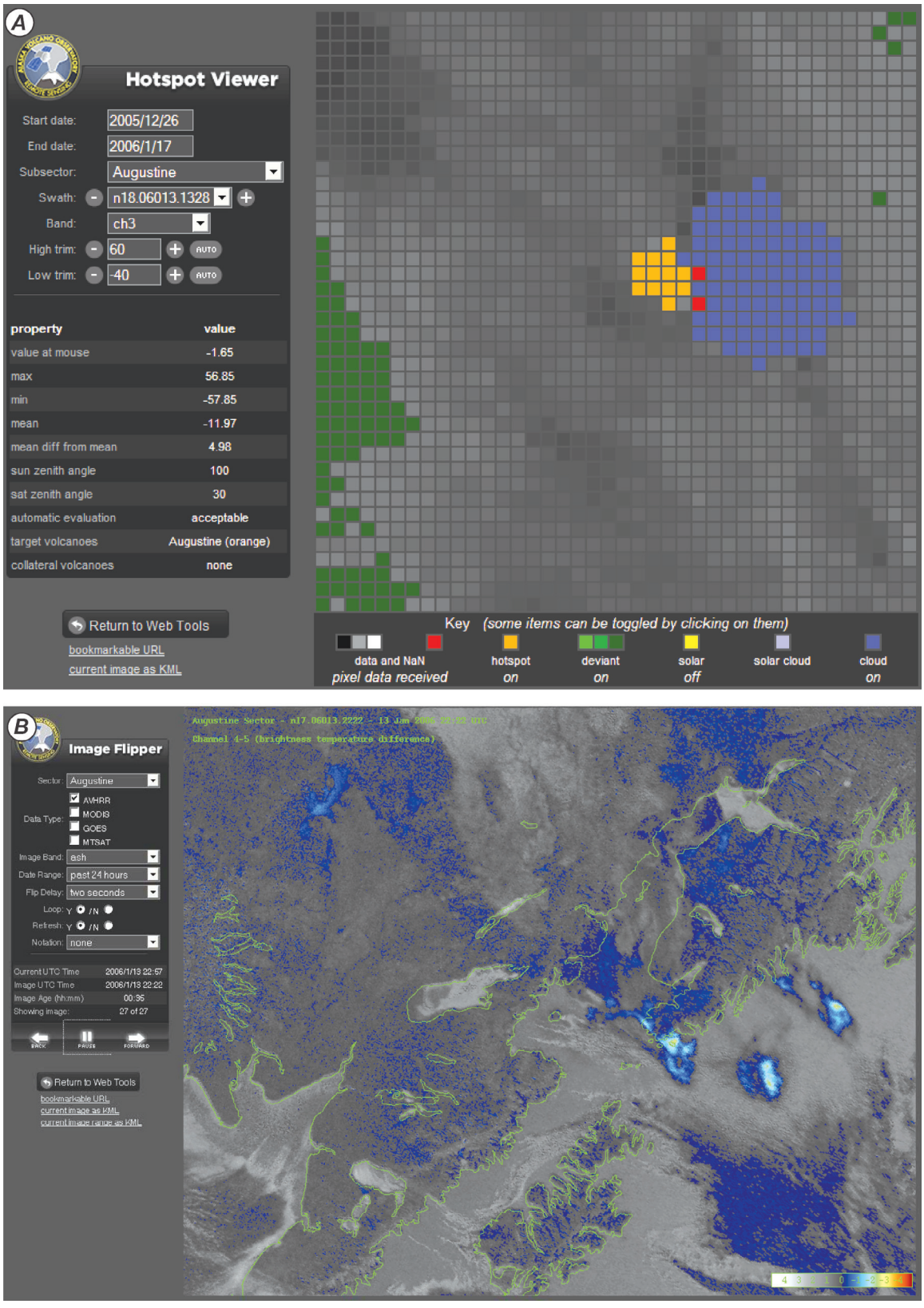

Figure 2. *A*, Web-based interface showing Okmok algorithm evaluation of an Advanced Very High Resolution Radiometer (AVHRR) image acquired at the start of Augustine Volcano's eruptive event 3 on January 13, 2006. *B*, Web-based interface showing a bright temperature difference evaluation of AVHRR bands 4 and 5 showing ash clouds from events 3, 4, and 5 at 1322 AKST (2222 UTC) on January 13, 2006.

Table 2. Augustine Volcano plume height observations.

[All satellite observations are based on AVHRR images unless noted. AKST, Alaska Standard Time; UTC, Coordinated Universal Time; NEXRAD, Next Generation Radar. See table 3 for dates of events]

Event	Satellite time (AKST/UTC)	Radar time (AKST/UTC)	Temperature based height (ft/km)	NEXRAD based height (ft/km)	Normalized difference wrt radar (%)	Comments
1	0456 1356	0449 1349	23,000 7.0	21,000 6.5	10	Tropopause (tropo) = 8.5 km., Plume < tropo.
2	0533 1433	0523 1423	28,900 8.8	33,500 10.2	−14	Tropo.= 8.5 km, Radar shows into tropo. Used 8.8 km for satellite.
3	0436 1336	0432 1332	29,500 9.0	33,500 10.2	−12	Tropo.= 8.5 km, Radar shows in tropo. Used 9 km for satellite.
4	1024 1924	0824 1749	NA	33,500 10.2	NA	Appears to be translucent cloud. Temperature values not valid.
5	1150 2050	1125 2025	29,500 9.0	34,500 10.5	−14	Tropo.= 9 km, Radar shows in tropo. Height 8 or 9 km for satellite.
6	1653 +0153	1642 +0142	32,000 10.0	34,000 10.5	−7	Tropo.= 9 km, Radar shows in tropo. Height 8 or 10 km for satellite.
7	1930 +0430	1930 +0430	36,000 11.0	34,500 10.5	4	Tropo.= 9 km, Radar shows in tropo. Height 7 or 11 km for satellite. GOES data.
8	0100 1000	0100 1000	23,000 7.0	20,000 6.1	15	Tropo.= 9 km, Radar < tropo. GOES data.
9	0838 1738	0801 1701	NA	45,000 13.7	NA	Tropo.= 9 km, Radar shows in tropo. Satellite temp. < meteoric cloud temp. suggests super cooling.
10	2042 +0542	2042 +0542	21,300 6.5	23,300 7.1	−9	Tropo. = 8 km, Radar shows < tropo.
11	NA	1140 +0840	NA	12,500 3.8	NA	No satellite data. Clouds translucent.
12	NA	0208 1108	NA	23,300 7.1	NA	No satellite data. Clouds translucent.
13	NA	0554 1654	NA	23,300 7.1	NA	Appears to be a translucent cloud.
14	NA	NA	NA	NA	NA	No satellite data.

occurred. The diversity of these datasets was further enriched by the range of activity displayed with explosive (of both phreatic and magmatic origins) and effusive events occurring. The evolution of the eruption was defined by four distinct phases, characterized by different styles of activity, and a hiatus (fig. 3; Coombs and others, this volume). The first phase was the precursory stage, which indicated increasing unrest at the volcano. Phase two saw the onset of explosive eruptions and culminated with a continuous eruption of material that defined phase three. This was followed by a hiatus during which the ash-cloud producing explosions stopped and the effusive activity that began sometime during phase two stalled. The fourth and final phase saw lava emplaced at the summit of the volcano.

The following sections describe the satellite observations for each phase of the eruption and give an overview of the events at the volcano. Other papers in this volume undertake a further exploration of these various aspects of the eruption using remote sensing techniques. McGee and others (this volume) describe the precursory and syn-eruption gas emissions at the volcano. Van Manen and others (this volume) combine satellite-derived thermal and seismic data to describe the activity beginning 10 days before the explosive phase. The distribution of tephra deposits produced during the eruption are defined by Wallace and others (this volume), whereas Webley and others (this volume) describe dispersion modeling of the plumes that produced these deposits. Ground-based imagery collected by time-lapse and infrared cameras is described in Sentman and others (this volume) and Paskievitch and others (this volume).

All times are given as Alaska Standard Time (AKST). In addition, times that relate to specific satellite images are also given in Universal Time (UTC) as the imagery UTC for its time/date identifier name. AKST is equal to UTC minus 9 hours.

Precursory Phase

The precursory phase began as an increase of micro-earthquakes beneath the volcano starting April 30, 2005 (Power and others, 2006). Initially occurring once or twice a day, the frequency steadily increased to 15 per day by mid-December (Jacobs and others, this volume). GPS measurements suggested pressurization of the volcano at sea level centered beneath the edifice (Cervelli and others, 2006). Starting in December small phreatic explosions were recorded by seismometers (McNutt and others, this volume), the largest of which occurred on the 10th, 12th and 15th. The December 12 event led to vigorous steaming and formation of a gas plume that was visible in AVHRR and MODIS data. Gas emissions started on December 12 at 1140 AKST (2040 UTC) and continued to at least 0442 AKST, December 13 (1342 UTC), although meteoric cloud cover prevented observations for the next 10 hours. The plumes were observed in visible and mid-infrared-band data. Most of the observed plumes were narrow and semi-translucent extending to 125 km or more, mostly to the south-east. No negative signal was detected in the BTD data, which combined visual observations by webcams on Augustine, suggested that there was little to no ash in these plumes. They were below 1,500 m altitude based on sounder data collected at 0000 UTC, December 6, 2005, at Kodiak. The best image showing this activity was recorded by the MODIS Aqua satellite at 1323 AKST (2223 UTC) (fig. 4). These events represented the first activity at Augustine that was visible in satellite data.

Explosive Phase

Generally cloudy conditions obscured views through December 2005 and early January 2006. On January 5, 2006, a break in the cloud cover allowed weak thermal anomalies (ΔT <3°C) to be detected at 2024 and 2119 AKST (0524 and 0619, January 6 UTC). Simultaneous webcam images collected at Homer showed clear views of a steaming edifice. Mostly cloudy weather returned and prevented further activity being seen in satellite images until 2245, January 10, AKST (0745 UTC, January 11) when a thermal anomaly (ΔT = 4.3°C) and a gas plume were detected. The plume was attached to the volcano indicating that material was still being emitted, and drifted to the southwest and west with the leading edge 74 km west of the summit of the volcano. It was only detected in band 3 data. No plume signal was detected in the longer TIR bands (B4 and B5) or in the split-window data, suggesting that little or no ash was in this emission.

January 11, 2006

Six hours later, two explosive eruptions occurred on at 0444 AKST (1344 UTC) and at 0512 AKST (1412 UTC) (table 3). Views of the edifice captured by AVHRR and MODIS in the hours after the eruptions showed a weak thermal anomaly located at the summit with low band 3 (B3) radiant temperatures (fig. 3). No thermal anomalies were observed immediately preceding the explosions, potentially suggesting that there was little or no fresh juvenile lava in the conduit

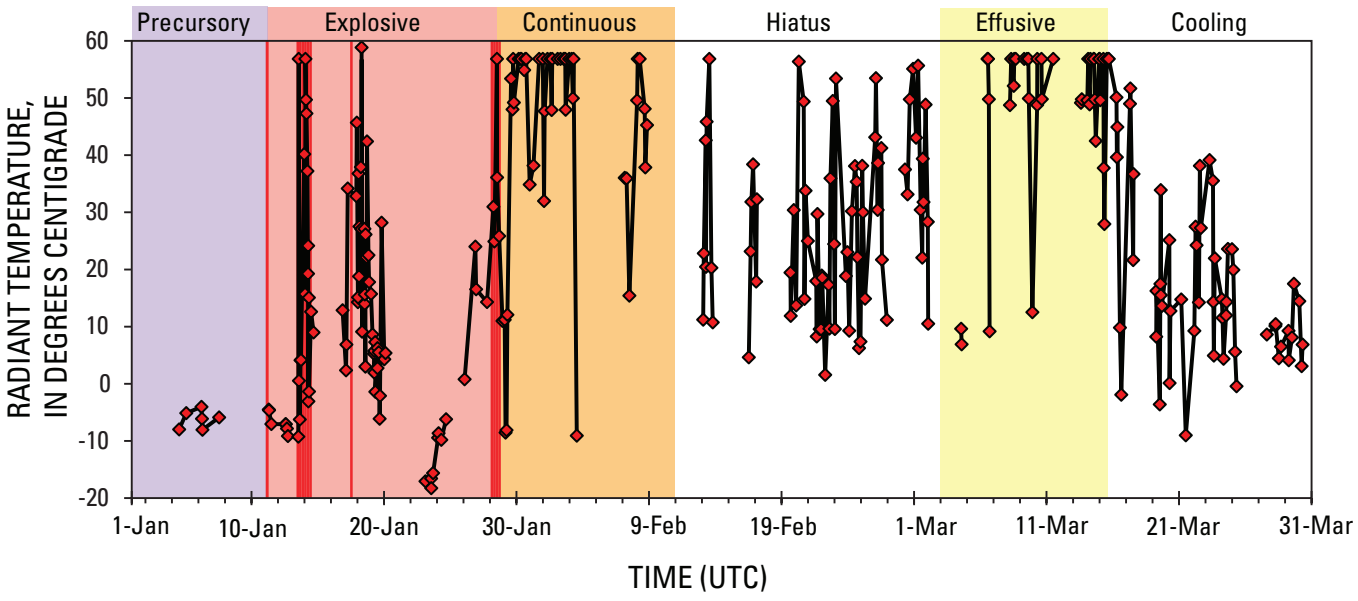

Figure 3. Plot of radiant temperatures of thermal anomalies seen at Augustine Volcano during the first 3 months of 2006 compared to eruption phases defined by geophysical measurements in Coombs and others (this volume). Vertical red lines represent explosive vents during the explosive phase.

that significantly contributed to the explosion. Analysis later confirmed that the ejected material was primarily older recycled debris (Wallace and others, this volume).

The material emitted by both of these eruptions was contained in a single opaque cloud although the curled tail of the second cloud may have been a remnant from the first eruption. The explosive eruptions were recorded on AVHRR satellite images within a few minutes of the start time of each event. The first image at 0448 AKST (1348 UTC) recorded the volcanic cloud 3 minutes after the explosive eruption ended (fig. 5*A*). This cloud was circular and directly over the volcano. The coldest volcanic cloud-top temperature was −46°C which corresponds to an altitude of approximately 7 km (23,000 ft) based on a dry atmosphere profile collected at Kodiak Island. Another image was recorded at 0525 AKST (1425 UTC), 10 minutes after the second eruption ended (fig. 5*B*). This cloud was also opaque and located over the volcano. It had a volcanic cloud-top temperature of −55°C, which corresponds to an altitude of approximately 8.5 km (28,000 ft) based on the same Kodiak atmospheric profile. Ground-based next generation radar (NEXRAD) estimates of volcanic cloud heights were similar for the first eruption with radar showing 6.5 km but were significantly different for the second with radar showing 10.5 km (Schneider and others, 2006). Wind directions suggested that the maximum cloud height was >8 km (~26,250 ft). The opaque cloud was observed in satellite images for 37 minutes, during which time the plume ascended 1.5 km (8,000 ft) at approximately 0.2 km/min (216 ft/min). On the basis of radar ascension rates were 0.108 km/min (355 ft/min).

GOES and AVHRR satellite passes recorded the movement, dispersion, and evolution of the plume. Images recorded

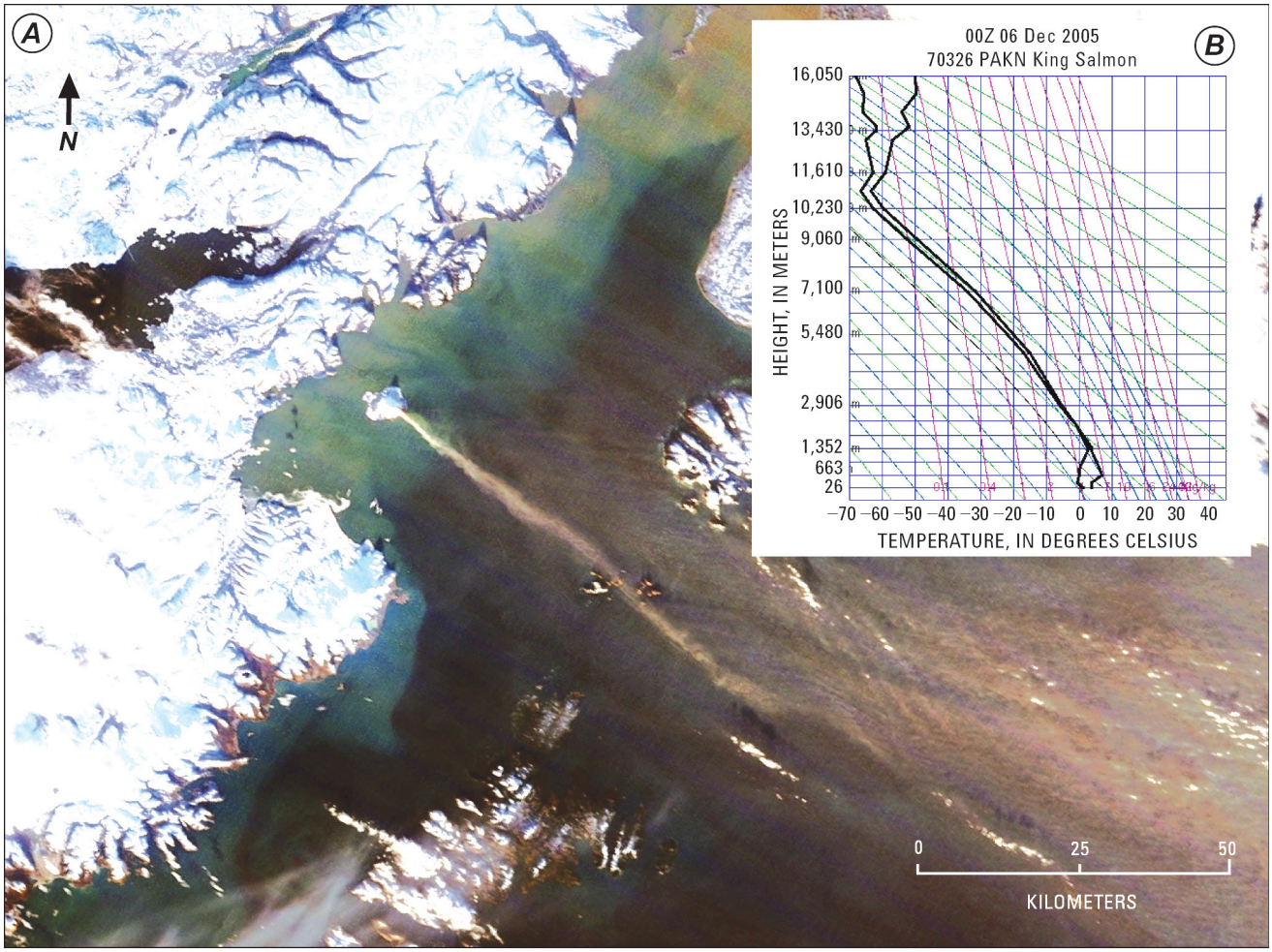

Figure 4. *A*, Moderate Resolution Imaging Spectroradiometer satellite true-color composite image showing a steam plume observed extending from Augustine Volcano for approximately 80 km (50 miles) to the southeast. There was no ash signal from the brightness temperature difference data indicating that this emission was most likely water vapor and SO_2. Image was acquired by the Terra satellite on 12 December 12, 2005 at 1216 AKST (2116 UTC) and processed by the Geographic Information Network of Alaska, University of Alaska Fairbanks. *B*, Regional radiosonde from the University of Wyoming's archive.

between 0530 and 0839 AKST (1430 to 1739 UTC) showed ash drifting to the northeast of the volcano, over Cook Inlet and the Alaska Peninsula. The opaque cloud began to disperse and become translucent at about 0530 AKST (1430 UTC), approximately 1 hour after the second explosion. These translucent clouds had BTD ash signals that ranged in value from −2.1 to −3.1, with the most negative values observed at 0730 AKST (1630 UTC; fig. 5). Data recorded after 0839 AKST (1739 UTC) had possible ash signals < −1, but these were not readily distinguishable from background noise. The cloud was mostly dispersed after 0930 AKST (1830 UTC). Generally, the strongest signals (< −3) were over water and within 20 km of the volcano. The majority of ash from these explosions probably fell into Cook Inlet. Very light ashfalls were reported approximately 100 km north-northwest at Lake Clark (Wallace and others, this volume) which is beyond the satellite-defined impact area. Most likely airborne ash in this region was at a concentration below the satellite detection threshold.

January 13–14, 2006

Six explosions (events 3 to 8) occurred on January 13 and 14 over a 25 hour period (fig. 6). Each explosion resulted in volcanic clouds that were tracked on 19 AVHRR satellite images, giving an average view of almost one image per hour. The first event for this period (event 3) occurred at 0424 AKST, January 13 (1324 UTC). An AVHRR image that was captured during the event (fig. 2*A*) showed an opaque cloud with a temperature of −54°C that reached an estimated altitude of 8.0 to 9.0 km based on sounder data collected at King Salmon. The cloud was still opaque when seen on a second image at 0456 AKST (1356 UTC), with a temperature of −52°C and was still at an altitude of approximately 8.0 to 9.5 km. NEXRAD radar reported a height of 34,000 ft (10.5 km). The cloud became translucent between images captured at 0637 and 0834 AKST (2 to 4 hours after the start of the eruption) with a BTD signal that weakened from −4.0 to −3.2 during this period. The volcanic cloud drifted east across Cook Inlet passing over the southern tip of the Kenai Peninsula. Ashfall was reported in the Homer, Seldovia, Port Graham, and Nanwalek areas between 0514 and 0850 AKST (Wallace and others, this volume). On the basis of satellite images, the ash cloud had moved east of Homer by 1024 AKST (1924 UTC) and by 1330 AKST (2230 UTC) the plume drifted over the coast near Seward, Alaska, and continued east across the Gulf of Alaska.

The second explosion (event 4) occurred at 0847 AKST (1747 UTC) and was recorded on an AVHRR image at 1024 AKST (1924 UTC). The image showed the cloud in transition from opaque to translucent and drifting east from the volcano. The cloud-top temperature of the opaque portion was −45°C, which suggested an altitude between 6.5 and 13.5 km based on sounder data collected at Kodiak. NEXRAD radar reported a height of 30,000 ft (9.1 km), and a pilot reported a height of 47,000 to 52,000 ft (14.3 to 15.8 km). The translucent portion of the cloud had a maximum BTD signal of −3.0 at the leading edge of the cloud that was approaching the Kenai Peninsula. This ash cloud passed over Seldovia and other towns at the southern tip of the Kenai Peninsula at 1130 AKST and then proceeded across the Gulf of Alaska. No ashfall was reported for this period from any towns in the area.

The third explosion (event 5) occurred at 1122 AKST (2022 UTC). Satellite images from 1130 to 1142 AKST (2030 to 2042 UTC) showed that the volcanic cloud was opaque with some translucent portions along its rim. The coldest cloud-top temperature of −54°C, observed at 1142 AKST (2042 UTC) translated to an altitude of 7.5 to 9.0 km based on sounder data collected at King Salmon. NEXRAD radar reported a height of 36,000 ft (11 km), and pilots reported a height of 52,000 ft (15.8 km). After 2042 UTC the cloud became more translucent as seen by an increase in cloud-top temperatures and increasing BTD signal strength. The ash cloud drifted east and passed over the lower Kenai Peninsula. It passed over towns in the vicinity of Seldovia from approximately 1322 to 1602 AKST and then continued across the Gulf of Alaska. No ashfall was reported for this period from any towns in the area.

The fourth explosion (event 6) occurred at 1640 AKST (0140 UTC, January 14). The first image recorded at 1645 AKST (0145 UTC, January 14) showed an opaque cloud with a translucent rim at the southern edge of Augustine Island that appeared to be still attached to the volcano. The minimum cloud-top temperature was −53°C, which corresponded to an altitude of 7.5 to 10.0 km based on the sounder at King Salmon. NEXRAD radar reported a height of 34,000 ft (10.4 km) and pilots reported a height of 30,000 to 35,000 ft (9.1 to 10.7 km). Images recorded around 1700 AKST (0200 UTC, 14 January) and later showed the cloud becoming translucent, as indicated by increasing cloud temperatures and increasing BTD signal strength. The most negative BTD signal of −4.0 was recorded at 1829 AKST (0329 UTC, 14 January). Unlike the previous events on this day, the ash cloud drifted to the south-east over Cook Inlet and the Gulf of Alaska. No ashfalls associated with this eruption were reported, and observations were unlikely because the cloud mostly drifted over the open ocean.

The fifth explosion (event 7) occurred at 1858 AKST (0358 UTC, January 14). GOES images recorded at 1900 AKST (0400 UTC, January 14) did not detect a volcanic cloud, probably due to its low spatial resolution at these latitudes, but the images at 1930 AKST (0430 UTC, January 14) and 2000 AKST (0500 UTC, January 14) showed an opaque cloud that was translucent along its periphery. The opaque cloud had a minimum temperature of −49°C on both of these images, which correlates to a height of 7 to 11 km based on the sounder at King Salmon. NEXRAD radar reported a height of 30,000 ft (9.1 km), and there were no pilot reports. The cloud became more translucent after 2000 AKST (0500 UTC, January 14), with the BTD-based ash signal reducing in strength over the next 3 hours. Time sequential GOES images

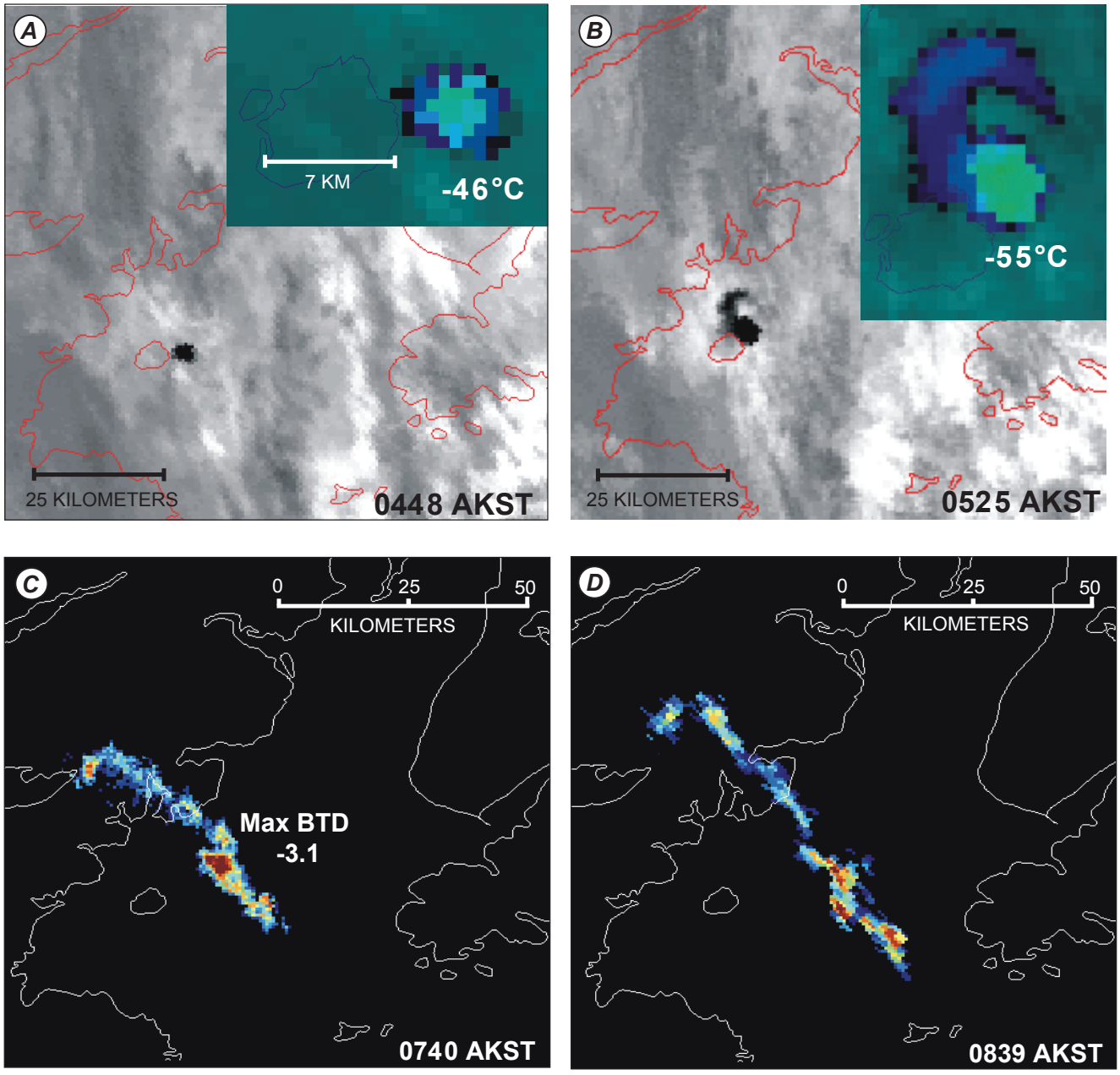

Figure 5. Advanced Very High Resolution Radiometer (AVHRR) satellite images of Augustine Volcano 2006 eruption event 1, the first explosive eruption. *A*, Band 4 thermal infrared image showing opaque cloud acquired at 0448 AKST (1348 UTC) on January 13, 2006. Insert shows enlarged view of the plume color-coded based on temperature. Coldest temperatures are indicated by light green pixels. *B*, Similar to *A*, acquired at 0525 AKST (1425 UTC). *C*, Brightness temperature difference (BTD) image showing the ash cloud drifting to the northeast over the Cook Inlet, acquired at 0740 AKST (1640 UTC). Most negative values of BTD are indicated by red pixels and indicate the highest concentration of ash. Moderate concentrations are shown by yellow and green pixels, with the blue pixels indicating the lowest concentrations of ash. *D*, Similar to *C*, acquired at 0839 AKST (1739 UTC).

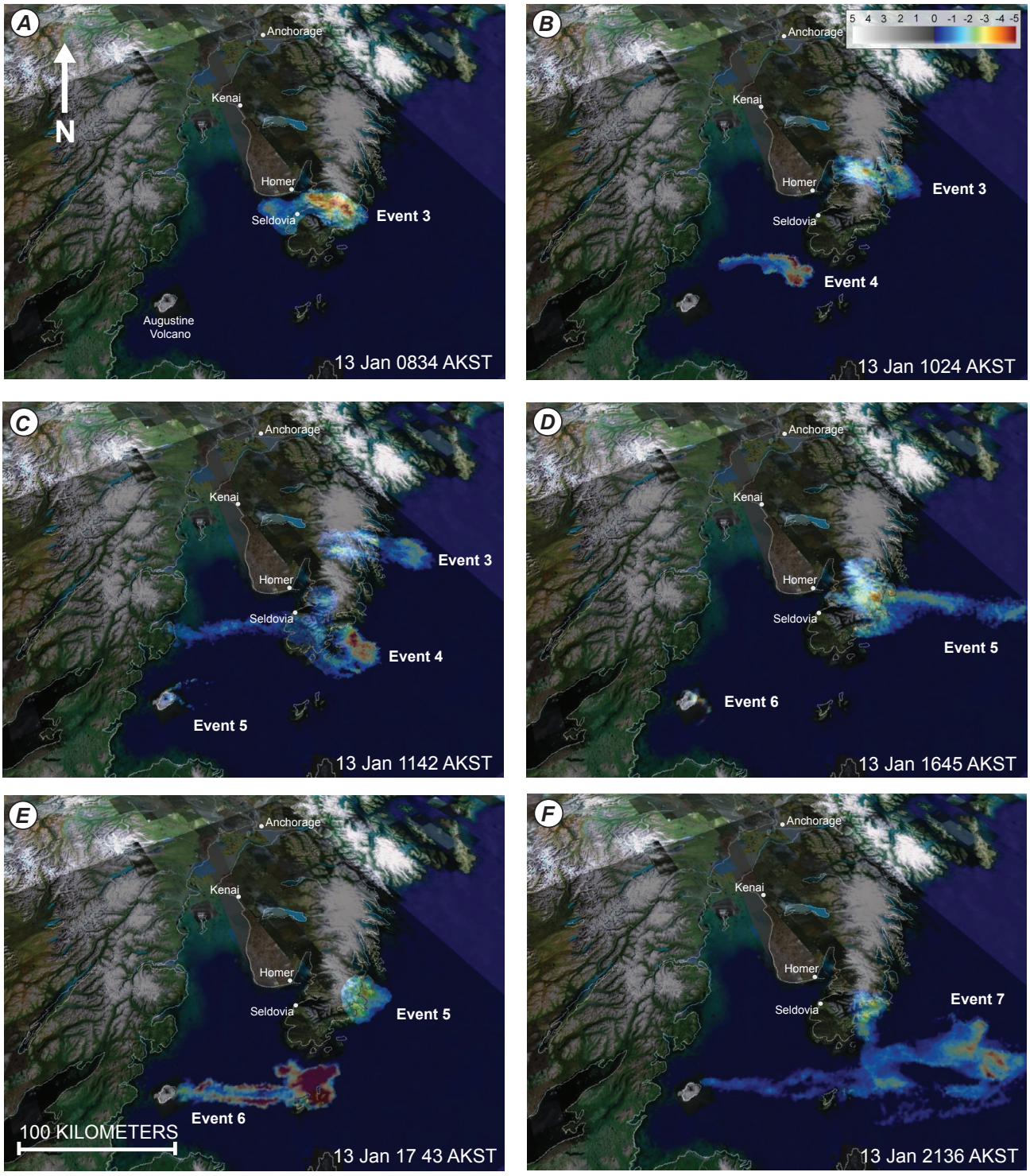

Figure 6. Advanced Very High Resolution Radiometer (AVHRR) data shown as brightness temperature difference images to detect ash clouds from the explosive events on January 13–14, 2006. The images are shown as overlays in Google Earth for geographic reference. Local time stamps are shown on images and equate to the following image UTC acquisition times: *A*, 1734, January 13; *B*, 1924, January 13; *C*, 2042, January 13, *D*, 0145, January 14; *E*, 0243, January 14; and *F*, 0636, January 14.

showed that the ash cloud drifted east over the lower Kenai Peninsula towns of Seldovia, Port Graham, and Nanwalek, but no ashfall was reported. Using just AVHRR data, it was difficult to distinguish event 7 ash clouds from previous ones in the general vicinity of the volcano. However, the high temporal resolution of time-sequential GOES data was sufficient to identify and track the movement of these ash clouds.

The sixth explosion (event 8) occurred on January 14 at 0014 AKST (0917 UTC). GOES satellite data recorded between 0030 and 200 AKST (0930 and 1100 UTC) showed an opaque cloud that became translucent as it dispersed. The opaque cloud had a minimum temperature of −50°C, which correlates to an altitude of 7.0 to 10.5 km. The translucent cloud had a maximum BTD signal strength of −3.2. The cloud moved east and north-east over the southern end of the Kenai Peninsula and the towns of Homer, Seldovia, Port Graham, and Nanwalek, then to the south-east across the Gulf of Alaska. No ashfalls were reported from this eruption.

Observations of thermal anomalies on January 13–14 were ambiguous due to the interaction of different effects. The maximum temperatures measured were a combined consequence of how long had passed since fresh, hot material was erupted and whether the volcanic cloud or steam at the volcano restricted views of the crater and surrounding deposits (fig. 3). In some images, solar reflection off the steam plumes also made the size of anomalies an uncertain parameter. In cases where images were collected with a clear view of the vent and/or fresh deposits around the edifice, AVHRR sensors reached their maximum calibration temperature (56.85°C) for band 3, and several pixels became saturated.

January 17, 2006

A further large explosion (event 9) occurred on January 17 at 0758 AKST (1658 UTC). GOES images recorded before the eruption showed a large weather cloud extending south-east and northwest from the volcano and approximately 200 miles long. The volcano erupted through this cloud. The GOES data recorded during and after the eruption did not show a distinct, coherent opaque volcanic cloud or definitive BTD ash signals that could be clearly distinguished from background weather signals. An AVHRR satellite pass at 0838 AKST (1738 UTC) did show a very distinct volcanic cloud in mid-infrared (B3) and thermal infrared (B4) wavelengths (fig. 7*B*). The B4 data showed minimum cloud-top temperatures of −56°C, which were colder than any height on the atmospheric temperature profiles collected at Kodiak. This suggested that the cloud was super-cooled, although this conclusion is tentative as the underlying meteoric cloud may have impacted the measured cloud temperature. The NEXRAD radar showed a maximum altitude of 45,000 ft (13.4 km), which indicated the ash cloud was well into the tropopause (Schneider and others, 2006).

Ashfall was reported from the Iliamna Lake and Lake Clark areas from 1200 to 1700 AKST (Wallace and others, this volume). A MODIS satellite image recorded on January 19, 2006 shows ash deposits on the snow-covered terrain west of Augustine Volcano beyond Iliamna Lake (fig. 7*A*). There was also a report of ashfall east of the volcano at Port Graham on the Kenai Peninsula. The AVHRR BTD data did not show the volcanic cloud extending to the east; however, Puff model predictions indicate that low level ash was predicted to pass over this area and thus the ash may have been below the detection limits of the satellite sensor (Webley and others, this volume). A similar situation occurred during the eruption of Cleveland Volcano in 2001, when a pilot reported the volcanic cloud well beyond the impacted area as defined by satellite data (Dean and others, 2004).

Similar to events on January 13–14, high radiant temperatures (>40°C) were only recorded in a few satellite passes following the explosion on January 17. The highest temperature measurement of 58.84°C was recorded at 2232 AKST (0732 UTC, January 18) in band 20b on Terra's MODIS sensor. Although values rapidly cooled from this peak, over the next 3 days elevated (above background) temperatures persisted (fig. 3). Poor weather conditions prevented observations January 20–23, but clear views on January 24 showed relatively weak thermal anomalies (ΔT = 10–15°C), with low radiant temperatures (<5°C).

Continuous Phase

Over the next 4 days the radiant temperatures increased rapidly, and activity moved into a phase that began with four more discrete explosions (events 10 to 14; table 3) that by 1430 AKST, (2330 UTC) January 28 transitioned into nearly continuous emission of gas and ash. Multiple ash clouds could be seen on most of the satellite data from this time until January 30 (fig. 8). The ash clouds drifted to the south on January 28 and 29 and then east after that time.

Eight minutes after the start of event 10, a satellite pass at 2042 AKST, January 27 (0542 UTC, January 28), showed an opaque cloud with a temperature of −45°C that correlated to estimated heights of 21,300, 31,200, or 47,600 ft (6.5, 9.5, or 14.5 km) based on atmospheric temperature profiles collected at King Salmon. Confusion in the true value was due to these heights being at or above the tropopause boundary. The maximum height recorded by radar was 34,500 ft (10.5 km), which puts the cloud top in the tropopause. The next satellite pass at 2115 AKST (0615 UTC, January 28) showed that the plume had become translucent with a BTD of −6.9 and was drifting south.

Events 11 and 12 were seen on four satellite passes between 2337 AKST, January 27 and 0745 AKST, January 28 (0837 to 1645 UTC, January 28). In the images translucent volcanic clouds with BTDs of −2.8 to −4.5, respectively, were seen drifting south over Kodiak Island. Event 13 was observed 34 minutes after the end of the eruption by a satellite pass at 819 AKST (1719 UTC) that showed a cloud which was part opaque and part translucent. The temperature of the opaque cloud was −45°C, which

corresponded to an estimated height between 19,700 and 32,800 ft (6.0 to 10.0 km) based on an atmospheric profile collected at Kodiak. The tropopause was at 19,700 ft (6.0 km). NEXRAD gave heights of 25,000 ft, and pilot reported heights suggested 35,000 ft. The translucent portion of the cloud had BTD values of −2.4, and as the cloud drifted south the BTD signal strengthened to a minimum of −7.4.

During the continuous phase, radiant temperatures at the summit anomaly remained consistently high (>45°C) until February 3, after which time cloudy weather prevented satellite observations. Thermal anomalies were observed in most images during this period with many images showing saturated pixels (fig. 9*A*), and most recording maximum AVHRR sensor values. The anomalies were large (10+ pixels) and varied in morphology. In some cases they were roughly circular and located around the summit, but in several images they were elongated along the flanks of the volcano. In a few instances the changes in size and morphology could be accounted for by solar reflection off steam and large satellite viewing angles, but in most cases these observations suggested pyroclastic flow activity on the volcano. This hypothesis was supported by webcam views (fig. 9*B*) and the color and morphology of deposits shown by a high resolution ASTER images (fig. 9*C*). Field studies later confirmed that there had been pyroclastic flow activity on the north and east flanks (Vallance and others, this volume).

Clear views on February 7 and 8 showed thermal anomalies with relatively high temperatures, but the values were decreasing in magnitude through the 8th. The thermal anomalies were much smaller than those observed a week before, and the greater size seen in some anomalies could be accounted for by radiation from, and solar reflection off, steam plumes. Poor weather prevented satellite views of the volcano from February 9–12, during which time the activity transitioned out of the continuous phase and average temperatures dropped to 20 to 30°C. The volcano now entered an eruptive hiatus that lasted almost a month. Ground-based observations, seismology, and geodesy all suggest that from February 10 to March 3 no new material was extruded from the volcano (Coombs and others, this volume).

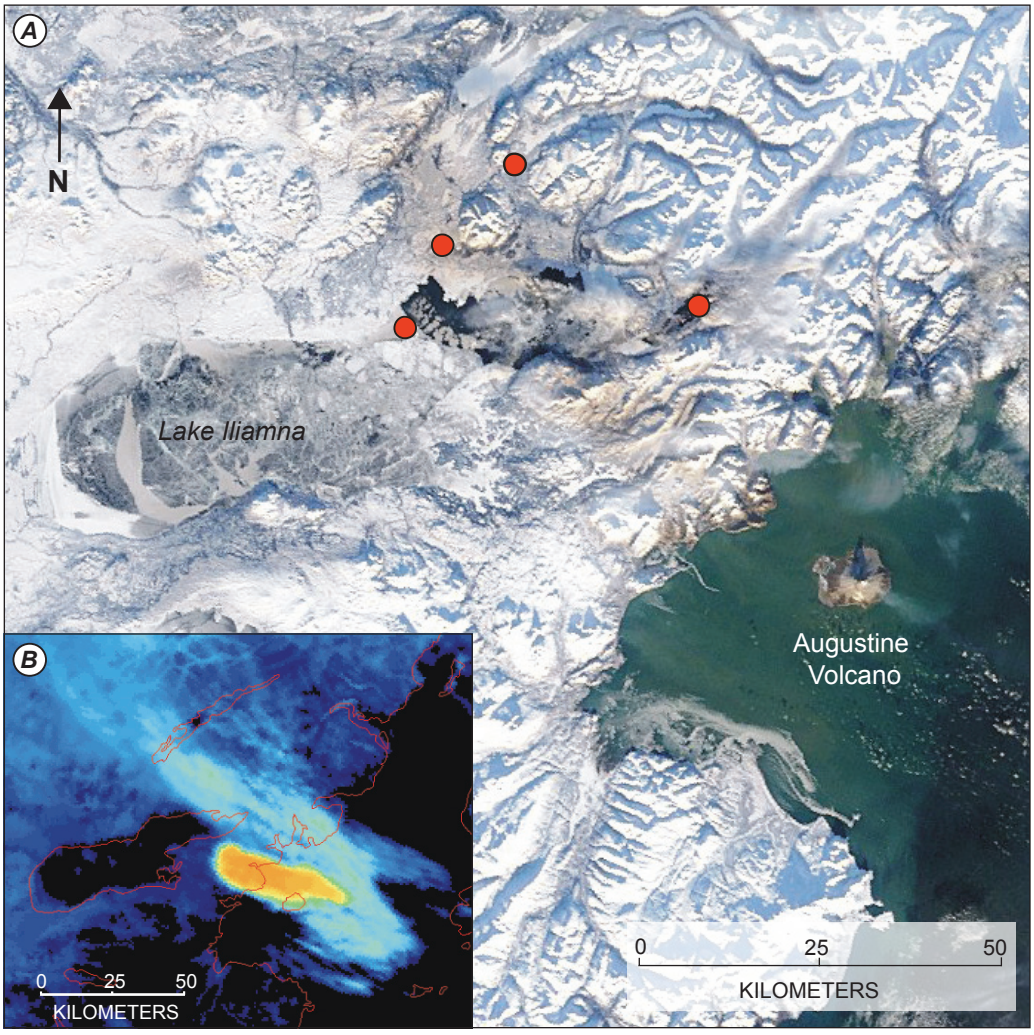

Figure 7. *A*, Moderate Resolution Imaging Spectroradiometer image showing ash fall from the eruption of Augustine Volcano on January 17, 2006. The ash cloud from the eruption drifted northwest from the volcano and dropped ash along a path that crossed the east end of Iliamna Lake, seen as brown tint in the snow. The red circles indicate (approximate) locations where light ash fall was reported or samples were collected. The image is a RGB color composite using visible bands 1, 4, and 3 acquired at 1240 AKST (2140 UTC) on January 19, 2006. *B*, Advanced Very High Resolution Radiometer band 4 view of the opaque ash cloud, acquired at 0838 AKST (1738 UTC) on January 17. Dense areas of ash are colored orange and yellow, with the distribution of finer ash shown in light blue.

Effusive Phase

During the 36 hours following the first explosions on January 11, several sequences of small, similar, regularly spaced volcano-tectonic earthquakes occurred, with rates as high as 3 to 4 per minute (Power and Lalla, this volume). Comparable sequences have been seen at other volcanoes, most notably Mount St. Helens (Dzurisin and others, 2005), in association with the emplacement of lava domes. During an over-flight on January 16, a new small dome was observed at the summit of Augustine Volcano. It was partly destroyed by the January 17 explosion, which blasted a 20 to 30 m crater in the dome. However, the lava dome continued to grow during January into early February and, after a period of hiatus, during March. The effusion of this final dome, and later two lava flows, defined the final phase of the activity (fig. 3).

The transition into the effusive phase was not observed by satellites due to cloudy weather that persisted from March 2–6. The radiant temperature values of two thermal anomalies that were observed on March 4 were greatly reduced by the cloud cover overhead. On the basis of seismic records, rockfalls increased on March 3 (Jacobs and McNutt, this volume), and on March 7 seismic activity once again became characterized by persistent, repetitive, and nearly identical earthquakes that increased in rate and size, forming a continuous signal by March 8 (Power and Lalla, this volume). Lava extrusion at the summit increased markedly in association with these signals (Power and others, 2006). As the volume of lava grew, two blocky lava flows moved down the volcano's north and north-east flanks (fig. 10). These deposits were highly unstable and generated multiple block-and-ash flows through regular collapses of volumes of fresh lava (Sentman and others, this volume; Vallance and others, this volume; Wessels and others, this volume)

The repetitive earthquakes began a slow decline in frequency after March 14 and disappeared by March 16 (Power and Lalla, this volume). A similar transition was seen in satellite data as thermal anomalies exhibited persistently high radiant temperatures (>45°C) until March 15–16, when temperatures began to decrease. Despite the cessation of effusive activity, frequent collapses of the dome and flows continued due to the unstable nature of the new material, leading to hotter material being exposed and contributing to the scatter seen in the overall cooling curve shown by the radiant temperatures (fig. 3).

Discussion

The eruption of Augustine Volcano provided an opportunity to robustly test monitoring methods and techniques recently developed by the AVORS group. The measurements these improvements made possible led to notable insights in three areas of interest: the patterns of thermal activity, ash cloud heights, and ash concentration mapping.

Table 3. Explosive events that occurred at Augustine Volcano during the explosive and continuous phase of its 2006 eruption.

[Time measurements are based on monitoring by seismic instruments. AKST, Alaska Standard Time; UTC, Coordinated Universal Time]

Event	Local time (AKST)	Time (UTC)	Duration (min: sec)
1	0444 11-Jan-06	1344 11-Jan-06	1:18
2	0512 11-Jan-06	1412 11-Jan-06	3:18
3	0424 13-Jan-06	1324 13-Jan-06	11:00
4	0847 13-Jan-06	1747 13-Jan-06	4:17
5	1122 13-Jan-06	2022 13-Jan-06	3:24
6	1640 13-Jan-06	0140 14-Jan-06	4:00
7	1858 13-Jan-06	0358 14-Jan-06	3:00
8	0014 14-Jan-06	0914 14-Jan-06	3:00
9	0758 17-Jan-06	1658 17-Jan-06	4:11
10	2024 27-Jan-06	0524 28-Jan-06	9:00
11	2337 27-Jan-06	0837 28-Jan-06	1:02
12	0204 28-Jan-06	1104 28-Jan-06	2:06
13	0742 28-Jan-06	1642 28-Jan-06	3:00
14	1430 28-Jan-06	2330 28-Jan-06	continuous

Patterns of Thermal Activity

Thermal anomalies for the Augustine eruption were defined by a combination of manual methods and automated detection using the Okmok II algorithm. Measurements using thermal-infrared channels on the GOES, AVHRR and MODIS satellite sensors are integrated values for areas of 1 km^2 and higher for each pixel (table 1). This limited spatial resolution limits the use of these datasets to describe the details of volcanic activity at Augustine. However, the high frequency of repeatability does allow trends to be seen. As described in the observations section these trends can be correlated to styles of activity, providing further supporting evidence for the definition of phases (fig. 2). More detailed descriptions of the activity and erupted products' thermal morphology require higher resolution thermal data (for example, ASTER), or use of ground-based thermal imaging (Sentman and others, this volume; Wessels and others, this volume). However, the satellite measurements can be used quantitatively to estimate erupted volumes and flux (Harris and others, 2007).

Ash Cloud Height Measurements

The 2006 Augustine eruption resulted in a large assortment of coincident observations that provided estimates or

measurements of volcanic cloud heights, more so than any previous Alaskan eruption. Typical measurement methods include cloud-top temperatures, wind shear, and pilot reports. Additionally, for the Augustine eruption a new technique, the ground-based NEXRAD radar, was available (Schneider and others, 2006). Each method can produce very different estimates of ash cloud heights and the recent Augustine eruptions were no exception (table 2).

Pilot observations provide on-site, instant estimates of the ash cloud heights but are also the least quantitative and generally give values much greater than other techniques. Measurements made by NEXRAD radar and the satellite cloud-top temperature also have the advantage of being collected at coincident times, allowing direct comparison. A normalized difference in percentage using the radar as control was calculated for each event using:

$$[(\text{Cloud-top Height Estimate} - \text{Radar Height Estimate}) / \text{Radar Height Estimate}] \times 100 \quad (1)$$

Radar is used as control because its radiometric response to the airborne particles is well known and the data were

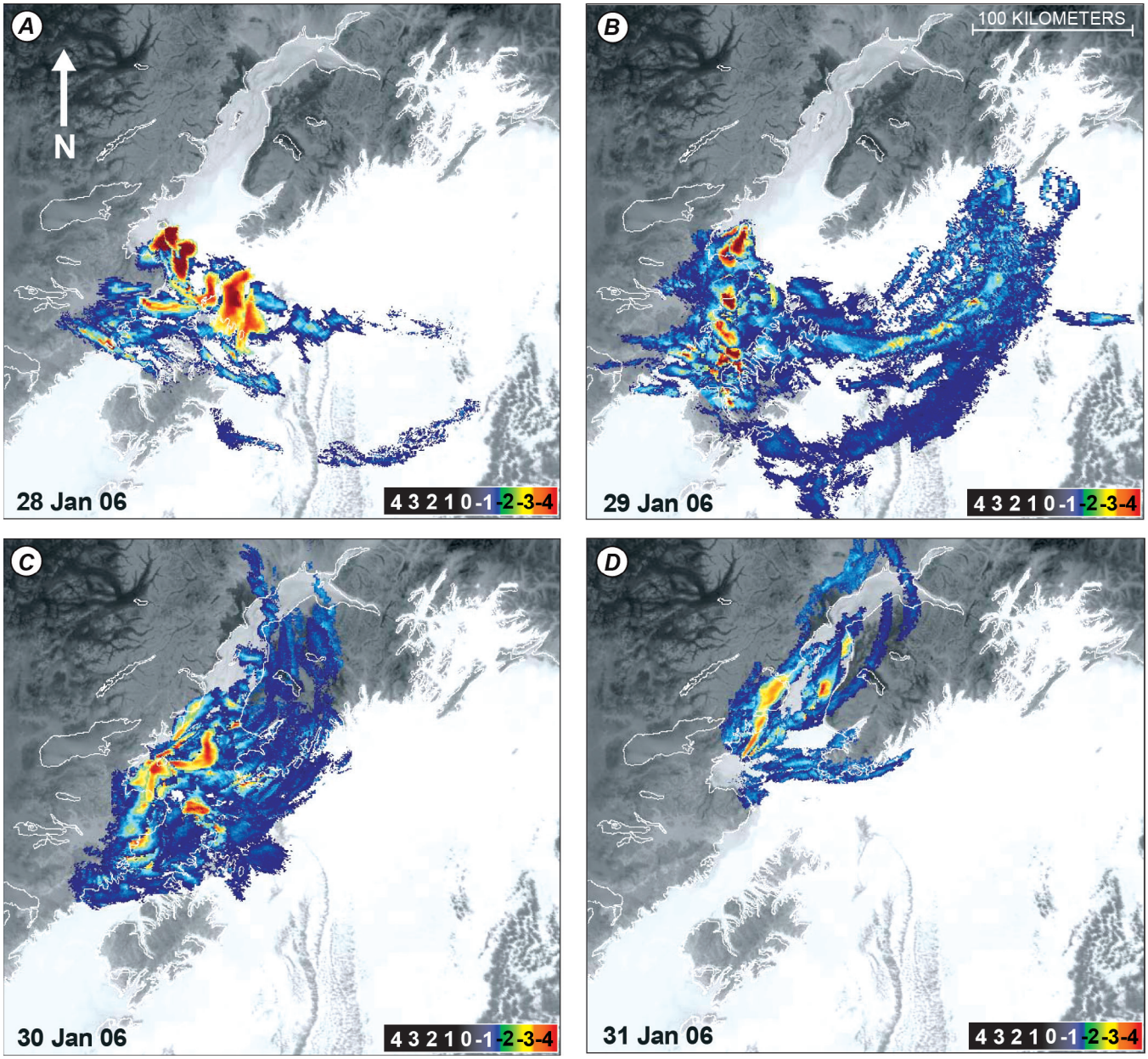

Figure 8. Composites of brightness temperature difference (BTD) data showing airborne ash distribution during the continuous phase of Augustine Volcano's 2006 eruption. Images show stacked data for one day's acquisitions on (*A*) January 28, (*B*) January 29, (*C*) January 30, and (*D*) January 31, 2006.

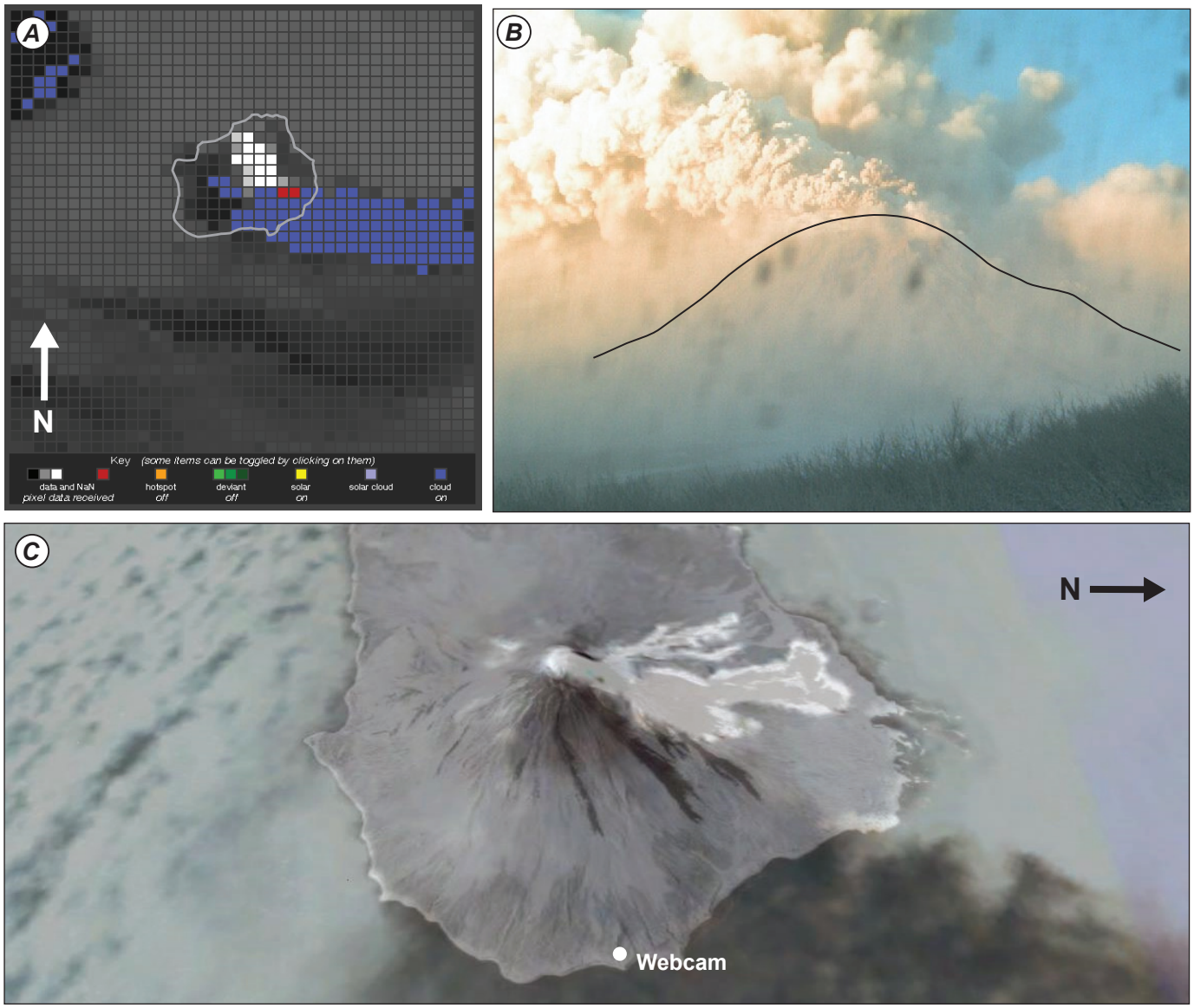

Figure 9. Views of ash clouds and pyroclastic flows generated during continuous phase of Augustine Volcano's 2006 eruption. *A*, Web viewer showing thermal anomaly (in white and shades of gray) in Advanced Very High Resolution Radiometer (AVHRR) image acquired 0829 AKST (1729 UTC) January 30. The white line defines Augustine Island. *B*, On island webcam view at 1016 AKST on January 29. The volcanic edifice is defined by a black line. *C*, Advanced Spaceborne Thermal Emission and Reflection Radiometer image acquired February 1, 2006, overlain on terrain in Google Earth. White areas show hot deposits. Views of hot deposits on east side of island are blocked by the ash cloud.

recorded consistently during the early stages of each eruption. Eight of the 14 events had sufficient satellite data to make this comparison. The comparison showed that all the cloud-temperature height estimates deviated by no more than 15 percent from the radar measurements (table 2).

However, there are some problems with the cloud-top temperature data. First, seven of the volcanic clouds were higher than 8.5 km, the approximate lower boundary for the tropopause, which means there are multiple heights that correlate to the cloud-top temperature. For these events it was assumed that the cloud ascended through the tropopause and reached natural buoyancy at the first height, which corresponded with the measured temperature. In reality, even if this was the case for the bulk of the cloud, there was likely some overshoot. Second, heights could not be estimated for six of the events due to missing data, because the cloud was translucent and valid temperatures could not be derived, or the cloud-top temperature was colder than the temperature of the atmosphere suggesting that this cloud was super-cooled and had not yet equilibrated to its surroundings (event 9).

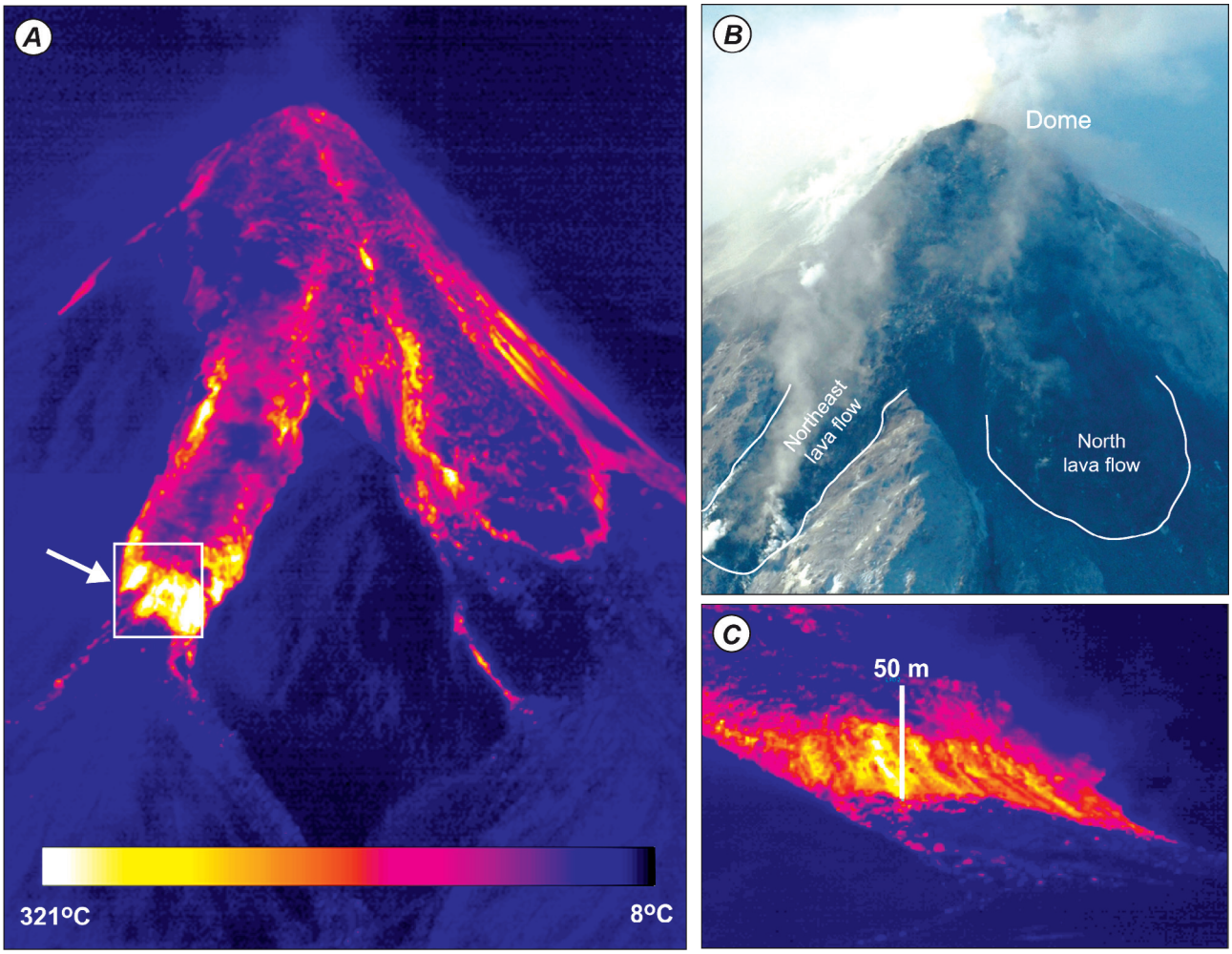

Figure 10. *A*, Forward looking infrared (FLIR) camera image showing Augustine Volcano summit lava dome and block flows on March 10, 2006 (FLIR images by Rick Wessels, AVO/USGS; Wessels and others, this volume). *B*, Photograph captured simultaneously with FLIR image (Photograph by Game McGimsey, AVO/USGS). *C*, Close-up of beveled front of the north-east lava flow. Location and angle of view shown by the white box and arrow in *A*.

Also, the comparisons for events 7 and 8 used GOES data, which has 8 km pixels, much larger than the 1.1 km pixels in AVHRR data. Thus GOES data are more likely to include a mixture of ground and cloud temperatures, resulting in a warmer reading and lower height estimate. Yet these still gave values to within the ±15 percent difference range.

Some of the variations in height estimates can be attributed to electromagnetic wavelengths used in detection. The NEXRAD method uses microwave energy and is sensitive to particle size and concentration. The cloud-top method uses thermal-infrared satellite data that detects smaller particles than radar does, and includes gaseous components (Schneider and others, 2006). Pilot reports are based on visual observations and are sensitive to water vapor and other gases appearing as the visible part of the cloud and are very qualitative (Simpson and others, 2001; Tupper and others, 2007). More quantitative visual measurements were made using oblique photography taken at the approximately the same time satellite images were acquired. These photos provided insight into the vertical structure of the eruption column and its relationship to the map view seen by satellites.

The eruption of event 6 provided an opportunity to compare and contrast these different techniques of cloud height measurement. Event 6 started at 1640 AKST on January 13. A satellite image at 1645 AKST (0145 UTC, January 14) showed a circular cloud over the volcano that was approximately 16 km across. A pilot reported a volcanic cloud up to 30,000 to 35,000 ft (9.1–10.7 km). The thermal-infrared image (fig. 11*A*) shows top-surface temperatures ranging from −15 to −30°C along its perimeter with much colder temperatures down to –53°C near the center, suggesting a height of 32,000 ft (10 km). Temperature differences in the cloud-top are usually

related to variations in height (Tupper and others, 2004), although if portions of the volcanic cloud are translucent, then the signal from the warm ground combines with the cold cloud and increases the detected temperature values. NEXRAD gave values of 34,000 ft (10.5 km).

A ground-based photograph at 1650 AKST (0150 UTC) showed a profile view of the same eruption column (fig.11*A*). The photograph was taken from Lake Clark, west of the volcano (fig. 11*B*). It shows a relatively flat cloud-top along the perimeter with a thin outer edge that thickens inward. Away from the perimeter the cloud's bottom extends below the ridge in the foreground and it is unclear whether it is still attached to the volcanic vent, making "plume" the more correct terminology. Seismic records indicated that the event had ended and additional material was no longer being erupted, implying it was at this point a volcanic cloud. Comparing the satellite image to the photograph shows that the warmer cloud temperatures approximately coincide with the thinner and translucent (few kilometers thick) perimeter. The central core is colder and most opaque. Towards the center of the cloud-top a high peak can be observed that most likely coincides with the coldest temperature. On the basis of measurements using the photograph, this cloud-top was estimated to be at an altitude of 9 km (29,500 ft), a value at the lower end of estimates by the other techniques.

Ash Composite and Concentration Maps

The ash composite technique is useful in delineating areas impacted by airborne ash. To show the area impacted by the Augustine eruptions, the most-negative ash composites were generated for January 11 (events 1–2), January 13 and 14 (events 3–8), January 28 through 31 (events 10–14 and continuous ash emission; fig. 8), and one image that combined images from all these dates (fig. 12). The eruption on January 17 was not included because it did not produce a cloud that could be identified by BTD techniques in satellite data. The combined image showed that the areas most heavily impacted based on airborne ash detected on satellite data are north, east, and south of the volcano.

These ash composites were used to identify and delineate concentrations based on ash signal strength. Ash signals less than −3 were assumed to include areas with the highest concentrations and were restricted to the area within approximately 80 km of the volcano (fig. 13). The ash signals with strengths 0 to −3 were assumed to include areas with moderate ash concentrations and extended as far as approximately 400 km from the volcano (fig. 13). Most of the ground-based ash samples, observations of ash deposits, and ash falling in the Cook Inlet area were located within the moderate ash concentration map unit. The majority of these samples and reports indicated light ash fall.

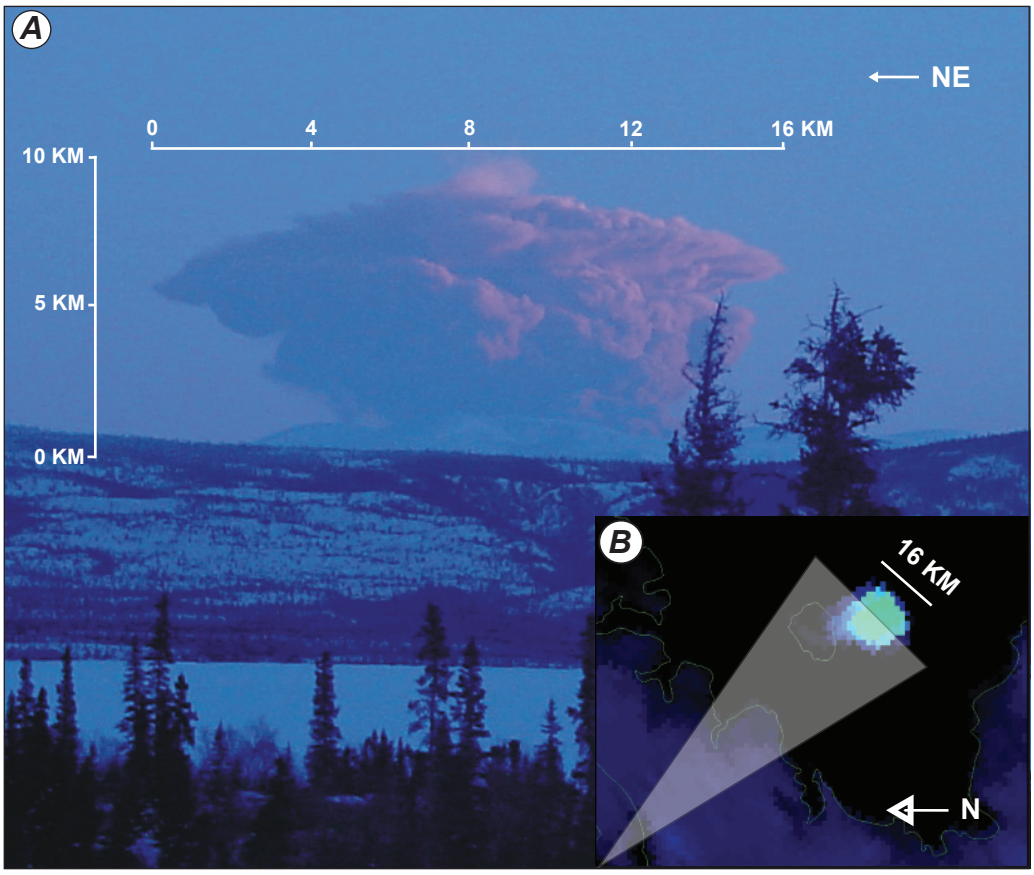

Figure 11. A comparison of an oblique photograph of an Augustine Volcano plume to a coincident satellite image. *A*, Oblique photograph of eruption cloud from event 6 on January 13, 2006 (Photograph by Leslie Beard). *B*, Advanced Very High Resolution Radiometer (AVHRR) band 4 image acquired at 1645 AKST, January 13, 2006 (0145 UTC, January 14).

The Puff dispersion model predicted the extent of ash beyond that observed on satellite data (Webley and others, this volume). These distal areas were north and east of the volcano and were considered to be the lowest concentrations (fig. 13). Measurements of airborne ash from ground-based LIDAR instruments at Fairbanks and Barrow (Sassen and others, 2007; Webley and others, 2008), aerosol samplers in Fairbanks and a snow sampler at Shasta, California (C. Cahill, written communication) validated the presence of the distal ash cloud. The Shasta ash was the most distant sample, at 1,800 miles (3,000 km) from the volcano. The distal portions of the plume presumably contained concentrations of ash below the detection limits of the satellite sensors and/or environmental conditions prevent detection by these sensors. It is likely that there were low airborne ash concentrations in these areas because no ash fall was reported by observers.

Conclusions

The 2006 eruption of Augustine Volcano provided an opportunity to test the robustness of several new tools that have been developed over the past few years by the AVORS group. It was also a catalyst for the development of new techniques and methodologies that have further complemented these primarily Web-based tools.

The thermal trends were observed at Augustine using satellite data in the 3 to 5 micron range. These data proved to be a good proxy for identifying the phases of eruption that were delineated using a range of geophysical measurements and visual observations. The success of the satellite data in defining the phases of eruption demonstrates the utility of remote sensing for monitoring Alaska's more remote but active volcanoes, such as Cleveland Volcano in the Aleutian Islands, which are not otherwise directly instrumented.

The multiple ash clouds erupted by Augustine allowed a comparison of multiple techniques that assessed the altitudes reached by these clouds. These methods included the use of satellite-based temperatures, ground-based radar, oblique photography, and pilot reports (PIREP). Instrument measurements proved to fairly consistent (table 2), but greater discrepancies occurred when comparisons were made to pilot's visual observations. These findings provide a cautionary tale for relying solely on one source for these data during monitoring operations.

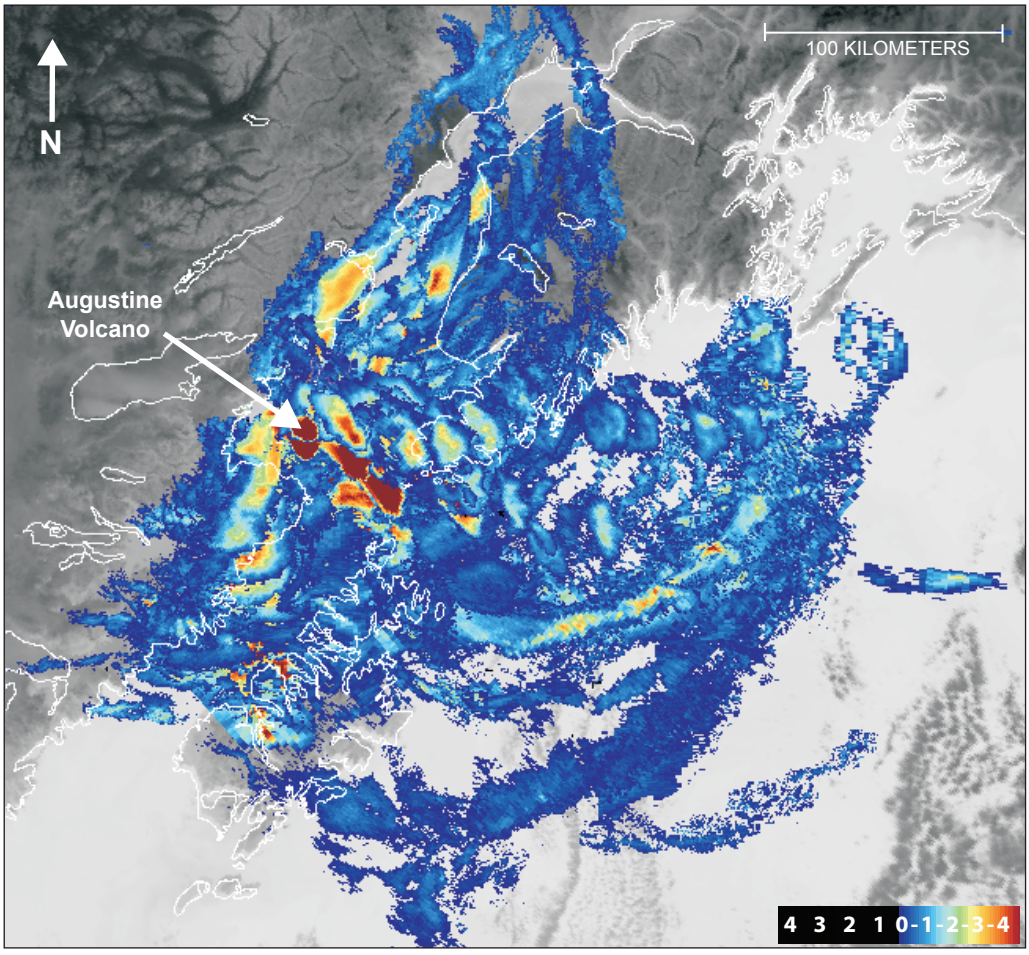

Figure 12. Brightness temperature difference (BTD) image showing combined airborne ash distributions from explosive Augustine Volcano eruptions. Image was created using Advanced Very High Resolution Radiometer (AVHRR) data showing the most negative ash composites for January 11 (events 1–2), January 13 and 14 (events 3–8), and January 28 through 31, 2006 (events 10–14 and continuous ash).

Airborne ash from the Augustine eruptions primarily impacted areas to the north, east, and south of the volcano, including Anchorage, Alaska's largest city, and towns on the Kenai and Alaska Peninsulas and Kodiak Island. Light ash fall was reported at many locations in the Cook Inlet region. Distal portions of the cloud drifted north over Fairbanks and Barrow, Alaska, and as far away as Mount Shasta, California. Various airlines cancelled multiple flights into the Ted Stevens International Airport, Anchorage, in response to this eruption.

A significant shortcoming of present hazard mitigation is the ability to detect or accurately predict the concentration of airborne ash. Quantitative ash concentrations are critical information to assess potential hazards to machinery (aircraft), transportation infrastructure, buildings and health (Blong, 1984; Horwell and Baxter, 2006). The U.S. military considers ash concentrations greater than 50 mg/m^3 dangerous to jet engines (Foreman, 1994). The concentration of ash that resulted in the failure of all four engines on the KLM 747 jet aircraft in Alaska in 1989 were estimated to be 2,000 mg/m^3 (Foreman, 1994), and ash concentrations based on those on the ground below the airspace of the encounter were estimated to be 500 g/m^2 with 75 percent of these particles smaller than 20 microns (Casadevall, 1994). The U.S. National Ambient Air Quality Standards (NAAQS) state that particles smaller than 10 microns are dangerous to human health, as they can enter and accumulate the respiratory system (U.S Environmental Protection Agency, 2007). Particles 2.5 microns and less are referred to as fine particles and can lodge deeply in the lungs. NAAQS, under the clean air act, requires particulate matter of 10 microns and smaller not to exceed 150 µg/m^3/24 hr, and particles 2.5 microns and smaller are limited to 35 µg/m^3/24 hr. These limits are based on values that protect public health, as well as damage to animals, crops, vegetation, and buildings.

The ash concentration map created using data from the Augustine eruption (fig. 13) is a prototype for the type of information that is required. One limitation of these data is

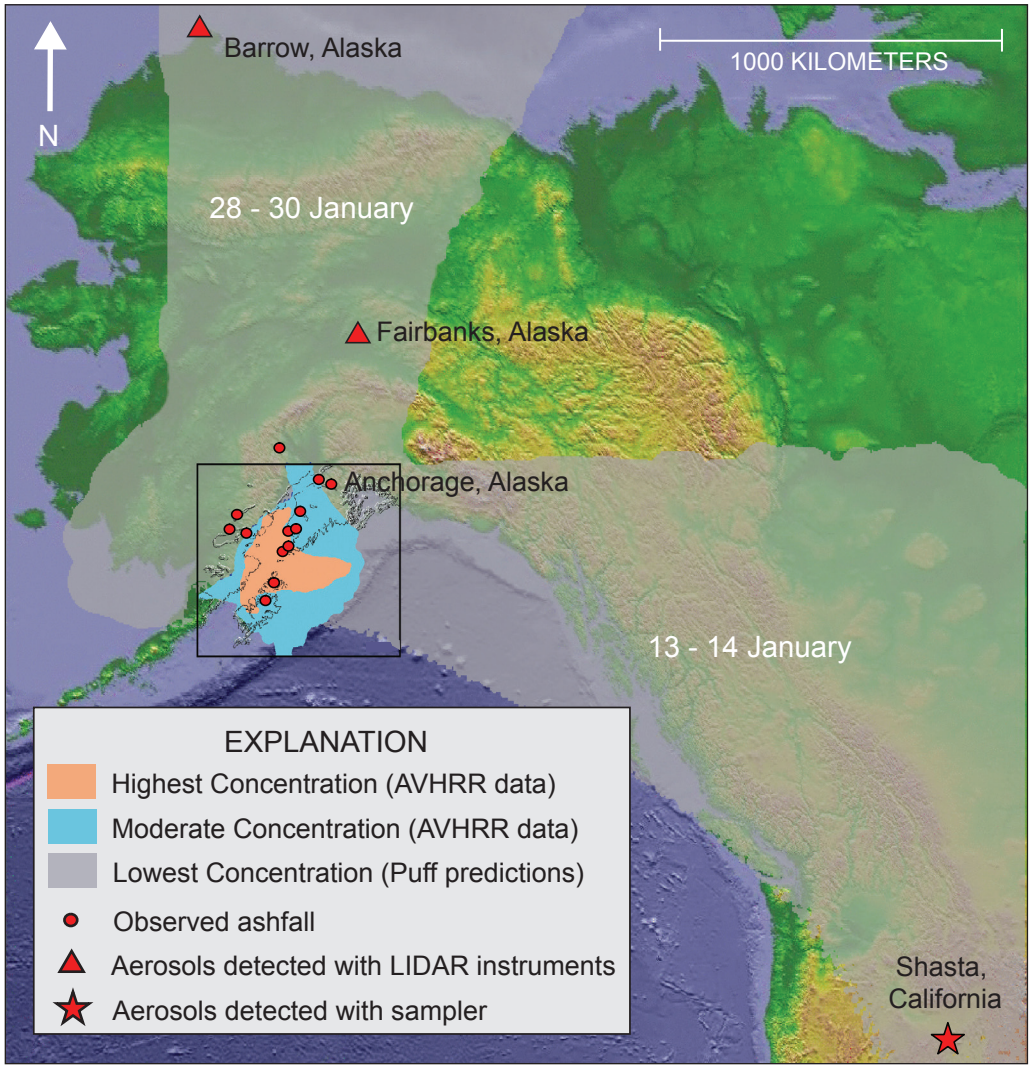

Figure 13. Map of relative ash concentrations from the eruptions of Augustine Volcano in January 2006. Based on combined airborne ash distributions (fig. 12), Puff model predictions (Webley and others, this volume), and ground-based observations and samples. AVHRR, Advanced Very High Resolution Radiometer; LIDAR, light detection and ranging.

that concentration assessments are based on relative quantities and do not give numerical values. The map units need to be calibrated so that they can be related to the hazard levels that can impact health and infrastructure, and to quantify the impact of a given event. This is an understanding that might prove crucial the next time Augustine or a similar volcano in the region erupts.

Acknowledgments

The authors would like to acknowledge the contributions of all the faculty, staff, and students that contributed to the AVORS's monitoring efforts during the eruption Augustine. In particular we thank Dave Schneider (AVO/U.S. Geological Survey) for his comments on cloud heights and William Ross (University of Alaska Fairbanks) and Joe Lovick (AVO/University of Alaska Fairbanks) for their contributions to the ash composite and distribution mapping.

References Cited

Blong, R.J., 1984, Volcanic Hazards—a sourcebook on the effects of eruptions: Sydney, Australia, Academic Press, 424 p.

Casadevall, T.J., 1994, The 1989–1990 eruption of Redoubt Volcano, Alaska—impacts on aircraft operations: Journal of Volcanology and Geothermal Research, v. 62,p. 301–316.

Cervelli, P.F., Fournier, T., Freymueller, J., and Power, J.A., 2006, Ground deformation associated with the precursory unrest and early phases of the January 2006 eruption of Augustine Volcano, Alaska: Geophysical Research Letters, v. 33, p. 5.

Coombs, M.L., Bull, K.F., Vallance, J.W, Schneider, D.J., Thoms, E.E., Wessels, R.L., and McGimsey, R.G., 2010, Timing, distribution, and volume of proximal products of the 2006 eruption of Augustine Volcano, *in* Power, J.A., Coombs, M.L., and Freymueller, J.T., eds., The 2006 eruption of Augustine Volcano, Alaska: U.S. Geological Survey Professional Paper 1769 (this volume).

Dean, K., Bowling, S.A., Shaw, G., and Tanaka, H., 1994, Satellite analyses of movement and characteristics of the Redoubt Volcano plume, January 8, 1990: Journal of Volcanology and Geothermal Research, v. 62, no. 1–4, p. 339–352.

Dean, K.G., Dehn, J., Engle, K., Izbekov, P., and Papp, K., 2002, Operational satellite monitoring of volcanoes at the Alaska Volcano Observatory, *in* Harris, A.J.H., Wooster, M., and Rothery, D.A., eds., Monitoring volcanic hotspots using thermal remote sensing: Advances in Environmental Monitoring and Modeling, v. 1, no. 3, p. 70–97.

Dean, K.G., Dehn, J., Papp, K.R., Smith, S., Izbekov, P., Peterson, R., Kearney, C., and Steffke, A., 2004, Integrated satellite observations of the 2001 eruption of Mt. Cleveland, Alaska: Journal of Volcanology and Geothermal Research, v. 135, no. 1–2, p. 51–73.

Dehn, J., Dean, K., and Engle, K., 2000, Thermal monitoring of North Pacific volcanoes from space: Geology, v. 28, no. 8, p. 755–758.

Dehn, J., Dean, K.G., Engle, K., and Izbekov, P., 2002, Thermal precursors in satellite images of the 1999 eruption of Shishaldin Volcano: Bulletin of Volcanology, v. 64, no. 8, p. 525–534.

Dzurisin, D., Vallance, J.W., Gerlach, T.M., Moran, S.C., and Malone, S.D., 2005, Mount St. Helens reawakens: EOS (American Geophysical Union Transactions), v. 86, no. 3, p. 25.

Foreman, P., 1994, Warning systems and pilot actions in ash and aviation safety, *in* Proceedings of the first international symposium on volcanic ash and aviation safety: U.S. Geological Survey Bulletin 2047, p. 163–168.

Harris, A.J.L., Blake, S., Rothery, D.A., and Stevens, N. F., 1997, A chronology of the 1991 to 1993 Mount Etna eruption using advanced very high resolution radiometer data—implications for real-time thermal volcano monitoring: Journal of Geophysical Research—Solid Earth, v. 102, no. B4, p. 7985–8003.

Harris, A.J.L., Dehn, J., Calvari, S., 2007, Lava effusion rate definition and measurement—a review: Bulletin of Volcanology, v. 70, p. 1–22.

Harris, A.J.L., Flynn, L.P., Dean, K., Pilger, E., Wooster, M. J., Okubo, C., Mouginis-Mark, P.J., Garbeil, H., Thornber, C., De la Cruz-Reyna, S., Rothery, D.A., and Wright, R., 2000, Real-time satellite monitoring of volcanic hot spots, *in* Mouginis-Mark, P.J., Crisp, J.A., and Fink, J.H., eds., remote sensing of active volcanism: Geophysical Monograph, American Geophysical Union, v. 116, p. 139–159.

Holasek, R.E., and Rose, W.I., 1991, Anatomy of 1986 Augustine volcano eruptions as recorded by multispectral image-processing of digital AVHRR weather-satellite data: Bulletin of Volcanology, v. 53, no. 6, p. 420–435.

Holasek, R.E., Self, S., and Woods, A.W., 1996, Satellite observations and interpretation of the 1991 Mount Pinatubo eruption plumes: Journal of Geophysical Research—Solid Earth, v. 101, no. B12, p. 27635–27665.

Horwell, C.J., and Baxter, P.J., 2006, The respiratory health hazards of volcanic ash—a review for volcanic risk mitigation: Bulletin of Volcanology, v. 69, p. 1–24.

Jacobs, K.M., and McNutt, S.R., 2010, Using seismic *b*-values to interpret seismicity rates and physical processes during the preeruptive earthquake swarm at Augustine Volcano 2005–2006, *in* Power, J.A., Coombs, M.L., and Freymueller, J.T., eds., The 2006 eruption of Augustine Volcano, Alaska: U.S. Geological Survey Professional Paper 1769 (this volume).

McGee, K.A., Doukas, M.P., McGimsey, R.G., Neal, C.A., and Wessels, R.L., 2010, Emission of SO_2, CO_2, and H_2S from Augustine Volcano, 2002–2008, *in* Power, J.A., Coombs, M.L., and Freymueller, J.T., eds., The 2006 eruption of Augustine Volcano, Alaska: U.S. Geological Survey Professional Paper 1769 (this volume).

McNutt, S.R., Tytgat, G., Estes, S.A., and Stihler, S.D., 2010, A parametric study of the January 2006 explosive eruptions of Augustine Volcano, using seismic, infrasonic, and lightning data, *in* Power, J.A., Coombs, M.L., and Freymueller, J.T., eds., The 2006 eruption of Augustine Volcano, Alaska: U.S. Geological Survey Professional Paper 1769 (this volume).

Miller, T.P., and Chouet, B.A., 1994, The 1989–1990 eruptions of Redoubt Volcano—an introduction: Journal of Volcanology and Geothermal Research, v. 62, p. 1–10.

Paskievitch, J., Read, C., and Parker, T., 2010, Remote telemetered and time-lapse cameras at Augustine Volcano, *in* Power, J.A., Coombs, M.L., and Freymueller, J.T., eds., The 2006 eruption of Augustine Volcano, Alaska: U.S. Geological Survey Professional Paper 1769 (this volume).

Patrick, M.R., Dehn, J., Papp, K.R., Lu, Z., Dean, K., Moxey, L., Izbekov, P., and Guritz, R., 2003, The 1997 eruption of Okmok Volcano, Alaska—a synthesis of remotely sensed imagery: Journal of Volcanology and Geothermal Research, v. 127, no. 1–2, p. 87–105.

Power, J.A., Nye, C.J., Coombs, M.L., Wessels, R.L., Cervelli, P.F., Dehn, J., Wallace, K.L., Freymueller, J.T., and Doukas, M.P., 2006, The reawakening of Alaska's Augustine Volcano: EOS (American Geophysical Union Transactions), v. 87, no. 37, p. 373.

Power, J.A., and Lalla, D.J., 2010, Seismic observations of Augustine Volcano, 1970–2007, *in* Power, J.A., Coombs, M.L., and Freymueller, J.T., eds., The 2006 eruption of Augustine Volcano, Alaska: U.S. Geological Survey Professional Paper 1769 (this volume).

Prata, A.J., 1989, Observations of volcanic ash clouds in the 10–12 um window using AVHRR/2 data: International Journal of Remote Sensing, v. 10, no. 4–5, p. 751–761.

Ramsey, M., and Dehn, J., 2004, Spaceborne observations of the 2000 Bezymianny, Kamchatka eruption—the integration of high-resolution ASTER data into near real-time monitoring using AVHRR: Journal of Volcanology and Geothermal Research, v. 135, no. 1–2, p. 127–146.

Roach, A.L., Benoit, J.P., Dean, K.G., and McNutt, S.R., 2001, The combined use of satellite and seismic monitoring during the 1996 eruption of Pavlof volcano, Alaska: Bulletin of Volcanology, v. 62, no. 6–7, p. 385–399.

Rose, W.I., Bluth, G.J.S., Schneider, D.J., Ernst, G.G.J., Riley, C.M., Henderson, L.J., and McGimsey, R. G., 2001, Observations of volcanic clouds in their first few days of atmospheric residence—the 1992 eruptions of Crater Peak, Mount Spurr volcano, Alaska: Journal of Geology, v. 109, no. 6, p. 677–694.

Rose, W.I., Delene, D.J., Schneider, D.J., Bluth, G.J.S., Krueger, A.J., Sprod, I., McKee, C., Davies, H.L. and Ernst, G.G.J., 1995, Ice in the 1994 Rabaul eruption cloud—implications for volcano hazard and atmospheric effects: Nature, v. 375, p. 477–479.

Rose, W.I., and Mayberry, G.C., 2000, Use of GOES thermal infrared imagery for eruption scale measurements, Soufriere Hills, Montserrat: Geophysical Research Letters, v. 27, no. 19, p. 3097–3100.

Sassen, K., Zhu, J., Webley, P., Dean, K., and Cobb, P., 2007, Volcanic ash plume identification using polarization lidar — Augustine eruption, Alaska: Geophysical Research Letters, L08803, v. 34, p. 1–4.

Schneider, D.J., Dean, K.G., Dehn, J., Miller, T.P., and Kirianov, V.Y., 2000, Monitoring and analyses of volcanic activity using remote sensing data at the Alaska Volcano Observatory; case study for Kamchatka, Russia, December 1997, *in* Mouginis-Mark, P.J., Crisp, J.A., and Fink, J.H., eds., Remote sensing of active volcanism: Geophysical Monograph, American Geophysical Union, v. 116, p. 65–85.

Schneider, D.J., Rose, W.I., and Kelley, L., 1995, Tracking of 1992 eruption clouds from Crater Peak vent of Mount Spurr Volcano, Alaska, using AVHRR, *in* Keith, T.E.C., ed., The 1992 eruptions of Crater Peak vent, Mount Spurr Volcano, Alaska: U.S. Geological Survey Bulletin 2139, p. 27–36.

Schneider, D.J., Rose, W.I., Coke, L.R., Bluth, G.J.S., Sprod, I.E., and Krueger, A.J., 1999, Early evolution of a stratospheric volcanic eruption cloud as observed with TOMS and AVHRR: Journal of Geophysical Research — Atmospheres, v. 104, no. D4, p. 4037–4050.

Schneider, D.J., Scott, C., Wood, J., Hall, T., 2006, NEXRAD weather radar observations of the 2006 Augustine Volcanic eruption clouds: Eos (American Geophysical Union Transactions), v. 87, no. 52, Fall Meet. Supplement, abstract V51C-1686.

Searcy, C., Dean, K., and Stringer, W., 1998, PUFF—a high-resolution volcanic ash tracking model: Journal of Volcanology and Geothermal Research, v. 80, no. 1–2, p. 1–16.

Sentman, D.D., McNutt, S.R., Stenbaek-Nielsen, H.C., Tytgat, G., and DeRoin, N., 2010, Imaging observations of thermal emissions from Augustine Volcano using a small astronomical camera, *in* Power, J.A., Coombs, M.L., and Freymueller, J.T., eds., The 2006 eruption of Augustine Volcano, Alaska: U.S. Geological Survey Professional Paper 1769 (this volume).

Simpson, J.J., Hufford G., Pieri D., and Berg J., 2001, Response to ‘‘Comments on ‘Failures in detecting volcanic ash from a satellite-based technique’’’: Remote Sensing of Environment, v. 78, p. 347–357.

Tupper, A., Carn, S., Davey, J., Kamada, Y., Potts, R., Prata, F., and Tokuno, M., 2004, An evaluation of volcanic cloud detection techniques during recent significant eruptions in the western “Ring of Fire”: Remote Sensing of Environment, v. 91, no. 1, p. 27–46.

Tupper A., Itikarai I., Richards M., Prata F., Carn S., Rosenfeld D., 2007, Facing the Challenges of the international airways volcano watch—The 2004/05 Eruptions of Manam, Papua New Guinea: Weather and Forecasting, v. 22, no. 1, p. 175–191.

U.S. Environmental Protection Agency, 2007, Technology Transfer Network, National Ambient Air Quality Standards (NAAQS): [http://www.epa.gov/ttn/naaqs/pm/pm10_index.html].

van Manen, S.M., Dehn, J., West, M.E., Blake, S., and Rothery, D.A., 2010, The 2006 eruption of Augustine volcano—Combined analyses of thermal satellite data and reduced displacement, *in* Power, J.A., Coombs, M.L., and Freymueller, J.T., eds., The 2006 eruption of Augustine Volcano, Alaska: U.S. Geological Survey Professional Paper 1769 (this volume).

Vallance, J.W., Bull, K.F., and Coombs, M.L., 2010, Pyroclastic flows, lahars, and mixed avalanches generated during the 2006 eruption of Augustine Volcano, *in* Power, J.A., Coombs, M.L., and Freymueller, J.T., eds., The 2006 eruption of Augustine Volcano, Alaska: U.S. Geological Survey Professional Paper 1769 (this volume).

Wallace, K.L., Neal, C.A., and McGimsey, R.G., 2010, Timing, distribution and character of tephra fall from the 2005–2006 eruption of Augustine Volcano, *in* Power, J.A., Coombs, M.L., and Freymueller, J.T., eds., The 2006 eruption of Augustine Volcano, Alaska: U.S. Geological Survey Professional Paper 1769 (this volume).

Webley, P.W., Dean, K.G., Collins, R., Fochesatto, J., Sassen, K., Atkinson, D., Cahill, C., and Prata, A.J., 2008, Validation of a volcanic ash dispersion model during late January/early February 2006 eruption of Mount Augustine Volcano: Bulletin of American Meteorological Society, v. 89, p. 1647–1658.

Webley, P.W., Dean, K.G., Dehn, J., Bailey, J.E., and Peterson, R., 2010, Volcanic-ash dispersion modeling of the 2006 eruption of Augustine Volcano using the Puff model, *in* Power, J.A., Coombs, M.L., and Freymueller, J.T., eds., The 2006 eruption of Augustine Volcano, Alaska: U.S. Geological Survey Professional Paper 1769 (this volume).

Wen, S., and Rose, W., 1994, Retrieval of sizes and total masses of particles in volcanic clouds using AVHRR bands 4 and 5: Journal of Geophysical Research — Atmospheres, v. 99, no. D3, p. 5421–5431.

Wessels, R.L., Coombs, M.L., Schneider, D.J., Dehn, J., and Ramsey, M.S., 2010, High-resolution satellite and airborne thermal infrared imaging of the 2006 eruption of Augustine Volcano, *in* Power, J.A., Coombs, M.L., and Freymueller, J.T., eds., The 2006 eruption of Augustine Volcano, Alaska: U.S. Geological Survey Professional Paper 1769 (this volume).

Appendix 1. Satellite Observations

Table 4. Satellite observations of gas emissions from Augustine Volcano on 12–13 December 2005.

[AKST, Alaska Standard Time; UTC, Coordinated Universal Time; AVHRR, Advanced Very High Resolution Radiometer; MODIS, Moderate Resolution Imaging Spectroradiometer]

Satellite sensor	Time, date (AKST)	Time, date (UTC)	Length (km)	Direction	Comments
AVHRR	1310, 12-Dec	2210, 12-Dec	>110	SE	Visible in B2 and B3, no B4m5 signal
MODIS	1323, 12-Dec	2223, 12-Dec	125	SE	Very distinct plume
AVHRR	1356, 12-Dec	2256, 12-Dec	85	SE	Very faint steam plume, faint B4m5 signal
AVHRR	1423, 12-Dec	2323, 12-Dec	120	SE	Faint steam plume, no B4m5
AVHRR	1452, 12-Dec	2352, 12-Dec	30	SE	Very faint steam plume, faint B4m5
AVHRR	1605, 12-Dec	0105, 13-Dec	NA	E	Mysterious cloud, defined by a few pixels
AVHRR	0442, 13-Dec	1342, 13-Dec	100	ENE	Very distinct plume, with some B4m5 signal

Table 5. Satellite observations of volcanic clouds on January 11, 2006.

[Height measurements based on cloud temperatures. AKST, Alaska Standard Time; UTC, Coordinated Universal Time; BTD, Brightness Temperature Difference; GOES, Geostationary Operational Environmental Satellites; AVHRR, Advanced Very High Resolution Radiometer]

Satellite sensor	Time, date (AKST)	Time, date (UTC)	Plume temp (°C)	Max. BTD signal	Plume height (km)
AVHRR	0448, 11-Jan	1348, 11-Jan	−46	NA	7
AVHRR	0525, 11-Jan	1425, 11-Jan	−55	NA	8.5
GOES	0530, 11-Jan	1430, 11-Jan	NA	−2.1	NA
GOES	0600, 11-Jan	1500, 11-Jan	NA	−1.7	NA
GOES	0630, 11-Jan	1530, 11-Jan	NA	−2.2	NA
AVHRR	0659, 11-Jan	1559, 11-Jan	NA	−2.7	NA
GOES	0730, 11-Jan	1630, 11-Jan	NA	−3.1	NA
AVHRR	0740, 11-Jan	1640, 11-Jan	NA	−1.8	NA
AVHRR	0839, 11-Jan	1739, 11-Jan	NA	−1.2	NA

Table 6. Satellite observations of volcanic clouds on January 13–14, 2006.

[Height measurements based on cloud temperatures. AKST, Alaska Standard Time; UTC, Coordinated Universal Time; BTD, Brightness Temperature Difference; GOES, Geostationary Operational Environmental Satellites; AVHRR, Advanced Very High Resolution Radiometer]

Satellite sensor	Time, date (AKST)	Time, date (UTC)	Plume temp. (°C)	Max. BTD signal	Plume height (km)
AVHRR	0428, 13-Jan	1328, 13-Jan	−54[1]	NA	8 to 9
AVHRR	0456, 13-Jan	1356, 13-Jan	−52[1]	NA	8, 9.5
AVHRR	0637, 13-Jan	1537, 13-Jan	NA	−4.0	NA
AVHRR	0655, 13-Jan	1555, 13-Jan	NA	−4.0	NA
AVHRR	0749, 13-Jan	1649, 13-Jan	NA	−3.4	NA
AVHRR	0834, 13-Jan	1734, 13-Jan	NA	−3.2	NA
AVHRR	1024, 13-Jan	1924, 13-Jan	−45[1]	−3.0	6.5, 13.5
GOES	1130, 13-Jan	2030, 13-Jan	−41	−2.1	NA
AVHRR	1142, 13-Jan	2042, 13-Jan	−54	NA	8 to 9
GOES	1200, 13-Jan	2100, 13-Jan	−46	−2.1	NA
AVHRR	1203, 13-Jan	2103, 13-Jan	−51	NA	7.5
GOES	1230, 13-Jan	2130, 13-Jan	−45	−2.3	NA
AVHRR	1246, 13-Jan	2146, 13-Jan	−49	−2.2	NA
GOES	1300, 13-Jan	2200, 13-Jan	−44	−3.3	NA
AVHRR	1322, 13-Jan	2222, 13-Jan	−45	−2.3	NA
AVHRR	1437, 13-Jan	2337, 13-Jan	NA	−1.5	NA
AVHRR	1645, 13-Jan	0145, 14-Jan	−53	NA	7.5, 10
GOES	1700, 13-Jan	0200, 14-Jan	−44	2.1	NA
GOES	1730, 13-Jan	0230, 14-Jan	−44	−2.5	NA
AVHRR	1743, 13-Jan	0243, 14-Jan	−49	−3.9	NA
GOES	1800, 13-Jan	0300, 14-Jan	−39	−3.0	NA
AVHRR	1829, 13-Jan	0329, 14-Jan	NA	−4.0	NA
GOES	1830, 13-Jan	0330, 14-Jan	−36	−3.4	NA
GOES	1930, 13-Jan	0430, 14-Jan	−49	−2.4	7, 11
GOES	2000, 13-Jan	0500, 14-Jan	−49	−3.9	7, 11
GOES	2030, 13-Jan	0530, 14-Jan	−46	−3.0	NA
GOES	2100, 13-Jan	0600, 14-Jan	−43	−3.3	NA
AVHRR	2136, 13-Jan	0636, 14-Jan	NA	−2.6	NA
AVHRR	2204, 13-Jan	0704, 14-Jan	NA	−2.9	NA
AVHRR	2316, 13-Jan	0816, 14-Jan	NA	−0.3	NA
GOES	0030, 14-Jan	0930, 14-Jan	−47	−3.2	7, 10.5
GOES	0100, 14-Jan	1000, 14-Jan	−50	−3.0	7, 10.5
GOES	0130, 14-Jan	1030, 14-Jan	−50	−2.3	7, 10.5
GOES	0200, 14-Jan	1100, 14-Jan	−47	−3.1	7, 10.5

[1]Measurement uncertain.

Table 7. Satellite observations of volcanic clouds on January 17, 2006.

[Height measurements based on cloud temperatures. AKST, Alaska Standard Time; UTC, Coordinated Universal Time; BTD, Brightness Temperature Difference; GOES, Geostationary Operational Environmental Satellites; AVHRR, Advanced Very High Resolution Radiometer; MODIS, Moderate Resolution Imaging Spectroradiometer]

Satellite sensor	Time, date (AKST)	Time, date (UTC)	Plume temp. (°C)	Max. BTD signal	Plume height (km)
GOES	0830, 17-Jan	1730, 17-Jan	−51	NA	7.5, 9.1, 11
AVHRR	0838, 17-Jan	1738, 17-Jan	−56	NA	NA
GOES	0900, 17-Jan	1800, 17-Jan	−50	−2.2[1]	7.3
GOES	0930, 17-Jan	1830, 17-Jan	−47	−1.6[1]	NA
GOES	1200, 17-Jan to 1800, 17-Jan	2100, 17-Jan to 0300, 18-Jan	NA	NA	NA
MODIS	1240, 19-Jan	2140, 19-Jan	NA	NA	Ash fall on ground

[1]Measurement uncertain.

Table 8. Satellite observations of volcanic clouds on January 28–29, 2006.

[Height measurements based on cloud temperatures. AKST, Alaska Standard Time; UTC, Coordinated Universal Time; BTD, Brightness Temperature Difference; AVHRR, Advanced Very High Resolution Radiometer]

Satellite sensor	Time, date (AKST)	Time, date (UTC)	Plume temp. (°C)	Max. BTD signal	Plume height (km)
AVHRR	2042, 27-Jan	0542, 28-Jan	−45	NA	6.5, 9.5, 14.5
AVHRR	2115, 27-Jan	0615, 28-Jan	NA	−6.9	NA
AVHRR	0332, 28 Jan	1232, 28 Jan	NA	−4.5	NA
AVHRR	0349, 28-Jan	1249, 28-Jan	NA	−2.8	NA
AVHRR	0516, 28 Jan	1416, 28 Jan	NA	−3.6	NA
AVHRR	0819, 28-Jan	1719, 28-Jan	−45[1]	−2.4	6, 6.5, 10
AVHRR	0917, 28-Jan	1817, 28-Jan	NA	−7.4	NA
AVHRR	1211, 28-Jan	2111, 28-Jan	NA	−3.7	NA
AVHRR	1334, 28-Jan	2234, 28-Jan	NA	−4.3	NA
AVHRR	1516, 28-Jan	0016, 29-Jan	NA	−7.5	NA
AVHRR	1911, 28-Jan	0411, 29-Jan	NA	−6.8	NA
AVHRR	0709, 29-Jan	0709, 29-Jan	NA	−3.0	NA

[1]Measurement uncertain.

The 2006 Eruption of Augustine Volcano, Alaska
Power, J.A., Coombs, M.L., and Freymueller, J.T., editors
U.S. Geological Survey Professional Paper 1769

Chapter 21

Volcanic-Ash Dispersion Modeling of the 2006 Eruption of Augustine Volcano Using the Puff Model

By Peter W. Webley[1], Kenneson G. Dean[1], Jonathan Dehn[1], John E. Bailey[1,2], and Rorik Peterson[3]

Abstract

Volcanic ash is one of the major potential hazards from volcanic eruptions. It can have both short-range effects from proximal ashfall and long range impacts from volcanic ash clouds. The timely tracking and understanding of recently emitted volcanic ash clouds is important, because they can cause severe damage to jet aircraft engines and shut down major airports. Dispersion models play an important role in forecasting the movement of volcanic ash clouds by being the only means to predict a clouds' trajectory. Where available, comparisons are possible to both remote-sensing data and observations from the ground and aircraft. This was demonstrated in January 2006, when Augustine Volcano erupted after about a 20-year hiatus. From January 11 to 28, 2006, there were 13 explosive events, with some lasting as long as 11 minutes and producing ash clouds as high as 10–12 km (33,000–39,000 ft) above mean sea level (a.m.s.l). From January 28 to February 4, 2006, there was a more continuous phase, with ash clouds reaching 4–5 km a.m.s.l (13,000–16,000 ft). During the eruption, the Puff dispersion model was used by the Alaska Volcano Observatory for trajectory forecasting of the associated volcanic ash eruption clouds. The six explosive events on January 13 and 14, 2006, were the first time the "multiple eruptions" capability of the Puff model was used during an eruption response. Here we show the Puff model predictions made during the 2006 Augustine eruption and compare these predictions to satellite remote-sensing data, Next Generation Radar (NEXRAD) radar, and ashfall measurements. In addition, we discuss how automated predictions for volcanoes at elevated alert status provide a quicker assessment of the risk from the potential ash clouds.

Introduction

Volcanoes can inject large volumes of ash into the atmosphere, posing a threat to international and domestic aircraft as well as disrupting local communities. Ash clouds can cause severe damage to jet aircraft engines and fuel lines, abrade aircraft internal and external surfaces and shut down major airports (Blong, 1984; Casadevall, 1993; Casadevall and Krohn, 1995; Miller and Casadevall, 2000). The North Pacific (NOPAC) region is a vast expanse, 5,000 km by 2,500 km, containing numerous active volcanoes, most of which are located in uninhabited areas along the Aleutian Islands and Kamchatka Peninsula, Russia (fig. 1). From 1975 to 2006, there were more than 200 separate volcanic ash clouds that reached at least 6 km (20,000 ft) above mean sea level (a.m.s.l) and potentially jeopardized aircraft safety. Within the NOPAC region, the agencies responsible for monitoring volcanoes and their associated eruptions are: Alaska Volcano Observatory (AVO), Kamchatka Volcano Emergency Response Team (KVERT), and Sakhalin Volcanic Eruption Response Team (SVERT) who work together with the Tokyo, Washington and Anchorage Volcanic Ash Advisory Centers (VAAC) to provide advisories of airborne volcanic ash. These advisories are used by the local meteorological watch offices to provide a Significant Meteorological Information (SIGMET) warning to the aviation community and volcanic ashfall warnings to local communities.

Volcanic Ash Transport and Dispersion (VATD) models play an important role in forecasting the movement of volcanic ash clouds and provide information that is otherwise

[1]Alaska Volcano Observatory, Geophysical Institute, University of Alaska Fairbanks, 903 Koyukuk Drive, Fairbanks, AK 99775.

[2]Now at: Scenarios Network for Alaska Planning, University of Alaska Geography Program, Fairbanks, AK 99775.

[3]Department of Mechanical Engineering, University of Alaska Fairbanks, P.O. Box 755905, Fairbanks, AK 99775.

difficult or impossible to collect from other data sources. When remote-sensing data and observations from the ground and aircraft are available, these model predictions can be compared and validated. Before, and in the initial stages of volcanic eruptions, VATD models are invaluable in predicting the movement of volcanic ash clouds and ensuring aviation safety. A warning system should be capable of a 5-minute response time once an eruption has been detected (Hufford and others, 2000). During these initial minutes, predicting the movement of the ash cloud and the potential impacts on aircraft are critical. Within Alaska, AVO's level of response to remote volcanic activity varies depending on the source and content of the observation. After receiving a report of an eruption, AVO works with the National Weather Service (NWS) and Federal Aviation Administration (FAA) for corroboration and to solicit additional information. AVO itself is a joint program of the United States Geological Survey (USGS), the Geophysical Institute of the University of Alaska Fairbanks (UAF-GI) and the State of Alaska Division of Geological and Geophysical Surveys (ADGGS).

VATD models provide the only means to quantitatively predict an ash cloud's trajectory. There are three VATD models often used for forecasting ash cloud motion in the NOPAC region: Canadian Emergency Response Model (CanERM: Pudykiewicz, 1988, 1989), Hybrid Single-Particle Lagrangian Integrated Trajectories (HYSPLIT: Draxler and Hess, 1997, 1998), and Puff (Searcy and others, 1998). Peterson and others (2010) provide a detailed description

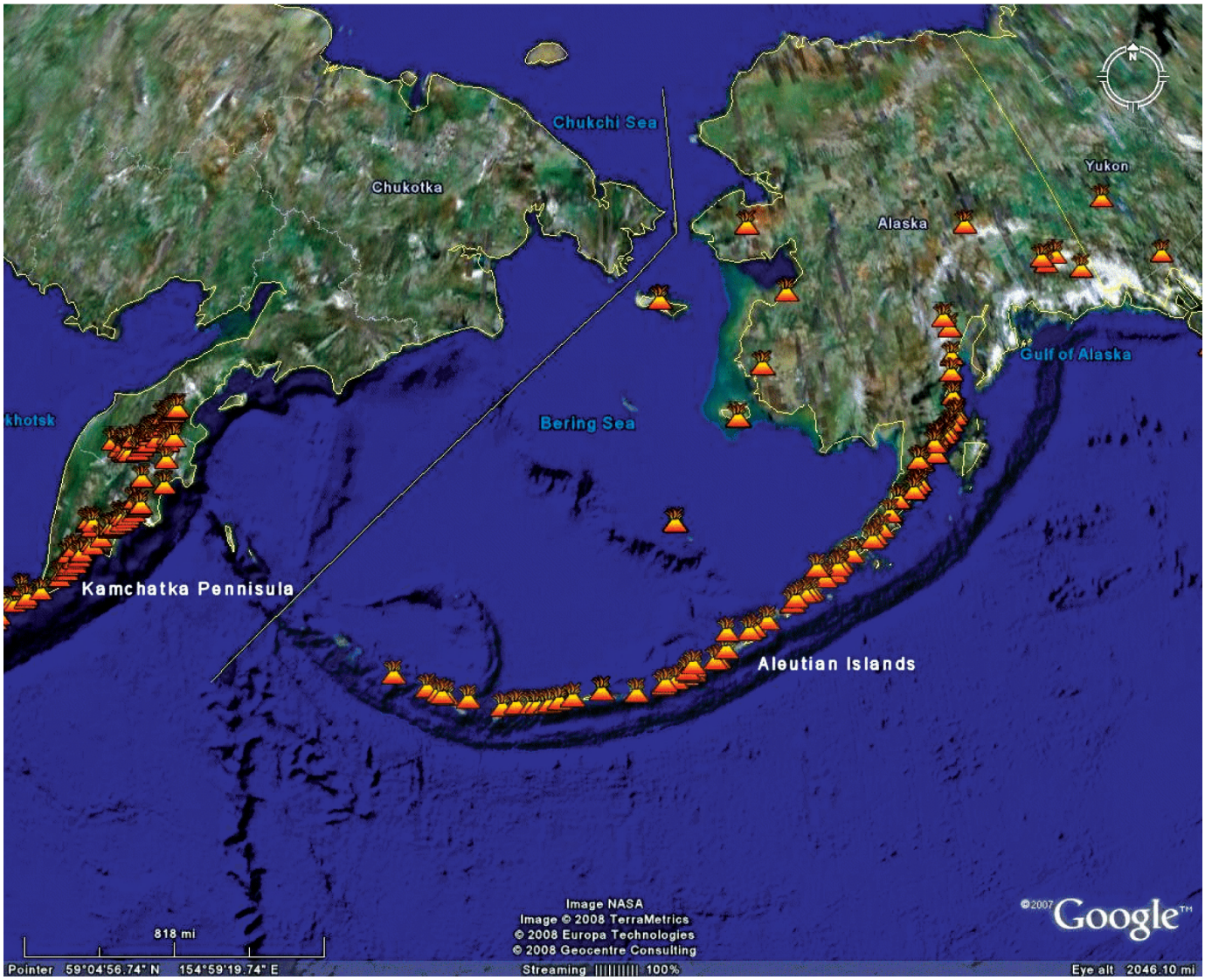

Figure 1. Map of North Pacific region, illustrating the numerous volcanoes (colored triangles) from Kamchatka in the west to the Alaska mainland and Canada in the east (image courtesy of Google Earth).

of all three models. Puff is primarily focused on forecasting volcanic ash transport and dispersion using an adjustable number of tracer particles to represent a volcanic ash cloud. The model is designed to rapidly predict the extent and movement of airborne ash particles during an eruption (Searcy and others, 1998). Model simulations place hypothetical particles above a selected volcano, release them into a gridded wind field and calculate their movement. Current numerical weather prediction (NWP) model forecasts are used for real-time predictions.

Puff is used at AVO, Anchorage and Washington VAACs, the Airforce Weather Agency (AFWA), and other national agencies and universities worldwide. The Puff model has been used as a VATD model for numerous volcanic eruptions in the North Pacific. The first use of the model was during the eruption of Redoubt Volcano in 1989–90 (Tanaka, 1994). Searcy and others (1998) demonstrated the model's use by comparing predictions to satellite images of the eruptions of Crater Peak at Mount Spurr in 1992 and of Klyuchevskoi Volcano in 1994. Dean and others (2002) predicted the movement of the ash cloud from the 2001 eruption of Cleveland Volcano and showed possible limitations of satellite data when compared to the model predictions, and Aloisi and others (2002) used the model to analyze the July 1998 eruption cloud from the Mount Etna paroxysm. Additionally, Papp and others (2005) investigated the probability of ash distribution in the NOPAC based on multiple, hypothetical eruptions over several years, and Peterson and others (2010) compared model predictions from Puff, HYSPLIT, and CanERM for selected eruptions in the NOPAC.

Most recently, the Puff model was used in January 2006, when Augustine Volcano (fig. 2) reawakened and over a period of 20 days produced 13 explosive eruptions, followed by a period of continuous ash emission. The 2006 eruption was preceded by approximately 8 months of increasing unrest that included escalating seismic activity, deformation of the volcanic edifice, gas emission, and small phreatic explosions (Power and others, 2006). The eruption progressed through four phases. In May 2005, the volcano started a precursory phase with increasing microearthquakes (Power and others, 2006). From January 11 to 28, 2006 the volcano was in an explosive phase characterized by 13 discrete explosions, followed by a more continuous phase of lesser explosivity and lava effusion from January 28 through February 10 and concluding with an effusive phase from March 3 to 15 (Coombs and others, this volume).

In this paper, we show the use of the Puff model during the 2006 eruption of Augustine Volcano. New modeling capabilities are introduced, many of which were used for the first time during an eruption response, with validation of these model simulations. Also shown is how the frequency of the explosive events at Augustine led to both new developments and new data-visualization tools. We compare the Puff model simulations to satellite data and ashfall measurements to assess the reliability of the eruption response predictions. We describe the Puff model's use by separating the explosive phase into three parts on the basis of the timings of the events: (1) January 11, (2) January 13 and 14, and (3) January 17, with the early part of the following continuous phase as one period, (4) January 28 to February 2, 2006.

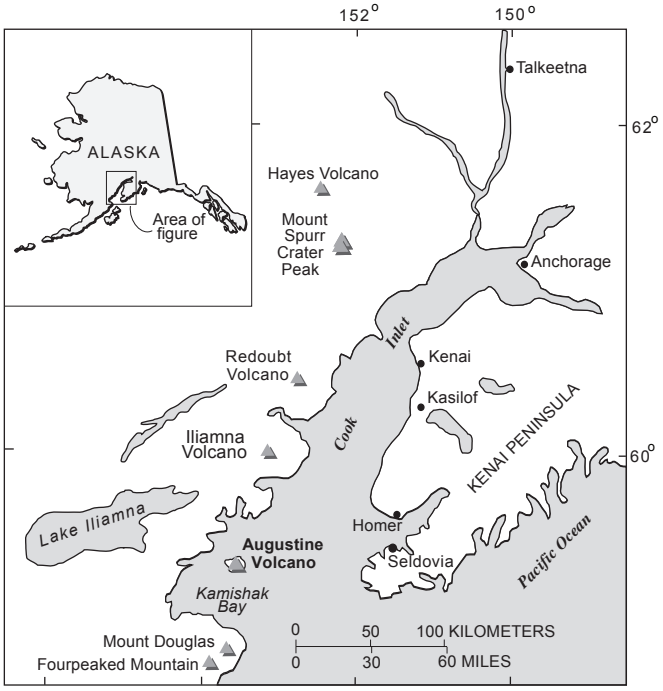

Figure 2. Map showing location of Augustine Volcano, in Cook Inlet, southwest of Anchorage, Alaska. Grey triangles show the locations of the volcanoes within this region of Alaska.

The 2006 Eruption at Augustine Volcano

The 2006 eruption of Augustine Volcano was preceded by increased seismicity beginning in May 2005. By January 11, 2006, there were significant satellite detected thermal anomalies and strong seismic signals, and on that day two explosions occurred, each lasting less than 4 minutes (Power and others, 2006). The January 11 explosions produced ash plumes, reported by NWS to have reached heights greater than 9 km a.m.s.l. (approximately 30,000 ft), which moved slowly to the north and northeast (Power and others, 2006). On January 13, a third explosive event occurred, which lasted for 11 minutes and produced volcanic plumes/ash clouds detected to 10 km (33,000 ft) a.m.s.l. During January 13, there were five discrete events, followed by events on January 14 and 17 (see table 1). Figure 3*A* is a time-lapse camera image from Augustine Island that shows that the events on January 13 were ash rich, and by January 28, the continuous-phase eruptions were a mixture of steam, gases and some ash (fig. 3*B*).

In response to these explosive eruptions, the Puff model was used by AVO to track and predict the movement of the volcanic ash clouds. The model simulations were

compared with all available satellite remote-sensing data. During the 2006 eruption, satellite data were available from the Advanced Very High Resolution Radiometer (AVHRR) on the National Oceanic and Atmospheric Administration (NOAA) satellites, the Moderate Resolution Imaging Spectroradiometer (MODIS) on National Aeronautics and Space Administration (NASA) Terra and Aqua satellites and the NOAA Geostationary Operational Environmental satellites (GOES). Bailey and others (this volume) provide a description of the data for both thermal monitoring and the detection of the volcanic ash clouds. On January 28, the volcano entered a period of more continuous eruptive activity that lasted until February 2. This phase began with four explosive eruptions that generated ash plumes up to 9 km (30,000 ft) a.m.s.l (Power and others, 2006). Ash plumes ascended to 4 km (~13,000 ft) a.m.s.l. frequently during the continuous phase. Winds carried ash to the south, depositing trace amounts on Kodiak Island and interrupting air traffic at the Kodiak Airport, and then carried ash north across Alaska (Webley and others, 2008).

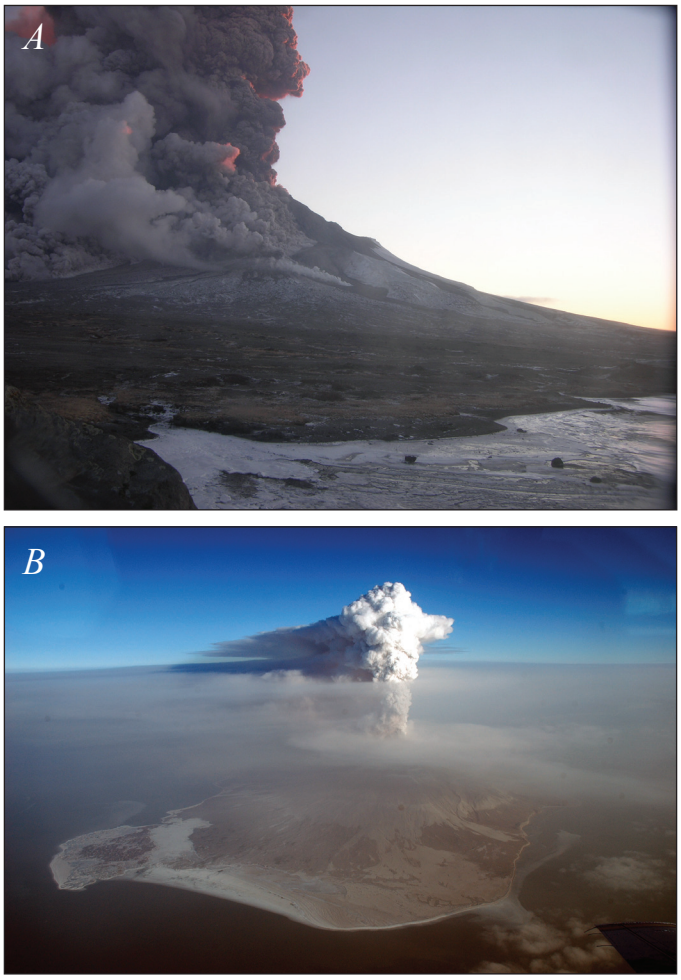

Figure 3. Photographs of Augustine Volcano's 2006 eruption. *A*, Time lapse camera image taken on January 13, 2006, from a site at Burr Point, 5 km north of Augustine's summit (Paskievitch and others, this volume). *B*, Oblique aerial photograph of a steam plume with minor ash, extending northeast from Augustine Volcano on January 30, 2006. The view is from southwest. AVO photo by R.G. McGimsey.

Puff Model Simulations

At AVO, once a volcanic event was confirmed, the Puff model was used to predict the movement of the subsequent ash cloud for the following 24-hour period. Initially, several assumptions were made for the plume height, eruption duration, particle-size distribution, and vertical distribution of the ash particles in the plume. As more information became available, the model prediction was updated to provide a better representation of the ash cloud movement. The Puff model uses numerical weather prediction (NWP) forecasts for its advective term when predicting the future movement of a volcanic cloud trajectory. During the Augustine eruption, the North American Mesoscale model (NAM) domain 216 was used; this is a 32-km spatial resolution data set. Additional NWP forecasts were available from the Weather Research Forecast (WRF) model at 1.67-km and 5-km spatial resolutions. However, this was an experimental data set and so was not used during the eruption response.

For this paper, AVHRR channel 4 (10.2–11.2 micron) and channel 5 (11.5–12.5 micron) data were used to detect ash clouds, including generating "split window" images, using the reverse absorption method, first noted by Prata (1989a, b). AVHRR channel 4 data are useful for detecting opaque ash clouds (Dean and others, 2002) and the reverse absorption method becomes a useful tool once the ash clouds are "semi-transparent". Here we use the reverse absorption method through a brightness temperature difference (BTD) of the infrared channels as stated by Prata (1989a). Eruption clouds early on in their development can fail to allow discrimination of ash, given that they are spectrally opaque (Wen and Rose, 1994; Krotkov and others, 1999; Simpson and others, 2000). Part of the ash cloud needs to be "translucent", which indicates a low optical depth, for the reverse absorption method to be successful. The ash signal can be affected by water vapor in the atmosphere, which can cause the signal sometimes to become slightly negative, even there is not ash present in the atmosphere (Simpson and others, 2000; Prata and others, 2001; Simpson and others, 2001). Additionally, ice within volcanic clouds can cause the reverse absorption method to be ineffective (Rose and others, 1995).

January 11, 2006

On January 11, 2006, Augustine Volcano had two explosive events at 0444 and 0512 Alaska Standard time (AKST; 1344 and 1412 UTC), as much as 3 minutes 13

Table 1. Volcanic eruption parameters for Augustine's 2006 explosive and continuous phases, as used by the Puff model.

[All heights a.m.s.l . UTC = coordinated universal time, AKST = Alaska Standard Time, Jan = January, Feb = February, km = kilometers, ft = feet, s = seconds, min= minutes. AKST = UTC – 9 hours. Note that the start and end times of the eruptive events were determined from AVO seismic stations]

Event No.	Date	Start Time (AKST)	End Time (AKST)	Duration	Plume Height[1]	Plume Height[2]
1	11 Jan 2006	04:44:00 (13:44:00 UTC)	04:45:18 (13:45:18 UTC)	1 min 18 s	30,000 ft (~9 km)	6.5 km
2	11 Jan 2006	05:12:00 (14:12:00 UTC)	05:15:18 (14:52:18 UTC)	3 min 18 s	28,000 ft (~8.5 km)	10.2 km
3	13 Jan 2006	04:24:00 (13:24:00 UTC)	04:35:00 (13:35:00 UTC)	11 min	34,000 ft (~ 10.4 km)	10.2 km
4	13 Jan 2006	08:47:00 (17:47:00 UTC)	08:51:17 (17:51:17 UTC)	4 min 17 s	30,000 ft + (~ 9 km+)	10.2 km
5	13 Jan 2006	11:22:00 (20:22:00 UTC)	11:25:24 (20:25:24 UTC)	3 min 24 s	36,000 ft + (~ 11 km+)	10.5 km
6	13 Jan 2006	16:40:00 (1/14 01:40:00 UTC)	16:44:00 (1/14 01:44:00 UTC)	4 min	34, 000 ft + (~ 10.4 km+)	10.5 km
7	13 Jan 2006	18:58:00 (1/14 03:58:00 UTC)	19:01:00 (1/14 04:01:00 UTC)	3 min	30,000 ft (~ 9 km)	13.5 km
8	14 Jan 2006	01:14:00 (09:14:00 UTC)	01:17:00 (09:17:00 UTC)	3 min	~ 30,000 ft (~ 9 km)	10.2 km
9	17 Jan 2006	07:58:00 (16:58:00 UTC)	08:02:11 (17:02:11 UTC)	4 min 11 s	45,000 ft (~ 13.7 km)	13.5 km
10	27 Jan 2006	20:24:00 (1/28 05:24:00 UTC)	20:33:00 (1/28 05:33:00 UTC)	9 min	30,000 ft (~ 9 km)	10.5 km
11	27 Jan 2006	22:37:21 (1/28 08:37:21 UTC)	22:38:45 (1/28 08:38:45 UTC)	1 min 2 s	< 10,000 ft (< 3 km)	3.8 km
12	28 Jan 2006	02:04:13 (11:04:13 UTC)	02:06:40 (11:06:40 UTC)	2 min 6 s	26,000 ft (~ 8 km)	7.3 km
13	28 Jan 2006	07:42:00 (16:42:00 UTC)	07:45:00 (16:45:00 UTC)	3 min	25,000 ft (~ 7.6 km)	7 km
continuous phase	28 Jan 2006	14:30:00 (23:30:00 UTC)	1 Feb 2006	4 days	10,000 – 14,000 ft [3] (~ 3 – 4.3 km)	3.8 km [4]

[1]Eruption response plume height from NWS.

[2]NEXRAD radar plume height.

[3]Discrete events to 30,000 ft.

[4]Discrete events to 7.2 km. 1 km = 3,280 ft.

seconds in duration, and that produced ash clouds of 8–9 km a.m.s.l. (26,000–30,000 ft) (table 1). Once the explosions were detected by the AVO seismic network, the Puff model was implemented to predict the movement of the emitted ash clouds using a default plume height of 16 km a.m.s.l (52,000 ft), to ensure that the full eruption column was included. For these two events, Puff predicted very similar patterns in both simulations (fig. 4): a spiral-shaped ash cloud with the ash above 6 km (20,000 ft) a.m.s.l drifting mostly east away from Augustine and across the Kenai Peninsula and the lower ash, < 6 km a.m.s.l, drifting mostly north. Initially, an opaque ash cloud was detected by satellite data (fig. 5*A*). Once translucent, this ash cloud was detectable by the reverse absorption method (fig. 5*B*), with

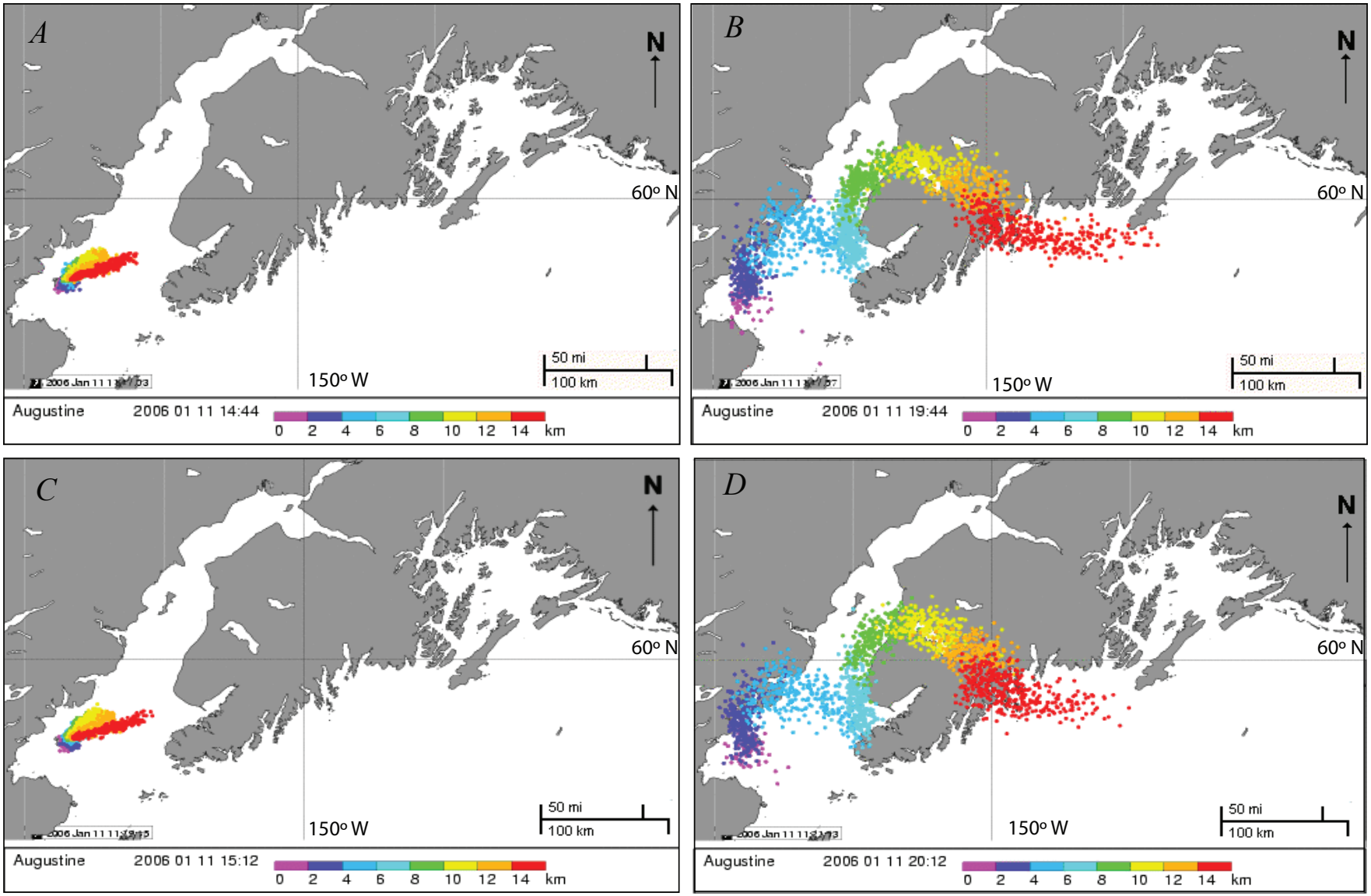

Figure 4. Puff eruption response simulations for the January 11, 2006 explosions. *A* and *B* for the first event at 0444 AKST (1344 UTC) eruptions at +1 and +6 hours. *C* and *D* are for the second event at 0512 AKST (1412 UTC) eruption at +1 and +6 hours. Times are in UTC, and particles are color-coded by elevation a.m.s.l.

a negative brightness temperature difference (BTD) signal. For these two events on January 11, the ash cloud was only detectable in a few satellite images. The NWS tracked the plume moving north towards the west side of Cook Inlet, corresponding to the low level sections of the Puff forecast below 6 km a.m.s.l. The explosive events on January 11 showed little ash in the satellite data, consistent with interpretation of seismic signals from the events, which suggest the explosions were mostly caused by gas release (McNutt and others, this volume).

January 13–14, 2006

Starting at 0424 AKST (1324 UTC) on January 13, Augustine Volcano had six further explosive events. On the basis of the AVHRR satellite sensor data, the events on January 13 and 14 (fig. 6) showed a stronger ash signal than seen for the second explosive event on January 11 (fig. 5). The first event on January 13 started at 0424 AKST (1324 UTC), had an 11-minute duration, and produced an ash cloud that ascended to approximately 10 km a.m.s.l (33,000 ft) (table 1). Within approximately 24 hours, there would be five more explosive events lasting around 3 to 4 minutes each, and producing ash columns from 9 to 11 km a.m.s.l (30,000–36,000 ft) (table 1). The movements of ash clouds from these events were predicted and simultaneously tracked using the "multiple eruption" option in the Puff model. This was the first time that this tool had been applied during an eruption response. The tool allows Puff to predict the movement of many volcanic ash clouds at one time. As each of the six events was confirmed, the model predictions were then updated. For each new prediction, the Puff model integrated the new and older ash clouds to track all of them together, so all six plumes' movements were forecasted simultaneously. These forecasts were then compared to any additional data once available.

Figure 6 shows the volcanic ash plumes detected on several AVHRR satellite images during January 13–14. Figure 6*A* shows the first plume at 0609 AKST (1509 UTC) on January 13 drifting east across Cook Inlet towards the Kenai Peninsula. Figure 6*B* shows that there were two ash plumes detectable in the satellite data at 1024 AKST (1924 UTC). The first was over the Kenai Peninsula, with a weak ash signal, and the second was to the east of Augustine Volcano, in Cook Inlet. Figure 6*C* shows three detected ash clouds at 1203 AKST (2103 UTC) that moved in an east-northeast direction. By 2020 AKST on January 13 (0520 UTC on January 14), these first three plumes had dispersed and moved out into the Gulf of Alaska. Figure 6*D* shows the fourth and fifth plumes (events 6 and 7 in table 1), which moved in a more south-easterly direction, through the strait between the Kenai Peninsula and Kodiak Island and out into the Gulf of Alaska, with the strongest ash signal at the

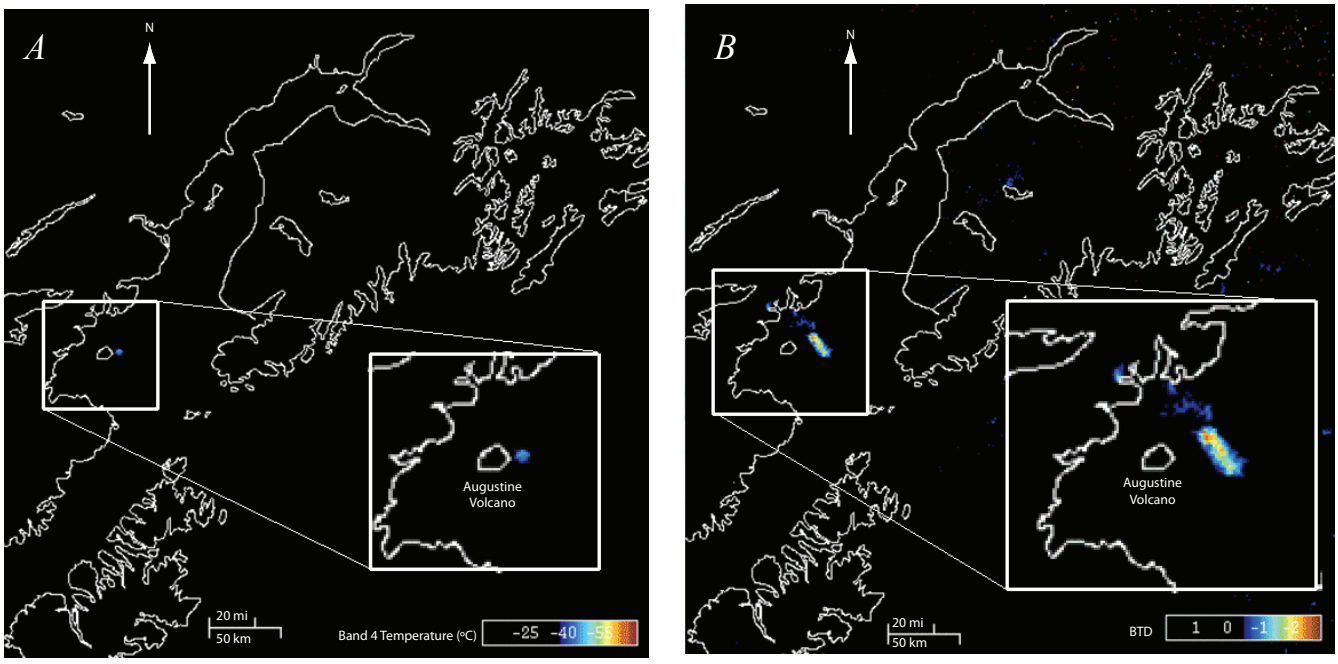

Figure 5. Advanced Very High Resolution Radiometer (AVHRR) satellite sensor data as images from January 11, 2006. *A*, Opaque ash cloud at 0448 AKST (1348 UTC). *B*, Ash signal, shown as brightness temperature differences (BTD), at 0659 AKST (1559 UTC). BTD scale is difference in AVHRR channels 4 and 5 using the reverse absorption method.

"head" of the ash clouds. Additional discussion of the satellite data collected on January 13–14 is included in Bailey and others (this volume). Figure 7 shows time-snapshots during the Puff model forecasts of the six plumes (events 3 to 8 in table 1) from January 13–14 as they drift across the Gulf of Alaska. The simultaneous forecast of the movement of these multiple ash clouds simplified a very complex geographic problem of displaying and accounting for all of the ash clouds at one given time and demonstrated that we can track and forecast all of them to make a hazard assessment.

Figure 8 shows a comparison of the Puff eruption response forecasts to the AVHRR satellite sensor data

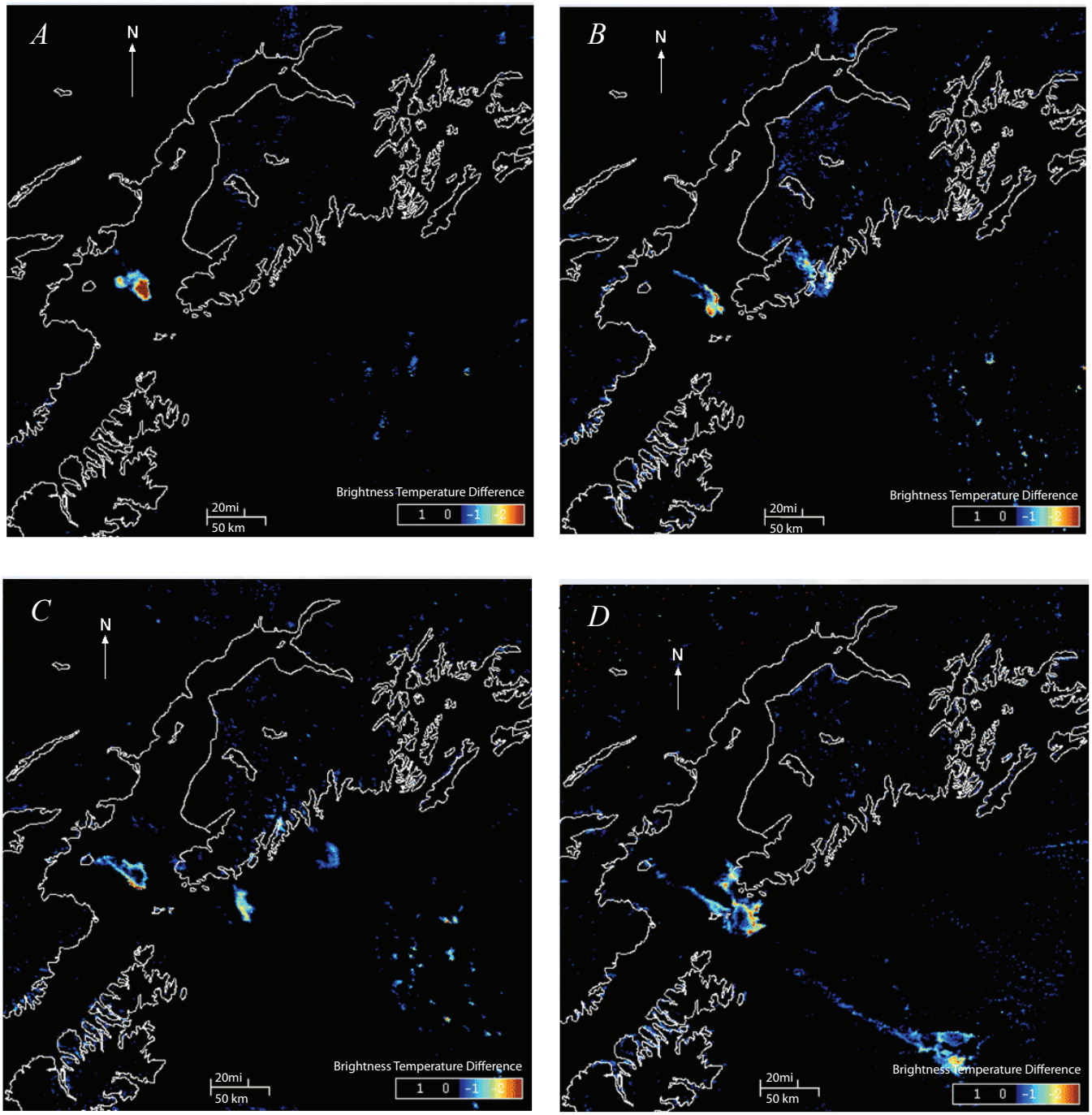

Figure 6. Time-snapshot series of the multiple plumes from Advanced Very High Resolution Radiometer sensor satellite data using reverse absorption method, BTD, on January 13, 2006. *A*, 0609 AKST (1509 UTC). *B*, 1024 AKST (1924 UTC). *C*, 1203 AKST (2103 UTC). *D*, 2020 AKST (0520 UTC on 14 January 2006). BTD scale is difference in AVHRR channels 4 and 5 using the reverse absorption method.

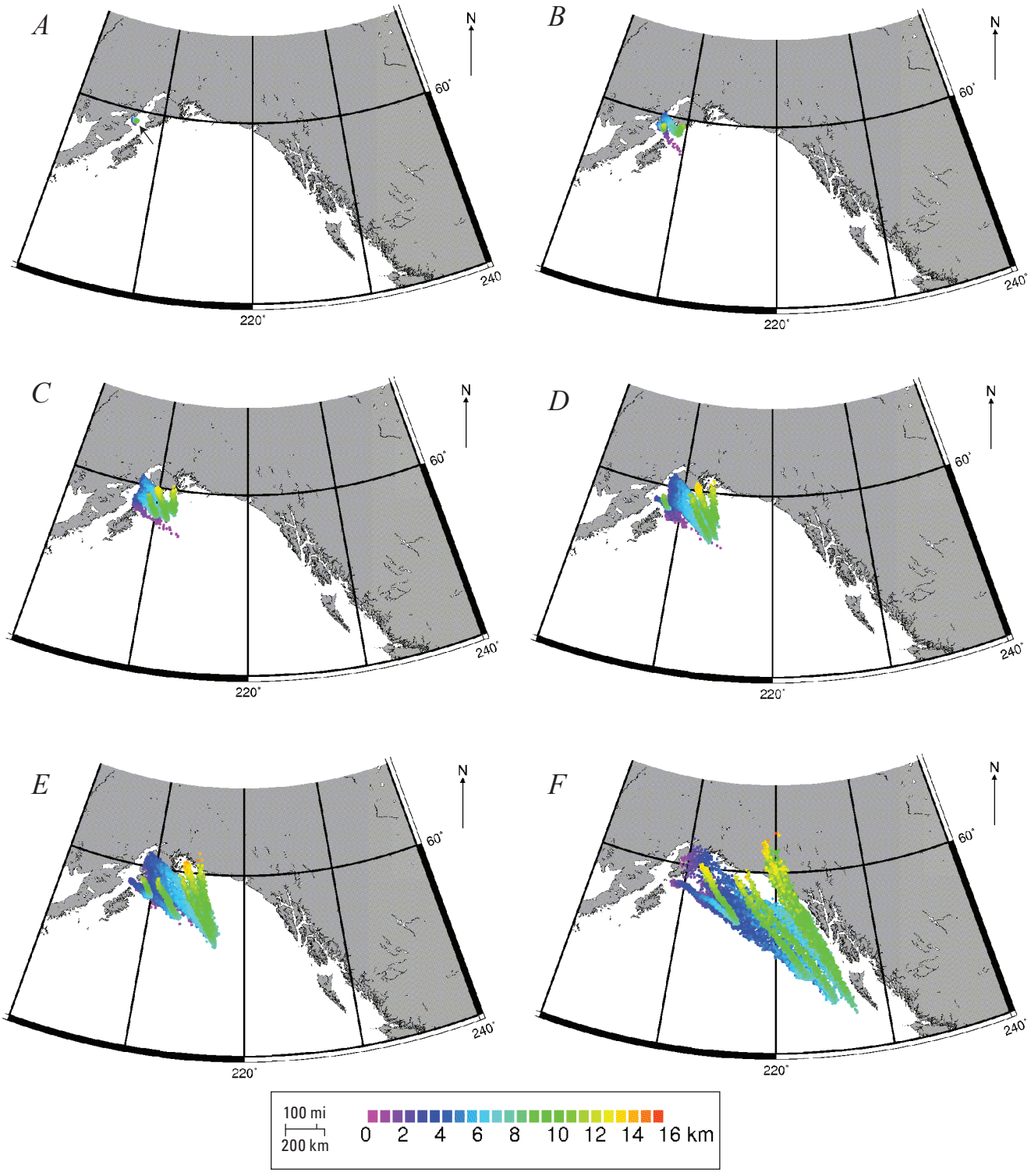

Figure 7. Time snapshots during the 24 hour Puff simulations from the six plumes during January 13–14, 2006. *A*, January 13 at 0520 AKST (1420 UTC). *B*, January 13 at 1020 AKST (1920 UTC). *C*, January 13 at 15:20 AKST (14 January at 0020 UTC). *D*, January 13 at 1820 AKST (14 January at 0320 UTC). *E*, January 13 at 2120 AKST (14 January at 0620 UTC). *F*, January 14 at 0720 AKST (1620 UTC). Date and times in Puff model forecasts are in UTC, and particles are color-coded by elevation a.m.s.l.

from the events on January 13 and 14. Figure 8*A* shows the AVHRR sensor satellite data at 1246 AKST (2146 UTC) on January 13. Here, the first three events from January 13, events 3–5 in table 1, are detected with the reverse absorption method in the satellite data, giving a negative BTD signal. Figure 8*B* shows the Puff forecast at 1250 AKST (2150 UTC), within 5 minutes of the satellite data. Figure 8*C* shows a comparison of the two data sets, by evaluating their spatial footprint. As we were unable to determine ash retrievals and then use the Puff model to predict airborne concentrations, a spatial comparison was the only possible method for data comparison. Here, the "footprint match" between the Puff predictions and the satellite data is emphasized by points labeled 1, 2 and 3 (fig. 8*C*). From the Puff forecasts, the modeled ash at altitudes from 8–10 km a.m.s.l. (26,000–33,000 ft) matches the satellite data. As the ash clouds were detectable in the satellite data using the reverse absorption method and a negative BTD signal, they were termed translucent. Determination of their altitude is only possible from this comparison method with Puff. The Puff

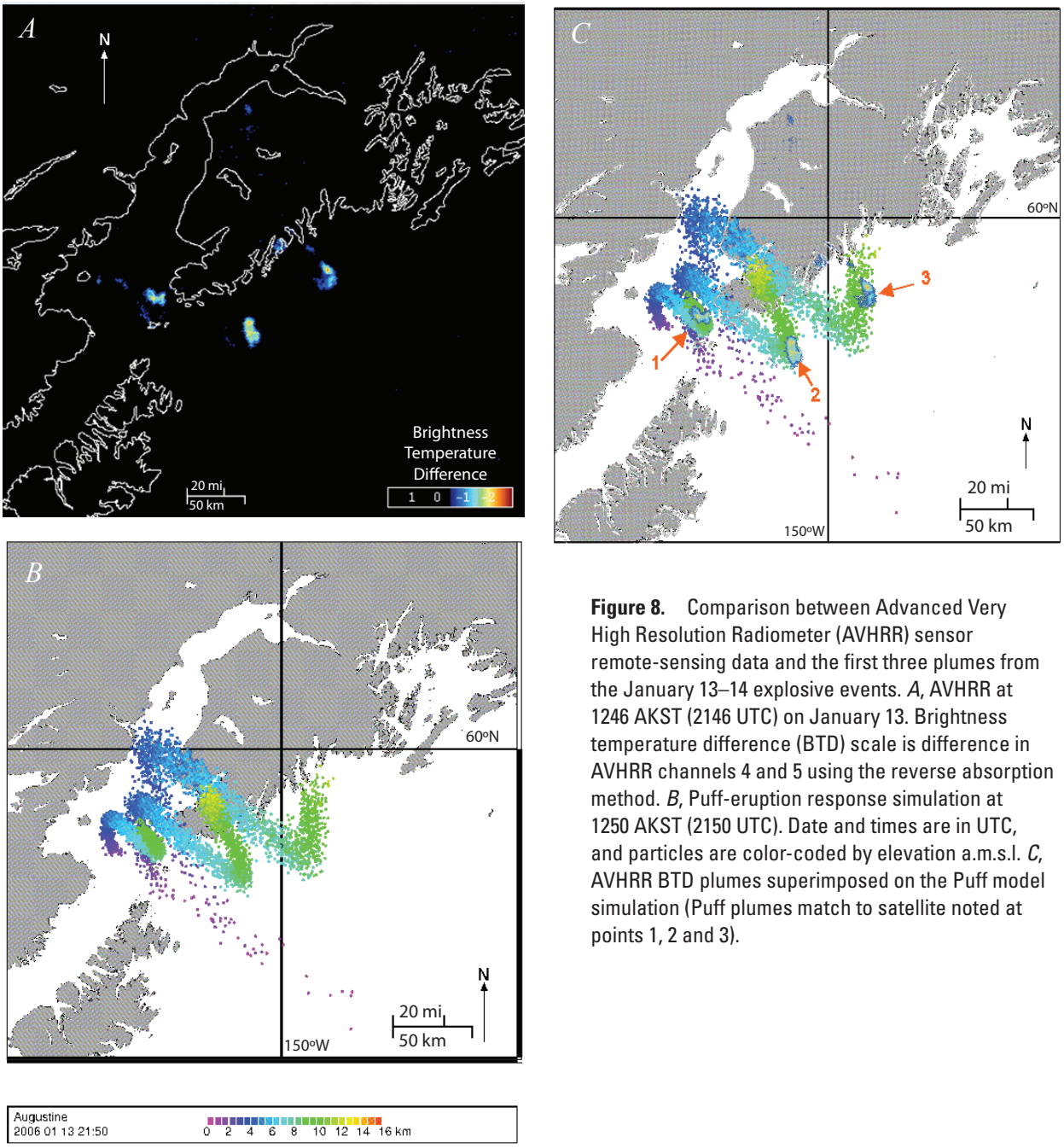

Figure 8. Comparison between Advanced Very High Resolution Radiometer (AVHRR) sensor remote-sensing data and the first three plumes from the January 13–14 explosive events. *A*, AVHRR at 1246 AKST (2146 UTC) on January 13. Brightness temperature difference (BTD) scale is difference in AVHRR channels 4 and 5 using the reverse absorption method. *B*, Puff-eruption response simulation at 1250 AKST (2150 UTC). Date and times are in UTC, and particles are color-coded by elevation a.m.s.l. *C*, AVHRR BTD plumes superimposed on the Puff model simulation (Puff plumes match to satellite noted at points 1, 2 and 3).

simulations were able to match the ash cloud movements, even though they showed a larger amount of dispersion. This increased dispersion could be a result of (1) the ash concentrations seen in the modeled cloud being below the detection limits of the reverse absorption technique or (2) in the model forecast, the dispersion factor being set too high.

In the past few years, virtual globes, specifically Google Earth™, have been used for displaying scientific data. They allow the Puff model predictions to be shown in their three-dimensional form. Figure 9 shows both a graphical representation of the Puff model forecast and a three-dimensional view of event 3 on January 13. Figure 9*A* shows the ash cloud's location in a graphical plan view, with no three-dimensional viewpoint. Here, the ash cloud altitudes are shown as color-coded particles from 0 to 16 km a.m.s.l (0 to 52,000 ft). Figure 9*B* shows a three-dimensional viewpoint of the same Puff prediction in Google Earth. Selecting each ash particle in Google Earth, the observer is provided with its location and altitude. In addition, there is a "time stamping option", highlighted within the box in figure 9*B*, which allows an animation of ash cloud movement. This three-dimensional viewpoint and interactive ability is a novel tool for analyzing the dispersion model forecasts, something that is not possible with the graphical map image.

Additional comparison data during the January 13–14 period included ashfall reports in Homer/Port Graham on January 13, as well as Shasta County, California, on January 16 (Wallace and others, this volume) and aerosol data collected in Homer on January 13 (Cahill and others, unpub. data). All reports indicate that ashfall was very light. Figure 8*B* shows the Puff simulation of the low level ash cloud moving towards Homer and the Kenai Pennisula, towards the ashfall reports in Port Graham and aerosol samplers in Homer. In addition, the Puff simulations of the six plumes (fig. 7*F*) show that the forecasted ash clouds could have passed over the northwestern contiguous United States,

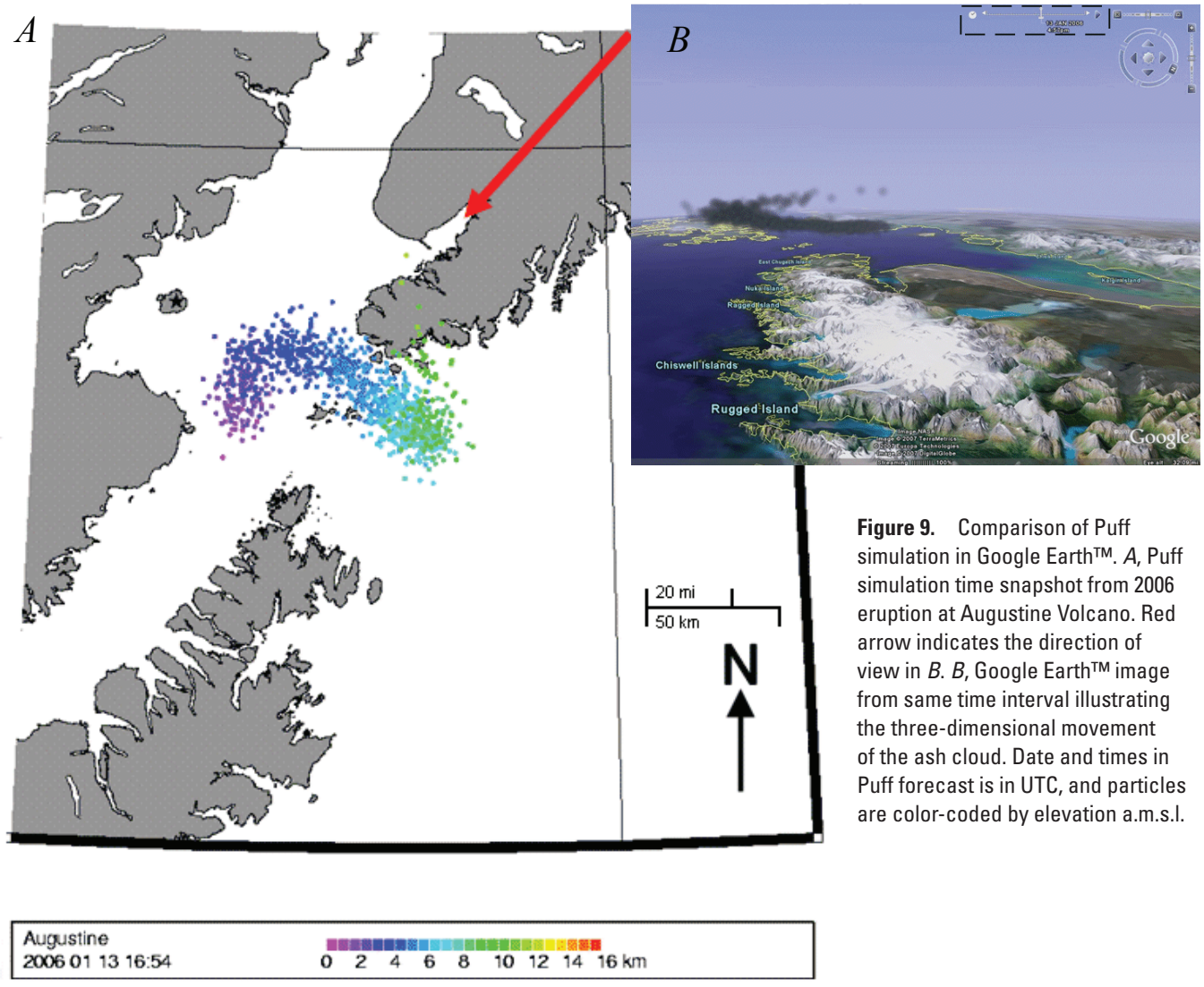

Figure 9. Comparison of Puff simulation in Google Earth™. *A*, Puff simulation time snapshot from 2006 eruption at Augustine Volcano. Red arrow indicates the direction of view in *B*. *B*, Google Earth™ image from same time interval illustrating the three-dimensional movement of the ash cloud. Date and times in Puff forecast is in UTC, and particles are color-coded by elevation a.m.s.l.

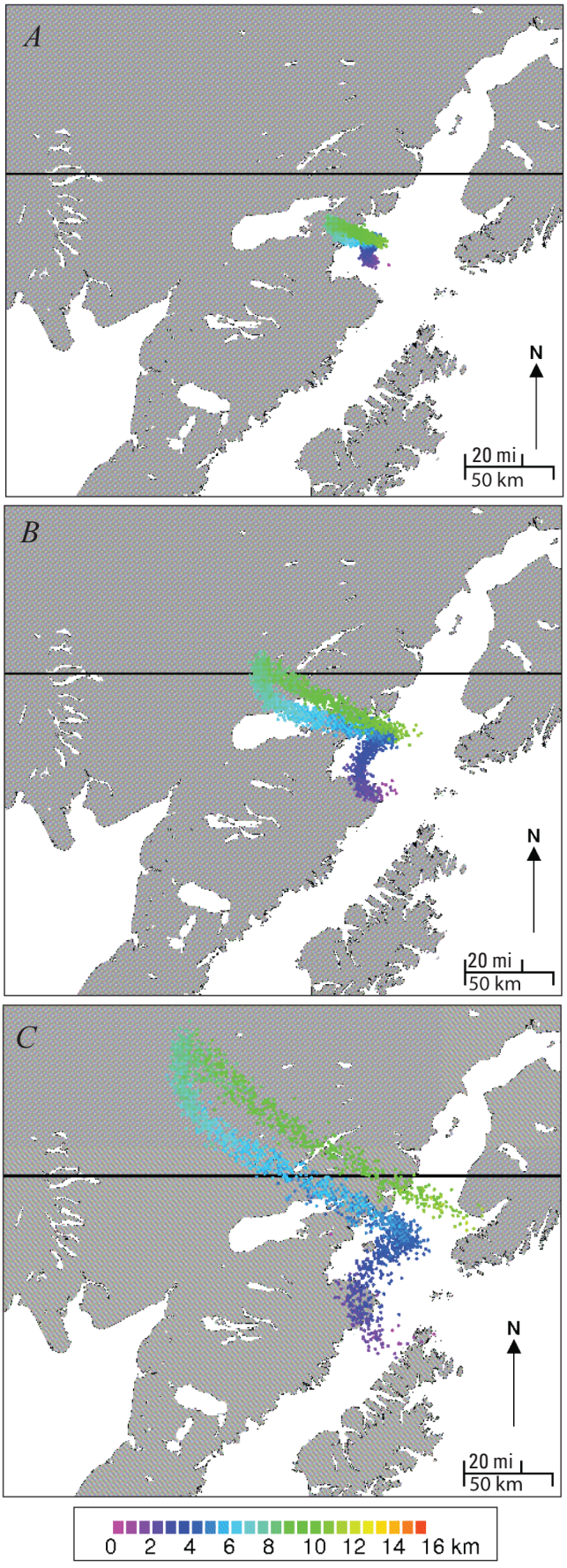

towards the reported ashfall in California. Peterson and others (2010) provide a comparison of the Puff simulations during the events on January 13–14 with those using the HYSPLIT and CanERM VATD models.

January 17, 2006

Following 3 days of relative quiescence, on January 17, 2006, Augustine had a single explosive event starting at 0758 AKST (1658 UTC), and lasting 4 minutes and 11 seconds, with a volcanic ash plume rising to an altitude of approximately 13 to 14 km a.m.s.l (43,000–46,000 ft) (event 9 in table 1). The ash cloud was only detected on 3 AVHRR satellite images (Bailey and others, this volume). Figure 10 shows the Puff model simulations in response to the detected eruption at 1 hour, 3 hours, and 6 hours after the start of the event. Here, the high altitude sections of the ash cloud travel north-northwest, and the low altitude sections travel to the southwest. Figure 11 shows a comparison between the Puff model simulations, the AVHRR satellite sensor data and the NWS Next Generation Radar (NEXRAD). Comparison between the Puff simulation (fig. 11*A*) and the satellite data (fig. 11*B*) show that the detected opaque ash cloud is at 8 to 10 km a.m.s.l (26,000–33,000 ft). The 0300 AKST January 17, 2006 radiosonde sounding collected from Kodiak, King Salmon, and Anchorage stations (http://weather.uwyo.edu/upperair/naconf.html), indicate that the −55.45°C temperature in figure 11*B* corresponds to approximately 8.5 to 9 km a.m.s.l (26,000-30,000 ft), using the altitude-temperature method of Sparks and others (1997) as developed from Kienle and Shaw (1979). NEXRAD, in clear air mode, shows very little reflectivity across Cook Inlet except for signals of +4 to +16 DBZ at Augustine (fig. 11*C*). The match in timing between the three datasets provides good agreement that (1) the radar was able to detect the ash cloud, (2) the Puff model results matched the satellite data, and (3) the ash cloud was at 8 to 10 km a.m.s.l. (26,000–33,000 ft).

In addition, a retrospective comparison between the Puff predictions and measured ashfall from the January 17 event was used to assess the Puff model's ability to reliably forecast ashfall (fig. 12). Figure 12*A*, adapted from Wallace and others (this volume), shows that ashfall occurred to the northwest of Augustine Volcano towards Lake Iliamna (location is shown in Figure 2). There are also ground observations of ashfall from Iliamna, Pedro Bay,

Figure 10. Puff time snapshots following simulation of January 17, 2006 explosive event. *A*, +1 hour or 0858 AKST (1758 UTC). *B*, +3 hours or 1058 AKST (1958 UTC). *C*, +6 hours or 1358 AKST (2258 UTC). Date and times are in UTC, and particles are color-coded by elevation a.m.s.l.

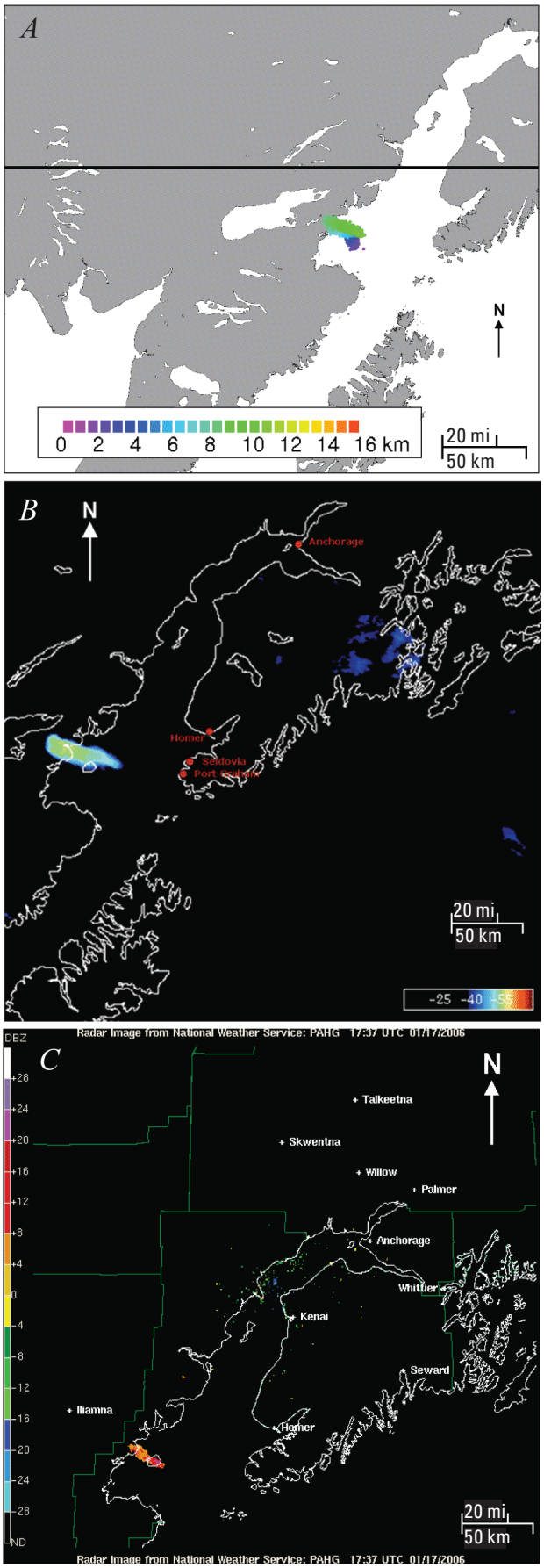

and Nondalton from local citizens. Figures 12*B*–12*D* show the Puff modeled ashfall predictions using three different wind-field datasets: National Centers for Environmental Prediction (NCEP) global reanalysis, WRF 5-km resolution and WRF 1.67-km resolution. For the reanalysis wind-field data (fig. 12*B*), the Puff-forecast ashfall occurs mostly over Cook Inlet. Although no ashfall samples were collected, there were ashfall reports at Port Graham, and the reanalysis forecast suggests that it could have been from this eruption, on the basis of a few predicted ashfall particles in the area. Because Puff is a tracer model, ashfall amounts can be simulated only relative to other locations, but light ashfall would be consistent with the model prediction.

Using the higher spatial resolution wind-field data from WRF, figures 12*C* and 12*D* show a very different ashfall pattern. Figure 12*C* predicts ashfall north of the volcano towards Pedro Bay and north-west towards Port Graham. Figure 12*D* predicts ashfall both southeast over the ocean and northwest towards Lake Iliamna (its location is shown in figure 2). This 1.67-km spatial resolution wind field was an experimental dataset used during the eruption, and as a result its spatial domain doesn't extend much beyond 20 km from the volcano. A larger domain at this finer spatial resolution could have resulted in a better match between the Puff model forecasts and the ashfall reports and measurements shown in figure 12*A*. The Puff model uses the wind field for its advection term, and the speed and direction for all particles is determined from the wind-field model data. A coarse resolution wind-field dataset requires interpolation to determine the wind field for each ash particle. Finer grids require less interpolation and hence more accurate representation of the actual atmospheric conditions.

This retrospective analysis suggests that an area like Cook Inlet, which has complex winds due to surrounding mountainous terrain and numerous valleys open to the ocean, requires higher resolution wind fields to better model the atmospheric boundary layer. This could result in more accurately modeled volcanic ashfall, an important factor for producing volcanic ashfall advisories in volcanic crises. Other factors, such as size distribution, aggregation, and deposition processes can also affect ashfall forecasts. However, a better representation of the wind field in the model's advective term will provide an improved forecast for both airborne ash movement and ashfall. Figures 10 through 12 have shown that the Puff model was able to match both the

Figure 11. Three views of the January 17, 2006, explosive event. *A,* Puff model output from 0838 AKST (1738 UTC). Times are in UTC, and particles are color-coded by elevation a.m.s.l. *B*, Advanced Very High Resolution Radiometer single channel satellite data from 0838 AKST (1738 UTC), showing cold temperatures of the infrared spectrally opaque ash cloud. *C*, NEXRAD radar from 0837 AKST (1737 UTC).

radar and satellite data for the January 17 event, but they also show how higher resolution wind-field data are needed for the Puff model to provide reliable forecasts of ashfall. After this single event on January 17, the next events occurred on January 28 and led to the continuous eruptive phase from January 28 to February 10, 2006, with declining vigor from February 2 to 10.

January 28 to February 2, 2006

On January 27–28, 2006, at 2024 to 0742 AKST Augustine Volcano again produced several explosions (events 10–13 in table 1), lasting as long as 9 minutes with ash plumes varying from 3 to 9 km (10,000–30,000 ft) a.m.s.l. that dispersed to the southeast and south-southwest.

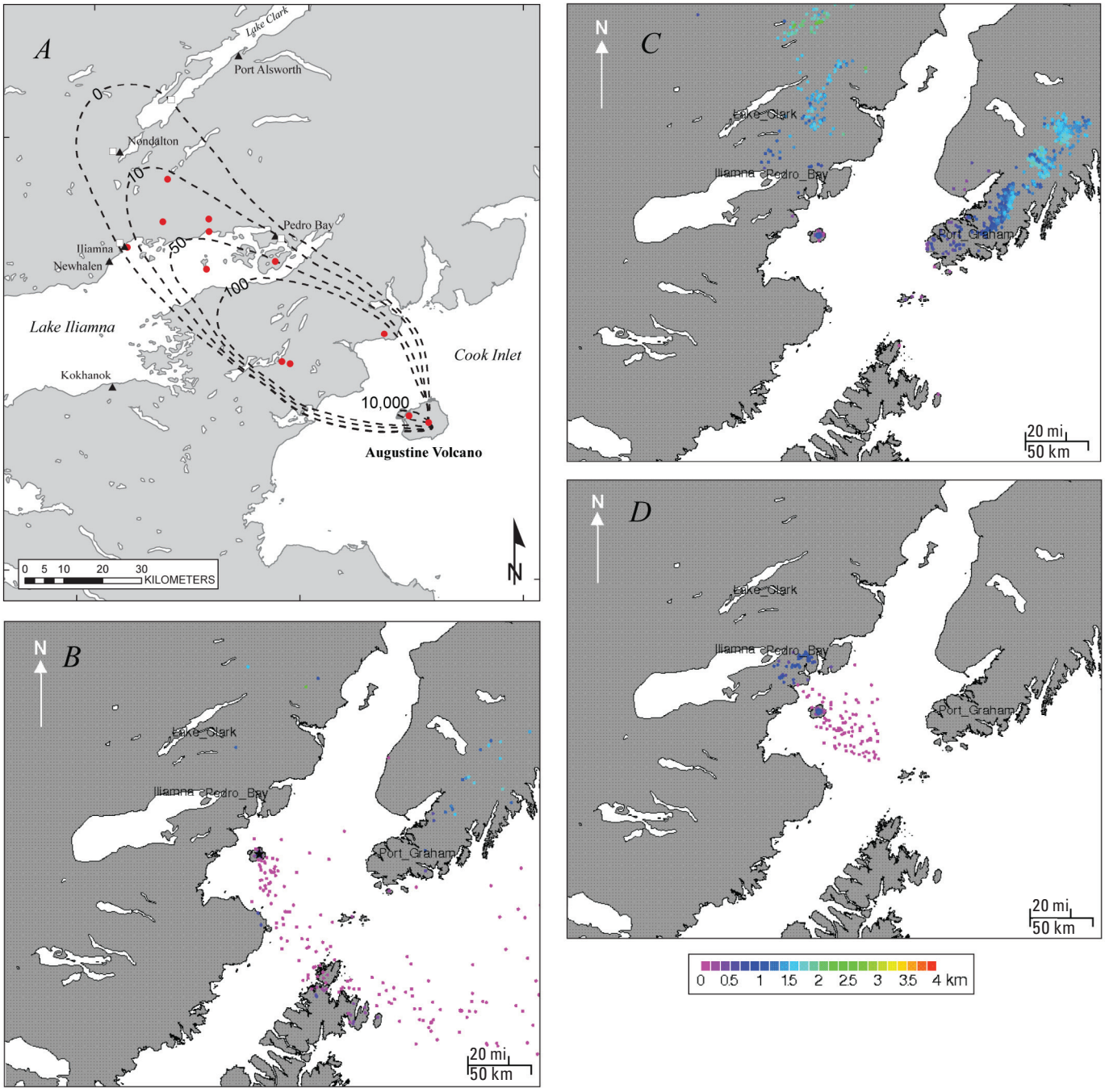

Figure 12. Measurements and simulations of ashfall from January 17, 2006 event. *A,* Ashfall isopach in g/m^2, (from Wallace and others, this volume). *B,* Puff model simulated ashfall from post event analysis with NCEP reanalysis wind field. *C,* Puff model simulated ashfall from post event analysis with WRF 5-km resolution wind field. *D,* Puff model simulated ashfall from post event analysis with WRF 1.67-km resolution wind field. Ashfall particles are color-coded by ground elevation a.m.s.l.

Then the volcano was relatively quiet for several hours from 0742 AKST (1642 UTC) until around 1430 AKST (2330 UTC), when seismicity began to increase. This led to the continuous phase as seen in the NEXRAD radar, which immediately started to detect a signal over the volcano, from ash emission, that continued for several days (D. Schneider, written communication (2006) and AVO Logs). Over the continuous phase, ash clouds reached approximately 3 to 4.5 km a.m.s.l (10,000–15,000 ft), with discrete events reaching 7.3 km (24,000 ft) (table 1). For the period from January 28, 2006, onwards, Puff used an initial 5 km (~16,500 ft) a.m.s.l ash plume and forecast wind fields from the NAM 216 model domain. To make the best use of the forecast data, the model was run for an initial 24 hours (from 1430 AKST/2330 UTC on January 28, 2006) and then restarted for another 24 hours, continuing in this way until February 2. Each new model run used the most recent forecast wind fields. Figure 13 is an example of the ash signal as detected from the BTD signal using the AVHRR satellite remote-sensing data on January 28 at 1731 AKST (January 29 at 0231 UTC). There is a very strong negative BTD signal to the south of the volcano across Kodiak Island. Additional discussion of the satellite data is included in Bailey and others (this volume).

At the beginning of the continuous phase, the synoptic conditions showed that volcanic material would initially move towards the southeast and then curve rapidly around with a northerly heading and be transported rapidly to the Alaska interior (Webley and others, 2008). Figure 14, adapted from Webley and others (2008), shows daily AVHRR and MODIS sensor data composites of the ash clouds from January 29 to 31. The movement of the ash clouds was initially in a southerly or south-easterly direction on January 28, shifting to a more southerly direction by January 29, then an easterly direction on January 30, and a northeasterly direction by January 31. These observations support Puff forecasts for this time period (fig. 15). Volcanic ash concentrations eventually receded to levels below the detection limits of the satellite data, with no ash clouds detected beyond the Cook Inlet area.

For the period from January 29 to February 1, the Puff predictions showed an ash-cloud trajectory towards Kodiak Island (fig. 15*A*) with a subsequent rotation to the northeast and across the Kenai Peninsula by the following day (fig. 15*B*). By the third day, predictions indicated a northeasterly trajectory (fig. 15*C*). Aerosol samples, from an eight stage impactor (described in Cahill, 2003) were collected at Homer, Alaska, and confirmed the presence of ash "at ground level there." These provide ground-based verification to go with the airborne ash detection (fig. 14) of the ash within Cook Inlet. Lidar measurements from three distinct systems across Alaska were also used to aid in confirming the Puff-model-predicted volcanic ash clouds from the continuous period (Sassen and others, 2007; Webley and others, 2008). The lidar measurements at two sites were collected in response to the Augustine volcanic activity and Puff simulations. Lidar detected the ash cloud under both clear skies and partially cloudy conditions. The characteristics of the volcanic ash were distinct from those of the atmospheric clouds. Figure 16 shows the Puff model prediction at 1900 AKST, January 31 (0400 UTC, February 1), during the acquisition of the lidar data at one station, as described in Webley and others (2008).

The lidar data confirmed the presence of the volcanic cloud overhead at Fairbanks, Alaska, and also confirmed the independent motion of the upper and lower level ash clouds. The location of the ash cloud in figure 16 shows ash passing over Fairbanks (marked as "F"). Aerosol analysis showed that ratios of iron to calcium at both Homer and Fairbanks indicated to a similar source and under "normal conditions" such ratios would not have been recorded at Fairbanks (Cahill and others, unpub. data). Figures 15*C* and 16 show that Puff-predicted ash clouds would have passed over Homer and

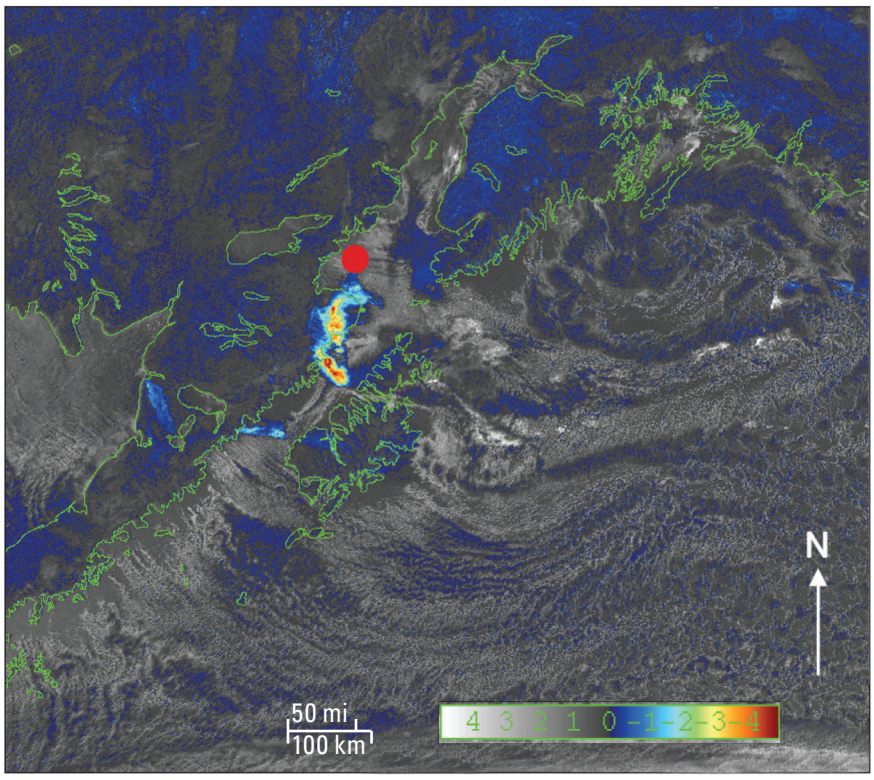

Figure 13. Advanced Very High Resolution Radiometer brightness temperature difference satellite data from January 28, 2006, at 1731 AKST (January 29, at 0231 UTC) showing the ash signal as detected through the reverse absorption method. Here, the ash is shown as a negative BTD signal. Location of the volcano is show by the red circle.

Fairbanks at the times the aerosol data were collected. The measurements of the aerosol signals in the lidar returns provided a unique confirmation tool to the Puff predictions.

The continuous phase of the eruption provided some unique validation opportunities for the Puff model predictions. Webley and others (2008) show the possibilities of lidar being used as a validation tool for volcanology. As shown by Sassen and others (2007), an autonomous lidar could be used by both the meteorological and volcanological communities for eruption crisis monitoring. Lidar measurements as an eruption response tool for volcano monitoring could be applied to known erupting volcanoes as well as the dispersed volcanic material from a much more distant eruption (Webley and others, 2008).

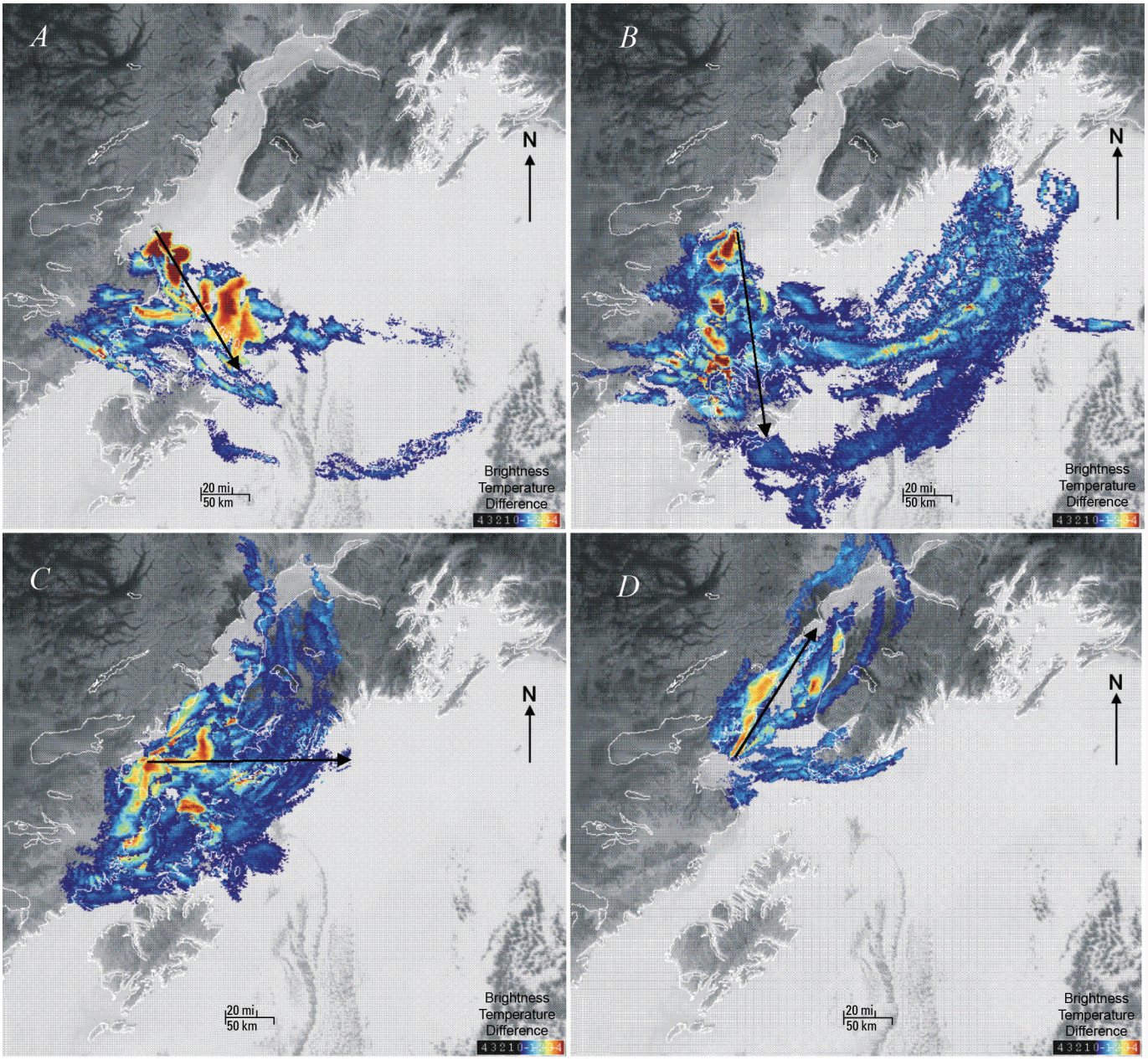

Figure 14 Moderate Resolution Infrared Spectrometer (MODIS) and Advanced Very High Resolution Radiometer data (AVHRR) ash-detection daily composites for (*A*), January 28, (*B*), January 29, (*C*), January 30 and ,(*D*), January 31 2006. Black arrows indicate general direction of ash cloud movement. Adapted from Webley and others (2008). Here, the ash is shown as a negative brightness temperature difference (BTD) signal.

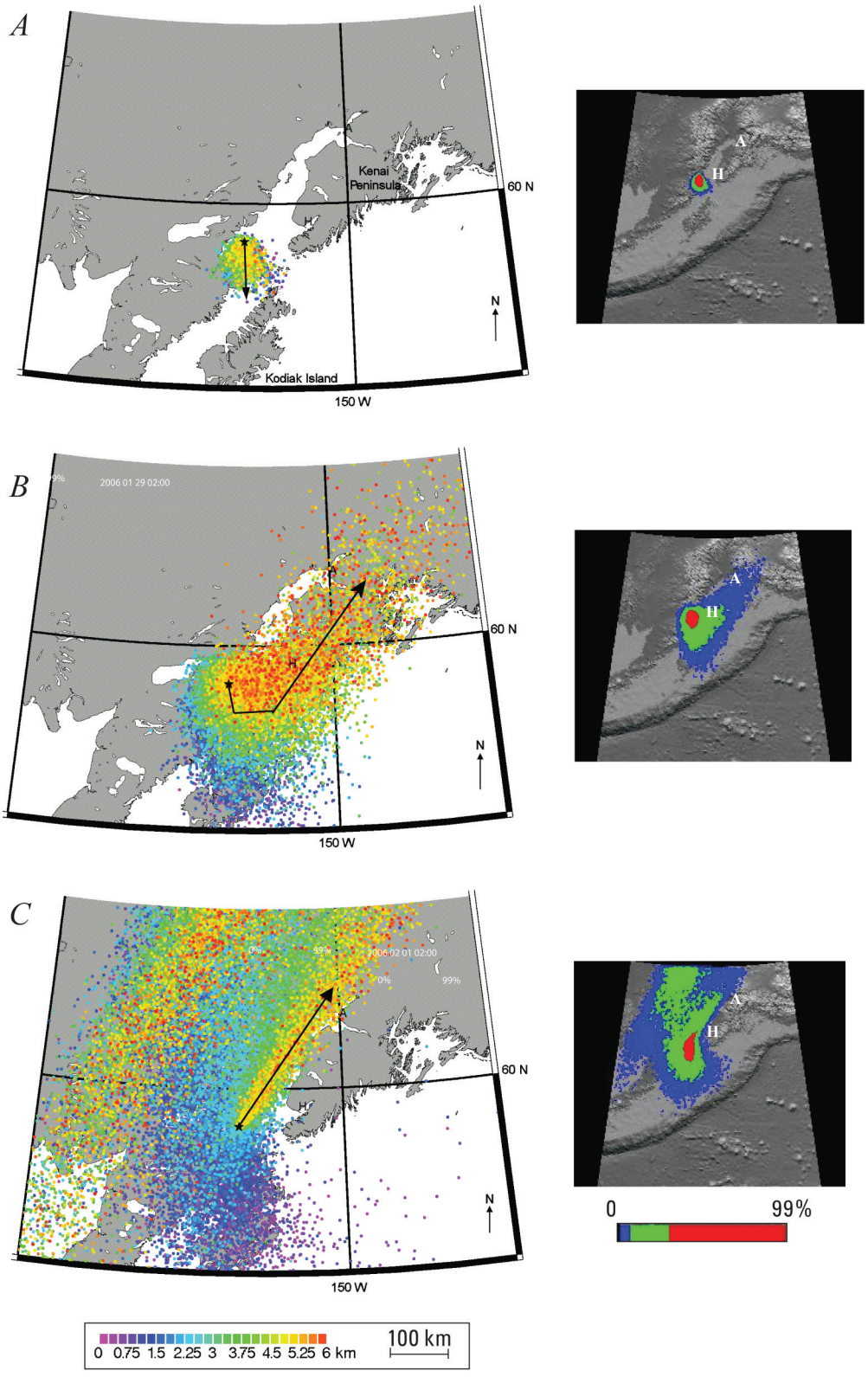

Figure 15. Puff model simulation of ash cloud movement in Cook Inlet during the continuous phase of the 2006 Augustine eruption, adapted from Webley and others (2008). Black arrows show general direction of the ash clouds movement. *A,* January 28 at 1700 AKST (January 29 at 0200 UTC). *B,* January 29 at 1700 AKST (January 30 at 0200 UTC). *C,* January 31 at 1700 AKST (February 1 at 0200 UTC). Date and times in Puff model forecasts are in UTC, and particles are color-coded by elevation. H, Homer; A, Anchorage. Thumbnail shows relative airborne concentration as a percentage of maximum predicted concentration.

Discussion and Conclusions

Volcanic ash clouds are a very real hazard during an eruption, even after the explosive/effusive activity has ended. They can pose a hazard to domestic and international air traffic and affect local communities. Also, they can be tracked over long distances for several days after the end of an eruptive period. The 2006 eruption of Augustine Volcano, Alaska, produced 13 explosive events over a 2-week period, followed by a continuous period of ash emission over several days.

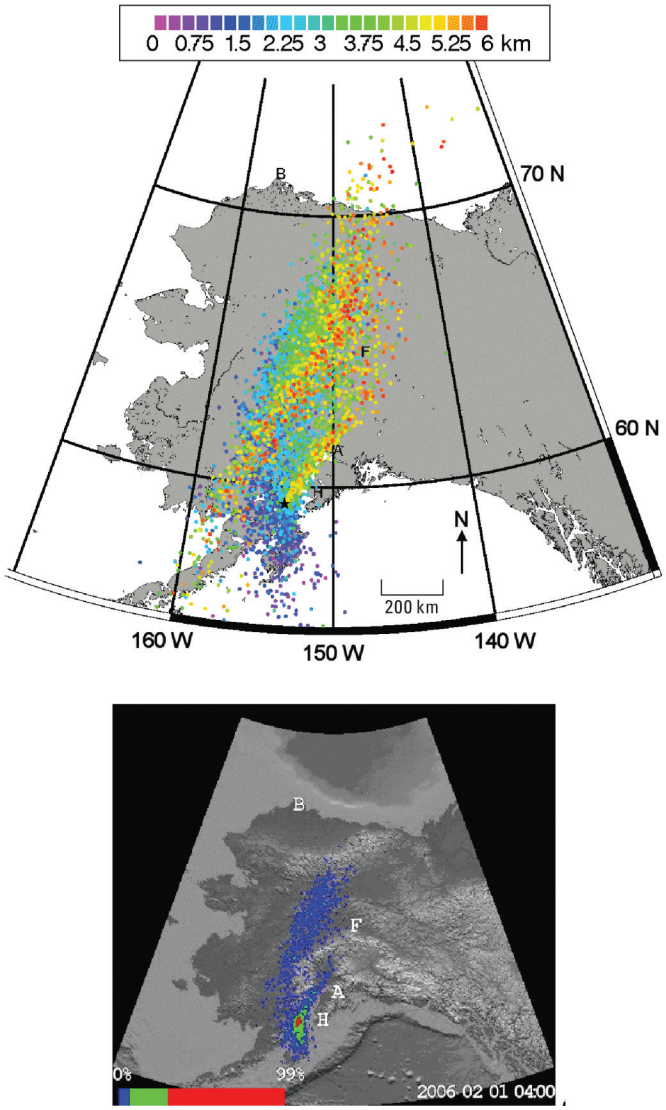

Figure 16. Puff model simulation snapshot on January 31, 2006 at 1900 AKST (February 1, 2006 at 0400 UTC) of ash cloud movement across Alaska mainland that coincided with lidar measurements, from Webley and others (2008). Particles are color-coded by elevation. Black star shows location of Augustine Volcano. H, Homer, A, Anchorage; F, Fairbanks. Lower panel shows relative airborne concentration as a percentage of maximum predicted concentration.

The Puff volcanic ash transport and dispersion model's ability to track multiple volcanic ash clouds was first used for an eruption response during this eruption. Its use was highly successful during the January 13–14 events and compared well with the satellite data (fig. 8). The NWS, with assistance from AVO, produced numerous volcanic ash advisories, and at one point Anchorage airport was affected, as airline flights were cancelled. Predicting the movements of these ash clouds from Augustine was critical to assess the impact they would have on their surroundings. The Puff model was able to provide forecasts of all the ash clouds from the events in table 1. The model's predictions were used during the eruption response by AVO and also the NWS to assess the cloud's movements and the impacts they would have on the aviation community and local residents.

As a result of the enormity of the data obtained during the Augustine eruption, the Google Maps™ application programming interface (API) is now used to display Puff automated predictions for potential eruptions at volcanoes of elevated alert status see Puff Web site (http://puff.images.alaska.edu). Webley and others (2009) provide a detailed description of the automated predictions and the API to all the Puff model predictions for these volcanoes. Virtual Globes are an excellent geographic frame of reference to display model results that can be easily understood. Figure 9 showed how displaying the data in a Virtual Globe provides (1) a better understanding of ash cloud movement and (2) an ability to visualize the data in three dimensions. Additional information, such as satellite and seismic data can be easily added to the Virtual Globe interface.

This paper illustrates the reliability of the Puff model airborne-ash predictions near Augustine Volcano and the distal ash plumes as compared to various other techniques, such as remote-sensing satellite data, aerosol samplers, and the lidar systems. Figure 11 for the January 17 event shows that use of higher spatial resolution wind fields would improve ashfall predictions, especially in a topographically diverse region such as Cook Inlet. Further work on the use of the WRF model for Puff predictions is required, both for airborne ash movement and for ashfall forecasts.

During the 2006 Augustine eruption, a large amount of information was provided by the model predictions. As a result, an improved tool to provide up-to-date analysis and allow quick assessments was required. The new automated predictions, now used by AVO, alleviated the requirement to initiate Puff model runs 24 hours a day, once an eruption was reported. The 5-minute assessment can be made from these automated Puff predictions and then "improved" once more information on the eruption is available. Since the 2006 eruption of Augustine, the Puff model predictions have been used for numerous volcanoes around the world (Webley and others, 2009). They are used by AVO, NWS, AFWA, and KVERT to determine the movement of volcanic eruption clouds in the NOPAC. Further developments for the Puff model will include determining reliable actual airborne volcanic ash cloud concentrations, through model initialization from satellite derived ash retrievals, and to

work with the USGS-led eruption source parameters working group (Mastin and others, 2009) to provide improved volcanic ash forecasts by taking account of past eruption history.

Acknowledgments

The authors wish to thank the staff and students in the AVO remote-sensing group for their monitoring of Augustine Volcano and analysis of the remote-sensing satellite data during the eruption response. The authors would like to thank the Arctic Region Supercomputing Center (ARSC) for its support of Webley's and Bailey's postdoctoral fellowships during the eruption crisis. The authors also appreciate the Geophysical Institute at the University of Alaska Fairbanks for their support of the AVO remote-sensing team.

References Cited

Aloisi, M., D'Agostino, M., Dean, K.G., Mostaccio G., and Neri, A., 2002, Satellite analysis and PUFF simulation of the eruptive cloud generated by the Mount Etna paroxysm of 22 July 1998: Journal of Geophysical Research, v. 107, no. B12, doi:10.1029/2001JB000630.

Bailey, J.E., Dean, K.G., Dehn, J., and Webely, P.W., 2010, Integrated satellite observations of the 2006 eruption of Augustine Volcano, *in* Power, J.A., Coombs, M.L., and Freymueller, J.T., eds., The 2006 eruption of Augustine Volcano, Alaska: U.S. Geological Survey Professional Paper 1769 (this volume).

Blong, R.J., 1984, Volcanic hazards: A sourcebook on the effects of eruptions. Sydney. Academic Press, 424 p.

Cahill, C.F., 2003, Asian aerosol transport to Alaska during ACE-Asia: Journal of Geophysical Research, v. 108, no. D23, doi:10.1029/2002JD003271.

Casadevall, T.J., 1993, Volcanic hazards and aviation safety, lessons of the past decade: FAA Aviation Safety Journal, v. 2, p. 1–11.

Casadevall, T.J., and Krohn, D., 1995, Effects of the 1992 Crater Peak eruptions on airports and aviation operations in the United States and Canada: U.S. Geological Survey Bulletin 2139, p. 205–220.

Coombs, M.L., Bull, K.F., Vallance, J.W., Schneider, D.J., Thoms, E.E., Wessels, R.L., and McGimsey, R.G., 2010, Timing, distribution, and volume of proximal products of the 2006 eruption of Augustine Volcano, *in* Power, J.A., Coombs, M.L., and Freymueller, J.T., eds., The 2006 eruption of Augustine Volcano, Alaska: U.S. Geological Survey Professional Paper 1769 (this volume).

Dean, K., Dehn, J. Engle, K., Izbekov, P., Papp, K., and Patrick, M., 2002, Operational Satellite Monitoring of Volcanoes at the Alaska Volcano Observatory: Advances in Environmental Monitoring and Modelling, v. 1, no. 1, p. 3–35.

Draxler, R.R., and Hess, G.D., 1997, Description of the Hysplit-4 modeling system: NOAA Technical Memo ERL ARL-224, 24 p.

Draxler, R.R., and Hess, G.D., 1998, An overview of the Hysplit 4 modeling system for trajectories, dispersion and deposition: Australian Meteorological Magazine, v. 47, p. 295–308.

Hufford, G.L., Salinas, L.J, Simpson, J.J., Barske, E.G., and Pieri, D.C., 2000, Operational Implications of airborne volcanic ash: Bulletin of the American Meteorological Society, v. 81, no. 4, p. 745–755.

Kienle, J., and Shaw, G.E., 1979, Plume Dynamics, thermal energy and long distance transport of Vulcanian eruption clouds from Augustine Volcano, Alaska: Journal of Volcanology and Geothermal Research, v. 6, no.1–2, p. 139–164.

Krotkov, N.A., Torres, O., Seftor, C., Krueger, A.J., Kostinski, A., Rose, W.I., Bluth, G.J.S., Schneider, D. and Schaefer., S.J., 1999, Comparison of TOMS and AVHRR volcanic ash retrievals from the August 1992 eruption of Mt. Spurr: Geophysical Research Letters, v. 26, no. 4, p. 455–458.

Mastin, L.G., Guffanti, M., Servranckx, R., Webley, P.W, Barsotti, S., Dean, K., Denlinger, R., Durant, A., Ewert, J.W., Gardner, C.A., Holliday, C., Neri, A., Rose, W.I., Schneider, D., Siebert, L., Stunder, B., Swanson, G., Tupper, A., Volentik, A., and Waythomas, C.F., 2009, A multidisciplinary effort to assign realistic source parameters to model of volcanic ash-cloud transport and dispersion during eruptions Mastin, Larry, and Webley, Peter, eds., *in* Special Issue on Volcanic Ash Clouds: Journal of Volcanology and Geothermal Research, v. 186, no. 1–2, p. 10–21. doi:10.0116/j.volgeores.2009.01.008.

McNutt, S.R., Tytgat, G., Estes, S.A., and Stihler, S.D., 2010, A parametric study of the January 2006 explosive eruptions of Augustine Volcano, using seismic, infrasonic, and lightning data, *in* Power, J.A., Coombs, M.L., and Freymueller, J.T., eds., The 2006 eruption of Augustine Volcano, Alaska: U.S. Geological Survey Professional Paper 1769 (this volume).

Miller, T.P., and Casadevall, T.J., 2000, Volcanic ash hazards to aviation. In: Sigurdsson, H., ed., Encyclopedia of Volcanoes: San Diego, Academic Press, p. 915–930.

Papp, K.R., Dean, K.G., and Dehn, J., 2005, Predicting regions susceptible to high concentrations of airborne volcanic ash in the North Pacific region: Journal of Volcanology and Geothermal Research. v. 148, p. 295–314.

Paskievitch, J., Read, C., and Parker, T., 2010, Remote telemetered and time-lapse cameras at Augustine Volcano, *in* Power, J.A., Coombs, M.L., and Freymueller, J.T., eds., The 2006 eruption of Augustine Volcano, Alaska: U.S. Geological Survey Professional Paper 1769 (this volume).

Peterson, R., Webley, P.W., D'Amours, R., Servranckx, R., Stunder, R., and Papp, K., 2010, Volcanic ash transport and dispersion models, *in* Dean, K.G., and Dehn, J., eds., Monitoring volcanoes in the North Pacific—observations from space: Springer Praxis, London.

Power, J.A., Nye, C.J., Coombs, M.L., Wessels, R.L., Cervelli, P.F., Dehn, J., Wallace, K.L., Freymueller, J.T., and Doukas, M.P., 2006, The reawakening of Alaska's Augustine Volcano: Eos (American Geophysical Union Transactions), v. 87, no. 37, p. 373–377.

Prata, A.J., 1989a, Infrared radiative transfer calculations for volcanic ash clouds: Geophysical Research Letters, v. 16, p. 1293–1296.

Prata, A.J., 1989b, Observations of volcanic ash clouds in the 10-12 μm window using AVHRR/2 data: International Journal of Remote Sensing, v. 10, p. 751–761.

Prata, F., Bluth, G., Rose, W., Schneider, D., and Tupper, A., 2001, Comments on ''Failures in detecting volcanic ash from a satellite-based technique": Remote Sensing of Environment, v. 78, p. 341–346.

Pudykiewicz, J., 1988, Numerical simulation of the transport of radioactive cloud from the Chernobyl nuclear accident: Tellus, v. 40B, p. 241–259.

Pudykiewicz, J., 1989, Simulation of the Chernobyl dispersion with a 3-D hemispheric tracer model: Tellus, v. 41B, p. 391–412.

Rose, W.I., Delene, D.J., Schneider, D.J., Bluth, G.J.S., Krueger, A.J., Sprod, I., McKee, C., Davies, H. L., and Ernst, G.G.J., 1995, Ice in the 1994 Rabaul eruption cloud; implications for volcano hazard and atmospheric effects: Nature, v. 375, p. 477–479.

Sassen, K., Zhu, J., Webley, P.W., Dean, K., and Cobb, P., 2007, Volcanic ash plume identification using polarization lidar; Augustine eruption, Alaska: Geophysical Research Letters. v. 34, no. 8, doi: 10.1029/2006GL027237.

Searcy, C., Dean, K.G., and Stringer, W., 1998, PUFF; A volcanic ash tracking and prediction model: Journal of Volcanology and Geothermal Research, v. 80, p. 1–16.

Simpson, J.J., Hufford, G., Pieri, D., and Berg, J., 2000, Failures in detecting volcanic ash from satellite based technique: Remote Sensing of Environment. v. 72, p. 191–217.

Simpson, J.J., Hufford, G., Pieri, D., and Berg, J., 2001, Response to Comments on "Failures in detecting volcanic ash from satellite based technique": Remote Sensing of Environment, v. 78, p. 347–357.

Sparks, R.S.J., Bursik, M.I., Carey, S. N., Gilbert, J.E., Glaze, L., Sigurdsson, H. and Woods, A. W., 1997, Volcanic Plumes: Chichester, Wiley, 589 p.

Tanaka, H.L., 1994, Development of a prediction scheme for volcanic ash fall from Redoubt Volcano, Alaska *in* Proceedings of the First International Symposium on Volcanic Ash and Aviation Safety: U.S. Geological Survey Bulletin, 2047, p. 283–291.

Wallace, K.L, Neal, C.A., and McGimsey, R.G., 2010, Timing, distribution, and character of tephra fall from the 2005–2006 eruption of Augustine Volcano, Alaska, *in* Power, J.A., Coombs, M.L., and Freymueller, J.T., eds., The 2006 eruption of Augustine Volcano, Alaska: U.S. Geological Survey Professional Paper 1769 (this volume).

Waythomas, C.F., Dorava, J. M., Miller, T. P., Neal, C. A., and McGimsey, R. G., 1998, Preliminary volcano-hazard assessment for Redoubt Volcano, Alaska: U.S. Geological Survey Open-File Report OF 98-0857, 40 p.

Webley, P.W., Dean, K., Collins, R., Fochesatto, J., Sassen, K., Atkinson, D., Cahill, C., and Prata, A., 2008, Predicting and validating the tracking of a volcanic ash cloud during the 2006 eruption of Mt. Augustine Volcano: Bulletin of American Meteorological Society. v. 89, no. 11, p. 1647–1658 doi: 10.1175/2008BAMS2579.1.

Webley, P.W., Dean, K., Bailey, J.E., Dehn, J., and Peterson, R., 2009, Volcanic ash modeling for North Pacific volcanoes automated operational monitoring and virtual globes, *in* Aviation Hazards from Volcanoes: Natural Hazards, special issue v. 51, no. 2, p. 345–361 doi:10.1007/s11069-008-9246-2.

Wen, S., and Rose, W.I., 1994, Retrieval of sizes and total masses of particles in volcanic clouds using AVHRR bands 4 and 5: Journal of Geophysical Research, v. 99, p. 542–5431.

The 2006 Eruption of Augustine Volcano, Alaska
Power, J.A., Coombs, M.L., and Freymueller, J.T., editors
U.S. Geological Survey Professional Paper 1769

Chapter 22

High-Resolution Satellite and Airborne Thermal Infrared Imaging of the 2006 Eruption of Augustine Volcano

By Rick L. Wessels[1], Michelle L. Coombs[1], David J. Schneider[1], Jonathan Dehn[2], and Michael S. Ramsey[3]

Abstract

Thermal infrared (TIR) images provided a timely pre- and syn-eruption record of summit changes, lava flow emplacement, and pyroclastic-flow-deposit distribution during the Alaska Volcano Observatory's (AVO) response to the 2006 eruption of Augustine Volcano. A series of images from both handheld and helicopter mounted forward looking infrared radiometers (FLIR) captured detailed views during a series of 13 overflights from December 2005 through August 2006. In conjunction with these images, data from the Advanced Spaceborne Thermal Emission and Reflection Radiometer (ASTER) provided frequent multispectral synoptic views of the eruption's emissions and deposits. The ASTER Urgent Request Protocol system also facilitated more frequent scheduling and faster data availability during the eruption. Airborne and satellite imaging provided 20 different days of TIR coverage over the 5-month eruptive period, with 4 of those days covered by both FLIR and ASTER. The high-resolution TIR images documented gradual pre-eruption heating of the summit, emplacement of pyroclastic-flow deposits, rapid temperature increase as the lava dome and flows formed, and slow cooling of the volcanic deposits that followed. The high-resolution data uniquely documented segmentation of the lava flows into hot areas of increased flow deformation and cooler, more stable crust on the active flows. In contrast, the satellite TIR data provided synoptic views of the areal distribution of volcanic products at Augustine including the extent and composition of the plumes.

Introduction

Thermal infrared (TIR) imaging of active volcanoes has increasingly become an important tool for monitoring and documenting dynamic volcanic processes. The Alaska Volcano Observatory (AVO) routinely monitors all volcanoes in the North Pacific using low-spatial-resolution (kilometer scale), high-temporal-resolution (multiple images per day) TIR data from the Advanced Very High Resolution Radiometer (AVHRR), Moderate Resolution Image Spectrometer (MODIS), and Geostationary Operational Environmental Satellites (GOES) (Harris and others, 1997; Dehn and others, 2002; Wright and others, 2002; see Bailey and others, this volume). Whereas these data work well for detecting gross thermal changes and large ash plumes that precede and accompany eruptions, higher-spatial-resolution data are commonly required to detect lower temperatures and the subtle changes that are common during ongoing volcanic phenomena (fig. 1). Satellite sensors, such as the Advanced Spaceborne Thermal Emission and Reflection Radiometer (ASTER) and the Thematic Mapper (TM)/Enhanced Thematic Mapper (ETM+) on Landsats 5 and 7, respectively, provide high-spatial-resolution (tens of meters), low-temporal-resolution (days to weeks) TIR data (Flynn and others, 2001; Ramsey and Dehn, 2004; Vaughan and Hook, 2006; Carter and others, 2008). Airborne or ground-based TIR imaging radiometers provide a very high spatial resolution (centimeters to meters) with a variable temporal resolution depending on the study (Harris and others, 2005; Ball and Pinkerton, 2006). High-resolution TIR images can document precursory changes in existing thermal features, such as fumaroles or hot springs, as well as track structural changes indicated by the formation of new fumaroles, hot fractures, and (or) the melting of snow and ice (Schneider and others, 2000; Andronico and others, 2005). Both satellite and airborne TIR images can also be used to effectively observe eruption plumes (see Bailey and others, this volume), to document lava dome and flow dynamics and effusion rates (Ramsey and Dehn, 2004; Harris and others, 2005), and to document pyroclastic flow emplacement (Carter and others, 2007).

[1] Alaska Volcano Observatory, U.S. Geological Survey, 4200 University Drive, Anchorage, AK 99508.

[2] Alaska Volcano Observatory, Geophysical Institute, University of Alaska Fairbanks, P.O. Box 755905, Fairbanks, AK 99775.

[3] Department of Geology and Planetary Science, University of Pittsburg, Pittsburg, PA 15260.

After more than 10 months of increasing seismicity, deformation, gas emission, and heat flow, Augustine Volcano, Alaska (fig. 1), explosively erupted on January 11, 2006. The volcano produced a total of 13 explosions during the last 3 weeks of January 2006. A new summit lava dome and two short, blocky lava flows were emplaced from February to March. A series of 13 forward looking infrared radiometer (FLIR) over-flights and 7 daytime and 15 nighttime Advanced Spaceborne Thermal Emission and Reflection Radiometer (ASTER) scenes were acquired in response to this activity. The FLIR and ASTER data provided several significant observations as part of a much larger suite of real-time or near-real-time data from other satellite (AVHRR, MODIS), airborne (visual, gas), and ground-based (seismometers, global positioning system [GPS], radiometers) sensors used at AVO (see Bailey and others, this volume; Cervelli and others, this volume, Coombs and others, this volume; McGee and others, this volume; Power and Lalla, this volume).

In this chapter, we summarize airborne FLIR observations acquired between December 2005 and August 2006 and the longer record of spaceborne ASTER observations acquired between December 2000 and May 2006. The high-resolution FLIR data document the gradual pre-eruption heating of the summit, the formation of pyroclastic-flow deposits, the rapid increase in temperature as the lava dome and flows formed, and the slow cooling of volcanic deposits after the eruption. In addition to these observations of the eruption, the ASTER data provide a baseline from which to examine temperature trends over several years leading up to and during the most recent volcanic unrest.

Instrumentation and Methodology

FLIR Surveys and Data Processing

The primary airborne imaging system used in this study consists of a FLIR Systems ThermaCAM PM595 infrared camera and a Sony EVI-370 NTSC video camera housed in a helicopter-mounted four-axis gyrostabilized gimbal (see Schneider and others, 2008, for system details). A handheld version of the PM595 camera was used for repeat ground-based time-lapse imaging. The infrared camera utilizes a 320×240 microbolometer detector array, which is sensitive from 7.5–13 µm, converting TIR emitted radiance into brightness temperature. The gimbal-mounted system has an integrated 12º lens with a horizontal field of view of 210 m and a pixel resolution of 65 cm at a distance of 1 km; the handheld system has an integrated 24º lens with a horizontal field of view of 420 m and a pixel resolution of 1.3 m at a distance of 1 km. The observation distance of each survey ranged from 0.5 to 5 km, averaging about 1.2 km. The measured FLIR brightness temperature is captured by using one of three ranges, −40 to 120ºC, 80 to 500ºC, and 350 to 1,500ºC. In the low

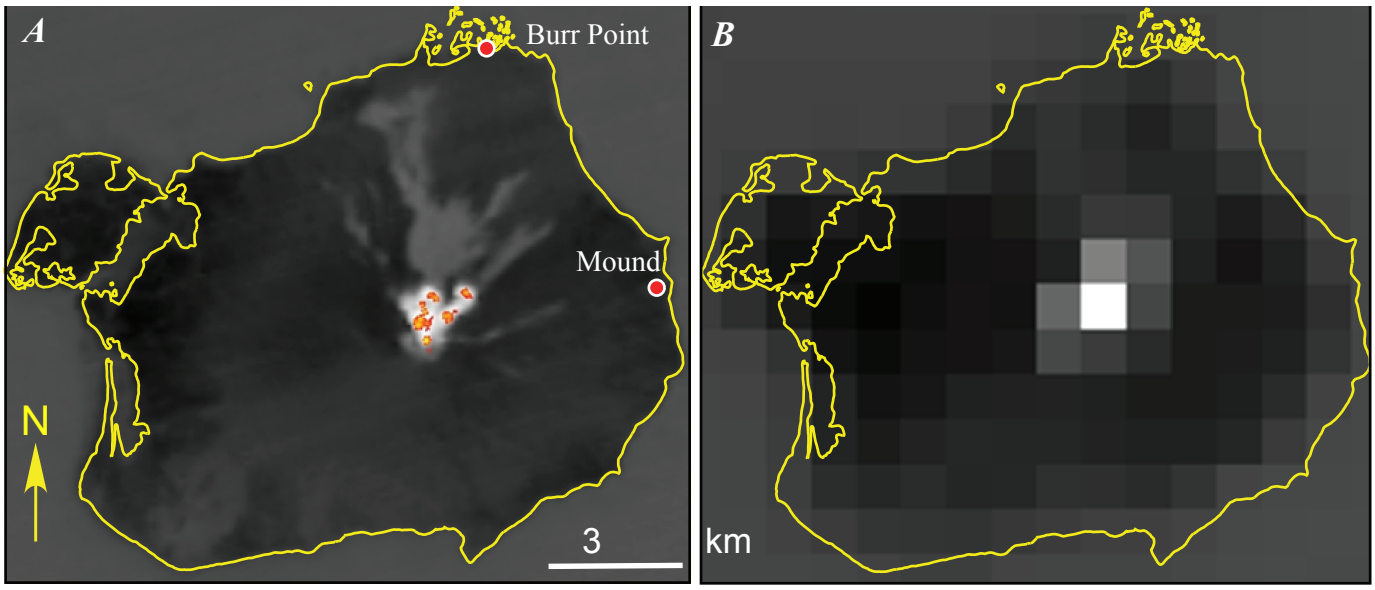

Figure 1. Nighttime 8.3-µm thermal infrared (TIR) images of Augustine Volcano acquired at 2245 AKST March 13, 2006, from the Terra spacecraft, oriented with north up. *A*, Advanced Spaceborne Thermal Emission and Reflection Radiometer (ASTER). *B*, Moderate Resolution Imaging Spectroradiometer (MODIS). Both MODIS and the Advanced Very High Resolution Radiometer (AVHRR) have ~1-km spatial resolution, which provides high-temporal-resolution views of North Pacific volcanic activity; however, these datasets lack sufficient spatial detail to capture persistent, low-level thermal features, smaller-scale activity, and eruptive deposits, are captured by ASTER TIR (90 m) and shortwave infrared (SWIR) (30 m) images.

range, the camera can record a maximum temperature of about 270ºC, but these measurements can be much less accurate because they fall outside the calibrated range. Because the temperatures measured at Augustine range from cool (ambient) to very hot (fumaroles/lava), no single PM595 gain setting covers the full range of possible temperatures, and so surveys were typically collected in at least the lower two dynamic ranges. For the FLIR temperatures reported here (see figs. 2, 5–12, 14–16), the color bar represents a linear scaling of most of the data, not the full temperature range; the lowest temperatures are clipped to black, and the highest are clipped to white.

Both the internal FLIR camera firmware (ThermaCAM PM595 Operator's Manual, 1999) and the FLIR desktop ThermaCAM Researcher software (ThermaCAM Researcher User's Manual, 2004) can convert the detected radiance to temperature-at-surface by making a first-order correction for atmospheric absorption and emission. The distance to target, ambient air temperature, relative humidity, and broadband emissivity of the surface must be inputted. Air temperature and humidity were measured onsite during each overflight. The distance to target was calculated from the difference between the time-synced GPS helicopter position and the estimated position of the feature being imaged. FLIR data were acquired during helicopter flights by several different flight crews as weather and volcanic activity permitted. For each flight, the track was recorded by using a hand-held GPS unit. The GPS tracking data provided the location and altitude at the time of the data collection, which allowed the distance to target to be calculated. The first flights conducted a general survey of the volcanic edifice and then focused on thermal changes at the summit. As the eruption progressed, later flights surveyed the fresh pyroclastic flow deposits and lava flows. Oblique aerial photographs and videos were acquired simultaneously for comparison with the TIR images. Although dates and times for geophysical data are typically recorded in UTC, we use Alaska standard time (AKST) (UTC+9) hours throughout this chapter (unless noted) to match other chapters in this volume. Alaska daylight time, which was in effect after March 21, is 1 hour later than AKST.

Satellite Data Acquisition and Processing

Visible and infrared satellite imaging of volcanoes needs to be frequent to record rapid changes in activity and to compensate for the obscuration by any heavy/recurring cloud cover. The primary high-resolution satellite-based TIR data used for this work were recorded by ASTER, which was launched in December 1999 onboard the Terra satellite. ASTER measures the top of atmosphere radiance in 14 spectral channels (Yamaguchi and others, 1998) that are collected by three subsystems, each at a different spatial resolution: the visible and near infrared (VNIR) sensor with three channels (0.56–0.81 μm) at 15-m spatial resolution, the shortwave infrared (SWIR) sensor with six channels (1.65–2.4 μm) at 30-m spatial resolution, and the TIR sensor with five channels (8.2–11.3 μm) at 90-m spatial resolution. ASTER TIR data saturate if the detected radiance exceeds a value that corresponds to a pixel-integrated brightness temperature of ~97°C. In these datasets, the at-sensor radiance from the higher-resolution SWIR channels was used to extract pixel-integrated brightness temperatures >100°C. We note that since January 2009, data from the SWIR sensor are no longer usable, owing to a failed cryocooler; however, the five TIR channels were used to extract most of the ASTER-derived temperatures presented in this chapter. Hot areas on active lava flows are typically smaller than the area covered by 90-m TIR pixels. As a result, the radiance measured is an area-weighted sum of the multiple-subpixel radiating components (Wright and Flynn, 2003). Depending on the magnitude difference of the measured temperatures, this averaging can produce a large underestimation or overestimation of the actual derived temperatures and errors in the surface emissivity (Rose and Ramsey, 2009). Therefore, the temperatures derived from mixed radiance data are commonly denoted as pixel-integrated temperatures.

The ASTER TIR data analyzed in this chapter are derived from the calibrated, at-sensor radiance. These data must first be corrected for atmospheric absorption/emission by using a standard atmospheric model with specific corrections for the image location and the time of year of acquisition (Thome and others, 1998). To then extract the pixel-integrated brightness temperatures from the atmospherically-corrected radiance, the downwelling sky radiance reflected off the surface must be removed, and the surface temperature separated from the emissivity in each pixel. These steps are applied in the temperature-emissivity separation (TES) standard data processing (Gillespie and others, 1998). The Level-2 Surface Kinetic Temperature product data distributed by the National Aeronautics and Space Administration (NASA) Land Processes Distributed Active Archive Center (LP DAAC) are presented here.

Observations and Results

Frequent FLIR missions before and during the 2006 eruption of Augustine Volcano provided detailed views of summit thermal features and fresh volcanic deposits (table 1). In this section we describe the key observations from FLIR TIR images acquired over 13 different overflights, as well as from ASTER data acquired before and during the eruption. A time series of FLIR images viewed from the same point north of the volcano show some of the changes to the volcanic edifice from January 9 to March 15, 2006 (fig. 2). For example, the January 9 images (figs. 2*A*, 2*B*) show the pre-eruption melting of the summit snow cover and warm air above caused by rising steam, and the February 24, images (figs. 2*C*, 2*D*) show the initial stages of the new summit lava dome and the north lava flow. These images also detect pyroclastic-flow deposits (unit Cpf, fig. 2) from late January, which are still warm. The March 10 (figs. 2*E*, 2*F*) and March 15 (figs. 2*G*, 2*H*) images detect a much larger lava dome and clear progression of the two lava flows.

Table 1. Summary of FLIR data for Augustine Volcano acquired 2005–2006.

Date	Time (AKST)[1]	FLIR: Tmax (°C)[2]	FLIR: Tbg (°C)[3]	FLIR: Tavg (°C)[4]	Observations (after Coombs and others, this volume)	Observation quality
December 22, 2005	1509	210	−3	5	Snow-covered summit and flanks; no flowage deposits; some increased heat flow and fumarole activity at summit	Summit partially obscured by steam
January 4, 2006	AM+PM	380	−5	0	Snow-covered flanks; no flowage deposits; maximum summit temperature at fumarole; overall heating of summit region	Summit partially obscured by steam
January 12, 2006	1204	121	−5	3	Ash from Events 1 and 2 on north flank; new vent visible through 1986 dome, just south of 1986 spine	Summit partially obscured by steam and ash plume
January 24, 2006	1229	140	−15	10	Fresh snow on summit and flanks, light ash on SE flank; dark, hot, steaming, levied flows on E, NE, and N flanks; ExD1 visible on east part of summit, Tmax 140°C	Summit mostly obscured by lenticular cloud
February 8, 2006	1149	120	−1	11	Dark Cpf and RPpf flows on north flank in high contrast to fresh white snow, range from 10−25°C with some bigger, hotter blocks.	Summit mostly obscured by lenticular cloud
February 20, 2006	AM+PM	277	0	40	Good views of Cpf, RPpf; EfLf dome and north flow visible especially in FLIR images	Summit mostly obscured by low cloud deck
February 24, 2006	1519	277	−13	38	Excellent views of summit, including north lava flow	Summit partially obscured by steam
March 10, 2006	AM+PM	700	−10	66	Clear views of both NE and N lava flows; active block-and-ash flows down East Chute and from front of NE lava flow	Summit partially obscured by light steam and ash
March 15, 2006	0953	335	−5	47	Both north and NE lava flows thickened and lengthened compared to March 10; rockfall activity and ash emission diminished	Summit partially obscured by steam
March 26, 2006	AM+PM	221	−2	16	No major changes from last observation; lava-flow fronts still hot, no significant temperature changes	Summit partially obscured by steam and clouds
April 6, 2006	AM+PM	652	−1	8	Lava-flow fronts cooler, flow tops similar as compared to previous surveys; lava-flow dimensions unchanged; Summit vent atop dome very hot (650°C)	Fresh snow has covered many deposits
May 13, 2006	0956	432	4	14	North-south linear trend of fumaroles and mineralization at summit; images of all flowage deposits; summit vent cooled to 432°C	Very clear summit views; rock sampling
August 7, 2006	1030	377	12	15	North-south linear trend of fumaroles and mineralization at summit; summit vent cooled to 377°C	Very clear summit views; rock sampling

[1]Overflight and field work typically span one-plus hours and are generally midday;

[2](Tmax) maximum pixel-integrated temperature (a value of 277 indicates FLIR gain setting was saturated);

[3](Tbg) FLIR-derived background temperature;

[4](Tavg) average surface temperature of of warm ground or active lava areas.

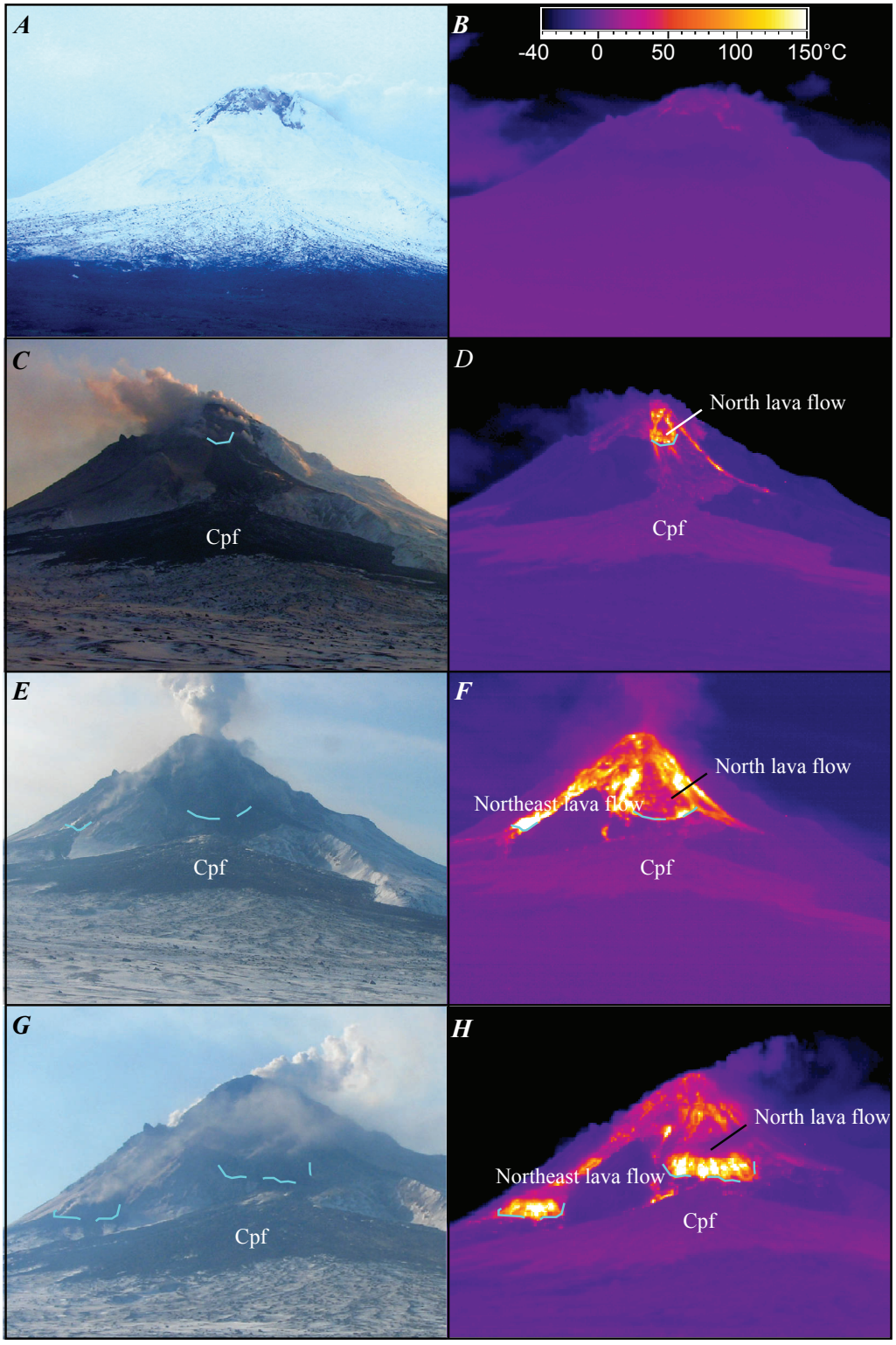

Figure 2. Photographs and Forward Looking Infrared Radiometer (FLIR) thermal infrared (TIR) images documenting growing thermal areas and new lava flows on Augustine Volcano. *A,B*, January 4, 2006. *C,D*, February 24, 2006. *E,F*, March 10, 2006. *G,H*, March 15, 2006. Images were acquired from Burr Point, which is on the coast 4.5 km north of summit (see fig. 1*A*). View southward. Cyan dashed lines denote approximate terminus of lava. Cpf pyroclastic-flow deposit.

Table 2. Summary of Advanced Spaceborne Thermal Emission and Reflection Radiometer (ASTER) data for Augustine Volcano acquired 2005–2006.

Date	Time (AKST)	Day/ night[1]	SWIR-Tmax (°C)[2]	TIR-Tmax (°C)[2]	TIR: Tbg (°C)[3]	TIR: Tavg (°C)[4]	Observations (after Coombs and others, this volume)	Scene quality
December 20, 2005	12:37:00	day	NA	−8.8	−13	−9.5	Summit area warmed above background, snow-free areas	Thin clouds, but can see island.
January 12, 2006	12:42:44	day	NA	NA	NA	NA	Plume extending south from summit	Summit obscured by volcanic plume and thin clouds
January 24, 2006	22:44:25	night	95	3	−18	−4	TIR and SWIR thermal features at summit. Weaker TIR features on flanks	Mostly clear
January 31, 2006	22:50:44	night	408	98	−18	25.4	RPpf and smaller NW flank Cpfs visible; surface to east of RPpf obscured by plume	Summit and NE flank obscured by gas and ash plume
February 22, 2006	12:37:03	day		98	−13	25.8	Good views of new dome and pf deposits	
March 13, 2006	22:45:18	night	463.9	98	−7	63	Extents of two lava flows and hottest areas within them match up well with low-light camera images from the same night	Mostly clear
April 5, 2006	22:51:30	night	239.5	13	−11	−3.5	Summit and deposits warm, small SWIR anomaly still at summit	Mostly clear
April 27, 2006	12:37:30	day	NA	NA	NA	NA	Dark lava and pf flows on summit and north flank in high contrast to fresh white snow	Partly cloudy with high cirrus over east part of island
May 17, 2006	22:45:16	night	194.5	20	−3	5.7	Summit and pf deposits still warm, but no active lava	Clear view
May 29, 2006	12:37:25	day	NA	36.7	17	19	Summit and pf deposits still warm	Clear image
October 15, 2006	22:51:16	night	174.7	8.4	−5	1.2	Average flow temps cooler, though summit fumarole still hot	Clear image

[1]Day images have VNIR, SWIR, and TIR data, night images have on SWIR and TIR;

[2](Tmax) maximum pixel-integrated temperature from SWIR and TIR;

[3](Tbg) TIR-derived background temperature;

[4](Tavg) average surface temperature of 2006 lava areas.

In addition to routine data acquisition by ASTER, the ASTER Urgent Request Protocol (URP) system (Ramsey and others, 2004) greatly improved the number of scheduled data acquisitions. A total of 25 ASTER scenes were acquired between October 30, 2005, and May 30, 2006 most during the height of activity from late January to mid-March. The volcano was clear to partly cloudy in 13 scenes, 10 of which were adequate for extracting TIR temperatures (fig. 3; table 2). During the 5 years preceding the 2006 eruption, ASTER averaged about one scene per month over the volcano.

Precursory Phase

Beginning in April 2005, an increase in the number of earthquakes below Augustine Volcano was detected by the on-island seismic network operated by AVO (see Jacobs and McNutt, this volume; Power and Lalla, this volume) and shallow inflation beneath the summit was first detected in June 2006 (Cervelli and others, 2006). By November 2005, summit GPS stations detected that this inflation had rapidly increased (Cervelli and others, 2006). In December 2005 and early

January 2006, increased seismicity and SO_2 output, as well as phreatic explosions, all suggested that volcanic unrest was intensifying (Power and others, 2006).

Of the 18 ASTER images acquired during 2005, a daytime image from December 20 (fig. 4) was the only partly clear TIR view of Augustine before the 2006 eruption. Thin cirrus-cloud cover prevented accurate TIR temperature retrievals from either the SWIR or TIR data. However, these data show a broad area of slightly elevated TIR radiance (fig. 4*C*), which corresponds to snow-free areas and fumaroles at the summit (figs. 3*A*, 4*A*). The two bright linear features visible in the SWIR image (fig. 4*B*) may represent the warmer, snow-free areas or fumarole plumes visible in the VNIR image (fig. 4*A*).

The first FLIR reconnaissance mission, which was conducted on December 22, 2005 (fig. 5), was the first of two flights during the precursory phase of the eruption. Several linear zones of warm bare rock were detected and active steaming was seen from several new fumaroles at the summit (figs. 5*A*, 5*B*). One warm (10ºC above background), snow-free area formed over a preexisting checkerboard pattern on the east side of the summit (figs. 5*C*, 5*D*). The maximum FLIR-derived temperature of a fumarole along the northeast edge of the 1986 dome was 80ºC, with a background temperature of −5ºC (figs. 5*E*, 5*F*). Fumaroles along the 1964 scarp ranged from 60 to 80ºC, and a vigorously jetting fumarole (informally referred to as Teapot) on the south flank below the summit at about 1,150-m elevation had a maximum temperature exceeding 210ºC (figs. 5*G*, 5*H*).

Photographs and FLIR images from January 4, 2006, show that the snow-free and steaming areas had expanded westward and covered more of the summit (figs. 6*A*, 6*B*). FLIR-derived pixel-integrated brightness temperatures of the snow-free areas ranged from 20 to 50ºC. The temperature of the fumarole along the northeast edge of the 1986 dome had increased to at least 380ºC, although thermal emission was likely attenuated somewhat by persistent steam (figs. 6*C*, 6*D*). The fumarole emissions had a yellow-green tint in the visible wavelengths, most likely due to reaction of SO_2 and H_2S to form native sulfur. Teapot was no longer jetting, and maximum temperatures had decreased significantly to 45ºC (figs. 6*E*, 6*F*).

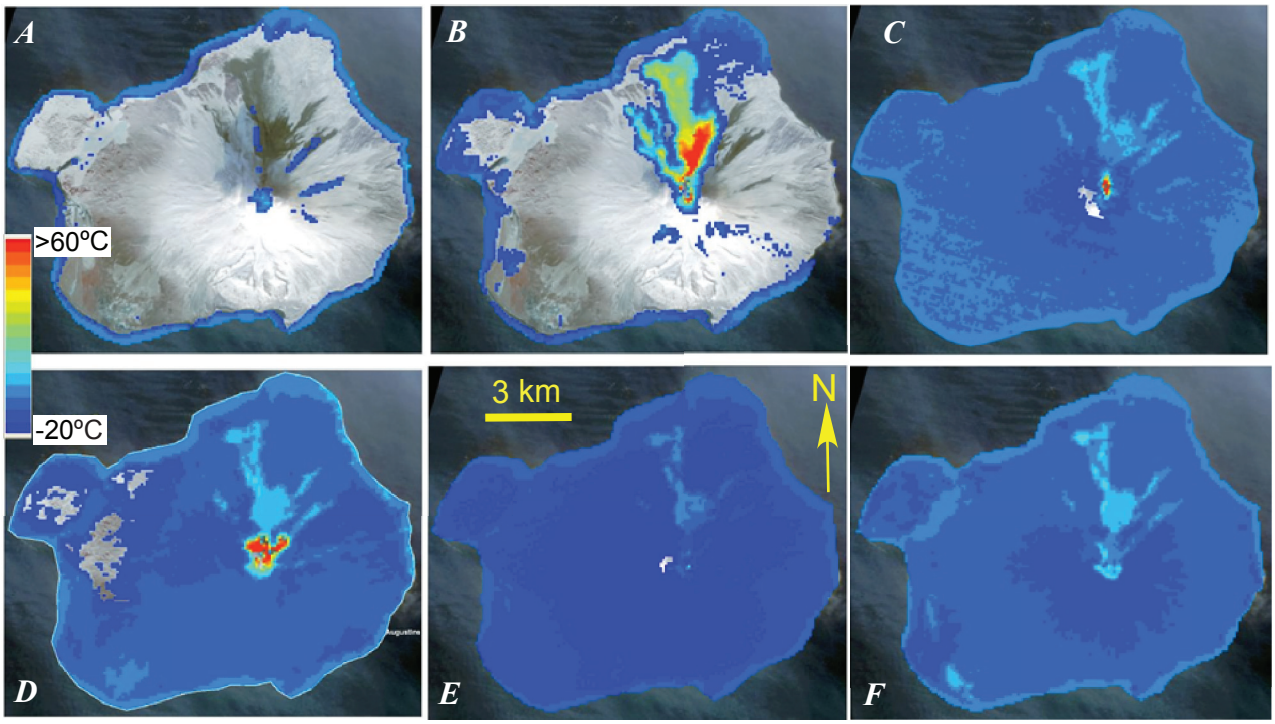

Figure 3. Advanced Spaceborne Thermal Emission and Reflection Radiometer (ASTER) pixel-integrated thermal infrared (TIR) temperatures higher than −20ºC on Augustine Volcano acquired between January 24 and May 6, 2006, showing the progression from heating of summit, through emplacement of initial pyroclastic-flow deposits after explosions in late January and early February, to effusion of first lava dome and subsequent flows as well as the gradual cooling of these volcanic deposits over time. *A*, 22:44:25 AKST January 24, 2006. *B*, 22:50:44 AKST January 31, 2006. *C*, 12:37:03 AKST February 22, 2006. *D*, 22:45:18 AKST March 13, 2006. *E*, 22:51:30 AKST April 5, 2006. F, 22:45:16 AKST May 17, 2006. Temperature data overlain on February 22, 2006, daytime ASTER visible and near-infrared (VNIR) image are visible in some images where temperatures below −20ºC were masked. North is at top of each image.

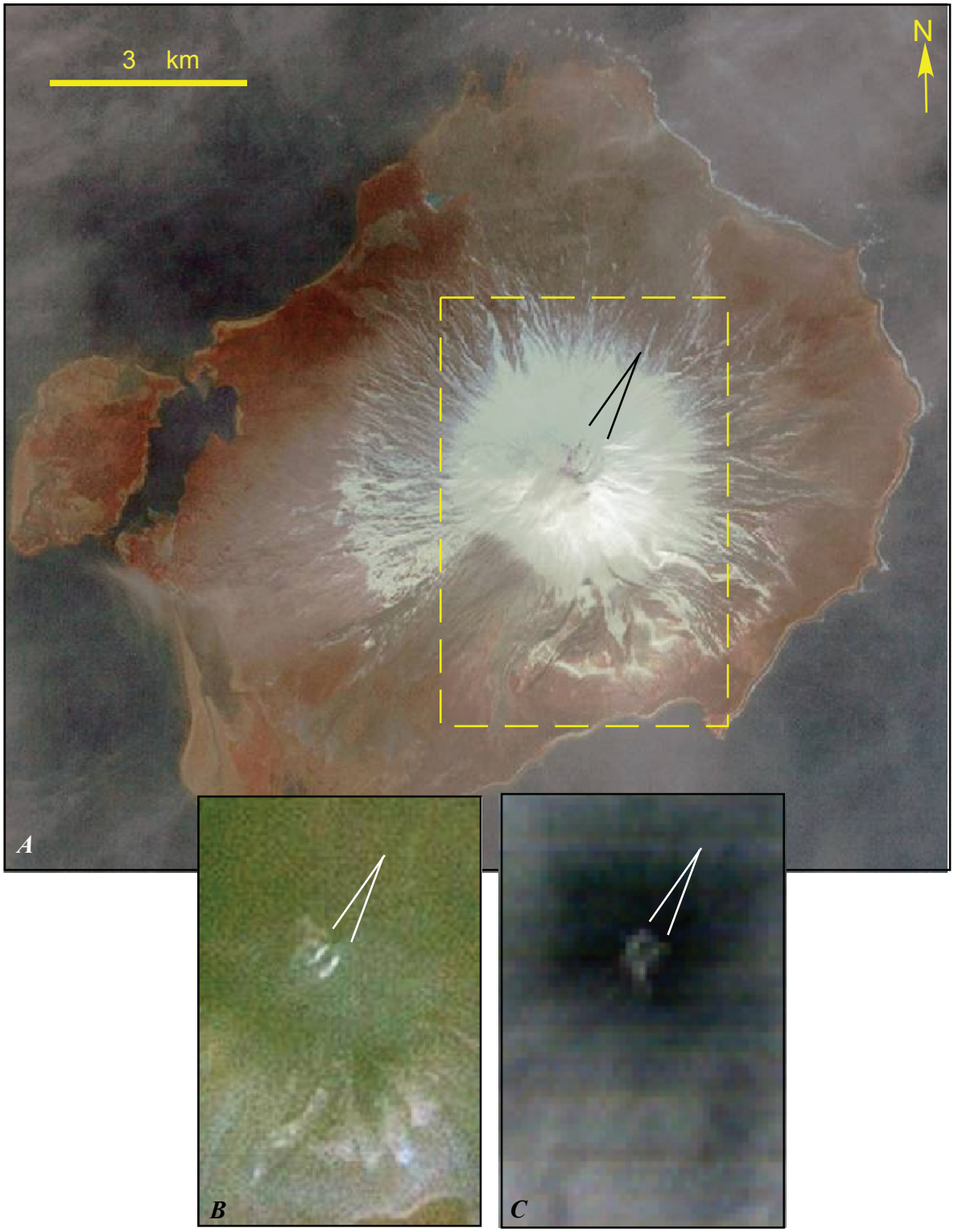

Figure 4. Partly cloudy Advanced Spaceborne Thermal Emission and Reflection Radiometer (ASTER) daytime data of Augustine Island acquired at 1235 AKST on December 20, 2005, which was only ASTER image acquired during precursory phase in late 2005 that was not completely obscured by clouds. *A*, 15 m visible and near-infrared (VNIR) image with channels 3,2,1 in R,G,B, respectively, showing the linear snow-free areas. Dashed yellow rectangle shows location of image subsets in *B* and *C*. *B*, Shortwave infrared (SWIR) image showing bright features trending same direction, likely from solar reflection off steam emanating from new fractures. *C*, Though partially obscured by thin clouds, thermal infrared (TIR) image showing elevated temperatures at the summit relative to summit temperatures in previous ASTER TIR winter observations.

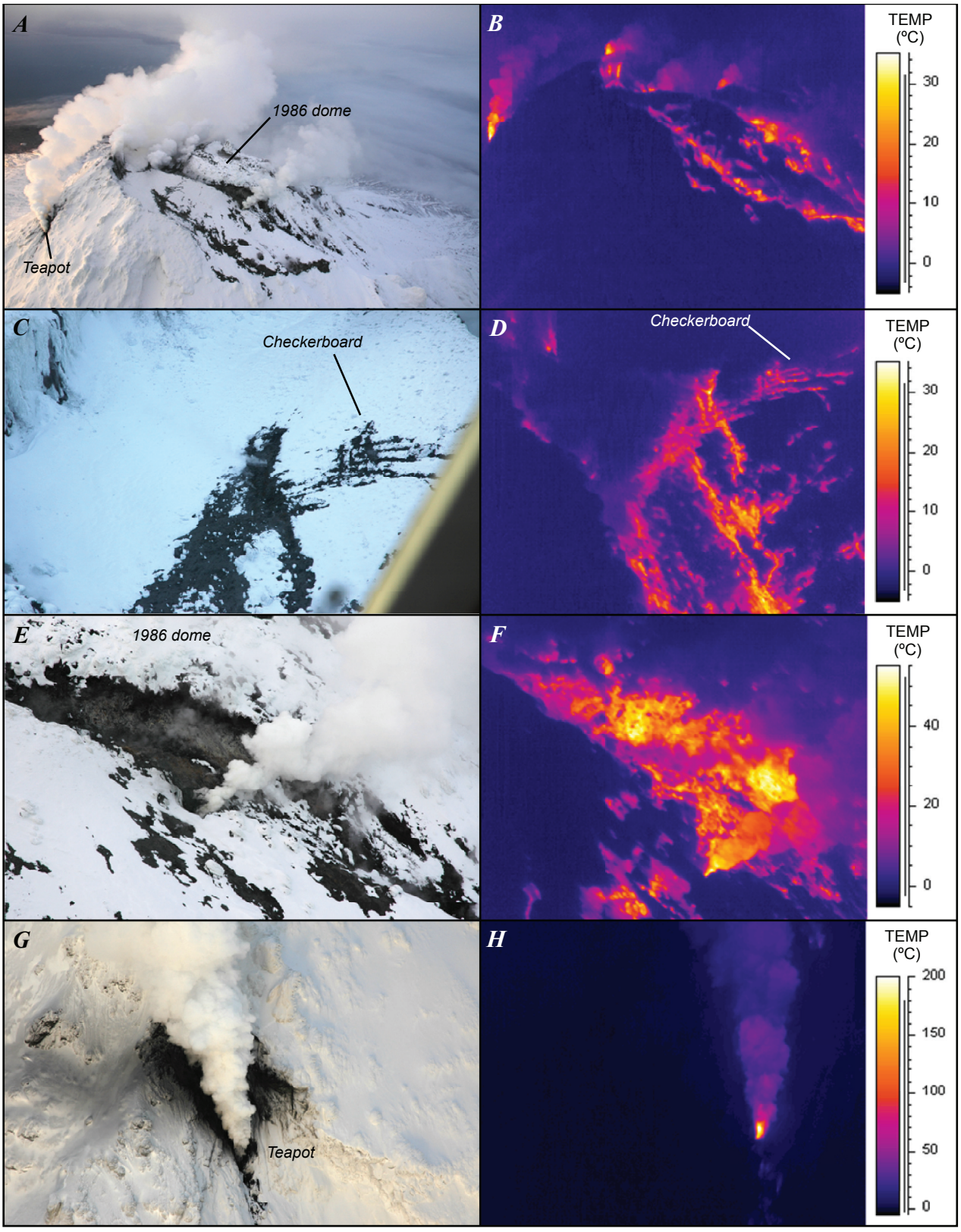

Figure 5. Photographs and thermal infrared (TIR) images of Augustine Volcano acquired during first Forward Looking Infrared Radiometer (FLIR) overflight on December 22, 2005, starting at 1509 AKST. *A,B*, Summit overview. View westward. *C,D*, "Checkerboard" pattern of snow-free fractures east of 1986 dome. *E,F*, New fumarole near edge of 1986 dome. View westward. *G,H*, Vigorously venting "teapot" fumarole on south flank.

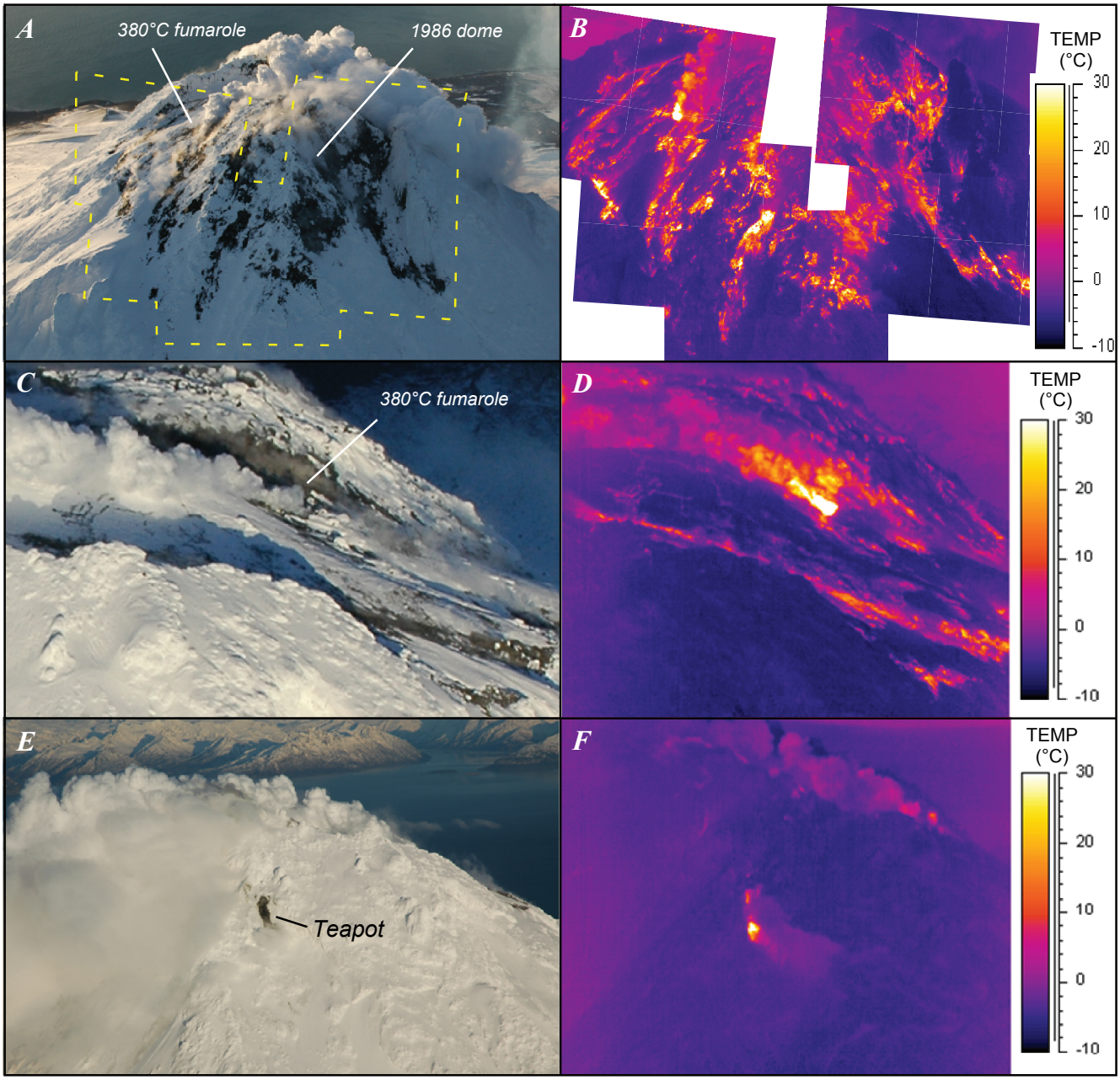

Figure 6. Photographs and thermal infrared (TIR) images of 1986 lava dome and upper flanks of Augustine Volcano acquired during Forward Looking Infrared Radiometer (FLIR) overflight on January 4, 2006. *A,B*, New warm snow-free areas extending from summit. Dashed yellow outline indicates approximate location of FLIR image mosaic shown in figure 6B. View westward. *C,D*, New fumarole along 1986 dome. View westward. *E,F*, Cooler, "Teapot" fumarole now showing only a thin steam plume. View northward.

Explosive Phase

Two explosions on the morning of January 11, 2006, heralded the beginning of the eruption's explosive phase. The explosions sent ash to 9 km above sea level (asl), but fall deposits appeared to lack juvenile material (see Wallace and others, this volume), and the explosions yielded no hot pyroclastic deposits on the island (see Coombs and others, this volume), suggesting that these explosions may have been primarily gas-release events. After about 48 hours of relative quiescence, seven more explosions on January 13 and 14 produced juvenile ash-rich clouds that rose to 14 km asl (Bailey and others, this volume; Wallace and others, this volume), hot pyroclastic flows, and secondary lahars and mixed avalanches, which were emplaced on most slopes of the volcano (see Coombs and others, this volume). Further explosions occurred on January 17, 27, and 28. A particularly explosive event on January 27 is believed to have emplaced the largest single pyroclastic-flow deposit of the entire eruption on the island's north flank (see Coombs and others, this volume). This deposit, known as the Rocky Point pyroclastic flow, approximately 4.8 km long and 17 million m^3 in volume, overran a small pond near its toe.

On January 12, 2006, 1 day after the first explosions, a FLIR helicopter mission observed that steam and ash emissions continued to reach a height of approximately 2,500 m asl and were moving southward (figs. 7*A*, 7*B*). Ash emissions waxed and waned during the time of the overflight, and a vigorous gas and ash plume emitting from a new vent, just south of the spine in the 1986 dome, was documented (figs. 7*C*, 7*D*). The maximum observed FLIR-derived brightness temperature was >275ºC, which was likely a minimum because the actual temperature exceeded the low gain setting on the FLIR. Further attempts to image this feature at a lower gain setting were unsuccessful because the vent was obscured by steam and ash emissions, which also obscured many of the elevated thermal regions visible in previous surveys, making them especially difficult to identify in images acquired from that day. Temperatures on the north face of the 1986 dome ranged from 20 to 40ºC, similar in intensity to the previous survey on January 4. Also, much less steam was observed in the south moat than during previous overflights. Drumbeat earthquakes (see Lalla

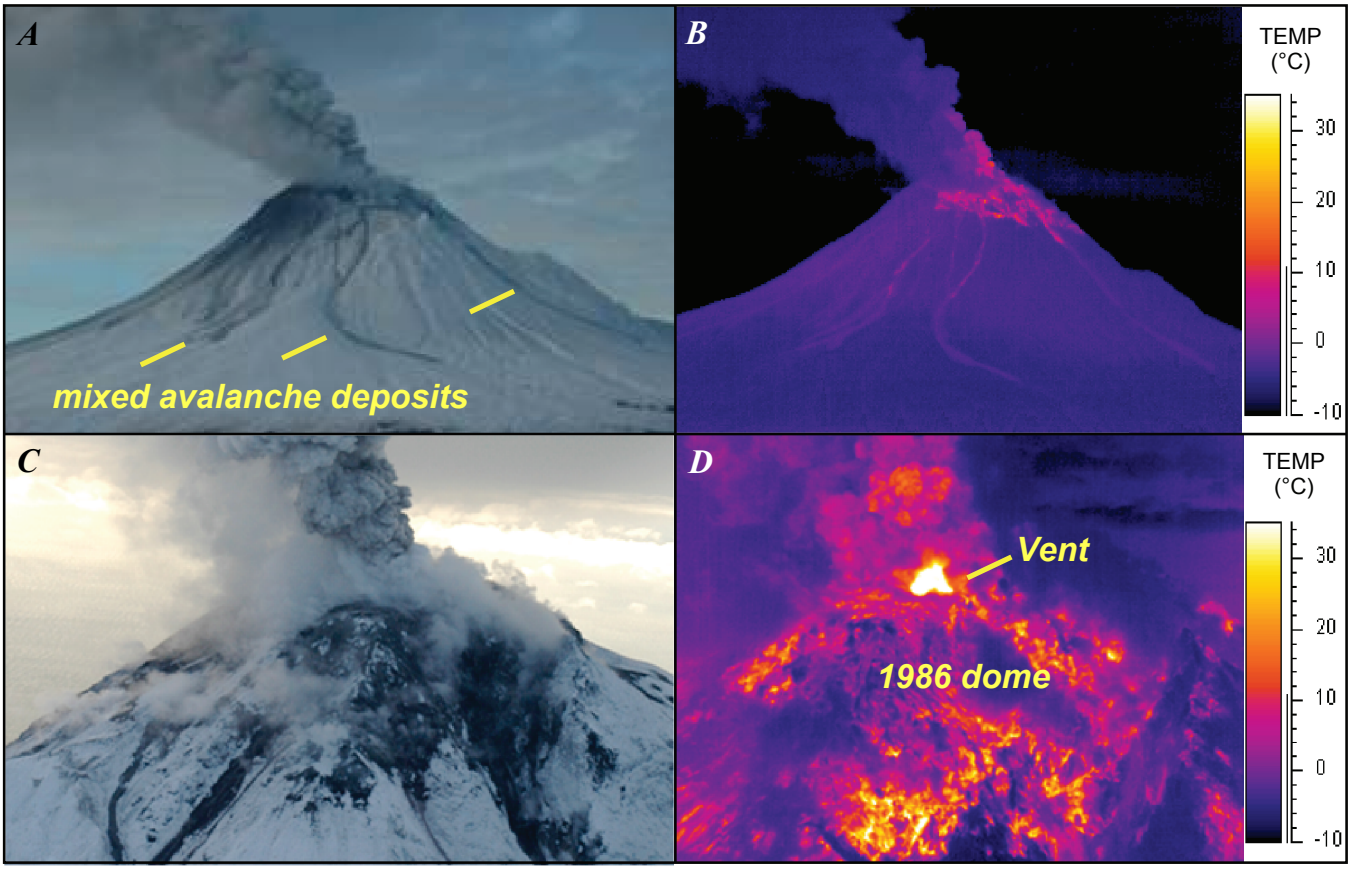

Figure 7. Photographs and thermal infrared (TIR) images of Augustine Volcano acquired during Forward Looking Infrared Radiometer (FLIR) overflight on January 12, 2006, starting at 1204 AKST. *A*,*B*, Gas and ash column venting from summit. Mixed avalanche deposits from explosions 1 and 2 on January 11, 2006, are visible on east flank. View northward. *C*,*D*, New vent (>275ºC) at top of 1986 dome. View southward.

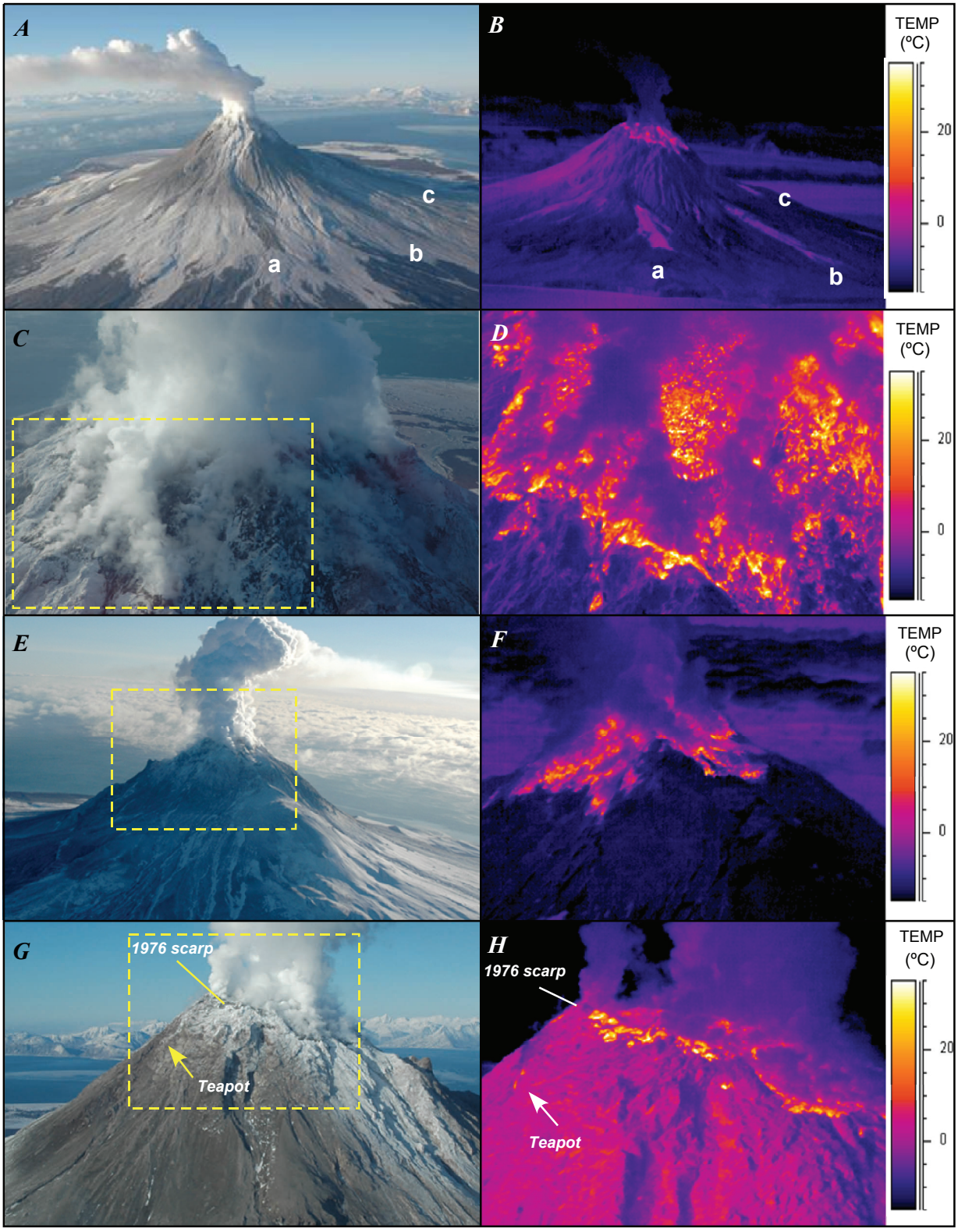

Figure 8. Photographs and thermal infrared (TIR) images of Augustine Volcano acquired during Forward Looking Infrared Radiometer (FLIR) overflight on January 24, 2006, starting at 1229 AKST. Dashed yellow boxes in *C*, *E*, and *G* indicate approximate locations of corresponding FLIR images to right. *A*,*B*, Cooling pyroclastic flows (a–c). View westward. *C*,*D*, Close-up of summit. View southwestward. *E*,*F*, Warming summit areas. View eastward. *G*,*H*, 1976 scarp at summit and "teapot" fumarole showing elevated temperatures. View westward.

and Power, this volume) and cessation of summit deformation (see Cervelli and others, this volume) suggest that lava effusion may have occurred on January 12. Saturated FLIR temperatures >275ºC were measured at the vent area through heavy steam and ash emissions, suggesting that new lava was likely present at or near the vent.

After the explosions on January 13, 14, and 17, 2006, photographs and FLIR images from January 24, showed no sign of magmatic temperatures at the summit. Cooling pyroclastic-flow deposits were observed on the east and north flanks, with surface temperatures ranging from 0 to 5ºC and a few large hot blocks, with temperatures of 30 to 40ºC (figs. 8*A*, 8*B*) were also visible. A maximum temperature of about 140ºC was observed near the new summit vent during brief views through the steam plume (figs. 8*C*, 8*D*). Steam plumes obscured much of the summit and were cold (figs. 8*E*–8*H*). Most of the summit region consisted of warm rubble, with temperatures ranging from 20 to 40ºC.

Nighttime ASTER TIR images from January 24, 2006, shows elevated summit temperatures and warm pyroclastic-flow deposits from the January 13–17 explosions on the northeast flanks (fig. 3*A*).

Continuous Phase

At about 1430 AKST on January 28, the volcano entered a period of more nearly continuous eruptive activity characterized by nearly constant ash-rich plume emissions to average heights of 3,600 m asl or less, as recorded by satellite data and radar (see Bailey and others, this volume). Occasional larger seismic signals, assumed to represent larger explosions, were associated with larger ash clouds up to 4,600 to 7,600 m asl. Subsequent observations showed that thick fans of pyroclastic material were deposited north and northeast of the summit during this period (see Coombs and others, this volume). This phase has been interpreted as the result of rapid effusion of lava at the summit, accompanied by nearly instantaneous collapse of parts of the growing lava dome to form numerous block-and-ash flows (see Coombs and others, this volume). Activity waned on February 3, and lower effusion rates produced a new lava dome and flow during the next week. Poor weather and low-lying ash obscured visual and satellite views during much of this period.

During the night of January 31, 2006, the ASTER URP system imaged an ash- and SO_2-rich plume and several large, hot pyroclastic-flow deposits on the volcano's north flank, including the Rocky Point pyroclastic flow that extends nearly to the north shoreline (fig. 3*B*). The 90-m ASTER TIR data show subtle temperature differences between the cooler distal ends of the pyroclastic-flow deposits and the warmer proximal areas. These temperature differences were likely controlled by both the age (hours) and thickness of the deposits. Multispectral TIR data also provide the means to identify silicate ash, ice, and SO_2 components in the plumes. ASTER SWIR (30 m) data from the same period show a ~700-m by 300-m region of hot pixels centered at the summit dome, with a maximum brightness temperature of 619°C.

A FLIR overflight on February 8, 2006, revealed several areas of cooling pyroclastic-flow deposits (fig. 9), the most extensive of which were in the northeast to northwest sectors. Smaller flows were deposited on the east flank (toward the Mound site), and a very small flow was observed on the southwest flank. Most of the pyroclastic-flow deposits had temperatures of 10–25°C, with numerous hotter large blocks (presumably dome fragments) with maximum temperatures >120°C. Pyroclastic-flow-deposit locations on the north and northwest flanks matched quite well with the warm features on the flanks observed in the nighttime TIR ASTER image of January 31 (fig. 3B). FLIR images of the summit were extremely difficult to acquire because of persistent steaming and cloud cover (fig. 9*A*). The maximum observed summit temperature of a contiguous area centered over the 1986 dome was ~50°C (fig. 9*B*); given the thick cloud cover, the actual temperature would have been much higher. Occasional photograph views through the steam and cloud showed a large black feature at the summit that was likely a new dome.

Eruptive Pause

From about February 10 through March 3, 2006, lava dome and flow effusion paused or at least slowed significantly (see Coombs and others, this volume). Limited thermal and visible views show little, if any, growth of the lava dome and flows during this period. FLIR and ASTER data spanning February 20–24 show a hot summit dome and rockfall deposits down the north flank and gradual cooling of the pyroclastic-flow deposits (figs. 3*C*, 10). FLIR images acquired on both February 20 and 24 detected maximum temperatures of 300°C at the edge of and below the active lava flow extending northward from the summit dome. The average surface temperature in mostly clear views of the summit dome was 40°C, whereas the average surface temperature of flows beneath the dome was 100°C. A wide area of steaming, bare rock surrounded the crater (figs. 10*C*, 10*E*), extending tens of meters down the flanks outside the 1976 crater (figs. 10*E*, 10*F*). The FLIR images, scaled for distance and pixel size, show that the warm north part of the dome was about 100 m wide and 115 m high. The slope distance from the top of the dome to the base of the 85-m-wide flow was approximately 390 m (275 m in plan view). Hot-rock deposits were also observed below the dome and along the lava flow in three distinct channels on the north flank (fig. 2*C*, 2*D*). The surfaces of the pyroclastic-flow deposits from late January had cooled to ~5°C.

Effusive Phase

After the apparent pause in eruptive activity throughout the second half of February, Augustine Volcano resumed

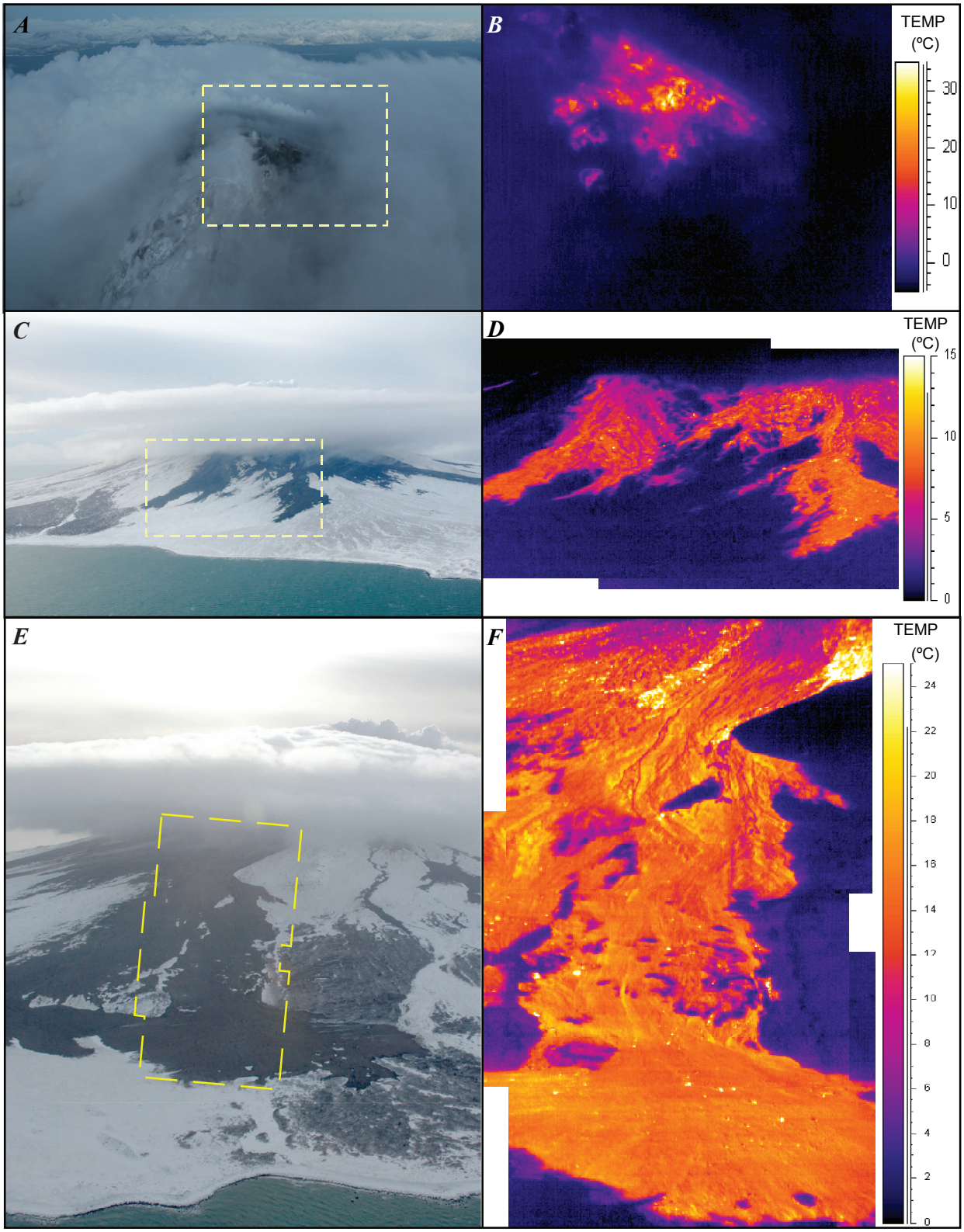

Figure 9. Photographs and thermal infrared (TIR) images of Augustine Volcano acquired during Forward Looking Infrared Radiometer (FLIR) overflight on February 8, 2006, starting at 1149 AKST. Dashed yellow boxes indicate approximate locations of corresponding FLIR image mosaics to right. *A*,*B*, Summit through thicker clouds. Dark, warm area might be obscured view of a new dome. View westward. *C*,*D*, Pyroclastic-flow deposits on northeast flank. View southwestward. *E*,*F*, Rocky Point pyroclastic-flow deposit. View southeastward.

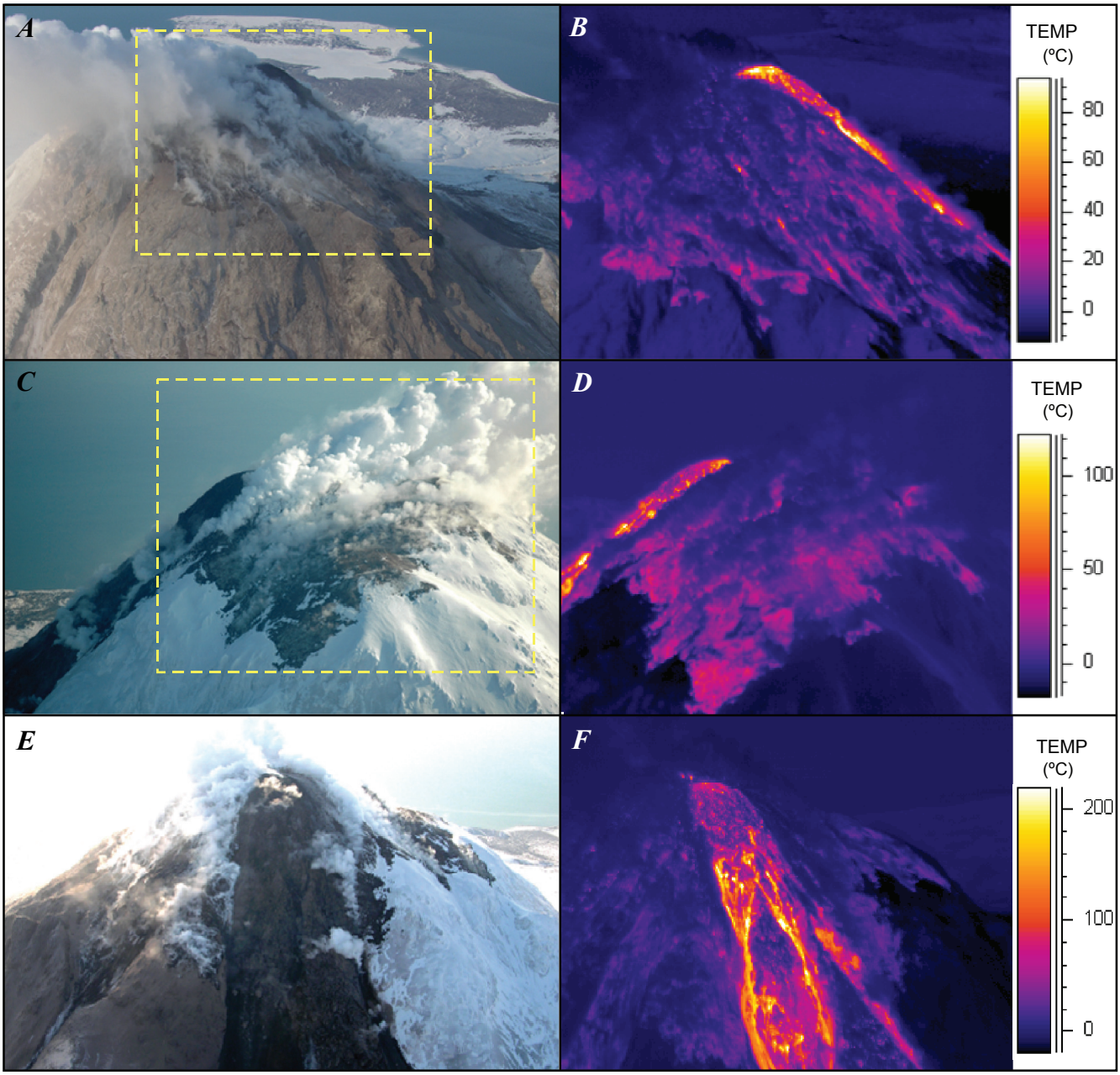

Figure 10. Photographs and thermal infrared (TIR) images of Augustine Volcano acquired during Forward Looking Infrared Radiometer (FLIR) overflight on February 24, 2006. Dashed yellow boxes in *A* and *C* indicate approximate locations of corresponding FLIR images to right. *A*,*B*, New summit lava dome, north lava flow, and hot rubble below flow, showing an expanded area of warm and steaming rock. View westward. *C*,*D*, Expanded area of warm and steaming rock at summit. View eastward. *E*,*F*, North lava flow and lava dome. View southward.

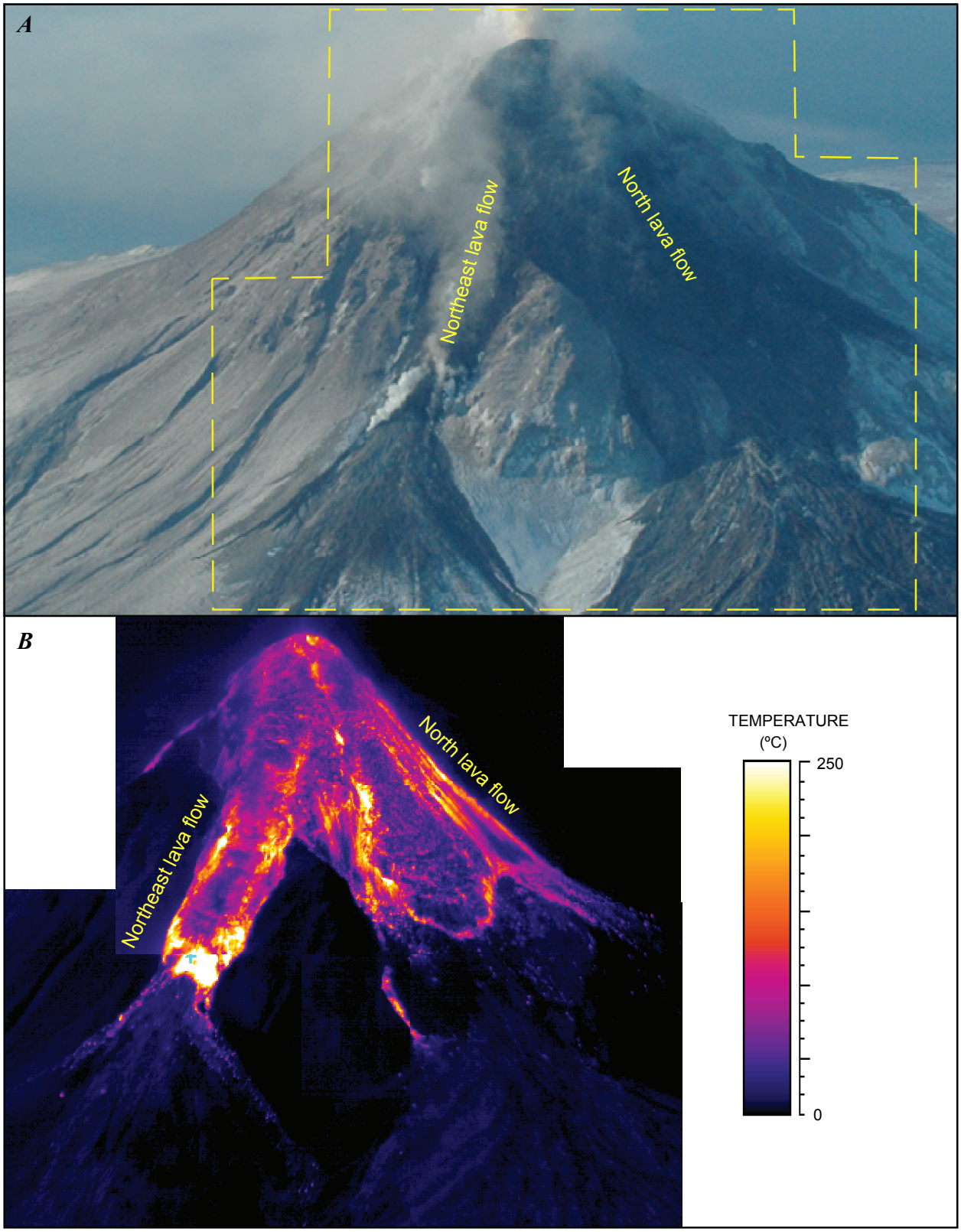

Figure 11. Photographs and thermal infrared (TIR) images of Augustine Volcano acquired 0959 AKST March 10, 2006, during Forward Looking Infrared Radiometer (FLIR) overflight. *A*,*B*, New summit lava dome and northeast and north lava flows. Summit and flows are partly obscured by dust and hot gas from frequent rockfalls from advancing flows, which are also visible in FLIR mosaic image. View southwestward.

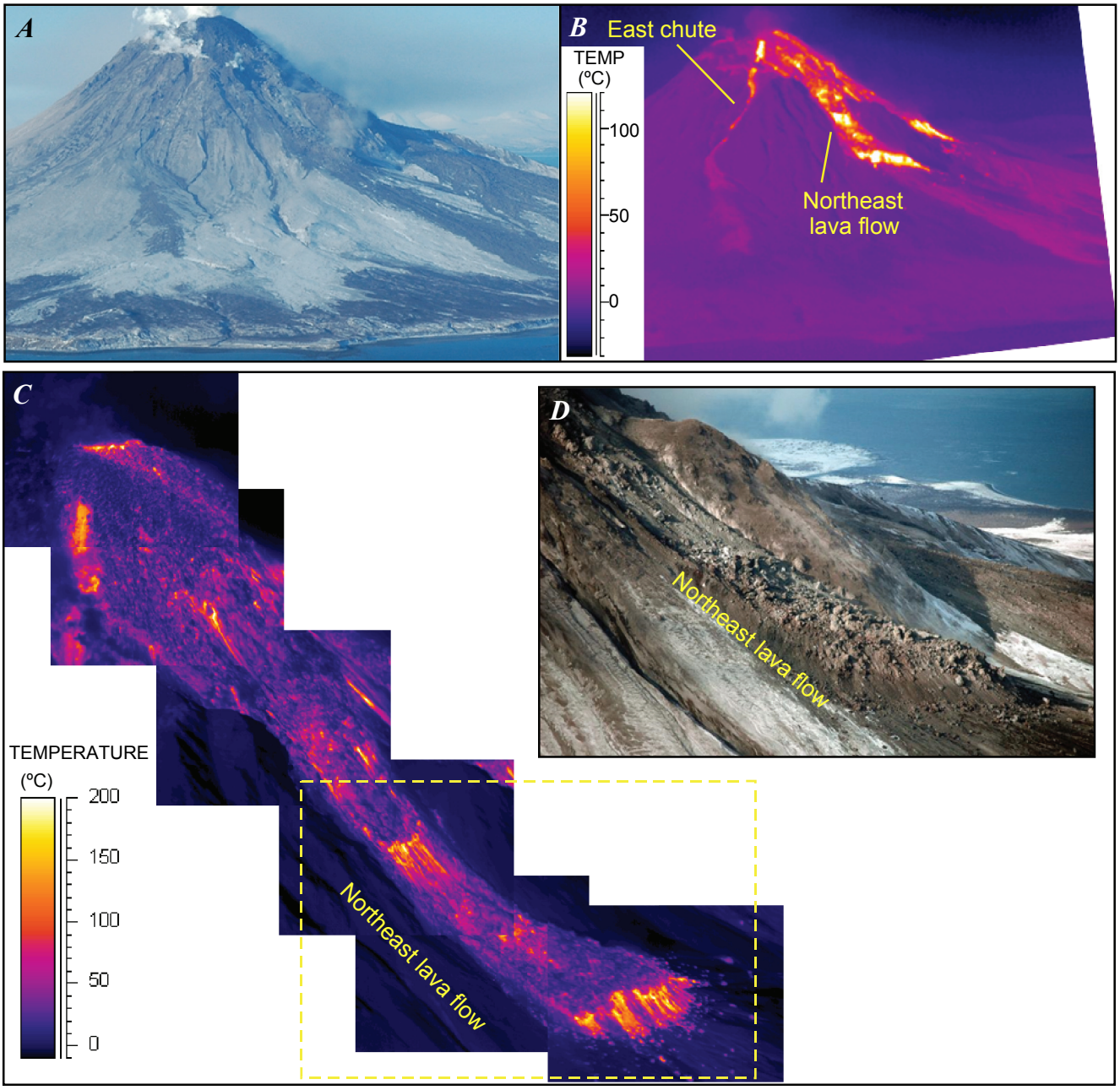

Figure 12. Photographs and thermal infrared (TIR) images of Augustine Volcano acquired during Forward Looking Infrared Radiometer (FLIR) overflight on March 15, 2006, starting at 0953 AKST. *A*,*B*, Entire volcano, with hot lava flows and small block-and-ash deposits extending down east chute below new summit lava dome. View westward. *C*,*D*, Mosaic of 6 close-up FLIR images of northeast lava flow and lava dome. Dashed yellow box indicates approximate location of figure 12*D*. View southeastward.

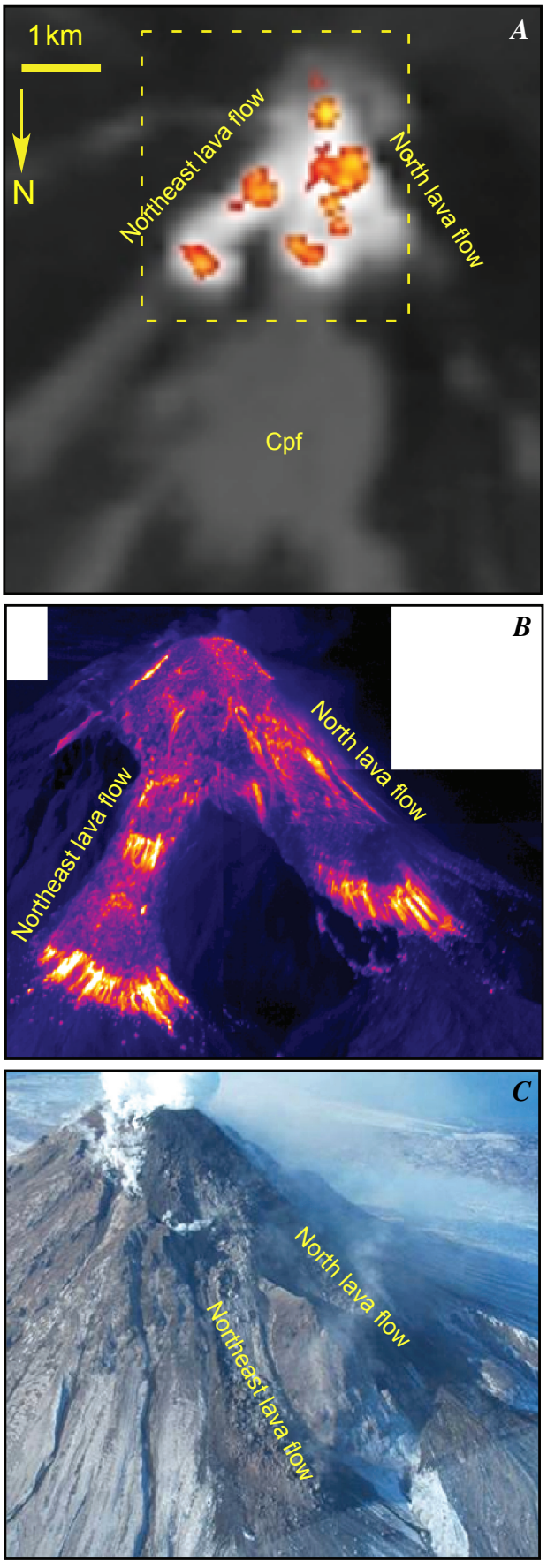

activity in March with the effusion of a larger summit dome, renewed growth of the north lava flow, and formation of a new lava flow confined to an erosional channel on the northeast side of the volcano, all accompanied by vigorous block-and-ash flows. This phase likely began on March 3 with an increase in the number of rockfall signals detected seismically, followed by a series of small explosions on March 4 (see Coombs and others, this volume; Power and Lalla, this volume). From March 8 to 16, seismic stations on the island recorded strong drumbeat earthquakes, indicative of lava effusion (see Power and Lalla, this volume), and incandescence was observed in Homer (see Sentman and others, this volume) and recorded by the Burr Point time-lapse camera (see Coombs and others, this volume). FLIR data acquired on March 10 and 15 provide some of the best information about growth of the new dome and flows (figs. 11, 12).

FLIR images from March 10, 2006, clearly show the larger dome and the two lava flows on the upper north and northeast flanks (figs. 2*E*, 2*F*, 11). A maximum temperature of 700°C was measured at the toe of the northeast lava flow, the highest temperature measured during the 2006 eruption. Mostly clear views of the summit dome revealed average surface temperatures of ~40°C; the average surface temperature of flows downslope from the dome was 100°C. The wide area of steaming, bare rock surrounding the crater that was observed in February persisted. The pyroclastic-flow deposits emplaced in late January had surface temperatures averaging 4°C, but were still steaming over the area of the now-buried pond.

On March 15, the north and northeast lava flows had both advanced and thickened since March 10. On the basis of scaled FLIR images from Burr Point (fig. 2*H*), the northeast flow advanced approximately 140 m to a total length of 930 m as measured from the base of the summit dome.

Figure 13. Comparison of multiscale, multispectral data of Augustine Volcano summit acquired March 13–15, 2006. *A*, March 13, 2006, Advanced Spaceborne Thermal Emission and Reflection Radiometer (ASTER) nighttime thermal infrared (TIR) image. *B*, Oblique airborne Forward Looking Infrared Radiometer (FLIR) image acquired 1.5 days later on March 15. *C*, Photograph taken at same time as FLIR image. ASTER image shows high temperature shortwave infrared (SWIR) (30 m) pixels in color over grayscale TIR (90 m) pixels. Map view in ASTER image is rotated with north at bottom to better match views in oblique photographs. Yellow dashed rectangle outlines approximate area of *B*. Combined TIR-SWIR ASTER image highlights benefit of having both datasets, with TIR image defining outline of active lava flows and SWIR image highlighting areas of exposed lava at surface. This SWIR image also reveals that both flows have zones of freshly exposed lava in areas of high extension-strain rate, as well as at summit and toes of flows.

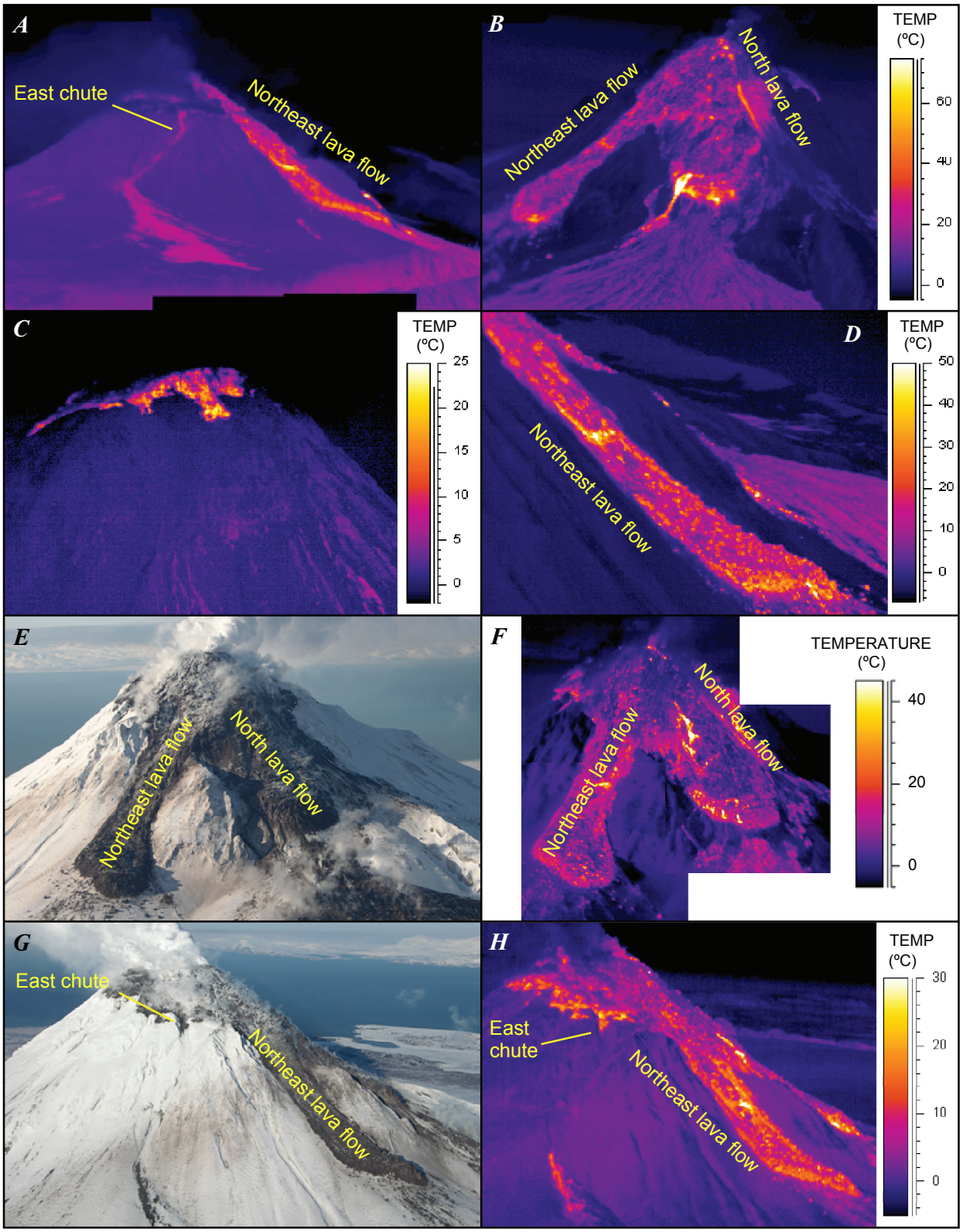

Figure 14. Photographs and thermal infrared (TIR) images of Augustine Volcano acquired during Forward Looking Infrared Radiometer (FLIR) overflights on March 26, 2006 (*A–D*), and April 6, 2006 (*E–H*). *A*, Northeast lava flow and warm, though apparently inactive, east chute (see fig. 12*C*). View westward. *B*, Northeast and north lava flows. Note active spalling along east side of north lava flow. View southward. *C*, Warm surface of summit scarp. View northeastward. *D*, Northeast lava flow. View westward. *E*,*F*, Lava flows. View southward. *G*,*H*, Northeast lava flow and east chute. View westward.

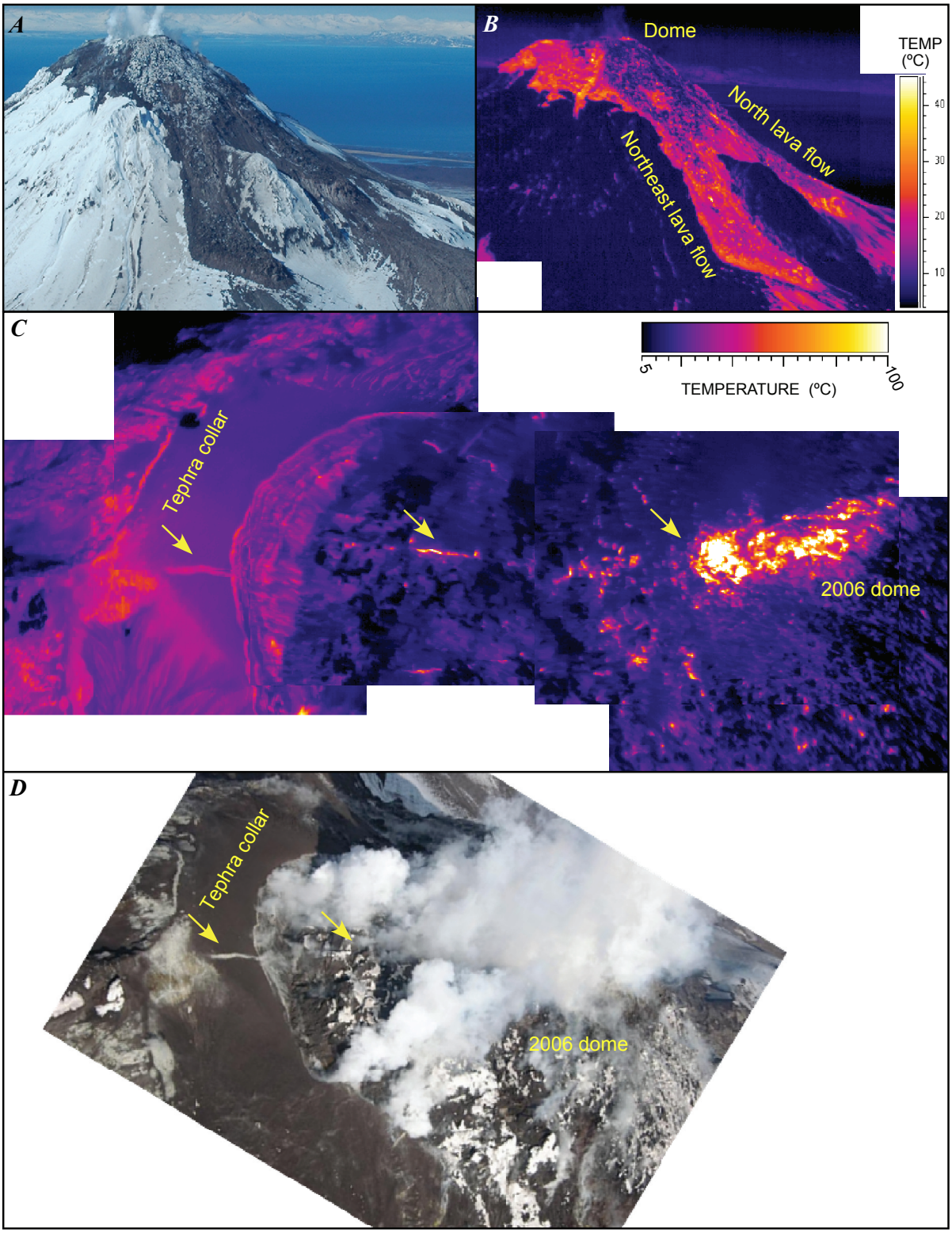

Figure 15. Photographs and thermal infrared (TIR) images of Augustine Volcano acquired during Forward Looking Infrared Radiometer (FLIR) overflight on May 13, 2006. *A*,*B*, Northeast and north lava flows, summit lava dome, and warm deposits on south side of summit. New dome rock is partly covered by a combination of snow, ice, and precipitates, whereas tephra deposits adjacent to dome remain snow free. View southward. *C*,*D*, Summit lava dome and tephra collar. Note elongate zone of high temperatures on dome and hot fractures extending southward from dome (arrows). South is to the left in both figures.

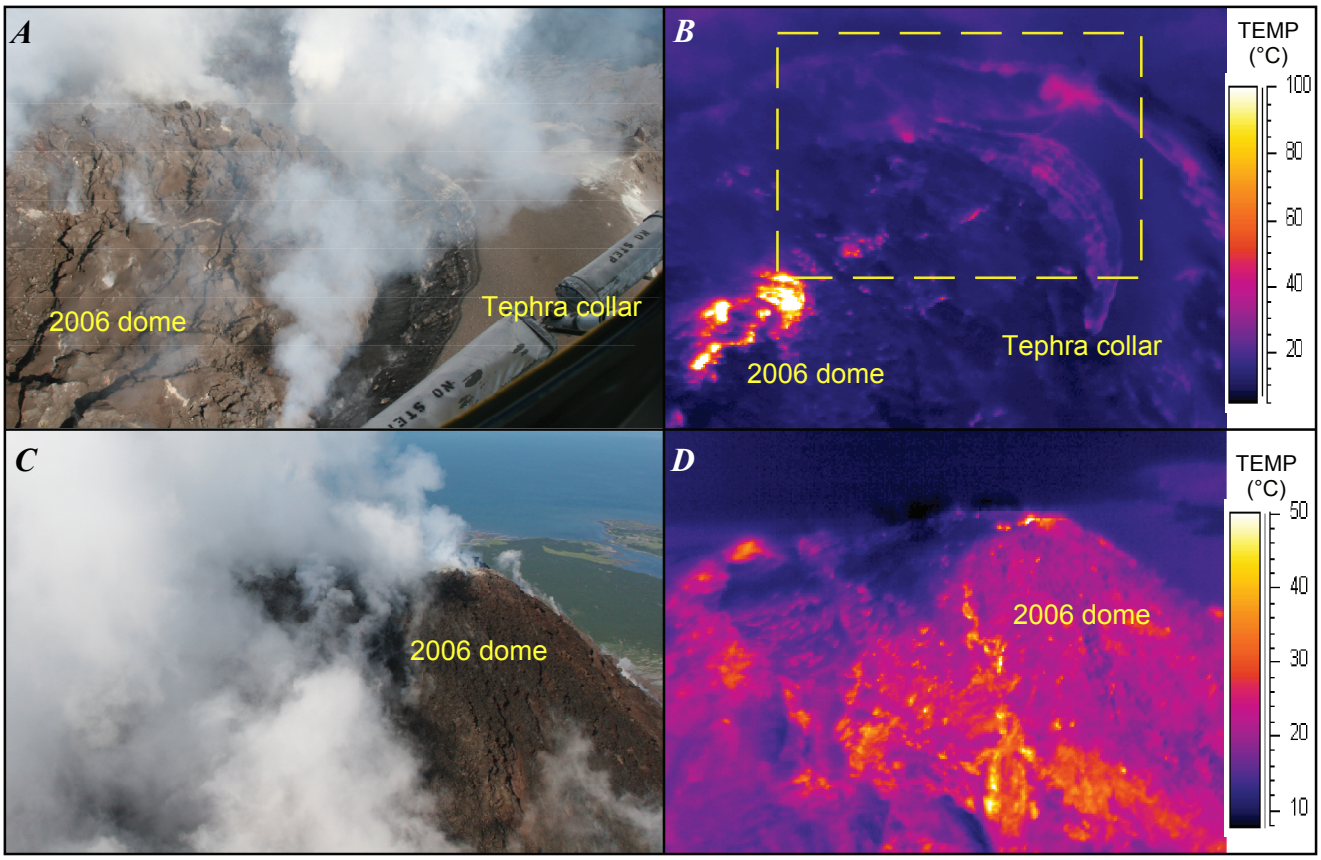

Figure 16. Comparisons between photographs and thermal infrared (TIR) images of Augustine Volcano acquired during final Forward Looking Infrared Radiometer (FLIR) overflight on August 7, 2006. *A–B*, Part of 2006 lava dome and 2006 tephra collar on south rim. Elongate zone of high temperatures on dome and hot fractures extending southward from dome persist. Dashed yellow box indicates approximate location of *A*. *C*,*D*, Summit lava dome, tephra collar, and remnants of east chute. View westward.

The north lava flow widened from by about 70 m to 410 m, but advanced downslope only approximately 20 m to a total length of 420 m. Most of the thermal energy was emitted from flow fronts and small windows through the rubble-covered carapace created by tensional fracturing as the flow advanced over steeper topography. This carapace was most notable on the east side of the dome, although no visible incandescence was observed anywhere along the flow edges (fig. 12*D*). Minimal rockfall activity suggested that the flows were generally advancing more slowly than on March 10. The average temperature measured on the flow and dome surfaces had decreased to ~40°C. The extent and temperatures of warm areas on the summit flanks were unchanged from March 10 and earlier.

FLIR data show the variation in temperature on the lava flow surfaces (fig. 12*E, 13B*). Both the lava flows and the dome edges have steeper areas of hotter material at the surface. The hot lava flows were observed about 34 hours before the FLIR survey by a nighttime ASTER image. The 90-m TIR image (figs. 3*D*, 13*A*) reveals the extent and temperature of the hot summit dome and flows as bright, sometimes saturated, pixels. The maximum pixel-integrated temperature extracted from ASTER 30-m SWIR (2.167 µm) radiance data was 463.9°C (fig. 13*A*).

Post Eruption

Seismic activity had dropped to pre-effusive-phase levels by March 20 (see Power and Lalla, this volume), and no new morphologic changes in the dome or lava flows were observed after March 15. Incandescence after this time was focused along the west margin of the north lava flow, where spalling and rockfalls continued to occur into May (see Coombs and others, this volume).

FLIR data from March 26 (figs. 14*A*–14*D*) showed that the average surface temperature was low, (~40°C). The lava flow fronts where fresh spalling had previously occurred had

maximum temperatures of 180°C. Viewed at close range (500 m), one summit fumarole had a maximum temperature of 221°C. The southwest side of the summit had warm areas extending a short distance downward from the summit.

On April 6 (figs. 14*E*–14*H*) the north and northeast lava flows had not advanced notably since previous observations on March 15 and 26. The flow fronts also appeared to be cooler relative to the previous surveys, with little rockfall from their fronts. The north-lava-flow front and margins appeared to be more active than those of the northeast flow. The average temperature of the flow and dome surfaces was similar to that in previous surveys in March (~40°C), and the extent and temperatures of the warm areas on summit flanks appear to be unchanged from previous surveys.

The maximum temperature of ~650°C in a fumarole at the top of the dome was considerably higher than that recorded on March 26 (220°C), possibly owing to better viewing conditions on April 6, but also reflecting changes in the vent geometry since the previous survey. Although gas measurements by McGee and others (this volume) show a gradual decrease in SO_2 flux from late March through April, day-to-day averages vary somewhat during this period. The measured April 6 average SO_2 flux (~2 kt/d) was nearly double the flux for March 22 (~1 kt/d).

A FLIR survey of Augustine Volcano on May 13, 2006 (figs. 15*A*–*15D*) showed no obvious morphologic changes to domes or flows since April. The maximum temperature of 428°C recorded at the top center of the 2006 dome was lower than that recorded on April 6 (650°C). Warm areas persisted around the summit region, unchanged from previous surveys. The north- south-trending fractures first observed on the summit in December 2005 continued to persist as linear

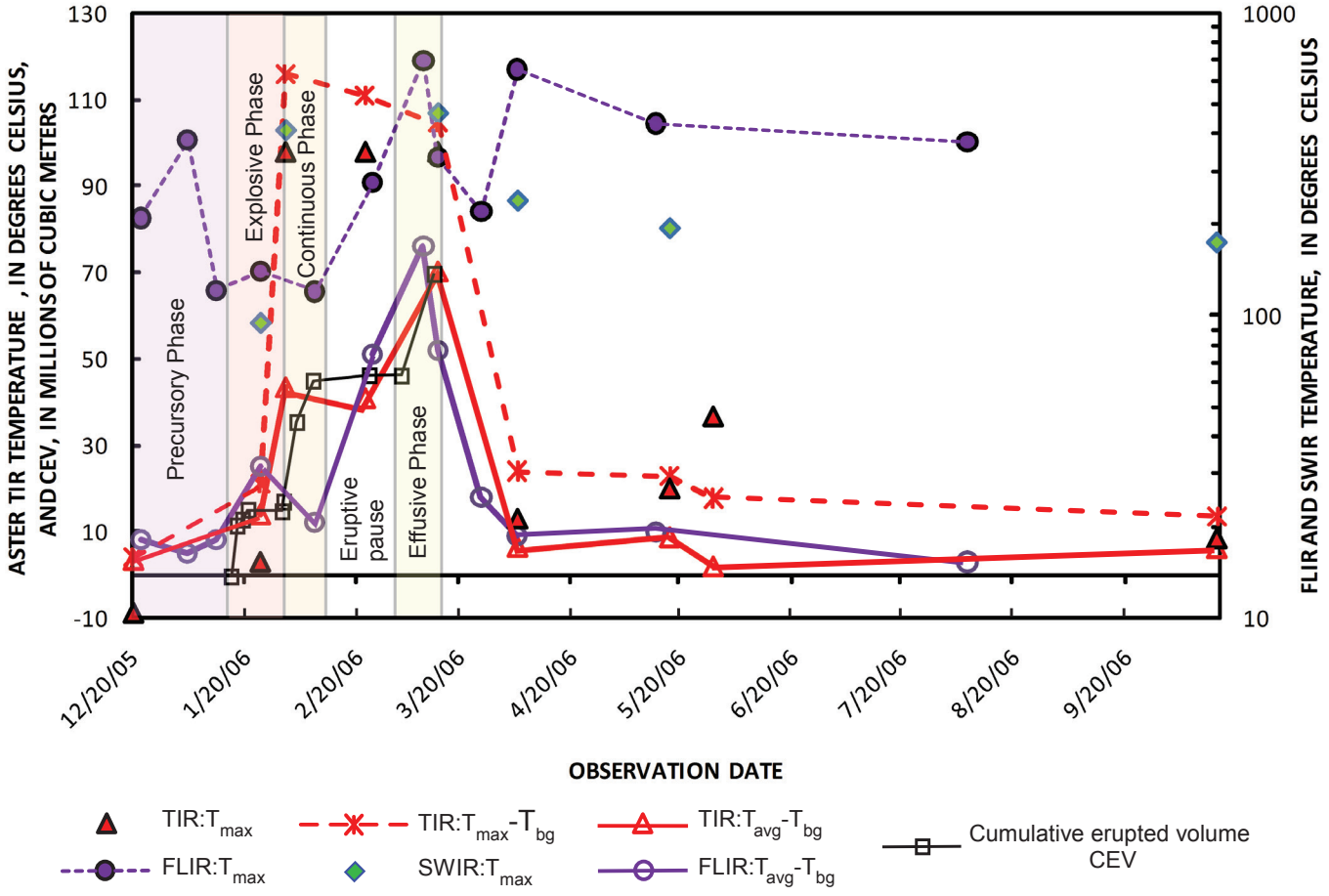

Figure 17. Advanced Spaceborne Thermal Emission and Reflection Radiometer (ASTER)- and Forward Looking Infrared Radiometer (FLIR)-derived temperatures (see tables 1, 2) and cumulative erupted volume (black squares; from Coombs and others, this volume) during each phase of 2006 eruption of Augustine Volcano versus date. Red solid triangles, maximum ASTER thermal infrared (TIR) temperatures at summit; red open triangles, ASTER TIR average lava-flow-surface temperature minus background temperature near summit elevation. Maximum ASTER TIR temperatures >100°C indicate data saturation during continuous and effusive phases. Green diamonds, maximum ASTER shortwave infrared (SWIR) brightness temperatures at summit; Purple dots, maximum temperature in multiple airborne FLIR images. Purple circles show average FLIR lava surface temperature minus FLIR background temperature.

warm areas atop the new dome and tephra collar with the same orientation.

The final FLIR survey of Augustine Volcano was conducted on August 7, 2006 (figs. 16*A–16D*). The summit lava dome surface and tephra collar had temperatures similar to those in the May survey. Corrected for background temperature, the flow surfaces had cooled ~7°C since May to ~3°C above background. FLIR data show that most of the new lava flow surfaces were barely above ambient temperature, although several areas of warm rubble had average surface temperatures of 30°C. Hot fumaroles persisted at the summit and in several parts of the new lava flows. The temperature of the 2006 summit dome fumarole was still ~370°C, and several fumaroles around the perimeter of the new flows had maximum temperatures of 150°C. The pyroclastic-flow deposits and the north and northeast lava flows were not imaged with FLIR during the final survey.

Summary and Conclusions

The combined near-real-time utilization of both airborne and satellite TIR images during the eruption of Augustine Volcano provided valuable insights into the eruption hazards and dynamics. The high-resolution TIR images documented gradual pre-eruption heating of the summit, growing pyroclastic-flow deposits, rapid temperature increases as the lava dome and flows formed, and slow cooling of the volcanic deposits after the eruption (fig. 17). These high-resolution images uniquely documented segmentation of the lava flows into hotter areas of increased flow deformation and cooler, more stable crust on the active flows.

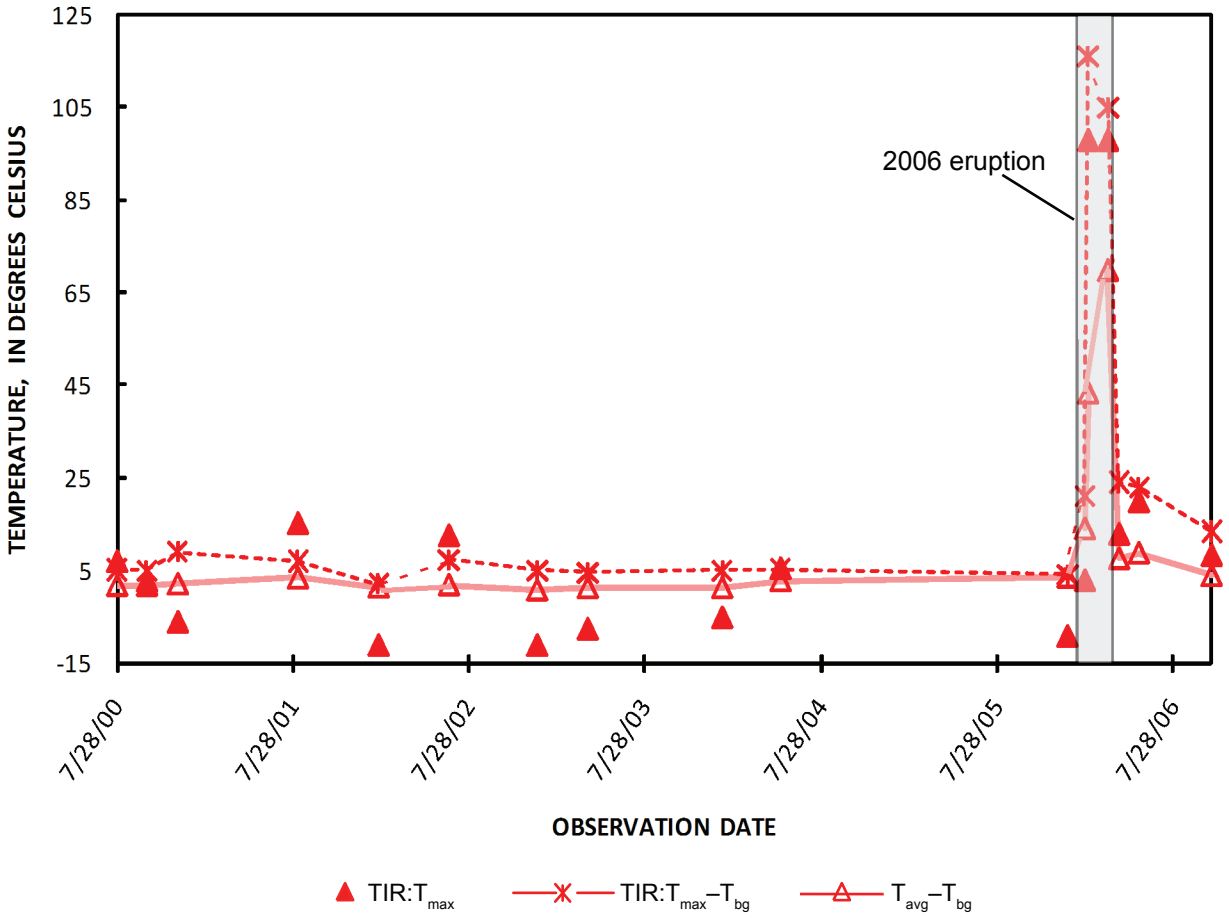

Figure 18. Advanced Spaceborne Thermal Emission and Reflection Radiometer (ASTER)-derived temperatures from July 28, 2000, to October 15, 2006. Red solid triangles, maximum ASTER thermal infrared (TIR) temperature at summit; red open triangles, average ASTER TIR surface temperature at summit minus background temperature near summit elevation; asterisks, maximum ASTER TIR temperature at summit minus background temperature near summit elevation.

The temperatures derived from FLIR and ASTER images are plotted against the cumulative erupted volume and eruptive phases (see Coombs and others, this volume) in figure 17. The widely varying maximum FLIR-derived temperatures (FLIR:T_{max}, fig. 17; table 1) for each overflight were from thermal features ranging from fumaroles at the summit during the precursory phase, through individual hot blocks in fresh pyroclastic-flow deposits during the explosive and continuous phases, to large incandescent fractures and spalling lava flow fronts and the summit vent during the effusive phase, back to fumaroles on the summit and cooling lava flows after the eruption ceased. The highest maximum FLIR-derived temperatures were recorded during the precursory (fumaroles) and effusive (lava) phases. Such results indicate that caution should be taken when using an average maximum temperature in models of effusion rates. Although these models can be highly accurate, they could be extracting temperatures from active lava flows, hot fumaroles, or simply exposed cracks. With lower-resolution satellite, discrimination of these features commonly becomes difficult.

To reduce the scatter and better assess overall temperature trends, the average surface temperatures of warm summit areas and, later, lava surfaces were measured (FLIR:T_{avg}, fig. 17; table 1). To further reduce meteorologic influences on FLIR-derived temperatures, the ambient background temperature near the summit (FLIR:T_{bg}, fig. 17; table 1) was subtracted from the average surface temperature (FLIR:T_{avg}). The resulting plot (FLIR:$T_{avg} - T_{bg}$, fig. 17) shows an increase in surface temperature during the precursory phase through the end of the effusive phase, with one anomalously low temperature likely due to poor observation conditions at the summit (February 8, 2006). The average surface temperature drops rapidly in late March, after the likely end of the effusive phase. Because the much larger ASTER pixels tend to integrate much of the variation in temperature documented by FLIR, maximum ASTER TIR (TIR:T_{max}, fig. 17; table 2) and ASTER SWIR (SWIR:T_{max}, fig. 17; table 2) -derived temperatures more closely follow the trend of FLIR:T_{avg} showing much elevated temperatures during the explosive through effusive phases. Deriving the average surface temperature from ASTER TIR (TIR:T_{avg}, table 2), the background-corrected plot (TIR:T_{avg}–T_{bg}, fig. 17) shows a steep rise in average surface temperature during the explosive and continuous phases, a slight decrease during the eruptive pause, an increase to the highest surface temperature during the effusive phase, and a steep drop in temperature after the eruption. The periods of rapid increase in ASTER-derived temperature appear to correlate with the higher effusion rates suggested by the cumulative erupted volumes estimated by Coombs and others (this volume).

Because Augustine Volcano is relatively close to communities in south-central Alaska, AVO was able to conduct many FLIR flights during the course of the eruption. However, most Alaskan eruptions occur in much more logistically difficult locations, making FLIR observations a rare occurrence outside the Cook Inlet region. high-resolution satellite TIR data from ASTER, in contrast, can be used to monitor any eruption no matter how remote. ASTER is well suited to volcanic observations because of its 15- to 90-m spatial resolution, its ability to be scheduled and point off-nadir, and its ability to collect multispectral data during both the day and the night. Aided by the high latitude of Augustine Volcano, ASTER was able to provide frequent repeat imaging as short as 1 day between scenes, with an average 6-day repeat during the height of eruptive activity in 2006 (fig. 17). A higher temporal resolution at ASTER TIR spatial resolution would be useful to more adequately establish volcano temperature trends, but owing to frequent clouds, volcanic emissions, and infrequent ASTER scheduling, better temporal coverage with high spatial resolution is not currently possible in Alaska for this type of detailed study.

Finally, ASTER also provides a means for reviewing volcano temperature trends since 2000. TES-derived kinetic temperature data extracted from 11 clear nighttime pre-eruption ASTER TIR images provide a timeline for low-temperature thermal activity at Augustine Volcano's summit (fig. 18). For the 6-year-period preceding the 2006 eruption, the background-adjusted ASTER TIR:T_{max} value averaged 5.4°C, with a standard deviation of 1.8°C. Over the same period, the background-adjusted ASTER TIR:T_{avg} averaged 1.9°C, with a standard deviation of 0.9°C. The sole pre-eruption ASTER TIR observation from December 20, 2005, 22 days before the first major explosions, had an ASTER TIR:T_{avg} value of 3.5°C at the summit, only about 1.6°C above the 6-year average but greater than 1σ.

Although ASTER did acquire another 3 daytime and 10 nighttime images during the year preceding the December 20 view, the volcano summit was obscured by clouds in all of them. The absence of cloud-free pre-eruption ASTER data demonstrates why future high-resolution satellite missions need to be designed to provide more frequent and regularly scheduled TIR acquisitions both day and night. The pre-eruption ASTER data, in combination with FLIR observations, suggest that if clear nighttime, high-resolution TIR data had been available days to weeks earlier, the anomalous summit temperatures might have been detected sooner than December 20, as occurred during both the 2005 and 2007 eruptions of Kliuchevskoi Volcano in Kamchatka, Russia (Ramsey and others, 2007; Rose and Ramsey, 2009).

Acknowledgments

We thank Matt Patrick and John Power for their timely reviews and suggestions. This research was supported by the USGS-AVO and NASA (grants NNG04GO69G and NNX-08AJ91G). ASTER data were obtained courtesy of NASA/GSFC/METI/ERSDAC/JAROS and U.S./Japan ASTER Science Team. We thank helicopter pilots Ken Deyoe and Rick Farish for safely and skillfully flying us to the volcano.

References Cited

Bailey, J.E., Dean, K.G., Dehn, J., and Webley, P.W., 2010, Integrated satellite observations of the 2006 eruption of Augustine Volcano, *in* Power, J.A., Coombs, M.L., and Freymueller, J.T., eds., The 2006 eruption of Augustine Volcano, Alaska: U.S. Geological Survey Professional Paper 1769 (this volume).

Ball, M., and Pinkerton, H., 2006, Factors affecting the accuracy of thermal imaging cameras in volcanology: Journal of Geophysical Research, v. 111, no. B11, p. 1–14.

Calvari, S., Spampinato, L., Lodato, L., Harris, A.J.L., Patrick, M.R., Dehn, J., Burton, M.R., and Andronico, D., 2005, Chronology and complex volcanic processes during the 2002–2003 flank eruption at Stromboli volcano (Italy) reconstructed from direct observations and surveys with a handheld thermal camera: Journal of Geophysical Research, v. 110, no. B2, p. 1–23.

Cervelli, P.F., Fournier, T., Freymueller, J.T., and Power, J.A., 2006, Ground deformation associated with the precursory unrest and early phases of the January 2006 eruption of Augustine Volcano, Alaska: Geophysical Research Letters, v. 33, L18304, doi: 10.1029/2006GL027219, 5 p.

Coombs, M.L., Bull, K.F., Vallance, J.W., Schneider, D.J., Thoms, E.E., Wessels, R.L., and McGimsey, R.G., 2010, Timing, distribution, and volume of proximal products of the 2006 eruption of Augustine Volcano, *in* Power, J.A., Coombs, M.L., and Freymueller, J.T., eds., The 2006 eruption of Augustine Volcano, Alaska: U.S. Geological Survey Professional Paper 1769 (this volume).

Dehn, J., Dean, K.G., Engle, K., and Izbekov, P., 2002, Thermal precursors in satellite images of the 1999 eruption of Shishaldin Volcano: Bulletin of Volcanology, v. 64, no. 8, p. 525–534.

Flynn, L.P., Harris, A.J.L., and Wright, R., 2001, Improved identification of volcanic features using Landsat 7 ETM+: Remote Sensing of Environment, v. 78, no. 1–2, p. 180–193.

Gillespie, A. R., Rokugawa, S., Matsunaga, T., Cothern, J. S., Hook, S. J., and Kahle, A. B. 1998, A temperature and emissivity separation algorithm for Advanced Spaceborne Thermal Emission and Reflection Radiometer (ASTER) images: Institute of Electrical and Electronics Engineers Transactions Geoscience Remote Sensing, v. 36, p. 1113–1126.

Harris, A.J.L., Dehn, J., and Calvari, S., 2007, Lava effusion rate definition and measurement; a review: Bulletin of Volcanology, v. 70, n. 1, p. 1–22.

Harris, A.J.L., Dehn, J., Patrick, M., Calvari, S., Ripepe, M., and Lodato, L., 2005, Lava effusion rates from hand-held thermal infrared imagery; an example from the June 2003 effusive activity at Stromboli: Bulletin of Volcanology, v. 68, p. 107–117.

Jacobs, K.M., and McNutt, S.R., 2010, Using seismic *b*-values to interpret seismicity rates and physical processes during the preeruptive earthquake swarm at Augustine Volcano 2005–2006, *in* Power, J.A., Coombs, M.L., and Freymueller, J.T., eds., The 2006 eruption of Augustine Volcano, Alaska: U.S. Geological Survey Professional Paper 1769 (this volume).

McGee, K.A., Doukas, M.P., McGimsey, R.G., Neal, C.A., and Wessels, R.L., 2010, Emission of SO_2, CO_2, and H_2S from Augustine Volcano, 2002–2008, *in* Power, J.A., Coombs, M.L., and Freymueller, J.T., eds., The 2006 eruption of Augustine Volcano, Alaska: U.S. Geological Survey Professional Paper 1769 (this volume).

Power, J.A., Nye, C., Coombs, M.L., Wessels, R.L., Cervelli, P.F., Dehn, J., Wallace, K.L., Freymueller, J.T., and Doukas, M., 2006, The reawakening of Augustine Volcano, Alaska: Eos, (American Geophysical Union Transactions), v. 87, p. 373–377.

Power, J.A., and Lalla, D.J., 2010, Seismic observations of Augustine Volcano, 1970–2007, *in* Power, J.A., Coombs, M.L., and Freymueller, J.T., eds., The 2006 eruption of Augustine Volcano, Alaska: U.S. Geological Survey Professional Paper 1769 (this volume).

Ramsey, M., and Dehn, J., 2004, Spaceborne observations of the 2000 Bezymianny, Kamchatka eruption; the integration of high-resolution ASTER data into near real-time monitoring using AVHRR: Journal of Volcanology and Geothermal Research, v. 135, no. 1–2, p. 127–146.

Ramsey, M.S., Dehn, J., Wessels, R.L., Byrnes, J., Duda, K., Maldonado, L., and Dwyer, J., 2004, The ASTER emergency scheduling system—A new project linking near-real-time satellite monitoring of disasters to the acquisition of high-resolution remote sensing data [abs.]: Eos (American Geophysical Union Transaction), v. 85, n. 47, Fall Meeting Supplement, Abstract SF23A-0026.

Ramsey, M.S., Duda, K., Dehn, J., Wessels, R., Skoog, R., and Rose, S., 2007, Application of the ASTER rapid response protocol for eruption detection and volcano monitoring: ASTER Science Workshop, p. 3–4.

Rose, S.R., and Ramsey, M.S., 2009, The 2005 eruption of Kliuchevskoi volcano; Chronology and processes derived from ASTER spaceborne and field-based data: Journal of Volcanology and Geothermal Research, v. 184, p. 367–380.

Schneider, D, Vallance, J., Wessels, R., Logan, M., and Ramsey, M., 2008, Use of thermal infrared imaging for monitoring renewed dome growth at Mount St. Helens, 2004, *in* Sherrod, D.R., Scott, W.E., and Stauffer, P.H. eds., A volcano rekindled; the renewed eruption of Mount St. Helens, 2004–2006: U.S. Geological Survey Professional Paper 1750, p. 347–359.

Thome, K., Palluconi, F., Takashima, T., and Masuda, K., 1998, Atmospheric correction of ASTER: IEEE Transactions on Geoscience and Remote Sensing, v. 36, no. 4, p. 1199–1211.

Vaughan, R.G., Hook, S.J., Ramsey, M.S., Realmuto, V.J., and Schneider, D.J., 2005, Monitoring eruptive activity at Mount St. Helens with TIR image data: Geophysical Research Letters, v. 32, L19305, doi:10.1029/2005GL024112.

Vaughan, R.G., and Hook, S.J., 2006, Using satellite data to characterize the temporal thermal behavior of an active volcano; Mount St. Helens, WA: Geophysical Research Letters, v. 33, L20303, doi:10.1029/2006GL027957.

Wright, R., and Flynn, L., 2003, On the retrieval of lava-flow surface temperatures from infrared satellite data: Geology, v. 31, p. 893–896.

Wallace, K.L., Neal, C.A., and McGimsey, R.G., 2010, Timing, distribution, and character of tephra fall from the 2005–2006 eruption of Augustine Volcano, *in* Power, J.A., Coombs, M.L., and Freymueller, J.T., eds., The 2006 eruption of Augustine Volcano, Alaska: U.S. Geological Survey Professional Paper 1769 (this volume).

Yamaguchi, Y., Kahle, A.B., Tsu, H., Kawakami, T., and Pniel, M., 1998, Overview of Advanced Spaceborne Thermal Emission and Reflection Radiometer (ASTER): Institute of Electrical and Electronics Engineers Transactions Geoscience Remote Sensing, v. 36, no. 4, p. 1062–1071.

The 2006 Eruption of Augustine Volcano, Alaska
Power, J.A., Coombs, M.L., and Freymueller, J T., editors
U.S. Geological Survey Professional Paper 1769

Chapter 23

The 2006 Eruption of Augustine Volcano—Combined Analyses of Thermal Satellite Data and Reduced Displacement

By Saskia M. van Manen[1], Jonathan Dehn[2], Michael E. West[2], Stephen Blake[1] and David A. Rothery[1]

Abstract

Augustine Volcano erupted explosively after 20 years of quiescence on January 11, 2006, followed by approximately 2 months of dome building and lava extrusion. This is the best monitored eruption in Alaska to date; the diverse complementary datasets gathered enable an interdisciplinary interpretation of volcanic activity. An analysis of reduced displacement (continuous measure of seismic tremor amplitude) and thermal energy output (from satellite imagery) observed between January 1 and April 30, 2006, shows relationships linked to the type of eruptive activity. Three different types of volcanic behavior can be identified as they show specific patterns in the combined data sets: (1) explosive activity, (2) lava extrusion (dome growth), and (3) cooling of erupted products. Explosive activity was characterized by high reduced displacement values but relatively low radiative thermal flux. Lava extrusion occurred in three distinct sequences characterized by increased values of reduced displacement and increased thermal emissions. Two periods of elevated thermal energy output and reduced displacement coincided with times of deflation, suggesting an increase in extrusion rate. Periods of cooling were marked by decreasing thermal emissions and reduced displacement. This work highlights the value of combined observations, which reveal more about the status of an active volcano than individual methods alone.

[1]Volcano Dynamics Group, Department of Earth and Environmental Sciences,The Open University, Walton Hall, Milton Keynes, MK7 6AA U.K.

[2]Alaska Volcano Observatory, Geophysical Institute, University of Alaska Fairbanks, 903 Koyukuk Drive, P.O. Box 757320, Fairbanks, AK 99775-7320.

Introduction

Nearly 20 years after its last eruption, Augustine Volcano (59.361ºN, 153.426ºW; fig. 1) began to erupt on January 11, 2006 (Power and others, 2006). Augustine is an 8 by 11 km volcanic island located in the southern Cook Inlet, approximately 290 km southwest of Anchorage, Alaska. It has erupted 8 times since it was named in 1778 by Captain Cook (Miller and others, 1998). Its summit consists of an andesitic lava dome and lava flow complex, which has repeatedly collapsed resulting in debris avalanches, occasionally triggering tsunamis (Siebert and others, 1995). Currently, the primary hazard from Augustine arises from ash-rich plumes that traverse north Pacific air traffic routes (Miller and Casadevall, 1998). However, hazards also exist for nearby residents in the form of ashfall and tsunamis. An example of this is the 1883 eruption, which caused a tsunami that inundated large sections of Cook Inlet (Siebert and others, 1995; Waythomas and others, 2006).

The 2006 eruption was preceded by seismic unrest that started on April 30, 2005 (Jacobs and McNutt, this volume; Power and Lalla, this volume) and inflation of the edifice that started in July 2005 (Cervelli and others, this volume). Phreatic eruptions were reported throughout December 2005. In the 10 days preceding the first explosive event only three thermal anomalies were found by visual inspection in satellite data. However, more detailed changes in the thermal state of Augustine were observed in the higher resolution thermal camera (Forward Looking Infrared Radiometer, FLIR) data (Wessels and others, this volume). Explosive activity producing ash-rich plumes reaching up to 14 km above sea level (Petersen and others, 2006) started on January 11 and continued intermittently until January 28. Lava extrusion is thought to have commenced around January 13, as indicated by the presence of juvenile glass shards in ash samples (Wallace and

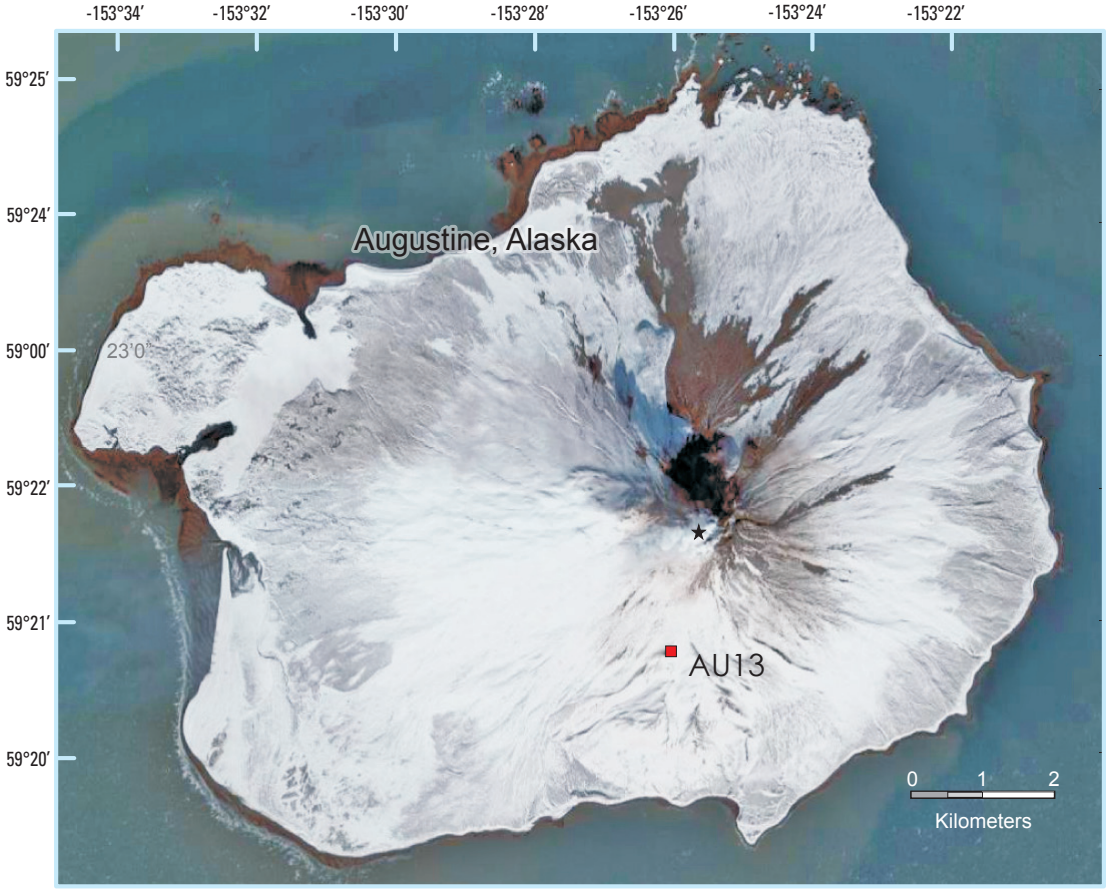

Figure 1. Location figure of Augustine Volcano. This Google Earth™ (DigitalGlobe) image of Augustine Volcano was taken after the 2006 eruption. The snow in the image highlights the location of the newly formed block and ash flows and pyroclastic deposits (all in black) on the north and northeastern slopes. Figure shows location of seismic station AU13, located 1.8 km from the summit of Augustine. This station is the source of the reduced displacement data.

others, this volume). Lava effusion continued until late March, resulting in a lava dome and two short (<1 km) blocky lava flows (Power and others, 2006). The exact date when lava effusion ceased is undocumented by field observations. During the course of the eruption Augustine went through three phases of inflation and two phases of deflation (Cervelli and others, this volume). In addition, numerous rock falls, pyroclastic flows, and block and ash flows were observed, likely related to the growth of the lava dome and flows (Coombs and others, this volume).

Lava dome emplacement is a nonlinear dynamic process accompanied by a wide range of phenomena, including the opening of fissures, increased fumarolic activity, extrusion of lava, earthquakes, dome collapse, explosions, and pyroclastic flows. In addition, phases of quiescence and violence often alternate depending on factors such as extrusion rate, magma rheology and thickness of the cooling top layer (Fink and Griffiths, 1998). Understanding the dynamics involved in the emplacement of lava domes is important because instability can result in collapses accompanied by pyroclastic flows, ash plumes and co-ignimbrite plumes that are capable of reaching air-traffic routes (Woods and Kienle, 1994; Miller and Casadevall, 1998).

This paper presents an interpretation of satellite and reduced displacement data obtained at Augustine Volcano between January 1 and April 30, 2006, spanning the entire eruption and part of the precursory phase, in order to form a more comprehensive understanding of how these signals relate to the observed volcanic activity. Relating thermal signatures to ground activity enhances remote-sensing and seismic monitoring capabilities, particularly in the Alaska-Aleutian-Kamchatka region where satellite data are often the only data source available.

Background

Satellite monitoring provides a means to characterize the thermal states of active volcanoes. Studying satellite-derived data in conjunction with ground-based data and visual observations may help to better understand the nature and significance of the thermal signals. This “ground truthing” permits improved interpretations of the satellite data, making it possible to better gauge volcanic activity at volcanoes monitored solely by remote sensing. Remote sensing of active volcanoes allows near real-time observation of a whole volcano in different parts of the electromagnetic spectrum (Mouginis-Mark and others, 2000). The temporal coverage depends on the satellite used. This study focuses on measurements of thermal flux and total radiated energy, other areas of remote sensing are discussed in other chapters in this volume (Webley and others, this volume; Lee and others, this volume).

This study uses Advanced Very High Resolution Radiometer (AVHRR) data. AVHRR is the primary instrument on the polar orbiting weather satellites operated by the National Oceanographic and Atmospheric Administration (NOAA). Each day, between 10 and 30 AVHRR images with a nadir pixel-size of 1.1 km, in five bands spanning the visible to the infrared, are acquired over the Augustine region. Not all of these images are of suitable quality for study; for example, images with a zenith angle greater than 55° are discarded, as data obtained from them is too geometrically distorted (Harris and others, 1997). The zenith angle is the angle between the local zenith and the line of sight to the satellite. This reduces the number of functional images to approximately half of those obtained. Drawbacks of AVHRR data include its coarse spatial resolution; however, this disadvantage is far outweighed by its high temporal coverage of the Alaska-Aleutian-Kamchatka area because of the polar convergence of the satellite orbits.

Seismology has long been a mainstay of volcano monitoring, as it provides one of the best means of assessing a volcano's state of activity. The central goal of volcano seismology is to understand the subsurface structure of volcanoes and track the movements of fluids, including gas and magma, through this structure. McNutt (2005) notes four main types of seismic signal that are observed at active volcanoes: (1) high-frequency events, also known as volcano-tectonic events (VT), (2) low-frequency events, also termed long-period (LP) events, (3) explosions and (4) volcanic tremor. These events can be divided into two groups based on the origin of their source energies: (1) those where fluid plays an active role in the source mechanism (Aki and others, 1977; Aki and Koyanagi, 1981) and (2) those where magmatic processes provide energy for rock failure (Shaw, 1980; Aki and Koyanagi, 1981; Weaver and others, 1981). The first group involves LP events and volcanic tremor, whereas the second category consists of VT earthquakes. Mixtures of the two types also occur, these are termed hybrid events (Shaw, 1980; Lahr and others, 1994).

Volcanic tremor is a common but poorly understood type of seismic signal that has been documented at more than 160 volcanoes (McNutt, 1994). Difficulty arises from the wide ranging definition of tremor, which covers many different types of behavior. A variety of source models have been proposed, including that it is a sustained sequence of LP events (Latter, 1979; Fehler, 1983; Malone and others, 1983). Others argue for a more continuous source formed by resonance in the conduit, possibly in conjunction with changing physical properties (Neuberg and O'Gorman, 2002; Benoit and others, 2003). Though the exact source of the tremor is debated and likely nonunique, all models associate tremor with the movement of fluids through the volcanic subsurface. Tremor often precedes and accompanies volcanic eruptions, although not all volcanic tremor culminates in eruptions (Julian, 1994).

Reduced displacement (D_r) is a continuous measure of tremor amplitude (Aki and Koyanagi, 1981). Tremor is a sustained phenomenon, because of this it dominates the seismic record when present. Reduced displacement is comparable to the RSAM (Real-time Seismic-Amplitude Measurement) method of Endo and Murray (1991), but it differs in that it adjusts the amplitude for a presumed source. Although this introduces a possible bias to the data, in practice it permits multiple seismic stations to be used together and allows comparisons between different eruptions on a common scale.

McNutt (1994) determined an empirical correlation between tremor amplitude and column height based on the analysis of 21 eruptions at 14 volcanoes. During the 1996 Pavlof (Alaska) eruption, a general relationship between plume height and tremor amplitude was observed by Roach and others (2001). In addition, the size of the observed thermal anomaly steadily increased before the eruption of the largest plumes, which reached an altitude of 10 km above sea level (Roach and others, 2001). However, Nye and others (2002) found that during the 1999 Shishaldin (Alaska) eruption there was a remarkable lack of correlation between reduced displacement and plume height. They also found that thermal anomalies often preceded volcanic tremor associated with strombolian outbursts. Galindo and Dominguez (2002) found good correlations between thermal and seismic data at Colima (Mexico) during 1997–2000. Using AVHRR and seismic data during precursory, effusive, and explosive stages of the eruption they recorded five seismic swarms, four of which coincided with periods of increased summit temperature and strong ash emissions. It is noteworthy that ash emissions were observed prior to the seismic swarms.

Data Acquisition

Thermal Imagery

Between January 1 and April 30, 2006, thermal anomalies centered over Augustine were identified in band 3 (3.55–3.93 μm) in 323 AVHRR images by the automated Okmok II algorithm. Thermally anomalous pixels are those that rise 5°C or more above the mean temperature of the surrounding eight pixels (AVO Remote Sensing Team, 2000). Okmok II improves upon its predecessor, Okmok (Dean and others, 1998; Dehn and others, 2000), by using a wider range of criteria to determine whether a pixel is a volcanic thermal anomaly or noise. The AVHRR images provide a snapshot of the thermal state of the volcano at that moment in time (fig. 2). The Okmok II algorithm automatically discards cloudy, daytime, and noisy images and then ascertains the apparent temperature of the hottest anomalous pixel in each image, as well as the accompanying background temperature. For the purposes of this paper it is assumed that the hottest pixel includes the summit of Augustine.

Thermally anomalous pixels were also manually identified in 526 images between January 1 and April 30, 2006, by the Alaska Volcano Observatory (AVO) as part of the twice-daily remote-sensing monitoring routine (Bailey and others, this volume). The number is much higher than determined by

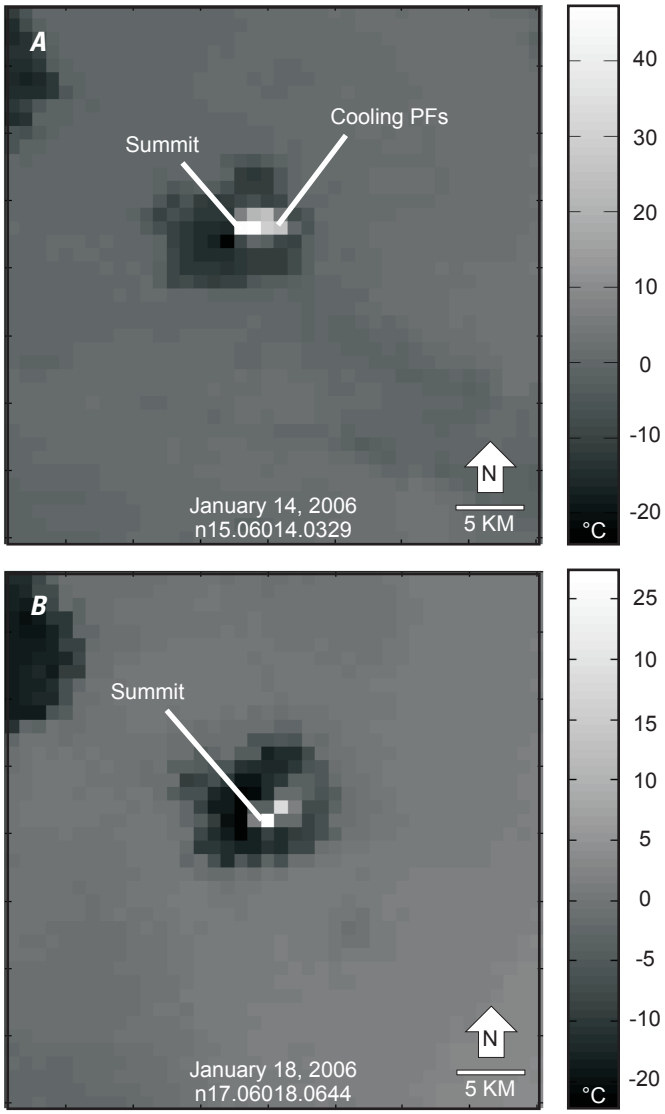

Figure 2. Selected band 3 (thermal infrared; 3.55-3.93 µm) AVHRR data over Augustine Volcano in January 2006 showing thermal anomalies at the summit of Augustine, as well as cooling pyroclastic flows. Both images are north oriented to the top, scalebar is in degrees Celsius (°C), the image identification numbers are noted on the bottom. *A*, January 14 at 03.29 UTC, zenith angle is 27°. *B*, January 18 at 0644 UTC, zenith angle is 42°.

the Okmok algorithm due to the fact that the Okmok algorithm excludes daytime, cloudy, or noisy images that an analyst can still use. For each of the images the number of hot pixels was recorded. This provides an indication of the activity that has occurred, taking into account the whole volcano. Small numbers of pixels with elevated temperatures generally suggest summit activity, whereas larger numbers can indicate cooling lava flows or pyroclastic deposits. However, increases in the number of hot pixels observed are only significant if they are large; with increasing zenith angle, pixels start to overlap, increasing the chance of a hotspot stretching across multiple pixels. In addition, even at lower zenith angles a hotspot can occasionally be on the border of two pixels, thus being reported in two or more pixels instead of one.

Radiative Thermal Flux and Total Radiated energy

The radiant temperature detected by AVHRR is a function of the sensor's field of view (FOV). It is integrated over the entire area of the pixel and can not directly reflect the temperature of the hottest volcanic material except in the highly unlikely event that such material homogenously occupies the whole pixel. This means that estimation of the volcanic temperature requires the simultaneous determination of the proportions of ground surface at various temperatures (Harris and others, 1997; Francis and Rothery, 2000). The radiance received will be affected by atmospheric attenuation and instrumental effects as well as by surface spectral emissivity. To calculate the thermal output from the summit at Augustine, the two-component method (Dozier, 1981; Rothery and others, 1988; Harris and others, 1997; Harris and others, 1998) was used in conjunction with the dataset gathered by the Okmok II algorithm. The manual data was only used to examine the number of hot pixels during the time period investigated. This was done as the Okmok II algorithm maintains constant criteria to determine whether or not a pixel is thermally elevated. This method assumes that a pixel with an elevated temperature (T_{int}) is composed of two parts; a subpixel hotspot at temperature (T_h), occupying a fractional area (p_h), while the remainder is at background temperature (T_{bg}) occupying ($1–p_h$). This assumption allows the temperature and the area covered by each component to be estimated using:

$$L(\lambda, T_{\text{int}}) = p_h L(\lambda, T_h) + (1–p_h)\, L\,(\lambda, T_{bg}) \quad (1)$$

Where L is the Planck function for a blackbody at wavelength λ. This results in three unknowns: the fractional area, the temperature of the hot component, and the temperature of the background. Background temperature can be estimated using the temperatures of surrounding nonanomalous pixels, allowing the remaining two parameters to be calculated if one of them can be assumed or constrained. This work uses an integrated pixel temperature (T_{int}) determined from band 3 (3.55–3.93 µm) and a background temperature determined from band 4 (10.3–11.3 µm). This is done because the peak emittance of the background is closer to the central wavelength of band 4. The two component method is a simplification because a volcano consists of more than one hot and one cold component; however, it provides an accurate first order approximation of the radiative thermal flux. In order for it to work, the ratio of the hot to cold pixel fraction needs to be correct. The fractional area occupied by the hot component was estimated by determining the dome radius; visual observations

indicate this was 110 m, this means approximately 3 percent of each pixel is considered to be at high temperature. Although the size and the shape of the dome changed throughout the course of the eruption, this size estimate provided a plausible ratio of the hot to cold pixel fraction because it is consistent with the satellite derived extrusion rates, which correspond to those observed in the field (Coombs and others, this volume). Having estimated the fractional area of the hot component allowed the temperature of the hot component (T_h) to be calculated. Consequently above-background summit radiative thermal flux (q_r) can be calculated using:

$$q_r = \varepsilon\sigma\tau p_h (T_h^4 - T_{bg}^4) , \quad (2)$$

where τ is the atmospheric transmissivity, σ is the Stefan-Boltzmann constant, and ε is the emissivity of the lava. Atmospheric transmissivity is difficult to account for as it is affected by the total transmissivity of the atmosphere as well as the concentration of volcanic gases above the vent (Dehn and others, 2002). However, due to the fact that the subarctic air is relatively dry, the effect of transmissivity only has a small effect on the absolute temperature values. Emissivity in the relevant wavelengths is assumed to be 0.9, an accepted value for andesitic lavas (Salisbury and D'Aria, 1992). The radiant thermal flux represents the average thermal flux integrated over the entire pixel. No correction for the pixel size is made, as the precise geometry of the edifice changes and the viewing geometry of the satellite is hard to constrain.

Using radiative thermal flux to monitor activity will result in underestimates of total energy flux at a volcano because other sources of heat loss such as convection, conduction, evaporation of rainfall, and hydrothermal circulation are ignored (Francis and Rothery, 2000). Radiative thermal flux is just one component of the total heat loss, however since it is the largest is provides a good proxy for the thermal state, and thus activity level, of a volcano. The total radiated energy was calculated by using the trapezoidal method of integration.

Seismic Tremor Data

Reduced displacement (D_r) is a low sample rate measure of seismic amplitude. It is widely used to normalize volcanic tremor recorded at varying distances from a volcano to a common scale and to allow comparisons between eruptions. It is a simple measure equal to the sustained root mean square (rms) ground displacement corrected for geometric spreading (Aki and Koyanagi, 1981). Site amplification can influence the results, but the order of magnitude scaling typically used with reduced displacement minimizes the influence of a constant scale factor.

For this study we use D_r calculated from channel HHZ (the vertical component) of station AU13 (59.3464ºN, 153.4341ºW). AU13 was chosen because it had a high signal-to-noise ratio, had few data gaps, remained on scale through the eruption, and was generally representative of D_r from other stations at Augustine. The sensor was a Guralp CMG-6TD (30 s) installed shortly before the eruption. This station was located 1.8 km from the summit (fig. 1). Because the station is within a few wavelengths of the source region beneath the summit, we use the body wave formulation of reduced displacement first presented by Aki and Koyanagi (1981). The original expression, formulated for paper records, is:

$$D_r = \frac{A}{2\sqrt{2}} \cdot \frac{r}{M} \quad (3)$$

where A is the peak-to-peak amplitude of the raw seismogram and the factor of estimates its root-mean-square value from the peak-to-peak measure. The source-to-receiver distance r, is the salient part of the expression which "reduces" the displacement to a common value. The magnification value, M, scales the seismogram from arbitrary units to true ground displacement. Although A is measured from raw seismic data, M, is frequency dependent. In this formulation M should be chosen at a frequency which best matches the tremor, thus introducing a frequency dependence to the reduced displacement expression.

The approach used in this study is true to the original definition of reduced displacement but benefits from digital processing techniques. In lieu of applying a frequency-dependent magnification factor, we use seismic data that have been corrected for instrument response and integrated from velocity to displacement. We calculate the root mean square of this signal directly. Although this is a more brute force approach, it can be written simply as:

$$D_r = RMS\,(X) \cdot r \quad (4)$$

where X is the instrument-corrected displacement record. In practice this is comparable to using the original formulation of Aki and Koyanagi (1981) without the frequency assumption introduced by the magnification factor. Here we calculate D_r on 30-minute windows of data, band-pass filtered for a frequency range of 0.5 to 8 Hz. The filter preserves the dominant frequencies of tremor, volcanic earthquakes, and rock falls while minimizing both the low-frequency microseism band and high-frequency wind noise. The wide frequency window is consistent with the use of reduced displacement in many monitoring environments.

It should be noted that this formulation for reduced displacement varies from a modified version used operationally by AVO (see McNutt and others, this volume). The operational version measures seismic amplitude in a narrow band around the dominant frequency of the signal. To make use of more distant stations, this approach also uses a geometric spreading term consistent with surface waves (Fehler, 1983). Because of the broader band approach, body wave decay term, and the use of stations close to the summit, values presented here are generally higher than those of McNutt and others (this volume). The discrepancy is inherent in the different approximations

required to reduce complex seismic records to a simple metric, such as reduced displacement. However it is precisely such simplifications that allow quantitative comparisons between different eruptive episodes.

Analyses and Results

Thermal emissions and reduced displacement data plots were made using data spanning the entire eruption. The coeruptive data were examined in detail and additional analyses were performed on selected subsets.

Thermal Imagery

Summit Radiative Thermal Flux and Total Radiated Energy

The data show three broad peaks during which the summit radiative thermal flux rose above the average eruption background value of less than 10^8 W (figs. 3*A*, 4*A*). An additional minor spike is visible near the end of April. On the basis of the thermal imagery, the total energy output from the summit region of Augustine between January 1 and April 30, 2006, is 2.15×10^{16} J. The thermal flux increases appear to occur predominantly in three sequences as indicated by three time periods showing a distinct increase in slope on the cumulative energy output plot (fig. *5A*).

Although thermal anomalies (figs. *3A, 4A*) are observed prior to the start of the explosive activity on January 11, thermal flux then was lower, not exceeding $1x10^8$ W. The first main spike in thermal flux is not until January 13 at 13.27 h UTC, almost 48 hours after the initial explosions, when the summit thermal flux reaches 1.1×10^{10} W. This spike is then followed by two smaller but slightly broader spikes on January 14 and 17. On January 18 another large narrow spike of 8.2×10^9 W can be observed.

After January 20, radiative thermal flux again falls below $1x10^8$ W, until January 26 after which it quickly starts to rise. A small spike of 7.2×10^9 W can be seen on January 28, coincident with the four explosions that occurred during this phase. A spike of 1.6×10^{10} W is observed on February 3, after this the thermal flux tapers off quickly until February 13. Minor spikes of 1.3×10^{10} W and 6.8×10^9 W are seen on February 8 and 13.

Summit thermal flux starts to increase again on February 20, this time ramping up more slowly to a maximum of 1.7×10^{10} W on March 8. Numerous minor spikes are visible, including ones on February 26, March 1, and March 11, which reach 8.2×10^9 W, 1.5×10^{10} W, and 1.3×10^{10} W, respectively.

A small spike of 2.4×10^9 W, with some minor ramping up to this peak, can be seen on March 23. Another anomalous single spike with some minor increases beforehand can be observed in the radiative thermal flux towards the end of April, spiking on April 19 at 4.0×10^9 W.

Number of Hot Pixels

The number of hot pixels (N_{HP}) observed (fig. 3*B*) shows three sequences during which their number increases from a background value of approximately 2 during the eruption to more than 10. The timing of these sequences coincides with the spikes observed in the thermal data. There is also a remarkable correlation between N_{HP} and the reduced displacement values: the number of days that both are elevated is almost equal, whereas the radiative thermal flux increases have longer durations (broader peaks).

The number of hot pixels observed starts to increase on January 13, reaching an initial peak of 18 on January 14. N_{HP} then decreases again only to peak on January 19 at 10. The number of hot pixels does not exceed 2 between January 20 and January 28. After this a sharp increase can be observed, with the series maximum of 37 pixels observed on January 28 at 0615 h UTC. From January 29 onwards N_{HP} remains high, varying between 6 and 30 until February 7. Throughout the rest of February values remain between 1 and 9 pixels per image. March 1 sees an increase to 15 pixels; however, this value then drops to 2 pixels per image until March 5. After this N_{HP} observed increases again, although less sharply than during the previous phase of increases, only to peak at 35 on March 8. A slow decrease after this continues until March 30, after which values do not exceed 6, but most images only show 2 anomalous pixels.

Reduced Displacement

In general the reduced displacement (fig. *3C*) shows a trend similar to those for thermal emissions data and the number of hot pixels observed; there are three distinct intervals when reduced displacement rises above the average eruption background level of 10 cm^2.

Reduced displacement shows a number of minor peaks above background level before the explosions on January 11. On January 11 the peak value reached 417 cm^2. Levels then dropped back to background levels until January 13 when the highest reduced displacement value recorded at station AU13 during the eruption, 1,680 cm^2, was observed. Additional spikes are seen on January 14, but they do not exceed 500 cm^2. Another major spike is seen on January 17, this peaks at 1,034 cm^2. Each of these high reduced displacement values coincides with one of the 9 recorded explosions during this time. Cumulative reduced displacement values (fig. 5*A*) show very sharp step-like increases in the values associated with the spikes observed in the 30 minute data.

After January 17 reduced displacement does not rise above 100 cm^2 until January 28. The cumulative values reflect this as a very shallow sloping increase. Four more explosions occurred on January 28; however, reduced displacement peaks at only 395 cm^2. Reduced displacement values remain high even after the explosions cease, peaking on January 30 and 31 and February 5 at 381 cm^2, 597 cm^2, and 536 cm^2,

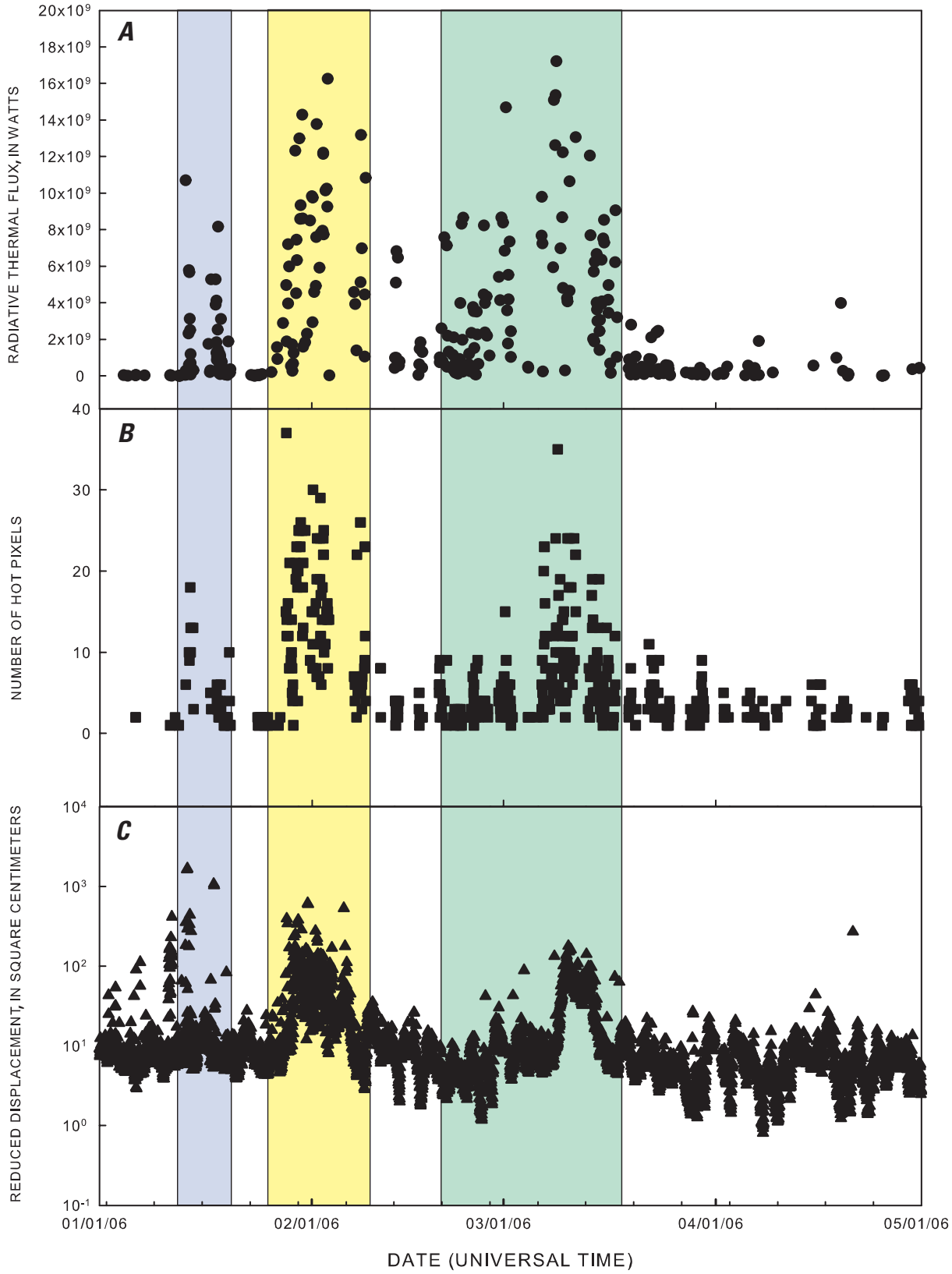

Figure 3. Summary of satellite thermal data collected from Augustine between January 1, 2006, and April 30, 2006. *A*, Summit thermal emissions; *B*, number of hot pixels per satellite image; and *C*, reduced displacement. All three data sets show three contemporaneous peaks. Please note the logarithmic scale on the y-axis of plot *C*. The colored bands indicate the three sequences of increased summit radiative thermal flux.

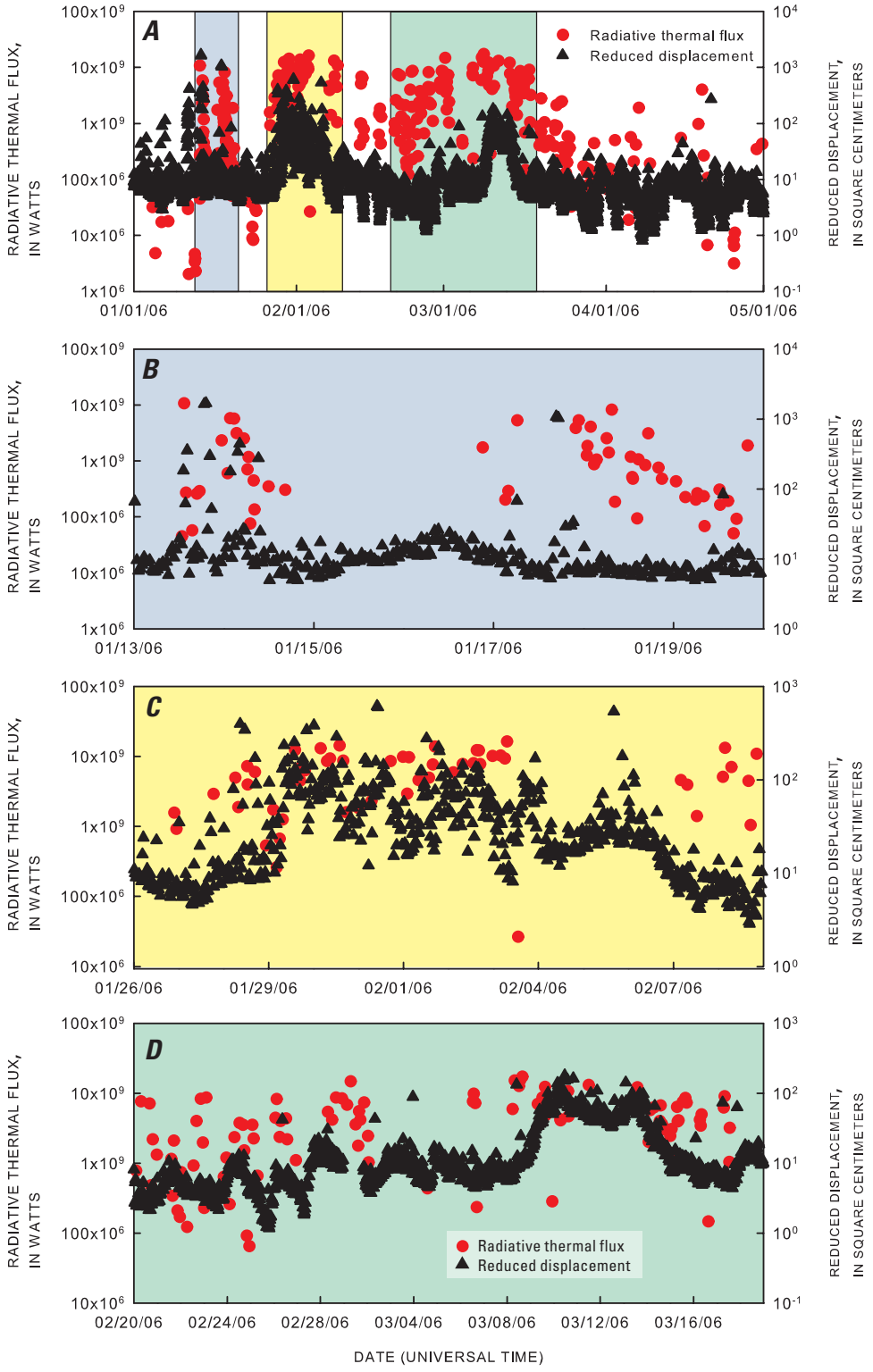

Figure 4. Summit thermal emissions (red) and reduced displacement (black) from Augustine Volcano as observed between January 1, 2006, and April 30, 2006. *A*, January 1, 2006, and April 30, 2006. The graph shows three areas where increases in thermal emissions and reduced displacement coincide. The colored bands indicate the three sequences of increased summit radiative thermal flux. *B*, First sequence of increased thermal emissions. *C*, Second sequence of increased thermal emissions. *D*, Third sequence of increased thermal emissions.

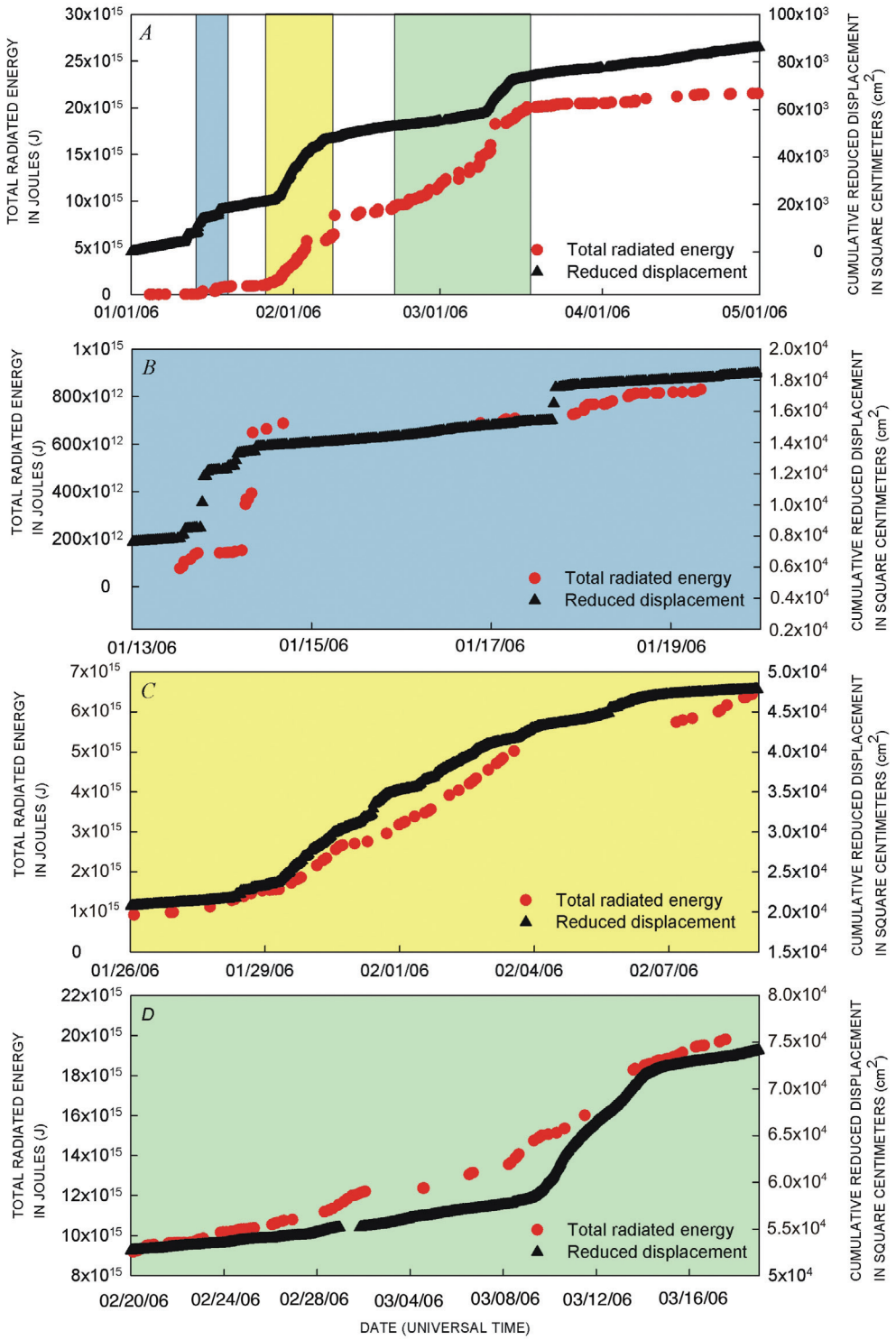

Figure 5. Total thermal energy output (red) and cumulative reduced displacement values (black) at Augustine Volcano between January 1, 2006, and April 30, 2006. *A*, January 1, 2006, until April 30, 2006. The graph shows the three phases as indicated by the colored bands. Note the differences in shape of the graph between phase 1 and 2 and phase 3. *B*, First sequence of increased thermal emissions; increases in thermal energy output postdate increases in reduced displacement. *C*, Second sequence of increased thermal emissions; increases in thermal energy output and reduced displacement occur almost contemporaneously. *D*, Third sequence of increased thermal emissions; increases in thermal energy output precede increases in reduced displacement.

respectively. This is reflected in the cumulative values in a steady increase in the slope.

Between February 7 and March 3 reduced displacement barely rose above background values, even at a maximum not exceeding 50 cm^2. Two minor peaks are visible on February 26 and March 2, but these do not rise to more than 42 cm^2. These background values are represented in the cumulative plot as a shallowly sloping line. Another single peak in the reduced displacement values is observed on March 8, reaching 133 cm^2. After this peak values drop to background levels only to slowly ramp up to a maximum of 179 cm^2 on March 10. Activity remains high, continuously exceeding 40 cm^2 with a minor peak on March 13 of 141 cm^2. The increase visible in the 30-minute reduced displacement values between March 8 and March 14 and is attributed to a continuous seismic tremor. After March 14 activity returns to background levels, manifested in the cumulative plot as a shallowly sloping line.

Combined Analysis of Thermal and Seismic Tremor Data

Two main types of behaviour are observed: (1) radiative thermal flux and reduced displacement have corresponding peaks, or (2) radiative thermal flux and reduced displacement do not have corresponding peaks (fig. 4). In general, peaks in the reduced displacement data and number of hotspots observed are much narrower in time than those of the radiative thermal flux.

The first explosions that occurred on January 11, 2006, did not produce a corresponding thermal signal (fig. 4*A*). The first time span that shows coincident increases in radiative thermal flux and reduced displacement is between January 13 and January 19. During this first peak in thermal output, high reduced displacement values coincide with the 9 recorded explosions (Petersen and others, 2006). The cumulative plot (figs. 5*A*, *B*) clearly shows that the total radiated energy did not increase until after the reduced displacement values had started to increase.

The second period when radiative thermal flux and reduced displacement display corresponding increases is between January 26 and February 6. In this case, the summit thermal flux started to increase coincident with the increase in reduced displacement (fig. 4*C*) and remained high after the reduced displacement has died down. High reduced displacement values do not correspond solely to explosions during this time, suggesting a contribution from other sources such as rockfalls.

During the third peak in summit radiative thermal flux, the rise of total radiated energy preceded increases in reduced displacement (figs. 4*D*, 5*D*). There is a very large jump in the total thermal energy output that coincides with the start of the increase in reduced displacement. Additional corresponding increases in thermal emissions and reduced displacement occur between March 8 and March 14. Reduced displacement increased at this time due to continuous seismic tremor. There are no directly corresponding peaks between the radiative thermal flux and the reduced displacement.

Interpretation

On the basis of the data there appear to be three sequences of increased summit radiative thermal flux—January 13–19 (figs. 4B, *5B*), January 26–February 8 (figs. 4*C*, 5*C*), and February 20–March 18 (figs. 4*D*, 5*D*). All three sequences are also characterized by increased numbers of hot pixels and increased reduced displacement; therefore, each of these three sequences has been interpreted as a period of lava extrusion (table 1). The first two sequences incorporate explosive activity whereas the last sequence is purely effusive. Figure 6 illustrates the changes occurring at the summit during these three sequences. There does not appear to be a correlation between the type of magma erupted (low and high silica andesite) as described in Coombs and others (this volume) and the seismic or thermal activity described here.

Sequence 1 (January 13–19)

The first sequence, which occurred during the explosive phase as identified by Coombs and others (this volume) and Power and Lalla (this volume), was characterized by high average reduced displacement values and low average thermal energy output compared to the other two sequences. However,

Table 1. Characteristics of each of the three sequences of increased thermal emissions.

Sequence	Dates	Duration (days)	Total radiated energy (x 10^{15} J)	Average radiated energy per day (x 10^{14} J)	Number of explosive events	Total reduced displacement (x 10^4 cm^2)	Average reduced displacement/day (x 10^3 cm^2)
1	01/13/06-01/19/06	7	0.82	1.3	7	1.09	1.57
2	01/26/06-02/08/06	14	5.53	4.01	4	2.71	1.98
3	02/20/06-03/18/06	27	10.60	4.18	0	2.14	0.75

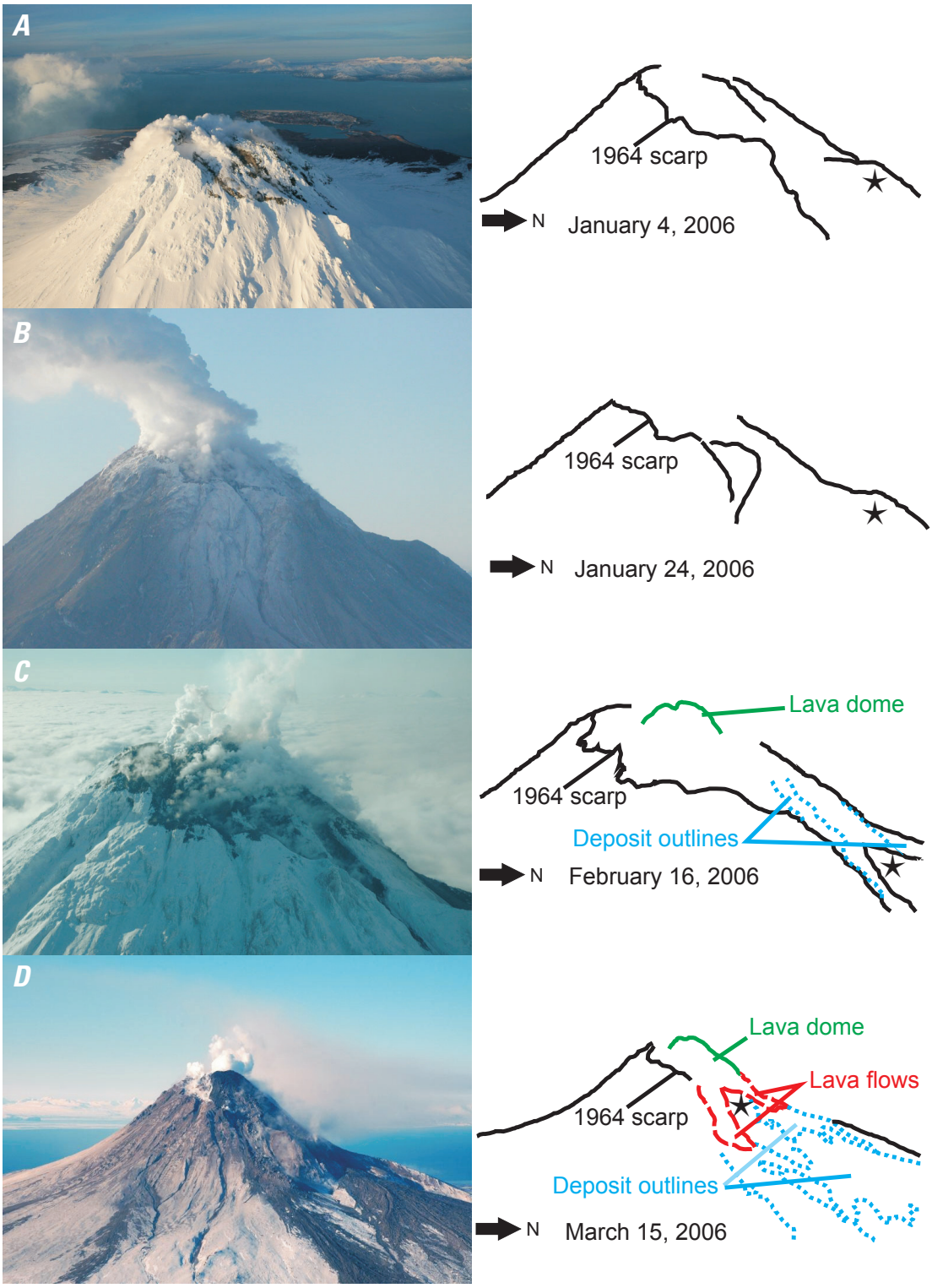

Figure 6. Pictorial time series of changes at the dome throughout the 2006 eruption of Augustine Volcano. The star in each image indicates the location of a feature known as "the Cleaver" for comparison purposes. *A*, The dome prior to magma extrusion, January 4, 2006 (AVO image by M. Coombs). *B*, January 24, 2006 (AVO image by J. Schaefer). *C*, The dome on February 16 after the second sequence of increased radiative thermal flux. (AVO image by R.G. McGimsey). *D*, The dome on March 15 2006, towards the end of the last phase of dome growth (AVO image by T. Plucinski).

the average thermal energy output still significantly exceeded background values. During this sequence a significant amount of mechanical energy was expended without bringing much hot material to the surface. In addition, the fact that increases in reduced displacement preceded increases in thermal energy output further suggests that this sequence was mainly conduit-clearing explosive activity accompanied by intermittent extrusion of lava and numerous pyroclastic flows. The number of hot pixels observed during this sequence did increase, suggesting both extrusion at the summit and the occurrence of pyroclastic flows. During this first sequence the volcano was still inflating, suggesting that the rate of magma accumulation at depth was greater than eruption rates. This interpretation is consistent with visual information obtained on overflights of the volcano; Coombs and others (this volume) reported a small new lava dome on January 16 (fig. 7) and fresh glass shards in ash samples on January 14. However, this small new dome was destroyed on January 17 by an explosion, so there was little change to the summit area compared to before the start of the sequence (figs. 6*A*, *B*). Coombs and others (this volume) list the explosive phase as the most voluminous at $30x10^6$ m^3 dense rock equivalent; however, the majority of this was extruded towards the end during January 27–28, which in this study falls into sequence 2. A lot of the material extruded during sequence 1 was in the form of tephra, which being cold is not accounted for in this paper. Large amounts of tephra in the form of ash in a plume could attenuate the thermal signal, although we think that this is not the case here as even during the almost continuous ash emissions observed during the start of sequence 2 (Coombs and others, this volume) saturation of the sensors occurred.

Sequence 2 (January 26–February 8)

The second sequence was contemporaneous with the redefined continuous phase of the eruption (Coombs and others, this volume). High thermal energy output in combination with high reduced displacement values (table 1) during this sequence lead to the interpretation that this was a significant period of lava extrusion and dome growth. The absence of explosive activity after January 28 indicates that an open conduit to the surface had been established. The fact that reduced displacement values remained high after the explosive activity ceased on January 28 suggests that at this time there was also major migration of gas, fluid, and magma occurring within the edifice. This is confirmed by the thermal radiative flux which indicates significant dome growth and high extrusion rates. It is important to note that the high radiative flux is due to a combination of heat from the dome and from pyroclastic deposits, which are an indirect indicator of dome growth. This would suggest that there was significant movement of magma, as was also reflected in the reduced displacement values. The rapid dome growth would have resulted in oversteepening of the dome, resulting in rockfalls. These rockfalls also form a contribution to the reduced displacement signal. Figures 6*B* and *C* illustrate the visual changes that occurred at the summit during this sequence; the new dome is clearly visible, as

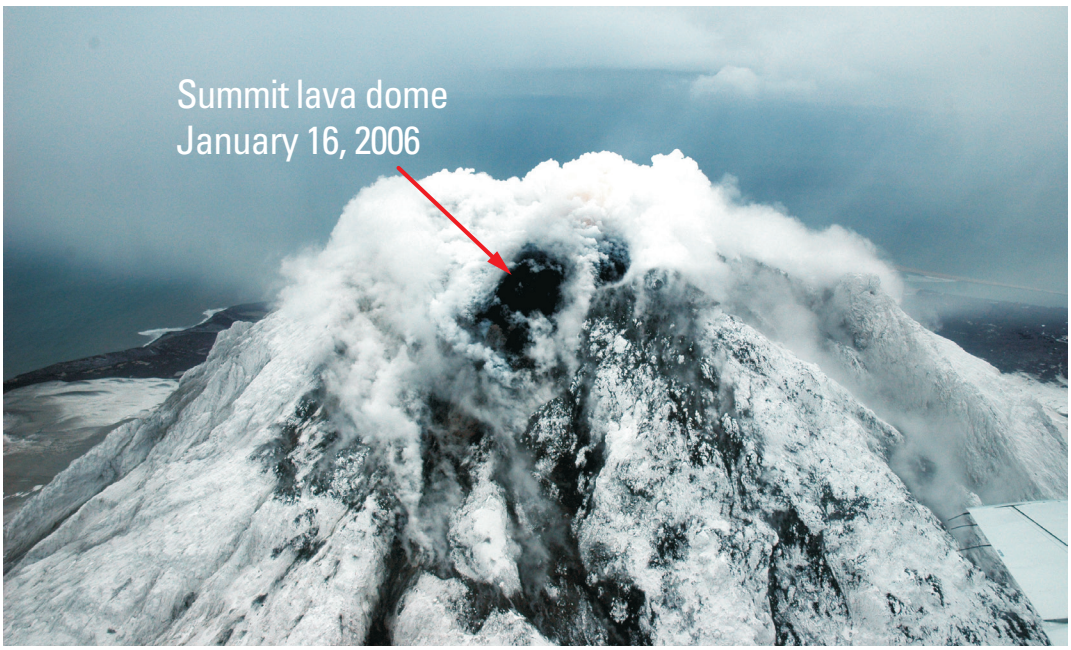

Figure 7. Augustine Volcano summit lava dome on January 16, 2006. Arrow points at the dome (AVO image by R.G. McGimsey).

are deposits from pyroclastic and block and ash flows. The emplacement of these deposits is reflected in the significant increase of the number of hot pixels recorded during this sequence. This sequence coincided with a period of deflation (Cervelli and others, this volume), also implying significant growth of the lava dome. It is likely that fresh magma was being erupted at this time, after the explosive behavior of both the first sequence and the January 28 explosions had cleared the vent.

Sequence 3 (February 20–March 18)

The third sequence, which occurred during the so-called hiatus and effusive phase (Coombs and others, this volume), was characterized by (1) high thermal energy output and (2) reduced displacement that was elevated but lower than during earlier eruptive phases (table 1). During the first part of this sequence little seismic energy was generated, suggesting that an open conduit to the surface had been established. The high radiative thermal flux values indicate there was significant extrusion of magma, not just to the dome but also to the two lava flows that formed to the north during this time. The peak thermal emissions during this sequence coincide with a period of deflation, which suggests that extrusion rates were greater than magma supply rates. This significant episode of dome growth would again have resulted in oversteepening of the dome and rockfalls, which are reflected in the reduced displacement signal. The radiative thermal flux peaks at the start of continuous tremor that occurred from March 8 until March 14. This suggests that towards the end of the eruption there was significant migration of gas, fluids, and magma, even though radiative thermal flux declines during this time. The movement of magma is reflected in the GPS data which indicate that at this time the edifice starts to inflate again (Cervelli and others, this volume). Visual observations (figs. 6*C*, *D*) show that during this sequence two short blocky lava flows were extruded and there were additional pyroclastic and block and ash flows. These lava flows and pyroclastic deposits are reflected in the number of hot pixels observed, which increased significantly during this time. Traditionally the end of lava effusion is estimated based on the time of the last image with saturated pixels in band 3; saturation generally occurs due to lava incandescence (Harris and others, 1997). Although this is a valid assumption for basaltic activity, dome growth can occur endogenously, thus not saturating the thermal signal. The last image with saturated pixels at Augustine was recorded on March 15; however, an image close to saturation was observed on March 17. Data were unavailable on March 18, whereas the temperatures observed on March 19 were significantly cooler. This suggested that extrusion of lava ceased between March 15 and 18; after this the thermal flux slowly decreased, indicating cooling of the extruded material. This is consistent with FLIR observations made on March 15 and March 26 (Wessels and others, this volume).

Implications for Future Monitoring

Although remote sensing data are important in the operational monitoring of active and potentially active volcanoes, there is a limit to the amount of information they can provide. To gain the most information regarding a volcanic system, thermal signatures need to be related to other observable activity. This will increase understanding of the processes occurring on the ground. This is particularly important for remote volcanoes that are monitored solely by remote techniques.

Analysis of the 2006 Augustine data has shown that summit thermal emissions and reduced displacement exhibit patterns that can be tied to specific types of volcanic behavior. It was found that high thermal energy output with corresponding high reduced displacement values indicate extrusion of magma whereas low thermal energy output values with correspondingly high reduced displacement values are associated with explosive behavior. The fact that most of the extrusion seemed to generate relatively little mechanical seismic energy suggests that after the explosive activity subsided an open conduit was established.

No reliable exploitable predictive trend that can be extrapolated to other dome building volcanoes has been found in the 2006 eruption Augustine radiative thermal flux. This is probably due to stochastic variations, as well as other factors such as the temporal coverage of the satellite data and local weather conditions.

This study highlights the importance of multiparametric synergistic studies. The joint analysis of both data sets is consistent with three sequences of lava dome extrusion. Interpretations of thermal emissions and correlations with other datasets can be optimized by monitoring thermal emissions at increased spatio-temporal resolution. Although AVHRR can be used to constrain the magnitude of the activity occurring at a volcano, it can not provide detailed data regarding the eruptive state of a volcano unless supplementary datasets (particularly continuous seismic data) are available. However, the temporal coverage in the Alaska-Aleutian-Kamchatka region makes AVHRR an invaluable tool for monitoring the gross behavior of hazardous volcanoes.

Acknowledgments

The authors would like to acknowledge the Alaska Volcano Observatory—a cooperative program between the U.S. Geological Survey Volcano Hazards Program, the Geophysical Institute at the University of Alaska Fairbanks, and the Alaska Division of Geological and Geophysical Surveys. A grant from the Geological Society of London funded Saskia M. van Manen's visit to AVO while the paper was being completed. In addition we would like to thank R. Wessels and M. Patrick for their helpful reviews.

References Cited

Aki, K., Christofferson, C., and Husebye, E.S., 1977, Determination of the three-dimensional seismic structure of the lithosphere: Journal of Geophysical Research, v. 82, p. 277–296.

Aki, K., and Koyanagi, R., 1981, Deep volcanic tremor and magma ascent mechanism under Kilauea, Hawaii: Journal of Geophysical Research, v. 86, no. NB8, p. 7095–7109.

AVO Remote Sensing Team, 2000, Manual for Satellite Monitoring of Volcanoes: Fairbanks, Alaska, Alaska Volcano Observatory, p. 47.

Bailey, J.E., Dean, K.G., Dehn, J., and Webley, P.W., 2010, Integrated satellite observations of the 2006 eruption of Augustine Volcano, *in* Power, J.A., Coombs, M.L., and Freymueller, J.T., eds., The 2006 eruption of Augustine Volcano, Alaska: U.S. Geological Survey Professional Paper 1769 (this volume).

Benoit, J.P., McNutt, S.R., and Barboza, V., 2003, Duration-amplitude distribution of volcanic tremor: Journal of Geophysical Research—Solid Earth, v. 108, no. B3, p. 15.

Cervelli, P.F., Fournier, T.J., Freymueller, J.T., Power, J.A., Lisowski, M., and Pauk, B.A., 2010, Geodetic constraints on magma movement and withdrawal during the 2006 eruption of Augustine Volcano, *in* Power, J.A., Coombs, M.L., and Freymueller, J.T., eds., The 2006 eruption of Augustine Volcano, Alaska: U.S. Geological Survey Professional Paper 1769 (this volume).

Coombs, M.L., Bull, K.F., Vallance, J.W., Schneider, D.J., Thoms, E.E., Wessels, R.L., and McGimsey, R.G., 2010, Timing, distribution, and volume of proximal products of the 2006 eruption of Augustine Volcano, *in* Power, J.A., Coombs, M.L., and Freymueller, J.T., eds., The 2006 eruption of Augustine Volcano, Alaska: U.S. Geological Survey Professional Paper 1769 (this volume).

Dean, K., Servilla, M., Roach, A., Foster, B., and Engle, K., 1998, Satellite monitoring of remote volcanoes improves study efforts in Alaska: Eos (Transactions American Geophysical Union), v. 75, no. 35, p. 413.

Dehn, J., Dean, K., and Engle, K., 2000, Thermal monitoring of North Pacific volcanoes from space: Geology, v. 28, no. 8, p. 755–758.

Dehn, J., Dean, K.G., Engle, K., and Izbekov, P., 2002, Thermal precursors in satellite images of the 1999 eruption of Shishaldin Volcano: Bulletin of Volcanology, v. 64, no. 8, p. 525–534.

Dozier, J., 1981, A method for satellite identification of surface temperature fields of subpixel resolution: Remote Sensing of Environment, v. 11, no. 3, p. 221–229.

Endo, E.T., and Murray, T., 1991, Real-time seismic amplitude measurement (RSAM)—A volcano monitoring and prediction tool: Bulletin of Volcanology, v. 53, no. 7, p. 533–545.

Fehler, M., 1983, Observations of volcanic tremor at Mount St Helens Volcano: Journal of Geophysical Research, v. 88, no. NB4, p. 3476–3484.

Fink, J.H., and Griffiths, R.W., 1998, Morphology, eruption rates, and rheology of lava domes—Insights from laboratory models: Journal of Geophysical Research—Solid Earth, v. 103, no. 1, p. 527–545.

Francis, P., and Rothery, D.A., 2000, Remote sensing of active volcanoes: Annual Review of Earth and Planetary Sciences, v. 28, p. 81–106.

Galindo, I., and Dominguez, T., 2002, Near real-time satellite monitoring during the 1997–2000 activity of Volcan de Colima (Mexico) and its relationship with seismic monitoring: Journal of Volcanology and Geothermal Research, v. 117, no. 1-2, p. 91–104.

Harris, A.J.L., Butterworth, A.L., Carlton, R.W., Downey, I., Miller, P., Navarro, P., and Rothery, D.A., 1997, Low-cost volcano surveillance from space—Case studies from Etna, Krafla, Cerro Negro, Fogo, Lascar and Erebus: Bulletin of Volcanology, v. 59, no. 1, p. 49–64.

Harris, A.J.L., Flynn, L.P., Keszthelyi, L., Mouginis-Mark, P.J., Rowland, S.K., and Resing, J.A., 1998, Calculation of lava effusion rates from Landsat TM data: Bulletin of Volcanology, v. 60, no. 1, p. 52–71.

Jacobs, K.M., and McNutt, S.R., 2010, Using seismic *b*-values to interpret seismicity rates and physical processes during the preeruptive earthquake swarm at Augustine Volcano 2005–2006, *in* Power, J.A., Coombs, M.L., and Freymueller, J.T., eds., The 2006 eruption of Augustine Volcano, Alaska: U.S. Geological Survey Professional Paper 1769 (this volume).

Julian, B.R., 1994, Volcanic tremor: nonlinear excitation by fluid-flow: Journal of Geophysical Research-Solid Earth, v. 99, no. B6, p. 11859–11877.

Lahr, J.C., Chouet, B.A., Stephens, C.D., Power, J.A., and Page, R.A., 1994, Earthquake classification, location and error analysis in a volcanic environment: implications for the magmatic system of the 1989–1990 eruptions of Redoubt volcano, Alaska: Journal of Volcanology and Geothermal Research, v. 62, no. 1–4, p. 137–152.

Larsen, J.F., Nye, C.J., Coombs, M.L., Tilman, M., Izbekov, P., and Cameron, C., 2010, Petrology and geochemistry of the 2006 eruption of Augustine Volcano, *in* Power, J.A., Coombs, M.L., and Freymueller, J.T., eds., The 2006 eruption of Augustine Volcano, Alaska: U.S. Geological Survey Professional Paper 1769 (this volume).

Latter, J.H., 1979, Volcanological observations at Tongariro National Park—2, Types and classification of volcanic earthquakes 1976–1978: New Zealand, Department of Scientific and Industrial Research Geophics Division Report no. 150., p. 60.

Lee, C.-W., Lu, Z., Jung, H. S, Won, J.-S., and Dzurisin, D., 2010, Surface deformation of Augustine Volcano, 1992–2005, from multiple-interferogram processing using a refined small baseline subset (SBAS) interferometric synthetic aperture radar (InSAR) approach, *in* Power, J.A.,

Coombs, M.L., and Freymueller, J.T., eds., The 2006 eruption of Augustine Volcano, Alaska: U.S. Geological Survey Professional Paper 1769 (this volume).

Malone, S.D., Boyko, C., and Weaver, C.S., 1983, Seismic precursors to the Mount St. Helens—Eruptions in 1981 and 1982: Science, v. 221, no. 4618, p. 1376–1378.

McNutt, S.R., 1994, Volcanic tremor amplitude correlated with eruption explosivity and its potential use in determining ash hazards to aviation: U.S. Geological Survey Bulletin 2047, p. 377–385.

McNutt, S.R., 2005, Volcanic seismology: Annual Review of Earth and Planetary Sciences, v. 33, p. 461–491.

McNutt, S.R., Tytgat, G., Estes, S.A., and Stihler, S.D., 2010, A parametric study of the January 2006 explosive eruptions of Augustine Volcano, using seismic, infrasonic, and lightning data, *in* Power, J.A., Coombs, M.L., and Freymueller, J.T., eds., The 2006 eruption of Augustine Volcano, Alaska: U.S. Geological Survey Professional Paper 1769 (this volume).

Miller, T.P., and Casadevall, T.J., 1998, Volcanic Ash, Hazards to Aviation, *in* Sigurdsson, H., Houghton, B., McNutt, S.R., Rymer, H., and Stix, J., eds., Encyclopedia of Volcanoes: San Diego, Academic Press, p. 915–930.

Miller, T.P., McGimsey, R.G., Richter, D.H., Riehle, J.R., Nye, C.J., Yount, M.E., and Dumoulin, J.A., 1998, Catalog of the historically active volcanoes of Alaska: U.S. Geological Survey Open-File Report 98-582, p. 104.

Mouginis-Mark, P.J., Crisp, J.A., and Fink, J.H., 2000, Remote sensing of active volcanism: Washington, D.C., American Geophysical Union, 272 p.

Neuberg, J., and O'Gorman, C., 2002, A model of the seismic wavefield in gas-charged magma—Application to Soufriere Hills Volcano, Montserrat, *in* Druitt, T.H., and Kokelaar, B.P., eds., The Eruption of Soufriere Hills Volcano, Montserrat, from 1995 to 1999: Geological Society of London, p. 603–609.

Nye, C.J., Keith, T.E.C., Eichelberger, J.C., Miller, T.P., McNutt, S.R., Moran, S., Schneider, D.J., Dehn, J., and Schaefer, J.R., 2002, The 1999 eruption of Shishaldin Volcano, Alaska—Monitoring a distant eruption: Bulletin of Volcanology, v. 64, no. 8, p. 507–519.

Petersen, T., De Angelis, S., Tytgat, G., and McNutt, S.R., 2006, Local infrasound observations of large ash explosions at Augustine Volcano, Alaska, during January 11–28, 2006: Geophysical Research Letters, v. 33, no. 12, p. doi:10.1029/2006GLO26491.

Power, J.A., Nye, C.J., Coombs, M.L., Wessels, R.L., Cervelli, P.F., Dehn, J., Wallace, K., Freymueller, J.T., and Doukas, M.P., 2006, The Reawakening of Alaska's Augustine Volcano: Eos (Transactions American Geophysical Union), v. 87, no. 37, p. 373, 377.

Power, J.A., and Lalla, D.J., 2010, Seismic observations of Augustine Volcano, 1970–2007, *in* Power, J.A., Coombs, M.L., and Freymueller, J.T., eds., The 2006 eruption of Augustine Volcano, Alaska: U.S. Geological Survey Professional Paper 1769 (this volume).

Roach, A.L., Benoit, J.P., Dean, K.G., and McNutt, S.R., 2001, The combined use of satellite and seismic monitoring during the 1996 eruption of Pavlof volcano, Alaska: Bulletin of Volcanology, v. 62, no. 6-7, p. 385–399.

Rothery, D.A., Francis, P.W., and Wood, C.A., 1988, Volcano monitoring using short wavelength infrared data from satellites: Journal of Geophysical Research, v. 93, no. B7, p. 7993–8008.

Salisbury, J.W., and D'Aria, D.M., 1992, Emissivity of terrestrial materials in the 8-14 μm atmospheric window: Remote Sensing of Environment, v. 42, no. 2, p. 83–106.

Shaw, H.R., 1980, The fracture mechanisms of magma transport from the mantle to the surface, *in* Hargraves, R.B., ed., Physics of Magmatic Processes: Princeton, N.J., Princeton University Press, p. 201–264.

Siebert, L., Beget, J.E., and Glicken, H., 1995, The 1883 and late-prehistoric eruptions of Augustine volcano, Alaska: Journal of Volcanology and Geothermal Research, v. 66, no. 1, p. 367–395.

Wallace, K.L., Neal, C.A., and McGimsey, R.G., 2010, Timing, distribution, and character of tephra fall from the 2005–2006 eruption of Augustine Volcano, *in* Power, J.A., Coombs, M.L., and Freymueller, J.T., eds., The 2006 eruption of Augustine Volcano, Alaska: U.S. Geological Survey Professional Paper 1769 (this volume).

Waythomas, C.F., Watts, P., and Walder, J.S., 2006, Numerical simulation of tsunami generation by cold volcanic mass flows at Augustine Volcano, Alaska: Natural Hazards and Earth System Science, v. 6, no. 5, p. 671–685.

Weaver, C.S., Grant, W.C., Malone, S.D., and Endo, E.T., 1981, Post-May 18 seismicity—Volcanic and tectonic implications, *in* Lipman, P.W., and Mullineaux, D.R., eds., The 1980 Eruptions of Mount St. Helens, Washington: U.S. Geological Survey Professional Paper 1250, p. 109–121.

Webley, P.W., Dean, K.G., Dehn, J., Bailey, J.E., and Peterson, R., 2010, Volcanic-ash dispersion modeling of the 2006 eruption of Augustine Volcano using the Puff model, *in* Power, J.A., Coombs, M.L., and Freymueller, J.T., eds., The 2006 eruption of Augustine Volcano, Alaska: U.S. Geological Survey Professional Paper 1769 (this volume).

Wessels, R.L., Coombs, M.L., Schneider, D.J., Dehn, J., and Ramsey, M.S., 2010, High-resolution satellite and airborne thermal infrared imaging of the 2006 eruption of Augustine Volcano, *in* Power, J.A., Coombs, M.L., and Freymueller, J.T., eds., The 2006 eruption of Augustine Volcano, Alaska: U.S. Geological Survey Professional Paper 1769 (this volume).

Woods, A.W., and Kienle, J., 1994, The dynamics and thermodynamics of volcanic clouds—Theory and observations from the April 15 and April 21, 1990, eruptions of Redoubt volcano, Alaska: Journal of Volcanology and Geothermal Research, v. 62, no. 1–4, p. 273–299.

This page intentionally left blank

The 2006 Eruption of Augustine Volcano, Alaska
Power, J.A., Coombs, M.L., and Freymueller, J.T., editors
U.S. Geological Survey Professional Paper 1769

Chapter 24

Imaging Observations of Thermal Emissions from Augustine Volcano Using a Small Astronomical Camera

By Davis D. Sentman[1], Stephen R. McNutt[1], Hans C. Stenbaek-Nielsen[1], Guy Tytgat[2], and Nicole DeRoin[1]

Abstract

Long-exposure visible-light images of Augustine Volcano were obtained using a charge-coupled device (CCD) camera during several nights of the 2006 eruption. The camera was located 105 km away, at Homer, Alaska, yet showed persistent bright emissions from the north flank of the volcano corresponding to steam releases, pyroclastic flows, and rockfalls originating near the summit. The apparent brightness of the emissions substantially exceeded that of the background nighttime scene. The bright signatures in the images are shown to probably be thermal emissions detected near the long-wavelength limit (~1 μm) of the CCD. Modeling of the emissions as a black-body brightness yields an apparent temperature of 400 to 450°C that likely reflects an unresolved combination of emissions from hot ejecta and cooler material.

Introduction

Augustine Volcano is one of a chain of 80 Alaskan/Aleutian volcanoes of which 41 have been historically active (see Power and Lalla, this volume). Augustine, the most active of the Cook Inlet volcanoes, erupted previously in 1812, 1883, 1935, 1964, 1976, and 1986. Volcanic plumes, which are well known to be accompanied by lightning and other atmospheric electrical phenomena (James and others, 2008) have recently been the subject of several studies (McNutt and Davis, 2000; Williams and McNutt, 2005; McNutt and Williams, 2010). Recent volcanic activity has permitted a wide range of new studies to be undertaken, including volcanic lightning (Thomas and others, 2007 this volume), infrasound both locally (see McNutt and others, this volume) and at regional distances (Olson and others, 2006), and low-light nighttime imaging. Preliminary imaging observations of volcanic lightning that were attempted during the Augustine eruption in early 2006 are the subject of this chapter.

An increase in seismic activity beneath the mountain began on April 30, 2005 (see Jacobs and McNutt, this volume), eventually reaching high enough levels to lead to the Alaska Volcano Observatory issuing a color-code change to yellow in November 2005 and, finally, to a series of explosive eruptions beginning in January 2006 (see Power and Lalla, this volume). After the initial explosions on January 11, 13, and 14, a small astronomical camera was deployed with the intention of capturing images of lightning associated with the volcanic plume, such as those detected in radio emissions and described by Thomas and others (this volume). After the camera deployment on January 21, two large explosions occurred on January 27 and 28 that pushed ash plumes to at least 9 km above sea level, but adverse weather prevented observations of these explosions. No other large explosive eruptions occurred during the deployment interval of January 21 to April 15 that may have been accompanied by lightning, and no lightning was detected during our observations. However, faint nocturnal optical emissions associated with steam releases, rockfalls, and pyroclastic flows were unexpectedly observed with the imaging system that were associated with seismic activity measured from instruments on the island. Here we describe the imaging experiment that recorded these new data, with an analysis indicating that the detected emissions are most likely near-infrared (NIR) thermal emissions registered near the upper wavelength sensitivity limit (1.1 μm) of the camera charge-coupled device CCD.

[1]Geophysical Institute, 903 Koyukuk Drive, University of Alaska Fairbanks, Fairbanks, AK 99775.

[2] 2IRIS PASSCAL Instrument Center, New Mexico Tech, 100 East Road, Socorro, NM 87801.

Observations

Location and Geometry Relative to Augustine Volcano

Observations were made from the University of Alaska's Homer field site (lat 59.658° N., long 151.652° W.), which sits atop a 200-m-high bluff overlooking Cook Inlet to the west. During clear weather the location permits an unobstructed view of Augustine Volcano (lat 59.367° N., long 153.430° W.) at a distance of ~105 km west-southwestward across the open water of the inlet. Geophysical monitoring stations located on the island were described by DeRoin and others (2007), McNutt and others (this volume), and Power and Lalla (this volume).

Imaging System

The imaging observations were made using a monochrome Starlight Xpress model SXV-M7 16-bits/pixel integrating astronomical camera with a USB 2.0 external interface. The camera uses a 1/2 inch format Sony ICX429ALL monochrome 752- by 582-pixel CCD array, with pixel dimensions 8.6.by 8.3 μm, and a single stage of unregulated Peltier cooling to reduce thermal noise. The EXview Hole Accumulation Diode (HAD) technology used in this class of silicon sensors exhibits an extended wavelength response, with some sensitivity to 1.1 μm. This is in the near-infrared (NIR) wavelength range, slightly beyond the range of human eyesight (0.4–0.7 μm).

Various standard C-mount lenses were tested during the experiment, but the lenses used for most observations were a Tamron 35 mm f/2.4 CCTV (11.0° by 8.2° field of view, 26.6-m/pixel resolution at the observing distance of 105 km to Augustine Island) and a Sigma 135 mm f/1.8 (2.85° by 2.0° field-of-view, 6.89-m/pixel resolution at Augustine Volcano). Images were typically obtained at 10–20 s intervals, with a 5 to 15 s integration times, followed by 5 s image readout to a USB 2.0 disk drive and pause to wait for the next open-shutter synchronization command. Images were saved in 16-bit Flexible Image Transport System (FITS) format, which also recorded the start time of image integration. Camera operations were controlled using a custom script running within Cyanogen Inc.'s MaxIM DL/CCD v4 software operating under Microsoft Windows XP on an IBM notebook computer. The imaging system was connected to the Internet and remotely controlled from Fairbanks by way of Windows Remote Desktop operating over a virtual private network (VPN). System time was maintained accurate to ~100 ms by way of Network Time Protocol (NTP), which was deemed to be sufficiently accurate for correlation with other types of Augustine observations. Image collection commenced shortly after local sundown and continued uninterruptedly until sunrise the following morning, with 2,000 to 3,000 images typically recorded each night. The images were downloaded over the Internet each morning for archiving and offline analysis.

Sample Images

During the early part of the observing campaign (January 21 to February 12, 2006) a 35 mm f/2.4 wide-angle (11.0° by 8.2°) lens was used for the observations. In one scene, recorded the night of February 8 (UTC; fig. 1), Augustine is visible in the lower midcenter, with bright emissions emanating from along its north (right) flank.

Figure 1 records the broadband brightness detected by the monochrome camera at each pixel in the scene and has been colorized to aid interpretation. As shown below, the bright emissions labeled "NIR thermal emissions" appear to originate in the black-body emission spectrum of a hot source and are detectable because of the NIR sensitivity of the CCD. The other features in the image, such as cirrus haze, stars, reflected moonlight from the waters of Cook Inlet, and the foreground moonlit snowfield, provide the context needed to interpret the image, including the ability to spatially locate the source of the thermal emissions relative to Augustine Volcano and meteorological information needed to determine the quality of the viewing conditions (snow, fog, wind, and so on).

During most of the observing campaign (February 13 to April 15, 2006) a 135 mm f/1.8 lens with a narrow field of view (2.85° by 2.0°) was used for the observations. A second sample image, recorded on March 15 shortly after sunset, is shown in figure 2. Here, a steam plume is visible, along with several small thermal emissions near the summit and along the right (north) flank of the volcano.

Because thermal imaging of hot sources is commonly performed using infrared cameras with sensing elements optimized for the the most intense thermal emission wavelengths, we were surprised to see thermal-emissions with a silicon-based CCD. Imagers in satellite systems (Dehn and others, 2002) or in forward looking infrared (FLIR) cameras (Calvari and others, 2005; Harris and others, 2005; Patrick and others, 2007) for detecting the thermal activity associated with terrestrial volcanoes generally utilize non-silicon technology. However, CCD imaging has been used to investigate the active volcanism on Jupiter's moon Io (McEwen and others, 1997), and the CCD camera aboard the Galileo spacecraft was able to detect brightness temperatures down to ~700 K (430°C) in panchromatic images, although 1,000 K (730°C) was a more practical limit. Tighter temperature constraints came from images at different wavelengths, which allowed color temperatures to be computed (McEwen and others, 1998; Radebaugh and others, 2004; Milazzo and others, 2005; Keszthelyi and others, 2007). The coincidence of the transient, bright emission features recorded in our images with the seismic activity simultaneously recorded by instruments located on the volcanic island (DeRoin and others, 2007) strongly suggested that the bright features were thermal emissions

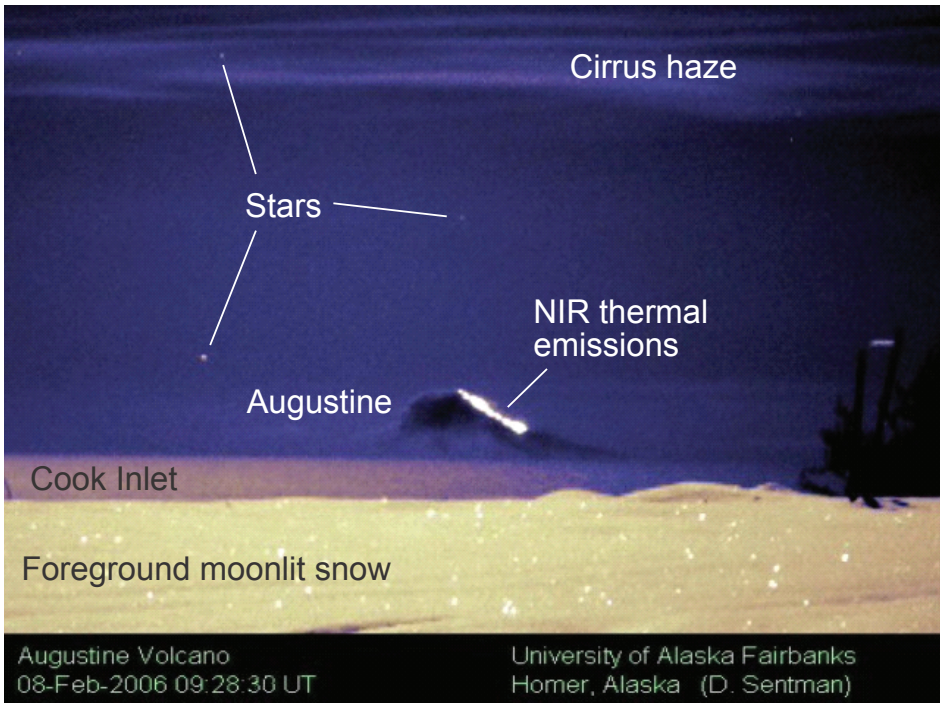

Figure 1. Augustine Volcano as observed the night of February 8, 2006 (UTC), from Homer, Alaska, when a bright moon illuminated the scene, including the steam from left (south) downwind side of the volcano. The image has been contrast stretched and colorized to facilitate feature identification.

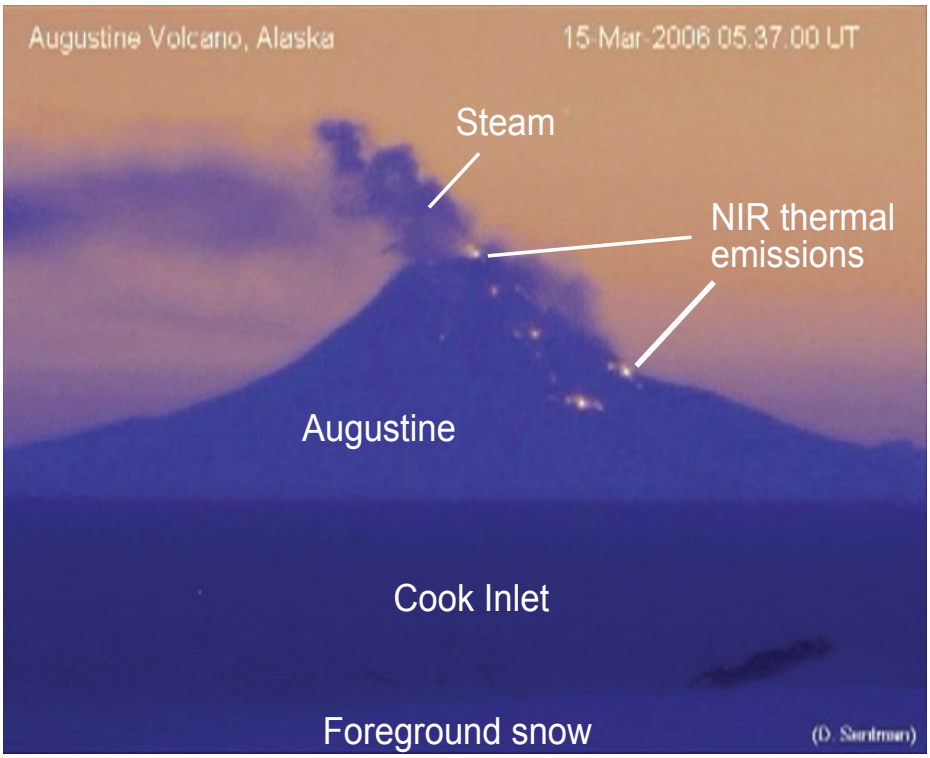

Figure 2. A zoomed image of Augustine obtained on March 15, 2006 (UTC), soon after local sunset using a 135 mm f/1.8 lens. As with figure 1, a false color palette has been used.

from pyroclastic flows or other hot ejecta. This prompted an analysis of the response of the camera to black-body thermal emissions with the aim of obtaining a general understanding of the various factors that enter into the analysis and ascertaining whether such observations might be useful as part of a more general program of volcano monitoring.

Analysis—Detectability of Thermal Emissions

The detectability of thermal emissions from a natural source depends on a combination of the source emission spectrum, the atmospheric radiative transfer characteristics between the source and the observer, the transfer function of the optical train in the sensor system, and the spectral response of the detector. For a silicon CCD detector, the measurements consist of the number of photons from the source emission spectrum that survive atmospheric absorption and losses in the optical train and within the sensor. To be a statistically meaningful observation, photon counts also must significantly exceed internal thermal and read noise associated with the sensor itself. Below we consider these factors in order.

Planck Black-body Emission Spectrum

Assuming that the bright emissions observed are black-body thermal emissions, Wien's displacement law relating the wavelength λ_{max} of peak emissions in the Planck radiation curve and the temperature T is $\lambda_{max} T = 2897\ \mu$m K, and so for a nominal temperature $T = 1{,}000$K we have $\lambda_{max} = 2.897\ \mu$m, which falls in the medium-wavelength infrared (MWIR) band. Thus, optical measurements of $\lambda < 1\ \mu$m using silicon sensors fall on the short-wavelength side of the Planck radiation curve. This curve falls off very steeply with decreasing wavelength below the peak of the thermal emissions, so the principal question to be addressed is whether enough energy from this part of the Planck curve intersects the sensor pass band to be detectable.

To understand the relation between camera sensitivity and wavelength in terms of a thermal emission spectrum, it is instructive to review the form of the Planck black-body radiation formula. The Planck formula for the spectral radiance $I(\lambda,T)$ of a black-body radiator in thermal equilibrium is (Rybicki and Lightman, 1979)

$$I(\lambda,T)=\frac{2hc^2}{\lambda^5}\frac{1}{e^{hc/\lambda k_B T}-1}, \qquad (1)$$

where λ is the wavelength in meters, T is temperature in Kelvins, $h = 6.63 \times 10^{-34}$ [J s] is Planck's constant, and $k_B = 1.38 \times 10^{-23}$ [J/K] is Boltzmann's constant. For a small wavelength interval $d\lambda$, the dimensions of $I(\lambda,d\lambda)d\lambda$ are energy flux per unit solid angle (in joules per square meter per second per steradian).

The Planck formula describes the black-body emissions for any temperature and wavelength. Emission contours illustrating the general features of the Planck formula over wavelengths and temperatures of interest to our observations are plotted in figure 3. For the present problem of detecting thermal radiation using silicon-based optical sensors sensitive in the wavelength range 400 to 1100 nm, nominal temperatures of 500 to 1,000°C (773 to 1273 K) for hot volcanic ejecta (Larsen 1929) correspond to a sensor response on the very steep short-wavelength side of the Planck curve. Here, the thermal-emission spectrum changes rapidly with wavelength and so is very sensitively dependent on the temperature. For example, near the range of temperatures under consideration, on the short-wavelength side of the Planck radiation curve a 10-percent decrease in wavelength produces an ~50-percent decrease in the flux density, whereas a 10-percent decrease in absolute temperature (127°C) produces an ~80-percent decrease in the flux density. The emissions therefore depend extremely sensitively on the emission temperature and wavelength, such that small calibration uncertainties are correspondingly magnified.

Imaging-System Response to Thermal Radiation

Imaging sensors detect quantized packets of energy in the form of photons, and so the energy flux at a given wavelength must be converted to to the equivalent photon flux. The energy (in joules) carried by a single photon is $E=h\nu=hc/\lambda$, so the photon flux corresponding to equation 1 is

$$P(\lambda,T)\,d\lambda=(\lambda/hc)I(\lambda,T)d\lambda, \text{ or}$$

$$P(\lambda,T)d\lambda=\frac{2c}{\lambda^4}\frac{1}{e^{hc/\lambda k_B T}-1}d\lambda, \qquad (2)$$

where $P(\lambda,T)d\lambda$ has the dimensions of photon flux per unit solid angle, (in protons per square meter per second per steradian).

The photon flux per unit wavelength incident on a pixel is then given by $N(\lambda,T)=P(\lambda,T)\,A\Omega$, where $N(\lambda,T)d\lambda$ is the number of photons per unit time in a small wavelength interval $d\lambda$ crossing a lens aperture of area A (in square meters) from a source region subtending a solid angle Ω (in steradians) as seen by an observer. The product $G=A\Omega$ (in square meters steradian) is the etendue (sometimes referred to as simply "A-omega") of the pixel-lens combination and is an important system element that determines the overall detected signal level.

For a circular lens of diameter D (in meters), the aperture area is $A=\pi D^2/4$ (in square meters). The aperture dimensions are not typically quoted for lenses used in imaging. Instead, this information is indirectly specified through the focal length L

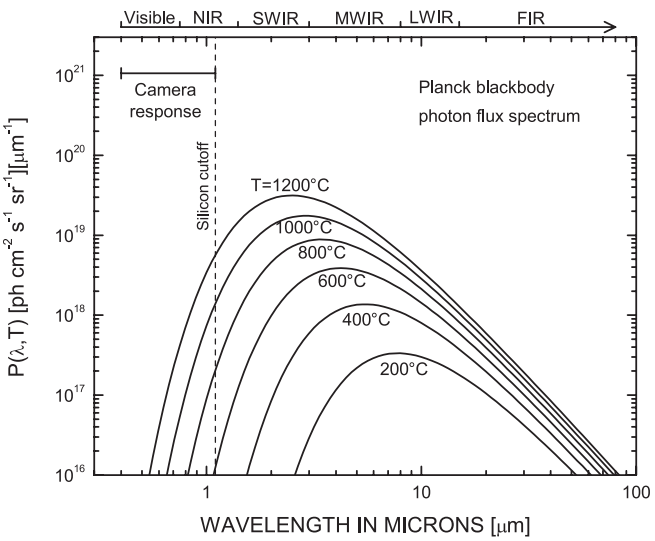

Figure 3. Photon flux spectrum $P(\lambda,T)$ for Planck blackbody radiation, expression (2) of the text. Note that here the unit area is expressed in cm^2 and the spectral density is in terms of mm^{-1}. The labels at the top refer to Near Infrared (NIR), Short Wavelength Infrared (SWIR), Medium Wavelength Infrared (MWIR), Long Wavelength Infrared (LWIR), and Far Infrared (FIR).

(commonly in mm), and the dimensionless speed (*f*-number) of the lens, where $f=L/D$, giving $A=\pi L^2/4f^2$.

For imagers where the focal plane of the lens is the CCD plane, the sensors are the individual pixels, and so the solid angle Ω subtended by the source is that of the field of view as seen by a single pixel. We assume that the source is of uniform brightness over the field of view of the pixel (diffuse-source approximation) and that the field of view is small, so angular apodization effects may be ignored. For a pixel of physical dimensions $p_x \times p_y$ (in square meters), the solid angle viewed by the pixel through a lens of focal length L is approximately $\Omega=p_x p_y / L^2$ (in sterdians).

Expressed in terms of the lens speed and pixel

dimensions, the etendue is $A\Omega=\frac{\pi}{4}\frac{p_x p_y}{f^2}$ (in square meters-steradians).

The number of blackbody photons per unit time incident on a pixel of dimensions $p_x \times p_y$ (in square meters) through a lens of speed *f* in a small wavelength interval $d\lambda$ centered on wavelength λ may then be written

$$N(\lambda,T)d\lambda = \frac{\pi c}{2\lambda^4}\frac{1}{\left(e^{hc/\lambda k_B T}-1\right)}\frac{p_x p_y}{f^2}d\lambda\ , \qquad (3)$$

which shows that for bare CCD imaging of diffuse sources, large pixel sizes and fast (small *f*-number) lenses are advantageous. We note that as expressed in equation 3, the physical area of the lens aperture, the focal length of the lens, and the solid angle of the source viewed by a single pixel are all implicitly contained in the ratio $p_x p_y / f^2$.

Atmospheric Transmission

The transmission of optical emissions through the atmosphere is highly susceptible to Rayleigh scattering, wavelength-dependent absorption from such atmospheric molecular species as water vapor, and absorption and Mie scattering from rain, snow, fog, aerosols, and dust. For observations through a large number of air masses over long horizontal distances, such as Augustine Volcano from Homer, Alaska, the transmissivity can vary widely and, in the absence of active calibrations that continuously monitor changing conditions, it can only be specified approximately. Typically, good observations were possible only on optically clear nights, but even under ideal conditions noticeable shimmering was evident in many images, possibly owing to refraction effects due to temperature gradients in the boundary layer, as well as to variations in the transmissivity from changing amounts of water vapor and aerosols. The level of shimmer in the images provided a useful gauge of boundary-layer stability.

To estimate the transmissivity of the atmosphere for the given viewing geometry, we computed a nominal transmissivity spectrum $S(\lambda)$ for the NIR wavelength range 0.7-1.5 μm using the U.S. Air Force Moderate Spectral Atmospheric Radiance and Transmittance code (MOSART) program, version 1.7. A horizontal pathlength of 105 km, corresponding to ~15 air masses, was assumed, with clean air and marine boundary-layer conditions. The model parameters used to calculate the atmospheric parameters were pressure, 10,135 Pa; temperature, 257.2 K; water vapor, 1,405 ppm by volume (ppmv) CO_2, 330 ppmv; ozone, 0.018 ppmv, N_2O, 0.32 ppmv and maritime aerosol conditions (from table 35, Subarctic (60° N) latitude winter atmosphere, "MOSART Model Atmospheres," Photon Research Associates, Inc., May 1993.)

The results are plotted in figure 4. Severe atmospheric absorption/attenuation bands are evident near ~0.76, 0.95, and 1.13 μm, and across a wide band of wavelengths 1.3 to 1.5 μm, which correspond to molecular absorption by water, and vary widely, depending on the overall pathlength and the air humidity. A general degradation in transmissivity from Rayleigh scattering occurs at wavelengths shorter than 0.7 μm. We propose that the observed bright emissions are from black-body radiation from hot Augustine ejecta and that the emissions are transmitted to the observation site through the relatively narrow atmospheric transmission band 1.0 to 1.1 μm.

The assumptions used for the transmissivity calculation represent ideal viewing conditions and omit the effects of fog or other types of atmospheric contaminant that frequently compromise viewing. The variability in atmospheric transmissivity due to changing weather conditions is the largest uncertainty in the interpretation of observations. The effective brightness temperature based on these assumptions is of only limited accuracy and should therefore be treated with appropriate caution.

Transmission Through the Optical Elements

Wavelength-dependent losses occur in various elements of the optical system, including the plexiglass window through which the camera viewed Augustine Volcano, and the camera lens. Calibrations were unavailable for these elements, and so a constant transmissivity of 0.5 was assumed for the window/lens combination.

Detector Response

The quantum efficiency as a function of wavelength, $R(\lambda)$, for the Sony ICX429ALL CCD sensor used in the camera is plotted in figure 5, where the normalized scale on the left corresponds to a maximum quantum efficiency of 70 percent at a wavelength of 600 nm. The manufacturer's data sheet does not extend beyond 1,000 nm, as shown, but it may be assumed the response continues to decrease uniformly to zero at the silicon cutoff at 1.1 μm. Most of the scene information in figures 1 and 2, including reflection of moonlight, stars, and evening sky brightness, comes from the main part of the sensitivity curve 400–700 nm. It is believed that the bright thermal emissions are being detected from the far right portion of the curve, at λ> 900 nm, where the quantum efficiency is very small (<5 percent). In this wavelength region, slight uncertainties in sensitivity can lead to large effects in the observed signal and the inferred temperature.

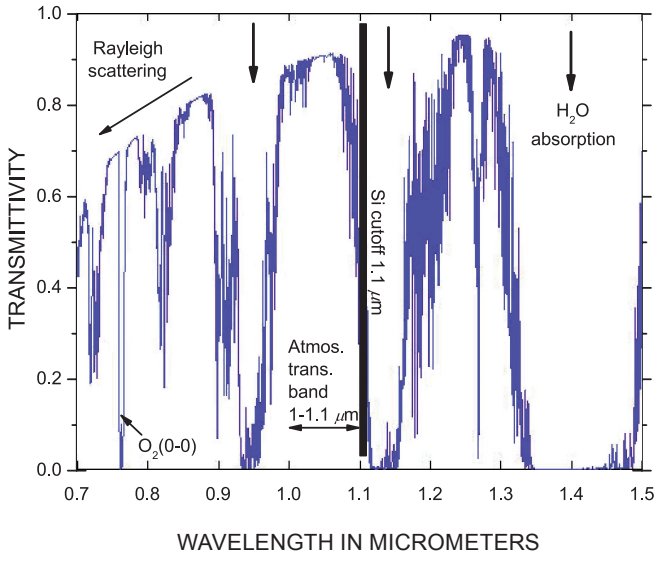

Figure 4. Atmospheric transmissivity versus wavelength 0.7-1.5 μm between Homer and Augustine volcano. The transmissivity was computed using MOSART code, assuming a horizontal path length looking through 15 air masses and marine boundary layer conditions. The heavy arrows at the top indicate major water- absoption bands, and the O_2(0-0) absorption line at 0.762 μm is also evident. The silicon cutoff wavelength at 1.1 μm is indicated. It is seen that there is a narrow transmission band between 1 and 1.1 μm.

End-to-End System Response Versus Black-Body Temperature

The photon counts from a thermal source accumulated over an integration interval of Δt is given by

$$N(T,\Delta t) = \Delta t \int_0^\infty N(\lambda,T) S(\lambda) R(\lambda) L(\lambda)\, d\lambda \ , \qquad (4)$$

where, from equation 3, the Planck formula for photon flux is

$$N(\lambda,T) = \frac{\pi c}{2\lambda^4} \frac{1}{(e^{hc/\lambda k_B T} - 1)} \frac{p_x p_y}{f^2} \ , \qquad (5)$$

in which we also include the etendue of the system. In equation 4, $S(\lambda)$ is the wavelength-dependent dimensionless atmospheric transmissivity function, and $R(\lambda)$ is the dimensionless CCD response function versus wavelength. Wavelength-dependent losses in the end-to-end transfer function of the optical train, given by $L(\lambda)$, include losses from lenses and filters, as well as from viewing ports such as glass or plexiglass windows. Additional factors that may be important for wide-angle scenes, but do not affect the present narrow field-of-view observations, include the apodization or obliquity factor needed to take into account the reduction in the apparent aperture area and pixel area for scene elements lying off the optical axis, and image vignetting that may occur if the physical size of the CCD detector is smaller than the image formed by the lens.

The photon counts into a pixel are given by the integral in equation 4, where the integrand is composed of four factors. On the short-wavelength side of the Planck spectrum near 1 μm the function $N(\lambda,T)$ increases rapidly with wavelength

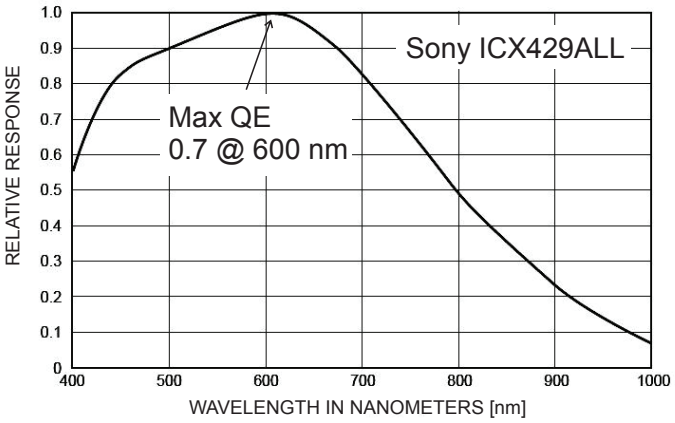

Figure 5. Relative response versus wavelength, normalized to the maximum quantum efficiency (QE), for the Sony model ICX429ALL CCD in the Starlight Xpress camera, per the Sony data sheet.

and temperature, while the sensor response $R(\lambda)$ decreases rapidly in this same wavelength region near the upper limits of its sensitivity. Their product, $P(\lambda,T)\ R(\lambda)$, is highly peaked around a wavelength of $\lambda \sim 1\ \mu$m and overlaps the atmospheric transmission window near 1 μm. The relations among these four factors are sketched in figure 6.

Given the overall uncertainties in the atmospheric transmissivity and detector sensitivity at wavelengths >1 μm, we use a crude approximation to estimate the value of the integral in equation 4. We assume that the integrand is highly peaked about some wavelength λ_0, as sketched in figure 6, that corresponds to transmission band $\lambda_0 \sim 1$ μm in figure 4. We further assume a width of the peaked function of $\Delta\lambda = 0.1$ μm, so that $\Delta\lambda << \lambda_0$. The integral may then be approximated using uniform response functions for $R(\lambda_0)$, $S(\lambda_0)$, and $L(\lambda_0)$. For a fixed geometry, the photon counts in a pixel as a function of source temperature and camera integration time is then

$$N(T,\Delta t) \approx \Delta t\, N(\lambda_0,T) R(\lambda_0) S(\lambda_0) L(\lambda_0)\, \Delta\lambda. \qquad (6)$$

Inserting system parameters for the present observations, we have: pixel dimensions of the Sony ICX429ALL CCD, 8.3 by 8.6 μm; relative response versus wavelength of the CCD (fig. 5), $\Delta\lambda = 0.1$ μm at $\lambda_0 = 1$ μm; quantum efficiency at $\lambda_0 = 1$ μm is ~0.01; lens speed $f/2.4$; integration time $\Delta t = 5$ s; atmospheric transmissivity $S(\lambda_0) = 0.8$; wavelength-dependent losses $L(\lambda_0) = 0.5$, which includes losses in the lens and from window absorption. With these parameters the expected number of pixel counts versus temperature T [°C] from thermal emissions is plotted in figure 7, where the curve labeled "Ideal emission spectrum" shows the pixel counts versus black-body source temperature for the assumed system parameters, and the dashed curves labeled "50%" and "25%" show the effects of including additional inefficiencies in the system. The recorded pixel counts of ~6,000 correspond to an apparent thermal temperature of 400 to 450°C for bright emissions.

Discussion

The observed emissions are consistent with thermal emissions at an apparent temperature of 400 to 450°C. With the given pixel resolution of several tens of meters at the source, each pixel would likely have included the combined effects of a heterogeneous mixture of hot emitters and cooler surfaces (Keszthelyi and others, 2003).

Although the emissions reported here were invisible to the unaided eye when spot checks were made at the time of the observations, other researchers reported incandescence during the eruption period that was visible through binoculars or when using color digital cameras and telephoto lenses. The human eye is generally insensitive to wavelengths longer than ~700 μm, even under dark-adapted conditions

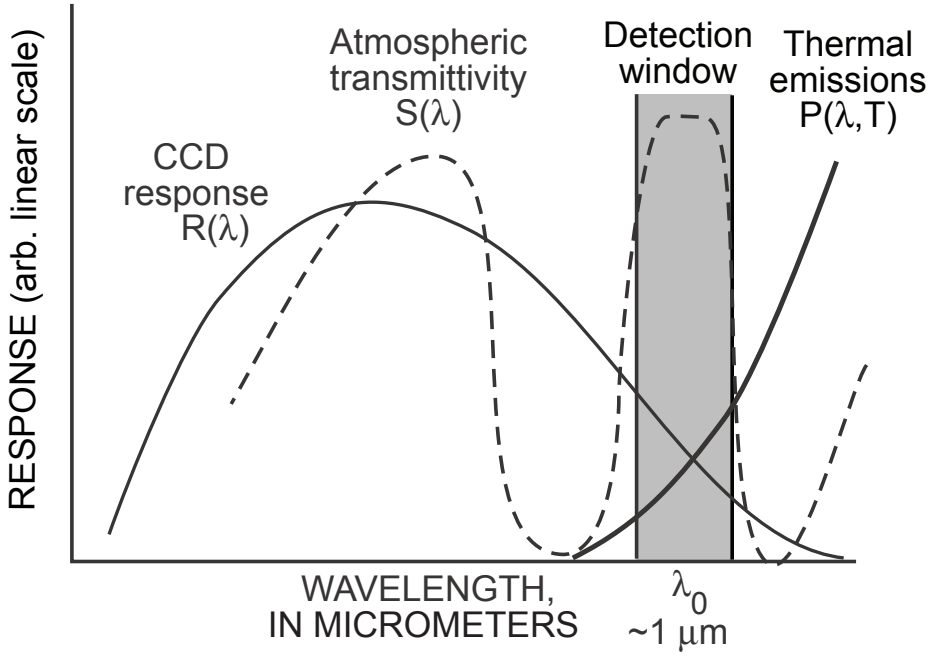

Figure 6. Sketch illustrating the various factors entering into the detectability of thermal emissions. The wavelength scale spans the general range of sensitivity of the camera CCD, from the blue on the left to the CCD cutoff wavelength slightly above 1 μm. The wavelength range believed detected in the images is indicated by the dark rectangle centered on $\lambda_0 \sim 1$ μm.

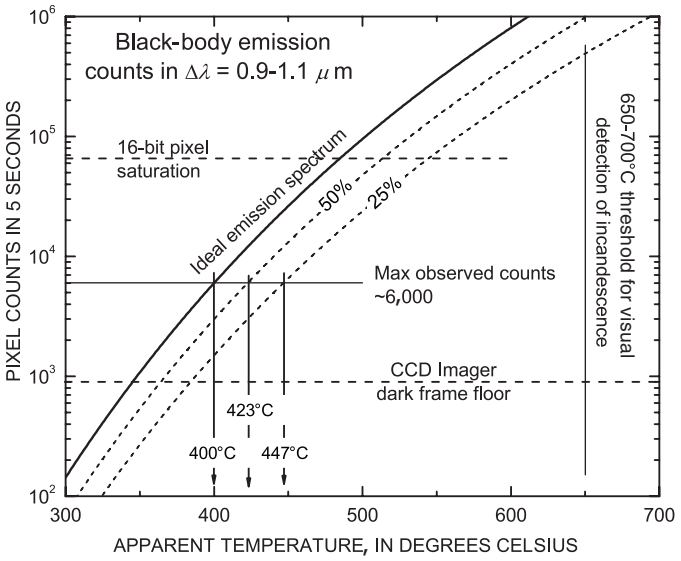

Figure 7. Number of counts in a 5 s integration interval for an f/2.4 lens and the system parameters given in the text. The heavy solid curve corresponds to the number of detector counts assuming an ideal black-body radiator at the given temperature on the abscissa. The effects on apparent temperature from departures from the ideal black-body due to additional inefficiencies beyond those assumed in the calculation are indicated by the dashed lines. The dark frame counts due to CCD thermal noise and bias are ~900 under typical operating conditions. The 16-bit saturation level is also shown. For the measured 6,000-count level shown, the apparent temperatures is ~400 to 450°C. The temperature threshold for visual detection of incandescence is indicated on the right.

(Kinney, 1958), so visual detection of incandescence implied that the temperatures at such times would have been at least ~650 to 700°C (see figure 7). We speculate that images of such visually detectable emissions made using the present camera system would have been much brighter than the examples presented here.

Conclusions

- Hot thermal emissions from steam releases, rockfalls, and pyroclastic flows from Augustine Volcano were detected in February to March 2006 using a small silicon-based astronomical camera. The observations were made over open water from a distance of ~105 km from Augustine.

- The emissions, which were quite bright in the optical images, were generally invisible to the dark-adapted human eye when spot checks were made, although informal observations of incandescence at other times were reported by other observers.

  Analysis of the emission brightness, taking into account the camera sensitivity versus wavelength and atmospheric transmissivity over the long distance between the volcano and the observing site, suggests that the detected emissions occurred within a narrow atmospheric-transmission window near the upper limit of the camera response at ~ 1 μm.

- The observed emissions are consistent with thermal emissions at an apparent temperature of 400 to 450°C. The uncertainties in this calculated apparent temperature are substantial because the observed emissions fall near the extreme limit of the camera response and the atmospheric transmissivity varies near this wavelength.

- Although silicon-based imagers are not optimal for detecting thermal emissions, the observations presented here suggest that they could provide a relatively inexpensive means to monitor some volcanoes for nocturnal thermal emissions.

Acknowledgments

We thank J. Dehn, J. Paskievitch, and K. Dean for useful discussions and D. Wilkinson for use of a camera lens. This work was supported by the Geophysical Institute University of Alaska Fairbanks, the Alaska Volcano Observatory, the U.S. Geological Survey as part of their Volcano Hazards Program, and by the State of Alaska.

References Cited

Calvari, S., Spampinato, L., Lodato, L., Harris, A.J.L., Patrick, M.R., Dehn, J., Burton, M.R., and Andronico, D., 2005, Chronology and complex volcanic processes during the 2002–2003 flank eruption at Stromboli volcano (Italy) reconstructed from direct observations and survey with a handheld infrared camera: Journal of Geophysical Research, v. 110, B02201, doi:10.1029/2004JB003129.

Dehn, J., Dean, K.G., Engle, K., and Izbekov, P., 2002. Thermal precursors in satellite images of the 1999 eruption of Shishaldin Volcano: Bulletin of Volcanology, v. 64, p. 507–519, doi:10.1007/s00445-002-0227-0.

DeRoin, N., McNutt, S.R., Reyes, C., and Sentman, D., 2007, Rockfalls at Augustine Volcano, Alaska—2003–2006: Eos (American Geophysical Union Transactions), v. 88, S43–1038.

Harris, A.J.L., Dehn, J., Patrick, M., Calvari, S., Ripepe, M., and Lodato, L., 2005, Lava effusion rates from handheld thermal infrared imagery; an example from the June 2003

effusive activity at Stromboli: Bulletin of Volcanology, v. 65, p. 101–117, doi: 10.1007/s00445-005-0425-7.

Jacobs, K.M., and McNutt, S.R., 2010, Using seismic *b*-values to interpret seismicity rates and physical processes during the preeruptive earthquake swarm at Augustine Volcano 2005–2006, *in* Power, J.A., Coombs, M.L., and Freymueller, J.T., eds., The 2006 eruption of Augustine Volcano, Alaska: U.S. Geological Survey Professional Paper 1769 (this volume).

James, M.R., Wilson, L., Lane, S.J., Gilbert, J.S., Mather, T.A., Harrison, R.G., and Martin, R.S., 2008, Electrical charging of volcanic plumes: Space Science Reviews, doi:10.1007/s11214-008-9362-z.

Keszthelyi, L., Harris, A.J.L., and Dehn, J., 2003, Observations of the effect of wind on the cooling of active lava flows: Geophysical Research Letters, v. 30, no. 19, p. 1989, doi:10.1029/2003GL017994.

Keszthelyi, L., Jaeger, W., Milazzo, M., Radebaugh, J., Davies, A.G., and Mitchell, K., 2007. New estimates for Io eruption temperatures—implications for the interior: Icarus, v. 192, p. 491–502.

Kinney, J.A.S., 1958, Comparison of scotopic, mesopic, and photopic spectral sensitivity curves: Journal of the Optical Society of America, v. 48, p. 185–190.

Larsen, E.S., 1929, The temperature of magmas: American Mineralogist, v. 14, p. 81–94.

McEwen, A.,Simonelli, D.P., Senske, D.R., Klaasen, K.P., Keszthelyi, L., Johnson, T.V., Geissler, P.E., Carr, M.H., and Belton, M.J.S., 1997. High-temperature hot spots on Io as seen by the Galileo Solid State Imaging (SSI) experiment: Geophysical Research Letters, v. 24, p. 2443–2446.

McEwen, A.S., Keszthelyi, L., Spencer, J.R., Schubert, G., Matson, D.L., Lopes-Gautier, R., Klaasen, K.P. , Johnson, T.V., Head, J.W., Geissler, P., Fagents, S., Davies, A.G., Carr, M.H., Breneman, H.H. and Belton, M.J.S., 1998, High-temperature silicate volcanism on Jupiter's moon Io: Science, v. 281, p. 87–90.

McNutt, S.R., and Davis, C.M., 2000, Lightning associated with the 1992 eruptions of Crater Peak, Mount Spurr Volcano, Alaska: Journal of Volcanology and Geothermal Research, v. 102, p. 45–65.

McNutt, S.R., and Williams, E.R., 2010, Volcanic lightning; global observations and constraints on source mechanisms: Bulletin of Volcanology, v. 72, p. 1153-1167, doi: 10.1007/s00445-010-0393-4.

Milazzo, M.P., Keszthelyi, L., Radebaugh, J., Davies, A.G., Turtle, E.P., Geissler, P., Klaasen, K.P., and McEwen, A.S., 2005, Volcanic activity at Tvashtar Catena, Io: Icarus, v. 179, p. 235–251.

Olson, J.V., Wilson, C.R., McNutt, S.R., and Tytgat, G., 2006, Infrasonic wave observations of the January 2006 Augustine Volcano eruptions: Eos (American Geophysical Union Transaction), v. 87, p. V51C–1685.

Patrick, M.R., Harris, A.J.L., Ripepe, M., Dehn, J., Rothery, D.A., and Calvari, S., 2007, Strombolian explosive styles and source conditions; insights from thermal (FLIR) video: Bulletin of Volcanology, v. 69, no. 7, p. 769–784, doi:10.1007/s00445-006-0107-0.

Power, J.A., and Lalla, D.J., 2010, Seismic observations of Augustine Volcano, 1970–2007, *in* Power, J.A., Coombs, M.L., and Freymueller, J.T., eds., The 2006 eruption of Augustine Volcano, Alaska: U.S. Geological Survey Professional Paper 1769 (this volume).

Radebaugh, J., McEwen, A.S., Milazzo, M.P., Keszthelyi, L.P., Davies, A.G., Turtle, E.P., and Dawson, D.D. , 2004, Observations and temperatures of Io's Pele Patera from Cassini and Galileo spacecraft images: Icarus, v. 169, p. 65–79.

Rybicki, G.B., and Lightman, A.P., 1979: Radiative processes in astrophysics: New York, Wiley-Interscience, 382 p.

Thomas, R.J., Krehbiel, P.R., Rison, W., Edens, H.E., Aulich, G.D., Winn, W.P., McNutt, S.R., Tytgat, G. and Clark, E. , 2007, Electrical activity during the 2006 Mount St. Augustine volcanic eruptions: Science, v. 315, no. 5815, p. 1097, doi:1126/science.1136091.

Thomas, R.J., McNutt, S.R., Krehbiel, P.R., Rison, W., Aulich, G., Edens, H.E., Tytgat, G, and Clark, E., 2010, Lightning and electrical activity during the 2006 eruption of Augustine Volcano, *in* Power, J.A., Coombs, M.L., and Freymueller, J.T., eds., The 2006 eruption of Augustine Volcano, Alaska: U.S. Geological Survey Professional Paper 1769 (this volume).

Williams, E.R., and McNutt, S.R., 2005, Total water contents in volcanic eruption clouds and implications for electrification and lightning, chap. 6 *of* Pontikis, C., ed., Recent progress in lightning physics: Kerala, India, Research Signpost Publishing, p. 81–93.

This page intentionally left blank

The 2006 Eruption of Augustine Volcano, Alaska
Power, J.A., Coombs, M.L., and Freymueller, J.T., editors
U.S. Geological Survey Professional Paper 1769

Chapter 25

Lightning and Electrical Activity during the 2006 Eruption of Augustine Volcano

By Ronald J. Thomas[1], Stephen R. McNutt[2], Paul R. Krehbiel[3], William Rison[1], Grayden Aulich[3], Harald E. Edens[3], Guy Tytgat[4], and Edward Clark[2]

Abstract

Lightning and other electrical activity were measured during the 2006 eruption of Augustine Volcano. We found two phases of the activity, the explosive phase corresponding to the explosive eruptions and the plume phase. We classified the lightning into three types, vent discharges, near-vent lightning, and plume lightning. Vent discharges are small, 10 to 100 m sparks, that occur at rate as great as 10,000 s^{-1} at the mouth of the volcano during the energetic explosive eruptions. The vent discharges were observed six different times. Near-vent lightning appears to develop upward from the volcanic cone into the developing column during explosions. This lightning is small, in the range of 1 to 7 km, and short, 0.01 to 0.1 s. The behavior of the near-vent lightning indicates an overall positive charge in the ejecta. The plume lightning resembled intracloud thunderstorm lightning. Often it was branched, spanned more than 10 km, and lasted more than 0.5 s.

Introduction

Throughout recorded history, spectacular lightning discharges have been observed in and from the ash clouds produced by large volcanic eruptions. Lightning has also been observed and photographed during much smaller eruptive activity. Early investigations of volcanic lightning were made during the Surtsey and Heimay eruptions in Iceland in 1963 and 1973 (Anderson and others, 1965, Brook and others, 1974). Lightning associated with eruption of Redoubt in 1989–90 (Hoblitt, 1994) and Spurr 1992 (McNutt and Davis, 2000) occurred in the ash cloud beginning 5 or more minutes after the explosion onsets. (This appears to represent only one type of volcanic lightning, referred to below as plume lightning.) The worldwide observations of volcanic lightning have recently been tabulated, encompassing more than 200 cases associated with 74 volcanoes (Mather and Harrison, 2006; McNutt and Williams, unpublished data), showing that lightning occurs for volcanoes with a wide variety of magma compositions, eruption types, and ash column heights. However, despite increasing interest and additional studies in recent years (reviewed in Mather and Harrison, 2006), volcanic lightning continues to be poorly understood.

Volcanic lightning is at the same time spectacular, dangerous, and interesting. It presents danger that most people close to the eruption will not be expecting. Its interests to science include its roll in the origin of life, similarities and difference to thunderstorms, and why the plume becomes electrified. Observing and monitoring lightning during an eruption opens many possibilities. First it could show where there may be danger to people and where fires could be started. The measurement techniques that we present, can detect lightning at a safe distance even when there is bad weather and visual observations are not possible. Thus, the occurrence of an eruption could be confirmed in remote locations or poor conditions if lightning signals were detected. The location of lightning in the drifting plume would show the location of the ash plume. Measurement of lightning and electrical activity can be another tool to help understand the processes occurring during the eruption.

Here we report observations of lightning during the 2006 eruption of Augustine Volcano, Alaska (Thomas and others, 2007), that have provided a much more detailed picture of volcanic lightning than heretofore available. The observations were obtained with a portable lightning mapping system that was recently developed at New Mexico Tech (NMT),

[1]Electrical Engineering Department, New Mexico Tech, Socorro, NM 87801.

[2]Alaska Volcano Observatory, Geophysical Institute, University of Alaska Fairbanks, 903 Koyukuk Drive, Fairbanks, AK 99775.

[3]Lagmuir Laboratory, New Mexico Tech, Socorro, NM 87601.

[4] IRIS Passcal Instrument Center, New Mexcio Tech, 100 East Road, Socorro, NM 87801.

and was deployed in cooperation with the Alaska Volcano Observatory (AVO).

We have designed and built a lightning mapping system which produces three-dimensional images of lightning discharges by measuring the arrival time of RF (radio frequency) radiation, at multiple ground stations (Rison and others, 1999; Thomas and others, 2004). The radiation is produced as the lightning channels form or are reionized. To make the system more versatile, we recently built a portable version for rapid deployment in field operations. In addition to studies of thunderstorm lightning, the portable version was built in anticipation of using it for studies of volcanic lightning. A few weeks after the construction of the first portable stations (December 2005), the recent eruption of Augustine began. After consultations about logistics between the New Mexico and Alaska groups, we moved quickly to deploy two stations to observe lightning from possible further explosive eruptions. These stations were installed on the east coast of Cook Inlet near Homer and Anchor Point (see fig. 1). Although more stations surrounding and closer to the volcano were desirable, the remoteness, the lack of power, and the winter conditions made this impossible in the short term. Installation of the two stations was completed only hours before the series of explosive eruptions that began on 27 January, 2006. In this paper, we report on the lightning observations made during these explosions.

In February of 2006, we installed two battery powered stations in remote locations, one on Augustine's informally named West Island (about 7 km from the vent) and one at Oil Point (520 m above Cook Inlet and about 34 km north of the volcano; see fig. 1). The stations operated automatically and unattended on battery power for a period of 1 to 1.5 months. Only a small amount of useful data from West Island was recorded, because the volcano went into a dome-building phase, with substantially decreased explosive activity. Also, due to an electronics problem, much of the data from the West Island station was unusable. On a few occasions during the effusive phase of the eruption, the remote systems recorded signals that were correlated to the signals received at the

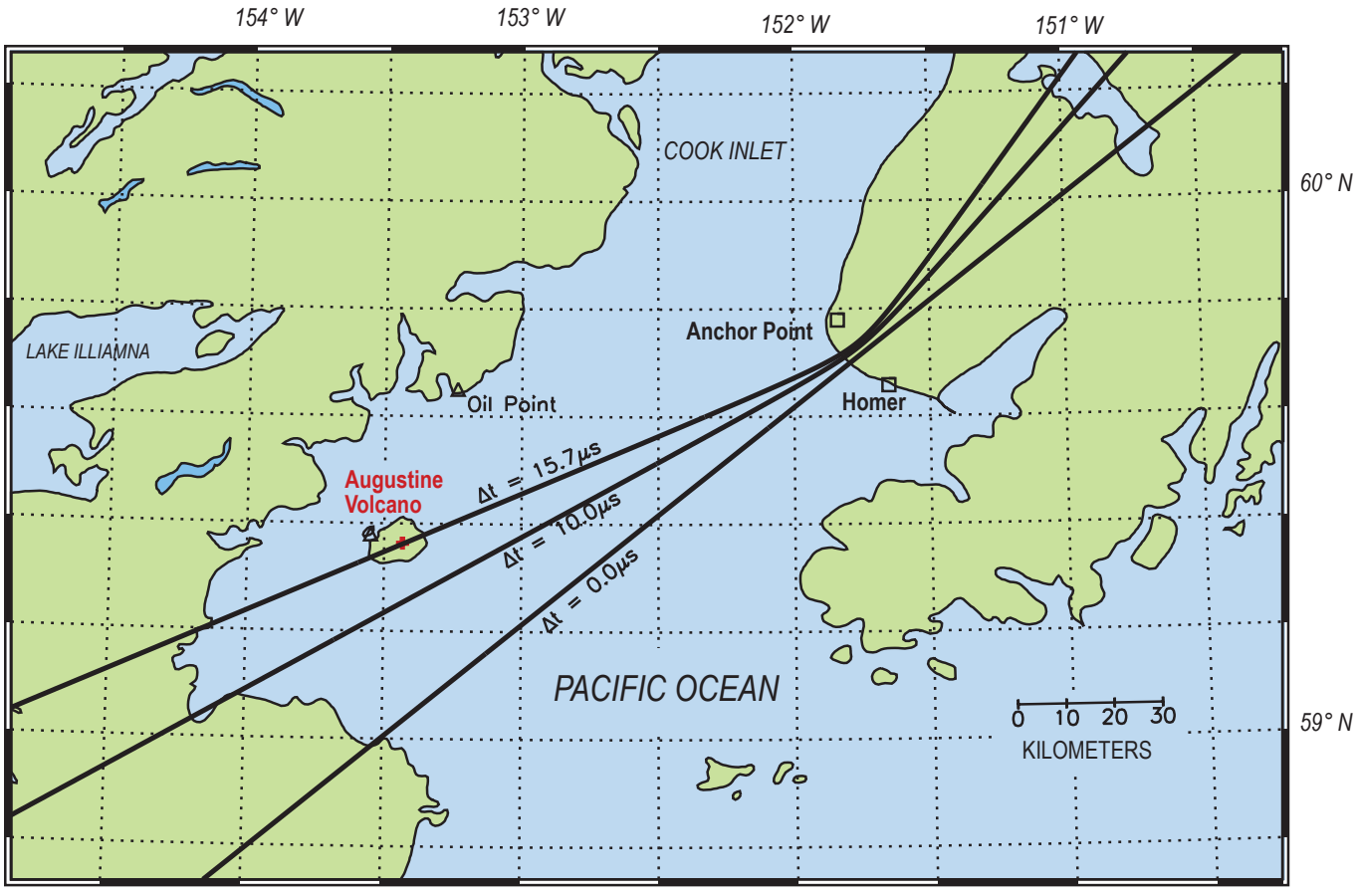

Figure 1. Map of the area surrounding Augustine Volcano and the locations of the lightning mapping stations. Anchor Point and Homer stations (squares) operated from January 27 to May 12, 2006. Oil Point station (triangle) operated from February 20 to March 16 and West Island (Augustine) station (triangle) operated from February 18 to April 2. The three hyperbola show the possible source location for different arrival time differences for the Homer and Anchor Point station pair.

Homer and Oil Point stations. These observations are also reported in this paper.

Other Observations of Lightning January 2006

Before the installation of the NMT Lightning Mapping Array (LMA) stations, lightning was observed accompanying 6 of the 9 explosions from January 11–17, 2006 (table 1). The data are from quite varied sources. A lightning detection system operated by the Bureau of Land Management (BLM) in central Alaska recorded two flashes during the January 13 explosions at 0424 AKST (1324 UTC) and one flash during the January 14 explosion at 0014 AKST (0914 UTC). As the primary use of the BLM system is to monitor summertime cloud-to-ground lightning, which may start forest fires, winter operation is not a high priority. Only four stations of the nine station network were operational during the Augustine eruption (T. Weatherby, written commun., 2006). Figure 3 of McNutt and Davis (2000) shows the locations of the BLM stations. The January 13 lightning flashes were both of positive polarity (as they transferred positive charge to ground) and occurred 10 and 12 minutes after the beginning of the explosion. This time difference is similar to intervals during the Redoubt eruption in 1990 (Hoblitt, 1994). One flash was cloud to ground (CG) and the other intracloud (IC) (T. Weatherby, written commun., 2006). The January 14 flash occurred 8 minutes after the explosion onset and was a CG flash with negative polarity. This event was also recorded on five seismic stations as an irregular spike, due to the interaction between the broadband lightning pulse and the seismic system electronics. The three Augustine flashes were the only lightning flashes recorded by the BLM system in all of Alaska for the first 2 weeks of January 2006.

The explosion on January 14 at 0847 AKST (1747 UTC) was observed by airline pilots flying 100 to 150 miles to the west. They state that they saw the eruption column rising "totally vertically, visibly growing as we watch it, probably 10–15 thousand feet above us now, static lightning discharges within the cloud, cloud is growing very fast…"

One other explosion on January 13 had lightning witnessed by ground observers within the radio station KDLG Dillingham listening area. We infer this to be the 1122 AKST (2022 UTC) explosion or the January 13 1858 AKST (January14 0358 UTC) explosion. Viewing conditions were favorable for both these explosions. The other report is from the January 17 explosion at 0758 AKST (1658 UTC).

During the explosions of January 27–29 there were no visual reports of lightning or detections by the BLM network.

Table 1. Observations of lightning during the Augustine Volcano, January 11-28, 2006, explosive eruption events.

[CG, cloud-to-ground; IC, Intarcloud; BLM, Bureau of Land Management; PIREP, Pilot Report; NMT, New Mexico Tech]

Event			Lightning	Data source	Plume Height (km)	Comments
Number	Date, 2006	Onset UT				
1	11-Jan	1344	No	-	6.5	
2	11-Jan	1412	No	-	10.2	
3	13-Jan	1324	Yes	BLM	10.2	2 flashes, positive polarity, 10 and 12 min after eruption onset, CG and IC
4	13-Jan	1747	Yes	PIREP	10.2	IC, viewed from aircraft 100-150 mi to the west
5	13-Jan	2022	Yes	Ground obs	10.5	telephone call from radio station KDLG Dillingham
6	14-Jan	0140	No	-	10.5	
7	14-Jan	0358	Yes	?	13.5	
8	14-Jan	0914	Yes	BLM	10.2	1 flash, negative polarity, 8 min after eruption onset, CG; also recorded on 5 seismic station
9	17-Jan	1658	Yes	?	13.5	
10	28-Jan	0524	Yes	NMT	10.5	365 flashes; 2 flashes showed up on pressure sensor at station AUE as interference with the pressure sensor electronics
11	28-Jan	0837	Yes	NMT	3.8	1 flash
12	28-Jan	1104	Yes	NMT	7.2	28 flashes
13	28-Jan	1642	Yes	NMT	7.0	6 flashes

Poor weather conditions at these times made for unfavorable viewing conditions.

Measurement Technique

The NMT LMA detects VHF (63 MHz) radio signals from electrical impulses that are produced by lightning and other sources. The arrival times of the signals are measured with 40 ns accuracy using a timing signal from a GPS receiver. With this timing accuracy a multistation LMA can determine the source location with 10-m horizontal error and 30-m vertical error, depending on the geometry of the station and source locations (Thomas and others, 2004). The system is a time-of-arrival system similar to the ones used to locate the source of seismic signals, except the radio signals travel at the speed of light in straight lines (as with light a clear path is needed between the source and receiver; however clouds will not block the signal but solid objects will). A system using eight or more stations spaced 10 to 20 km apart (fig. 2) can locate several thousand sources (in 3 dimensions; 3D) for a single lightning flash. Impulsive RF radiation is emitted as a lightning channel develops. A lightning channel develops in a bipolar manner, with negative breakdown at one end of the channel and positive breakdown at the other (Behnke and others, 2005). The radiation from the positive end of the channel is much weaker than that from the negative end, and the LMA detects primarily the breakdown associated with the extension of the negative end of the channel.

The LMA digitizes the log of the received power at a 25 MHz rate. If the peak amplitude in a short time interval exceeds the local noise level, the time and 8-bit amplitude of the strongest source is recorded. In this experiment this time interval (time window) was either 80 μs or 10 μs. Also, the number of events above the local noise threshold is recorded. This above threshold value will be between 1 and 2,000, with high value indicating continuous breakdown and a small value indicating that only one or a few impulsive events occurred in the 80 μs interval. The threshold is adjusted automatically so that during quiet periods background noise triggers the system about 10 percent of the time. If a source produces radiation strong enough to be detected by six or more stations, the 3D location of the source can be determined.

Figure 3 shows the LMA image of a lightning flash with a complex structure that is lower in altitude (2 to 6 km) and lasts a little longer (about 1 second) than a more typical discharge (6 to 10 km altitude with a duration of about half a second). This flash was selected because its characteristics are similar to the lightning in the Augustine plume after the initial explosion on January 27.

Due to time constraints and logistics, we were able to install only two receiving stations for the initial Augustine observations. The stations were located about 17.1 km apart and about 100 km north-northeast the volcano (see fig. 1). The line joining the stations was close to perpendicular to the direction to Augustine. The southern station was at the AVO field station north of Homer and the northern station was at the Anchor Point Public Library. The receiving antenna at the Homer station was located on the edge of a high (220 m) bluff overlooking Cook Inlet, with direct line of sight to Augustine. The Anchor Point station was located at 125 m altitude about 1.5 km inland from the coast and did not have a direct view of Augustine.

With this system we could determine the azimuthal direction to the radio source. Under these conditions it is a good approximation to assume that the arriving radio wave is a plane wave as shown in figure 4. The azimuthal direction θ to the source is given by $\sin(\theta) = c\, T_{13} / D$, where T_{13} is the difference in arrival times at the two stations, c is the speed of light, and D is the separation distance of the stations. An arrival time difference of 15.7 μs corresponded to signals arriving from the direction of Augustine's summit; signals originating in a southward direction from Augustine had decreased time differences as indicated in figure 1. The 40 ns resolution of the system

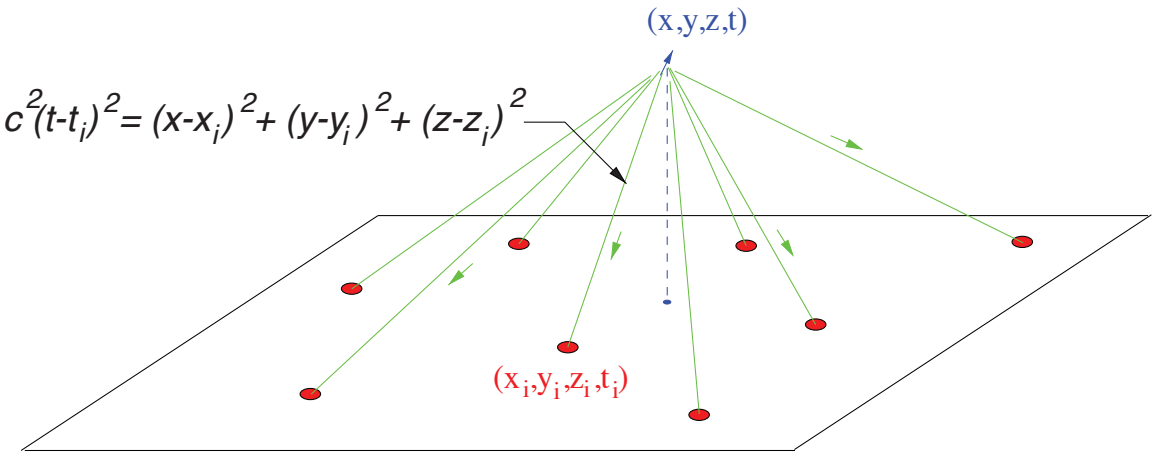

Figure 2. Diagram showing how lightning is located. The multiple station lightning mapping array locates the position of impulsive radio sources in three dimensions by carefully measuring the arrival times at each station.

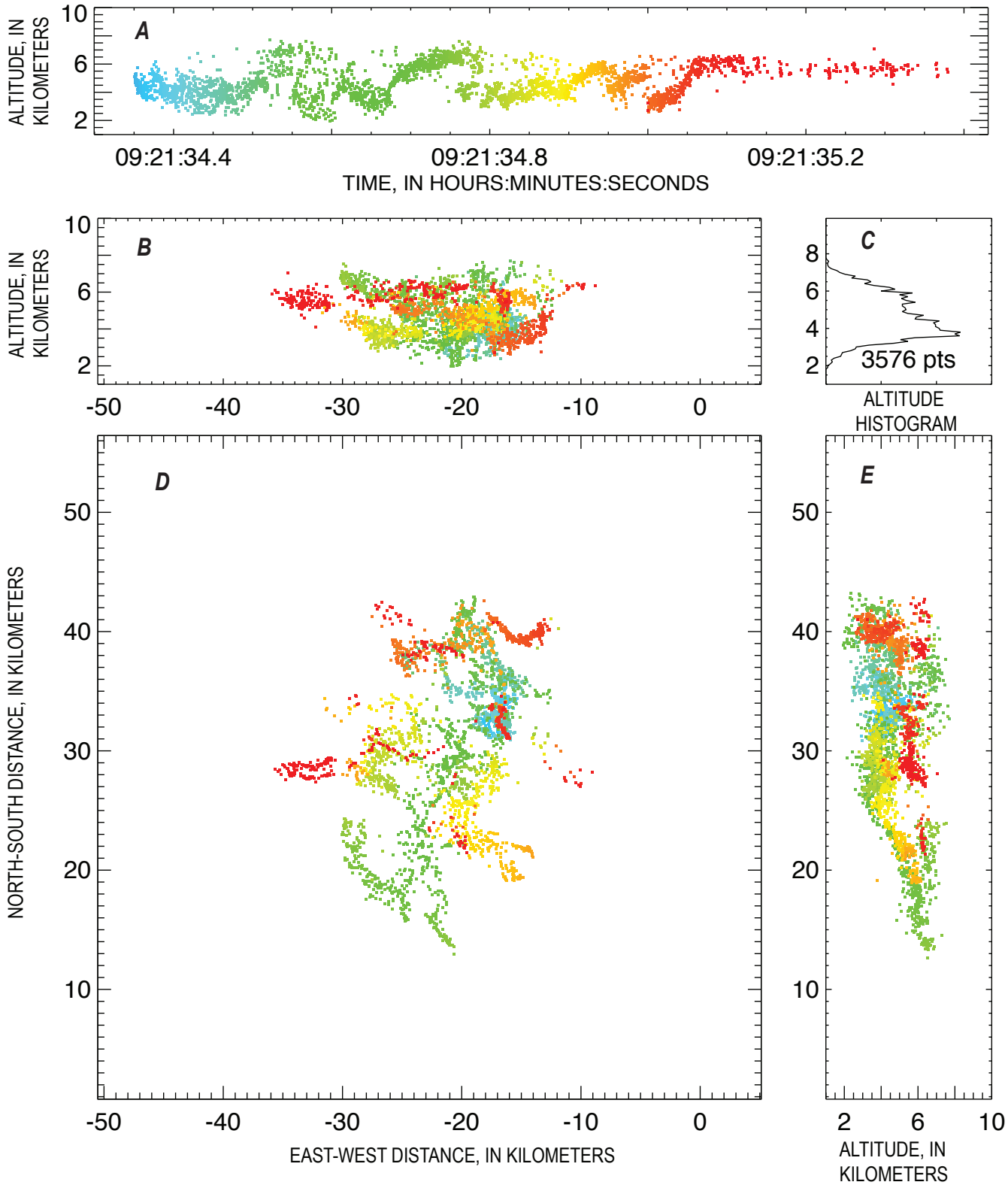

Figure 3. Three dimensional (3D) views of a low altitude intracloud lightning flash observed in eastern Colorado by the lightning mapping array (LMA). This flash was between a negative layer above 6 km and a positive layer below 6 km. The flash did not go to ground. *D* shows a plan view. Colors show the time development, beginning with blue and ending with red. *B* and *E* are vertical projections showing the altitude development. Part A shows the altitude versus time. *C* is an altitude histogram.

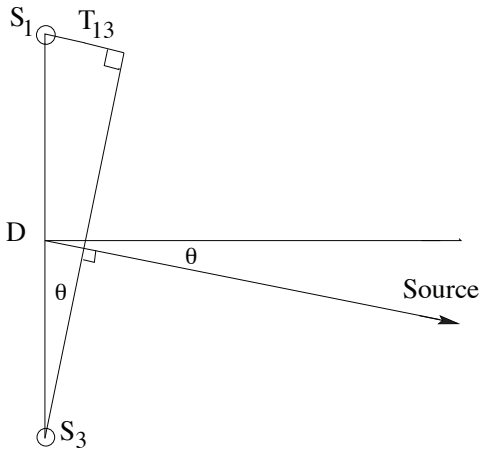

Figure 4. Diagram showing how the direction to a source is determined. Radio waves at an azimuth θ from the source in the distance arrive at station S_3 first and later at station S_1. T_{13} is the difference in arrival times at the two stations. *D* is the separation of the stations.

translates to 75 m (transverse distance, that is in a horizontal direction perpendicular to the line of sight, about north-south) resolution at the distance of the volcano. More precisely, using two stations, a measured time difference constrains the source to lie on a hyperbola (see fig. 1), and at large distances from the stations the azimuthal angle can be determined from the above relationship.

For comparison with the Augustine Volcano results, figure 5 shows the 3D locations of the thunderstorm lightning of figure 3 as they would be observed by a two station network. The top panel shows north-south position as a function of time as would be seen from the west or east. Branches that form continuously appear as lines; the slope can be used to determine the component of velocity perpendicular to the line between the stations and the lightning discharge. The second panel shows how the channels would look as observed from the north or south. The third panel shows the power emitted by the source in the 6 MHz bandwidth of the receivers. The fourth panel shows the number of points above threshold in

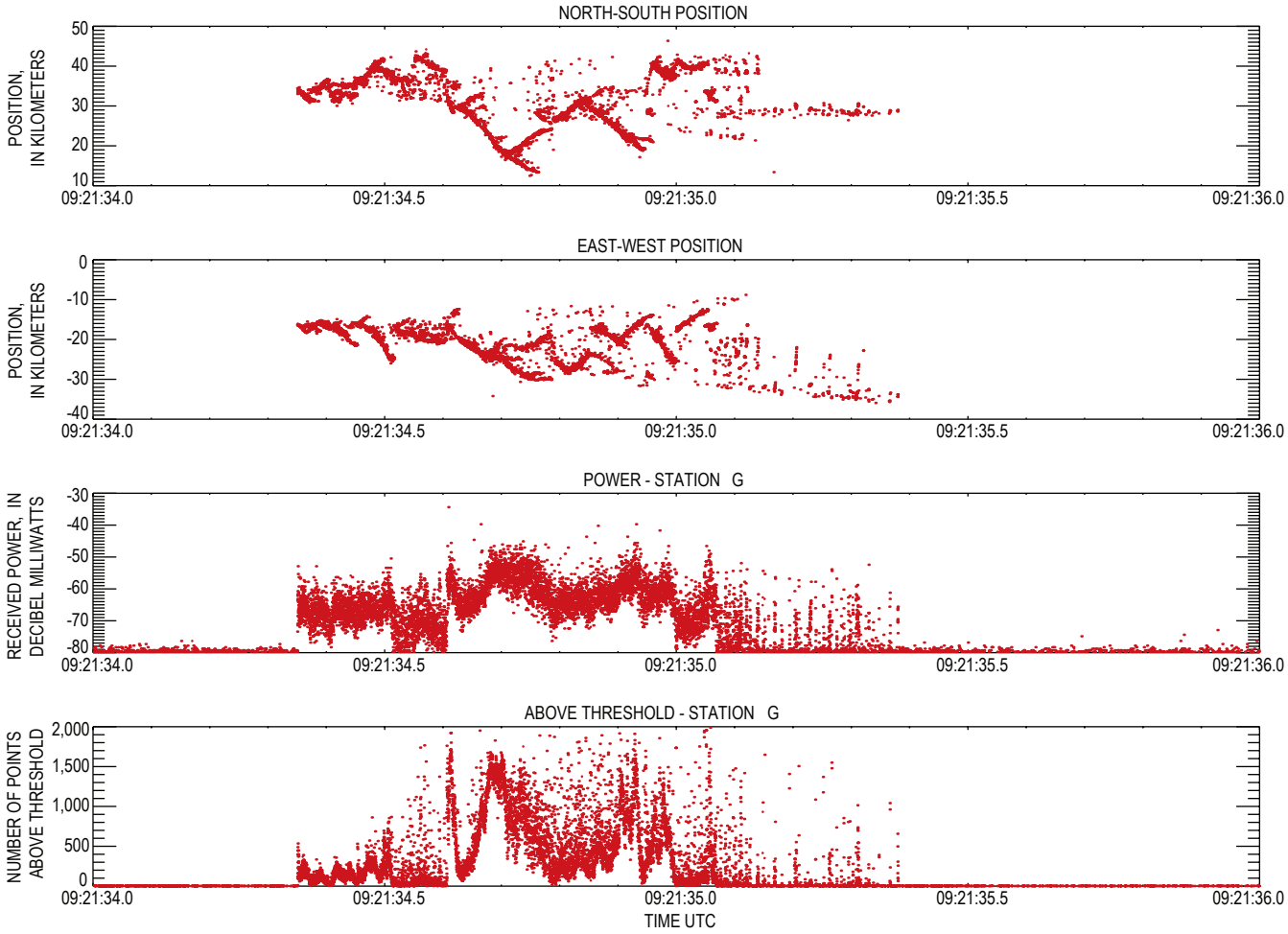

Figure 5. This set of plots show how the flash in figure 3 would appear to a two station network. The top two panels are the x and y positions versus time. The bottom two panels are raw data (power and number of points above threshold) from one station about 100 km from the flash. The times in this plot are in universal time (UTC).

each 10 μs window of the system. In this plot the flash divides into three parts of about equal lengths. During the middle phase of its development, RF radiation was mostly continuous (because the above threshold is near the maximum), and during the final phase, it consisted mostly of isolated impulses (since the above threshold is small).

Explosive Eruption at 2024 AKST on January 27, 2006

LMA Data

The raw data for the 2024 AKST (0524 UTC) explosion on January 27 (January 28 for UTC time) are shown in figure 6. The top panel shows the peak received power of the strongest event detected in each 80 μs interval (the time window was reduced to 10 μs at 1236 AKST (2136 UTC) for Homer and 1443 AKST (2343 UTC) for Anchor Point). In the top plot the color represents the relative density of the number of points at each power level. Several bands of background signals are observed. Most of these are due to local sources such as computers, other high speed electronics devices, motors, and transformers. The best way to identify signals caused by lightning is to correlate the signals from the two stations by looking for differences in arrival times consistent with sources near Augustine. (Peaks due to local sources will not correlate, because sources local to one station will not be detected at the other.) For this explosion we were interested only in time differences close to 15 μs (see fig. 1). Events we identify as correlated are marked with magenta in figure 7. We identified correlated points as groups of at least three points close in both time and arrival time difference.

The second panel shows number of points above threshold in each time window. The bottom panel displays the time between the strong events. During lightning flashes the rate increases and the time between events decreases. The three panels help to identify interesting events. Most of the events identified as correlated appear as vertical lines. Because lightning flashes generally last less than a second, have many high

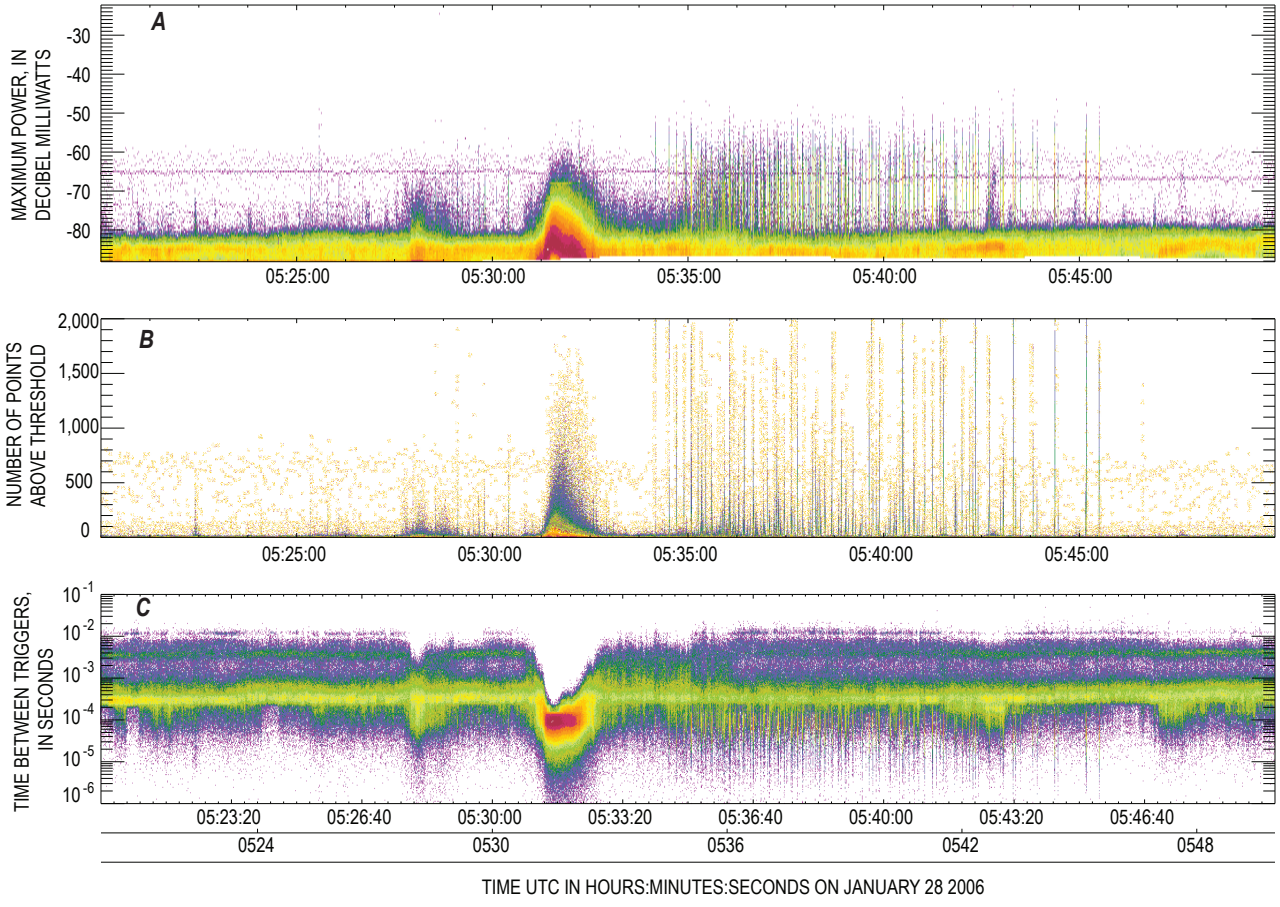

Figure 6. Plots of the raw lightning mapping data of the first explosive eruption on January 27 at 2031 AKST (January 28 at 0531 UTC) from the Homer station. The signature of the explosion is clearly visible as the bright red area. The power, the number of points above threshold, and the time between peaks are shown in the three panels as density plots; the color indicates the number of events with red being the most and blue-purple the least. The dates and times in this plot are in universal time (UTC).

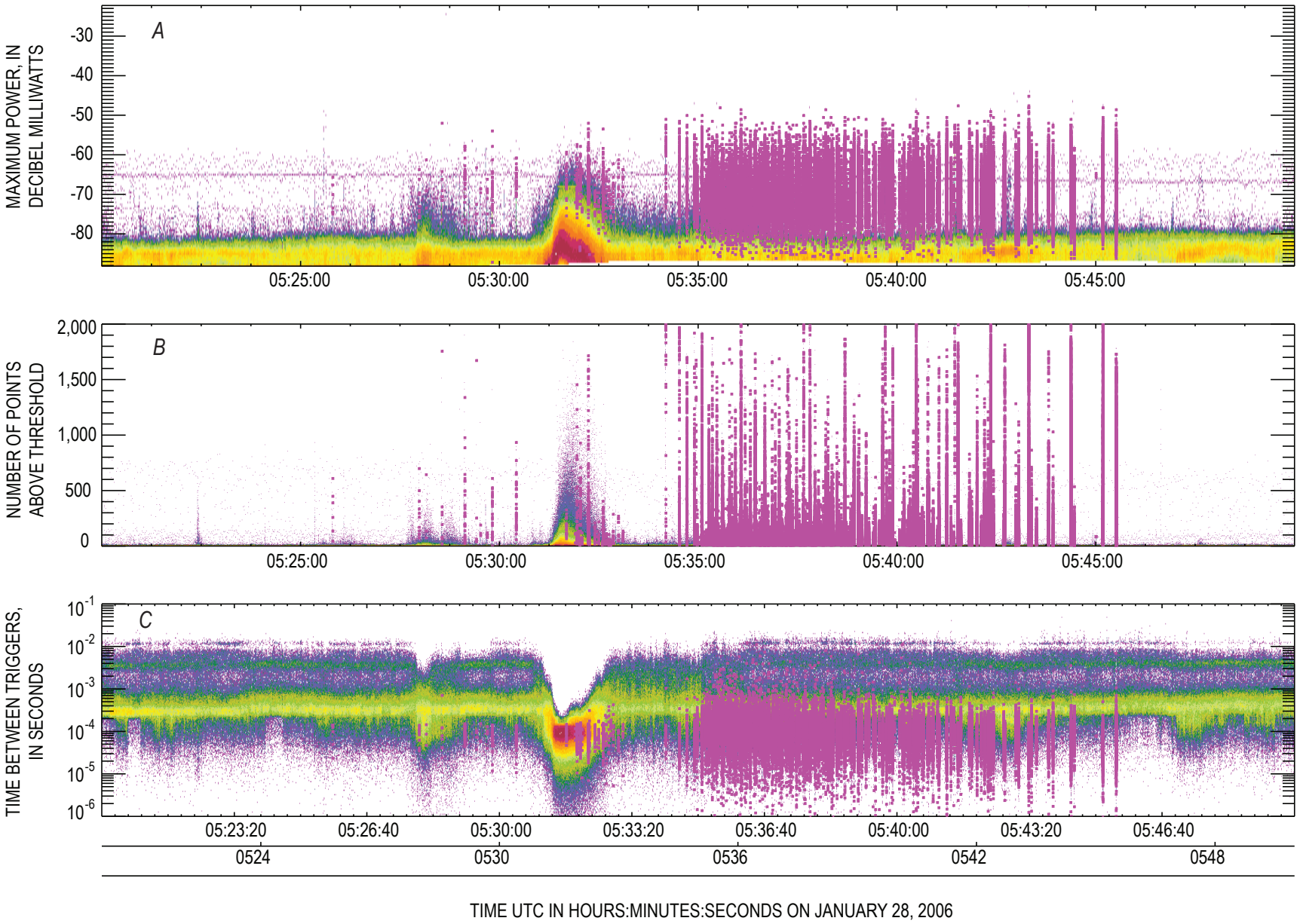

Figure 7. The raw data shown in figure 6 has been marked with magenta points to show events that are seen with both station and are correlated. The difference in the times of arrival show that these are from the volcano. The dates and times in this plot are in universal time (UTC).

power events, and many point above threshold, they should appear as vertical lines in plots with this time scale.

The explosion began at about 2024 AKST (0524 UTC), and was small at first. At 2027 AKST (0527 UTC) an increase in the energy of the explosion occurred, which can be seen as an increase in the LMA signal levels. At about 2031 AKST (0531 UTC) the largest eruptive pulse occurred as an enhancement lasting about two minutes and seen in all 3 panels of LMA data. This enhancement appears to have been caused by the explosion, as it is concurrent with the most intense part of the explosion based on seismic and infrasound data (see fig. 11 below) but is not correlated with data from Anchor Point. Because the station at Anchor Point was somewhat inland, was in a noisier radio frequency environment, and did not have line of sight to the Augustine summit, it was less sensitive to signals from Augustine than the Homer station. Although Anchor Point functioned well for higher-altitude events, it did not detect the noisy radiation during the explosive phases, even though the Homer data showed this radiation to be as strong as or stronger than that of more organized discharges. This indicates that the explosive-phase radiation originated at relatively low altitude at or slightly above Augustine's summit vent. The signals from the vent would have been more strongly attenuated at Anchor Point. The radiated source powers ranged from about 0 dBW up to 30 dBW (1 to 1,000 W) in the receiver passband, typical of values observed for ordinary lightning (Thomas and others, 2001). Because we saw similar enhancements during five other eruptive events (documented below), we conclude that the signals are due to electrical events at the vent during explosive eruptions. We will refer to these as vent discharges.

We have not observed similar electrical activity in thunderstorms (we have observed many thunderstorms with the same equipment and have not seen similar electrical signals). This type of electrical activity appears to be unique to volcanic explosions.

During the 2.2 minutes of enhanced signals starting at 2031 AKST (0531 UTC) there are 26 groups of events that correlate with Anchor Point. During this period only 573 events out of about 810,000 were correlated between the stations. The 810,000 events can be compared to the background of about 140,000 noise events in the same interval 10 minutes earlier. The correlated events are thought to be due to lightning higher up in the eruption column. The first lightning that is seen at both Homer and Anchor Point occurred much earlier, at 20:25:48.8 AKST (05:25:48.7 UTC), and was associated with the first phase of the explosion that began at 2024 AKST (0524 UTC). These lightning flashes have short durations (less than about 0.1 sec) and are few in number; we call these near-vent lightning.

Several minutes after the explosive phase signals ended (2033 AKST (0533 UTC)), there was a sequence of about 300 well-defined lightning discharges that continued for about 11 minutes (20:34:11 to 20:45:31 AKST (05:34:11 to 05:45:31 UTC); fig. 7). We believe that most of these were in the plume as the time differences slowly became smaller indicating a movement to the south in accordance with the wind direction and with radar images of the plume (Schneider and others, 2006). The transverse position of each source is shown in figure 8. The difference in the time of arrival of each correlated event gives the direction to the event, which can be translated to the distance from the summit of Augustine Volcano perpendicular to the

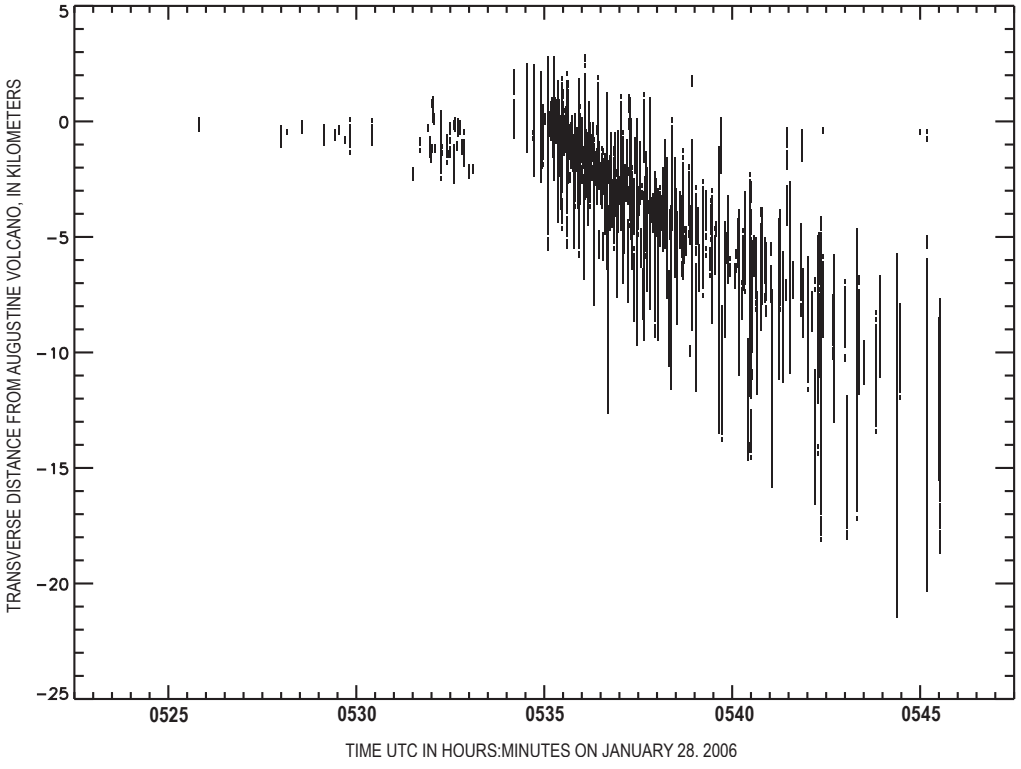

Figure 8. A plot of the transverse position of all the correlated points versus time. The position transverse to the line of sight at Augustine Volcano is found from the difference in the arrival times at the two stations and the distance to Augustine. During the explosion all the points are close to Augustine Volcano. After the explosion ended the location of the lightning drifted to the southeast. The transverse position is the distance from Augustine Volcano in a horizontal direction perpendicular to the line-of-sight from the station at Homer, about north-south. The dates and times in this plot are in universal time (UTC).

line of sight. It can be seen that during the explosion all the events are within 2 km of the volcano. After the explosion ended, the lightning is seen to drift to the south-east during this plume phase.

One of the final discharges lasted 650 ms and had a transverse extent of 15 km, extending to 22 km away from the volcano (fig. 9). The discharges undoubtedly occurred within the volcano's plume, which reached an altitude of 8 to 10 km. Hence we term this plume lightning. The lightning in both figures 8 and 9 undoubtedly also moved along the line of sight both toward and away from us. We were very fortunate that the movement of the plume and its elongation by the winds were mostly perpendicular to the line-of-sight.

The raw data for a plume lightning flash that occurred about a minute earlier are shown in figure 10. The format is similar to that of the thunderstorm flash of figure 5. Similar to the thunderstorm flash, numerous branches are observed, and both impulsive and continuous phases were present. The top panel of figure 10 shows the transverse source positions inferred from the differences in arrival times. The noisy background is a due to correlations which include a noise point at one of the stations which result in a time similar to the difference expected for events in the vicinity of Augustine. These noise correlations are easily removed, and the remaining points are assumed to be correlated.

Seismic and Acoustic Data

The relative timing between the signals from lightning (and other electrical activity) and the explosion as seen by the seismic and acoustic signals is key to understanding the mechanism for the production of lightning. In figure 11 lightning, seismic, and acoustic data are compared. The measured times are displayed, and signal propagation delays must be considered when comparing the two types of data. The lightning signals travel at the speed of light, which produces a delay of about 0.3 ms. The seismic signals travel at about 3 km/s, which produces delays of about 1.1 sec for the signals measured at Augustine Volcano and 6 sec for the signal measured at Oil Point (OPT). The acoustic signals travel more slowly in the air (about 330 m/s), resulting in a 10 s delay. All these delays are small compared to the time resolution of figure 11 and can be ignored here, but will be important for comparisons discussed later. The seismic signals from some of

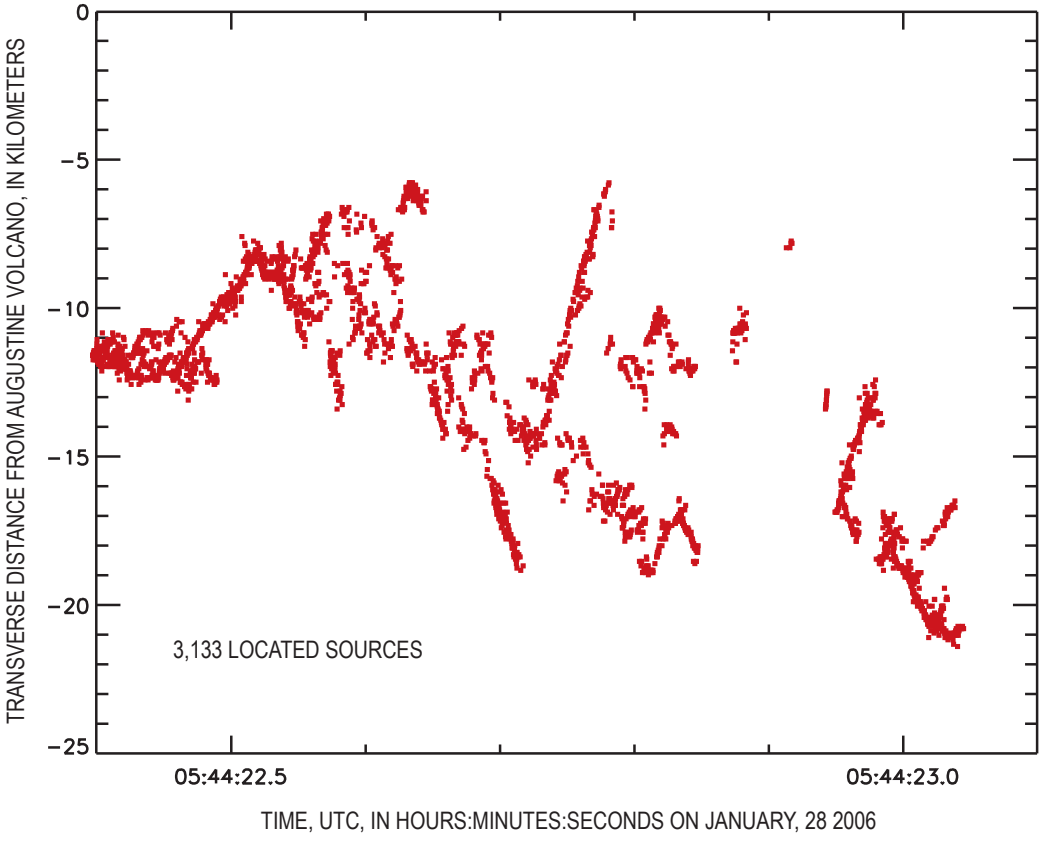

Figure 9. A plot showing the transverse position of the located points of single lightning flash near the end of the plume lightning on January, 27 AKST (January 28 UTC), 2006, during the eruption of Augustine Volcano. The transverse position shows it started about 12 km from Augustine and initially moves toward it. Later branches were as far as 21 km away from the volcano. The dates and times in this plot are in universal time (UTC).

the Augustine instruments saturated during the explosion. The seismic signal from Oil Point did not saturate, and making it suitable to compare seismic amplitudes with lightning signals throughout the explosion (Augustine station AU14 did not saturate and is very similar to that at OPT , see figure 4*B* in McNutt and others, this volume).

The seismic data indicate that the explosion lasted about 11 minutes, from 2025 to 2035 AKST (0524 to 0535 UTC), with a particularly energetic explosive pulse between 20:31 and 2033 AKST (0531 and 0533 UTC). A smaller explosive event occurred at about 2028 AKST (0528 UTC). An enhancement in the lightning background signal is observed at this time. These correlations in time and the similarities in the shapes in intensity are good evidence that the vent discharges are a result of small discharges occurring within the superheated ejecta as it exits the volcano. It also suggests that the number of discharges and their RF power is in some manner proportional to the explosion intensity. Further evidence of such vent discharges is shown by a spectacular photograph published in the September 2007 National Geographic (Grunewald, 2007). This time exposure of an eruption at Tavurvur Volcano, Papua New Guinea, shows about a dozen small electrical discharges that are spread throughout the ejecta. Most of these discharges are tens of meters long

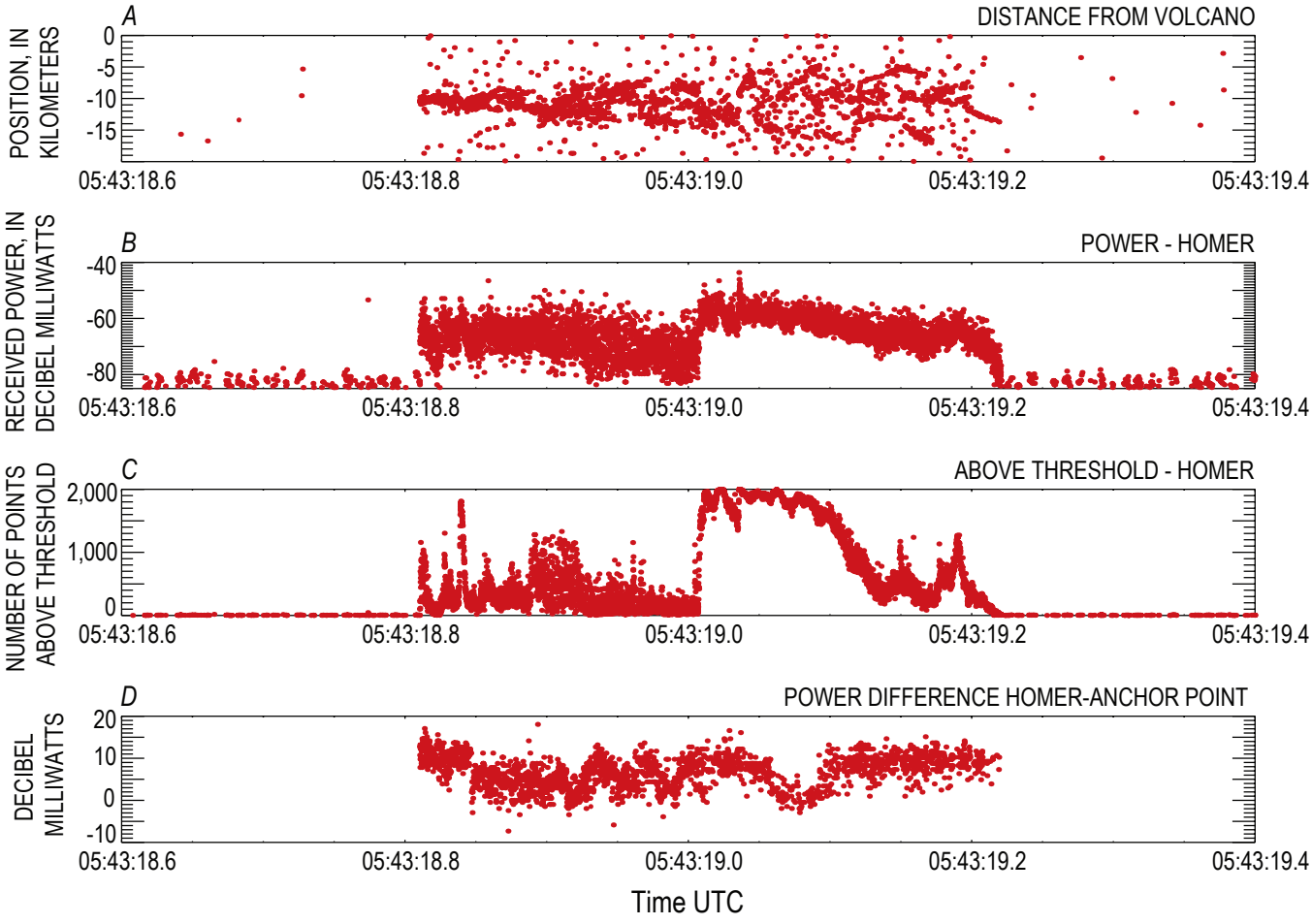

Figure 10. A set of plots showing how another flash from the plume phase evolves on January, 27 AKST (January 28 UTC), 2006, during the eruption of Augustine Volcano. It occurred about a minute before the one in figure 9. The format is similar to that of the thunderstorm lightning in figure 5. For the first 0.1 second the signals are just continuous enough to make the above threshold points reach values of several hundred. For the second 0.1 second the signals are more impulsive and the locations spread out. Beginning at 19.0 s the signals become very continuous and more powerful. In the top three panels all the raw data are included. The transverse positions (top panel) are a linear function of the arrival time differences at the two stations. The top panel also includes a noise background caused by one or both of the sources being a noise source. In the previous figure the noise points were removed by keeping only points that are in clusters. The lowest panel is the ratio of power measured in each station. Because the power is measured on a logarithmic scale the ratio is found by differencing the two measurements. The dates and times in this plot are in universal time (UTC).

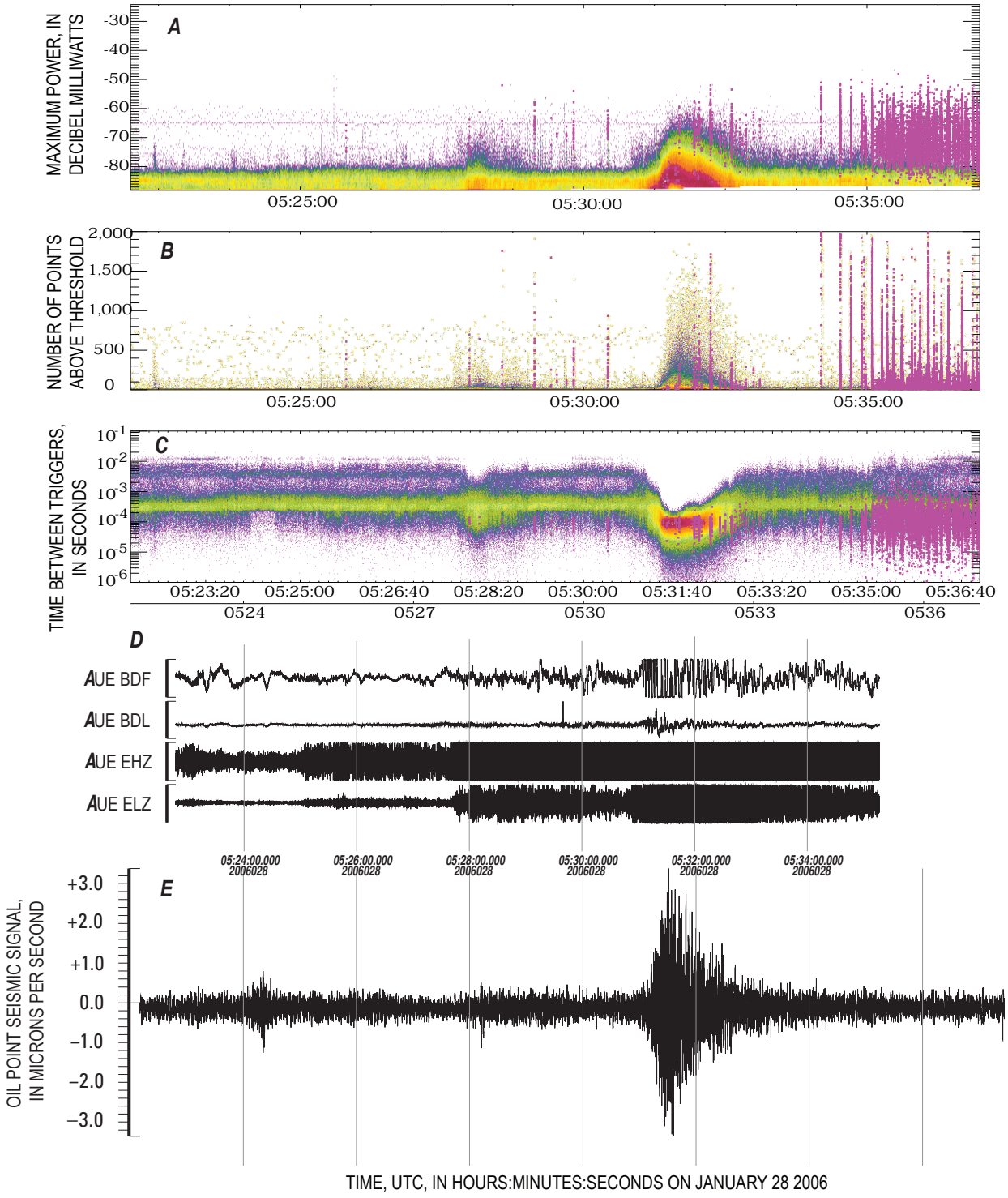

Figure 11. Seismic and acoustic data for the Augustine Volcano on January 27 AKST (January 28 UTC), 2006, are added to the plots of figure 7. The measured times for all the signals are aligned in this and following figures. Acoustic signals are from stations referred to as AUE BDF (high gain) and BDL (low gain). Seismic traces are from stations referred to as AUE EHZ (high gain) and ELZ (low gain). Station AUE is located 3.5 km east of Augustine Volcano's vent. The lowest trace is the seismic signal from Oil Point, about 34 km north of the volcano. The power, the number of points above threshold, and the time between peaks are shown in parts *A*, *B*, and *C* as density plots; the color indicates the number of events with red being the most and blue-purple the least. Units for acoustic and seismic data in part *D* are the same as shown in figure 17. The dates and times in this plot are in universal time (UTC).

and occur within a few tens of meters of the vent. Such small structures are compatible with our observations at Augustine, even though the details of the eruptions may differ.

LMA as an Interferometer

The station near Homer, on a bluff 220 m above the Cook Inlet, received radio signals directly from the lightning sources above the volcano and from their reflections off the sea surface. Because the reflected signal traveled slightly farther, the two signals were out of phase with each other when detected by the Homer station. Although we did not plan for or anticipate the effect, once recognized it allowed us to determine information about the altitudes of the sources. The same effect has been used by radio astronomers to infer the location and structure of astronomical radio sources (Bolton and Slee, 1953). Because the difference in path length varies with the altitude of the source, the interference pattern depends on source altitude. A path length difference that is exactly an integral number of wavelengths will result in constructive interference, whereas a path length difference of N + ½ (a phase change of π) will result in destructive interference. These effects were clearly present for a radiation burst at 20:32:14 AKST (05:32:14 UTC), during the main explosion.

Figure 12 shows how the Homer station functioned as a sea interferometer. The relatively simple discharge at 20:32:14 AKST (05:32:14 UTC) (a near-vent flash) produced received power values versus time that showed clear evidence of interference fringes. The raw data for this flash are shown in figure 13. Figure 13*A* shows the arrival time differences. The points due to the flash are tightly clustered while those associated with noise in one or both stations are scattered randomly, which illustrates how we identify our "correlated" events. Panels B and C show the received power of all points at the two stations.

While most of the high power points are from lightning, some of the high power points are due to weak local sources close to the station's antenna. The correlation allows us to reject high power noise points and identify weak lightning

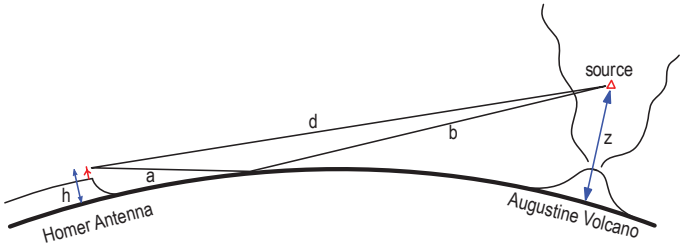

Figure 12. A diagram of the "sea-surface" interferometer. Signals could reach the antenna at the Homer station after bouncing off the water of Cook Inlet. Because the length of the two signal paths were slightly different the two signals interfered with each other depending on the altitude of the source. (From Thomas and others, 2007.)

events. To remove the effect of variations in the source power itself, the Homer power values were referenced to those of the same events at Anchor Point, which did not experience interference effects (fig. 14*C*). With the noise removed, the variations in the power ratio clearly show an interference effect.

The predicted interference pattern is shown in figure 14*D* along with the results of fitting the measurements to the predicted pattern. To obtain the predicted pattern it was necessary to take into account the curvature of the Earth, as well as the fact that seawater is a reasonably good conductor, with a phase shift close to π on reflection. Because of the extreme grazing nature of the reflections (the incidence angle varied between ~0.5 and 2.0 degrees from horizontal for the discharge of figure 12), the path length difference for the direct and reflected signals was only about 0.6λ for signals originating at Augustine's summit (1,260 m altitude) and increased at a rate of about 0.9λ per kilometer above Augustine. Thus, in going ~2 km upward, the discharge at 20:32:14 AKST (05:32:14 UTC) showed two complete interference fringes (fig. 14*D*).

Several steps were taken to fit the observed data to the predicted values. First, the logarithmic power differences needed to be shifted downward by 15 dB to compensate for the attenuation of the Anchor Point signals. Second, to match the depth of the interference minima, the reflection coefficient of the sea surface was adjusted to an effective value of 0.7 (versus 1.0 for an ideally smooth conducting surface). Finally, a piecewise-linear approach was used to map temporal intervals in the observed data to spatial intervals on the predicted interference fringes (figs. 14*A*, *C*). To accomplish this, a particular set of points in the temporal data was assumed to originate at heights that gave reasonable "eyeball" fits between the observed and predicted power values. The resulting time-height conversion (fig. 14*B*) was then used to convert the transverse distance versus time data of figure 14*A* to a 2-dimensional vertical projection plot.

Figure 15 shows the resulting vertical projection of the flash. The discharge appeared to begin about 250 m above Augustine's summit and progressed upward and leftward (southward) along a single, 4-km long path. The average speed of progression was about 0.7×10^5 m sec^{-1} vertically and about 1×10^5 m sec^{-1} overall in the transverse plane. Such propagation speeds are characteristic of negative polarity breakdown propagating toward or through net positive charge (Behnke and others, 2005). Lightning emits radio frequency radiation primarily from developing negative-polarity breakdown, which propagates into positive charge regions, rather than from positive breakdown, which propagates into negative charge regions. The upward radiation sources of figure 15 are similar in character to the initial breakdown observed in intracloud discharges in thunderstorms, which are of negative polarity and propagate into and through regions of net positive charge (for example, Behnke and others, 2005). (The propagating radiation segments seen in figures 9 and 10 are also produced by negative breakdown through positive charge regions.)

The origin of the upward discharge in figure 15 is only an apparent location that corresponded to the time that the

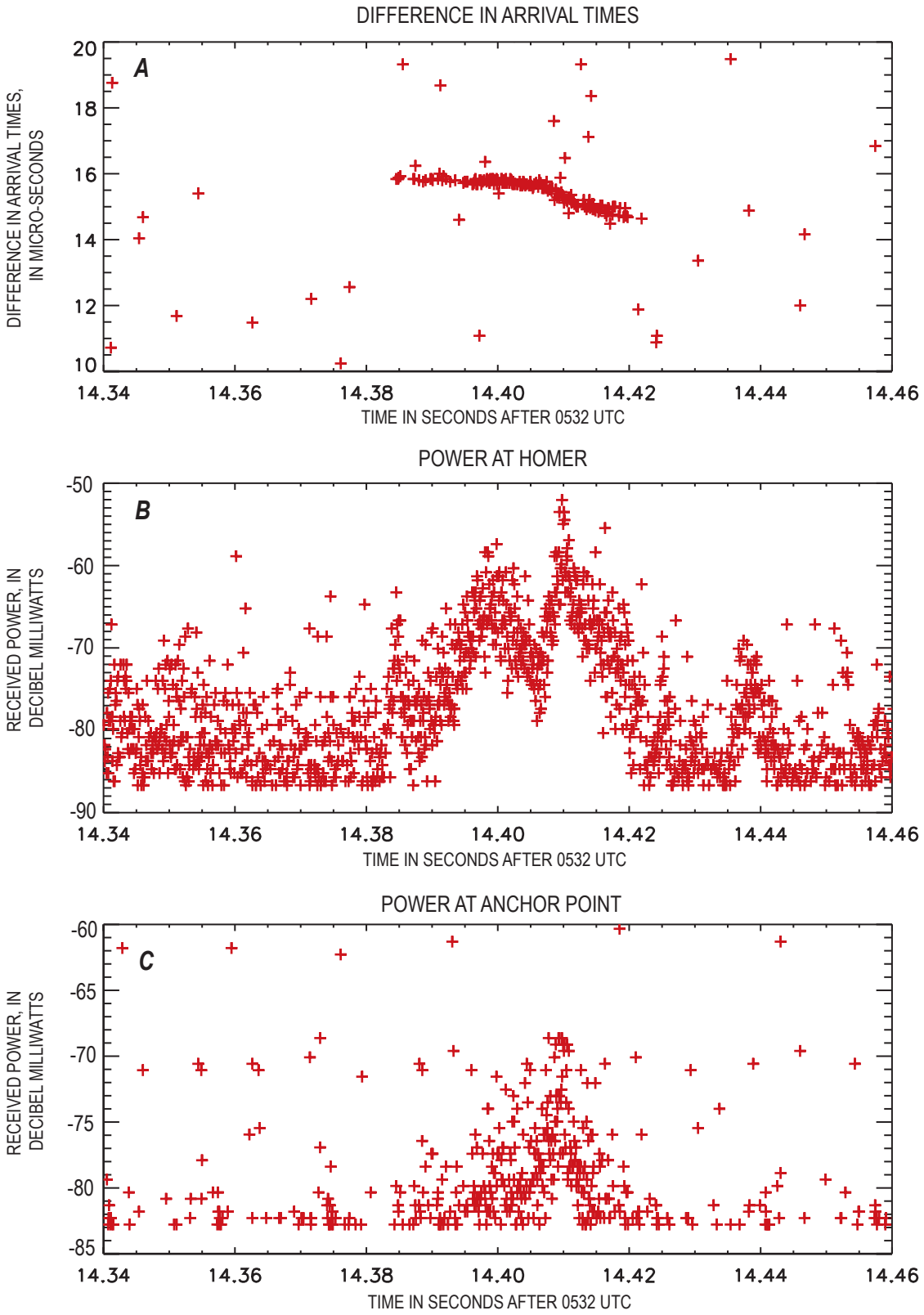

Figure 13. Plots of the raw data from a small lightning flash during the main explosion of the Augustine Volcano at 2032 AKST on January 27 AKST (0532 on January 28 UTC), 2006. All the measured power values are shown for the Homer and Anchor Point stations. The Anchor Point station is less sensitive as it is inland about 1.5 km. The power varies differently at each station. The dates and times in this plot are in universal time (UTC).

sources from the flash were strong enough to be detected by the Anchor Point station. The single-station power data from Homer show clear evidence of propagating breakdown prior to signals being detected at Anchor Point, indicating that the discharge began at lower altitude, almost certainly on the ground in the vicinity of the summit. Because the choice of the initial fringe is ambiguous, we cannot strictly rule out the possibility that the discharge began an integer number of fringes higher in altitude. However, this is considered unlikely in view of the above physical interpretation of the observations. There is also an ambiguity as to whether the discharge developed downward or upward, but this is readily resolved from the fact that downward development would give a physically incorrect picture of the discharge relative to the plume.

No cloud-to-ground discharges were detected by the BLM Alaska Lightning Detection System during the January 27–28 explosions. Upward-initiated discharges from the ground would not be detected by the BLM system because such networks locate the strong "sferic" produced by return strokes initiated by downward leader breakdown (Cummins and others, 1998). Low-frequency lightning location networks occasionally detect intra-cloud flashes, as the BLM network did for January 13 explosion. The BLM network detected cloud-to-ground discharges only during the early January explosions—one that

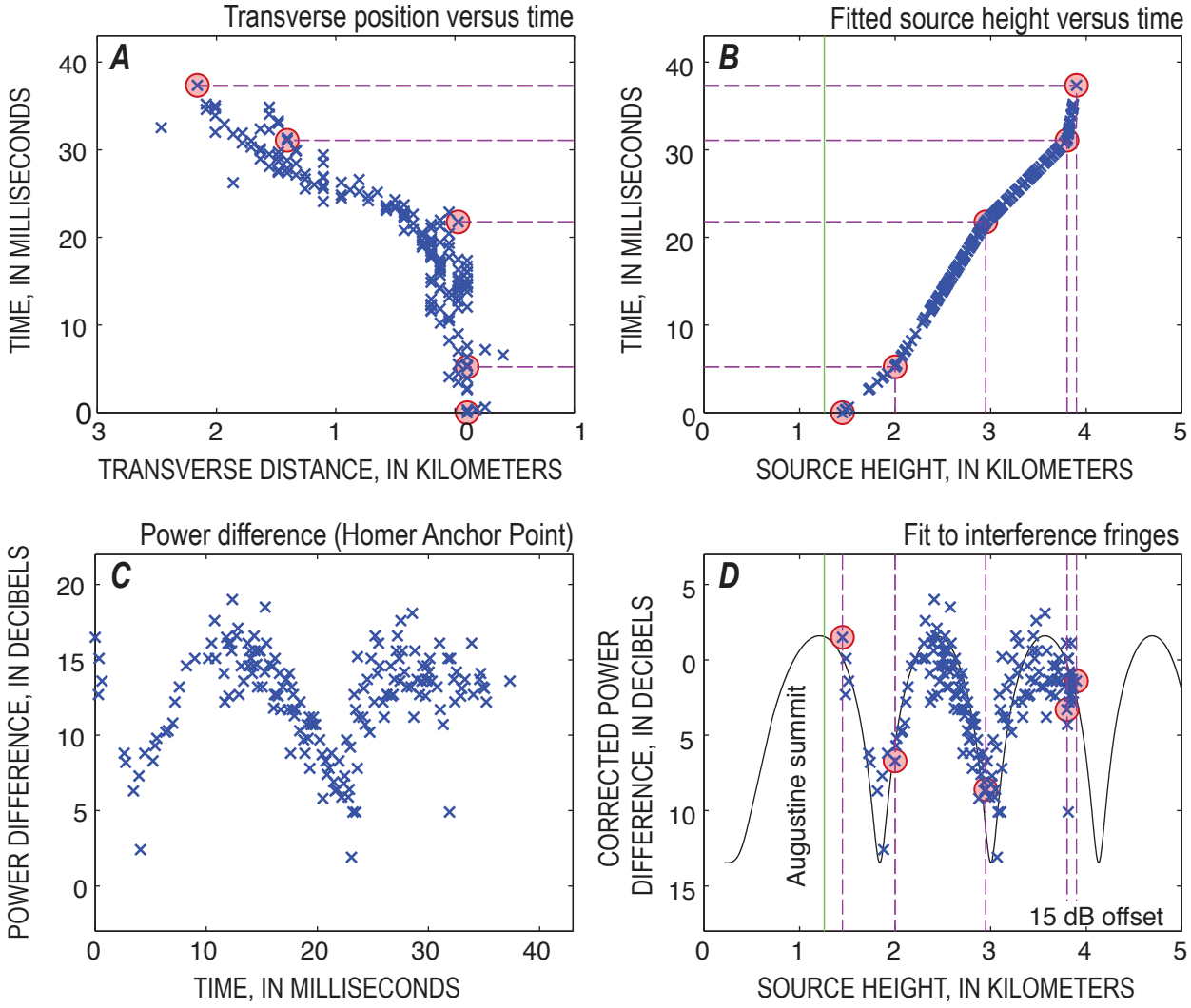

Figure 14. Four plots showing how the interference pattern is deciphered. This pattern is from a small lightning flash during the main explosion of the Augustine Volcano at 2032 AKST on January 27 AKST (0532 on January 28 UTC), 2006. *A,* Transverse distance versus time. *B,* Fitted source height versus time. *C,* Power difference between Homer and Anchor Point versus time. *D,* Corrected power difference versus height with interference fringes also shown. The pink circled points and dashed lines indicate breaks in the piecewise-linear fits. (from Thomas and others, 2007).

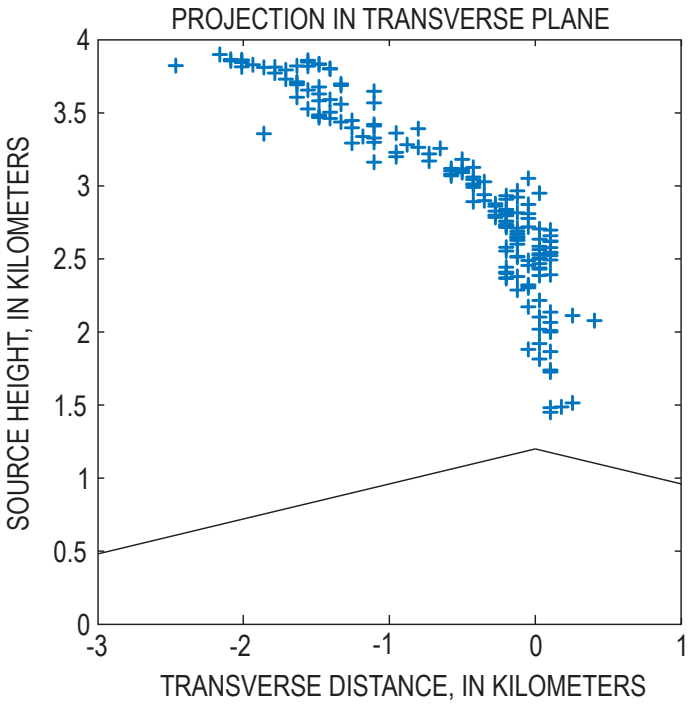

Figure 15. Plot showing the path of the lightning channel above Augustine Volcano. This lightning occured during the main explosion of the Augustine Volcano at 2032 AKST on January 27 AKST (0532 on January 28 UTC), 2006. The lightning began at the summit of Augustine and went up and then to the southeast where the wind was moving the plume. The volcano is represented by a simple line drawing. (from Thomas and others, 2007).

lowered positive charge to ground during the initial explosion (January 13 at 0424 AKST (1324 UTC); table 1), and one that lowered negative charge to ground during a later explosion (January 14 at 0014 AKST (0914 UTC)).

Flash Durations

Various aspects of the flash durations are plotted in figure 16. Initially the flashes lasted only a few milliseconds (fig. 16*A*); these are near-vent lightning discharges. During the explosion they increased in length to about 70 milliseconds. With a typical velocity of 10^5 m/s this implies a total length of less then 7 km. During the main eruptive phase, many of the flashes in the plume last several hundred milliseconds. During the initial part of this phase there are many fast small flashes, but their numbers decrease with time. figure 16*B* shows that most of the small flashes appear to be near the volcano vent, most likely in the rising plume column. Initially the flashes are separated by 10 or more seconds (fig. 16*C*), similar to what is seen in a small thunderstorm. As the plume lightning begins at about 2035 AKST (0535 UTC) the rate is more than 5 flashes per second. Such high rates are generally seen only in large thunderstorms, such as those produced by meos-scale systems in the Great Plains (MacGorman and Rust, 1998). At the end of the plume lightning phase the flash rate is typical of rates observed in similar sized thunderstorm in New Mexico. Interestingly, the number of points per millisecond seems to increase with the flash size (fig.16*D*).

Explosion at 2337 AKST on January 27, 2006

A very short and impulsive second explosion on this day occurred at 2337 AKST on January 27, 2006 (0837 UTC on January 28). Infrasound measurements show a short burst (20 s) with the highest peak acoustic pressure (105 Pa) for the entire eruption [Peterson and others, 2006]. The plume height was estimated to be 3.8 km (Schneider and others, 2006). Lightning, infrasound and seismic data are shown in figure 17. Both the signals from the electrical and acoustic sources begin very abruptly and last about 20 seconds. Because both the signals began so quickly their onsets can be determined to $\pm$0.1 seconds. Using the time delay for the acoustic signal from Peterson and others (2006) of 9.4 s would indicate that the electrical activity began about a second before the acoustic signal. However, Peterson and others (2006) based their acoustic delay on an assumed atmospheric acoustic velocity of 340 m/s, which is velocity at room temperature. Correcting the velocity to a temperature of –10°C indicates that the onset of both signals was simultaneous within the measurement error of 0.1 s. This supports the argument that electrical activity is generated at the vent of the volcano and is produced by the high velocity ejecta. Both the electrical and acoustic signals indicate activity above ground. The strong seismic signal of the main event appears to begin several seconds before indicating the beginning of the explosion, deeper in the vent. A small seismic subevent began about 15 s before the main phase (fig. 17).

Plots of the electrical activity recorded at the Homer station (fig. 18) show about 10 vertical lines consistent with small lightning flashes. Only one of these flashes, a 10-ms-long flash at 23:38:19.36 AKST (08:38:19.36 UTC on January 28), correlated with signals at Anchor Point. Using an average velocity of lightning of about 10^5 m/s, we can estimate a length of 1 km for this flash. This indicates that the flash is near-vent lightning. It can be seen that there are very few vertical lines both before and after the minute of eruptive activity (fig. 18). Thus, it is very likely that the vertical lines during this period were produced by other small near-vent lightning flashes (lasting 5 to 10 ms).

A summary of parameters for the various types of lightning and electrical activity is given in table 2 for all the events in this study.

Table 2. Summary of lightning parameters measured by the Lightning Mapping Array for the Augustine Volcano eruptions in January 2006.

Date January 2006	Time UTC	Plume Height (km)	Vent Discharges		Near-Vent Lightning			Plume Lightning		
			Max power (dBm)	Duration (sec)	Number of flashes	Duration (min)	Delay (sec)	Number of flashes	Duration (min)	Delay (sec)
28	0524	10.5	-50	120	22	7.4	108	300+	11.4	10.5
28	0837	3.8	-70	20	1	-	42	0	-	-
28	1104	7.2	-65	30	28	1.2	60	0	-	-
28	1642	7.0	none	-	6	2	300	0	-	-
29	0040	3.8	none	-	35	18	n.a.	0	-	-
29	2019	7.2	-65	120	2	0.05	118	0	-	-
30	1228	7.2	-70	132	0	-	-	0	-	-
30	1522	7.2	-72	25	2	0.1	25	0	-	-

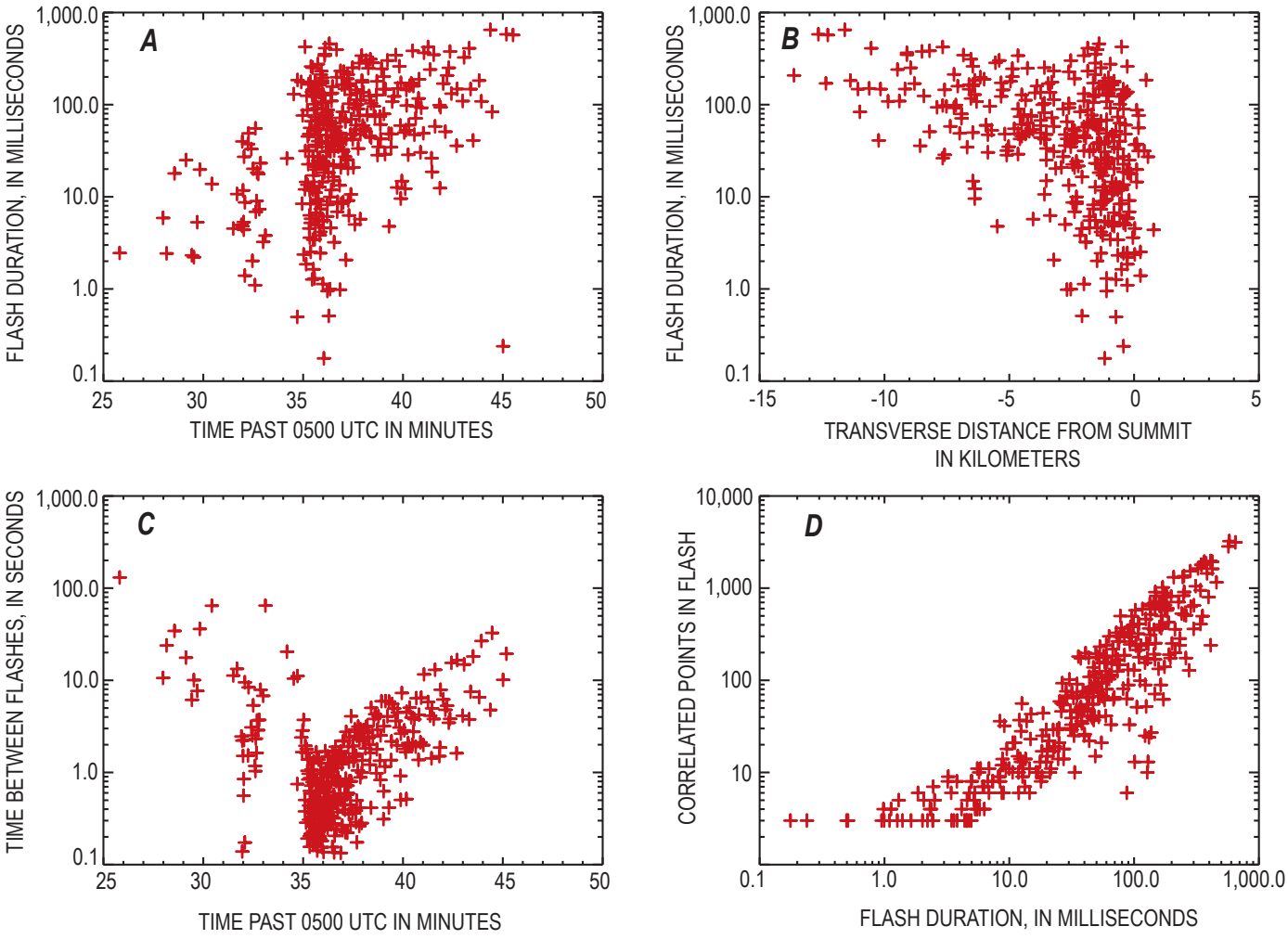

Figure 16. Plots showing the flash durations as a function of other parameters for the Augustine Volcano eruption on January 27 AKST (January 28 UTC), 2006. The panels show (*A*) the duration of each flash versus time, (*B*) the duration versus position, (*C*) the separation of flashes versus time, and (*D*) number of points in the flash versus duration. The dates and times in this plot are in universal time (UTC).

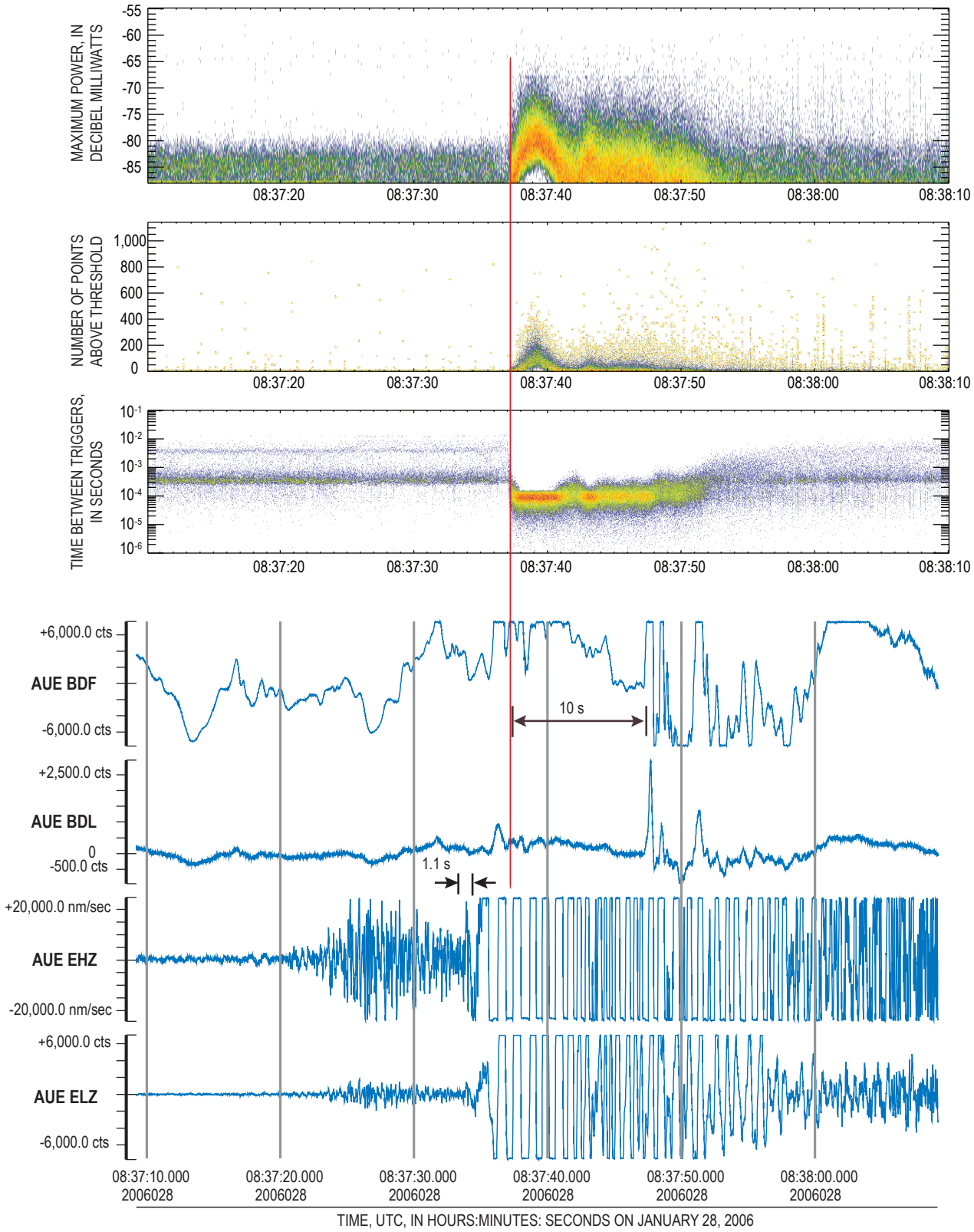

Figure 17. Plots of the data from Augustine Volcano's explosion at 2337 AKST on January 27 (0837 UTC on January 28), 2006 showing lightning mapping, seismic, and acoustic signals. When the acoustic travel time of 10 seconds is taken into account the beginning of the electrical and acoustic signals are coincident (vertical red line). Upper three panels show electrical data and lower four show acoustic and seismic data. See figure 11 caption for details. The dates and times in this plot are in universal time (UTC).

Explosion at 0204 AKST on January 28, 2006

The explosion at 0204 AKST (1104 UTC) on January 28, had smaller acoustic and seismic amplitudes than the previous two events. The peak acoustic pressure was 66 Pa and the plume height was 7.2 km. The seismic duration was longer than the 2337 AKST (0837 UTC) event but shorter than the 2024 AKST (0524 UTC) event (Petersen and others, 2006; McNutt and others, this volume). The data in figure 19 show similar behavior in the electrical, acoustic, and seismic signals. As in the previous explosions, we see both continuous background activity due to vent discharges and correlated signals indicating the development of lightning channels upward into the erupting column. All the correlated lightning appears to be near-vent lightning.

Figure 20 shows that most of the flashes lasted less than 10 ms and, therefore, had lengths of less than a km. A few could have been several km long. These are similar to the events in the first few minutes of the 2024 AKST (0524 UTC) explosion (fig. 16) that occurred before the plume lightning began at 2034 AKST (0534 UTC).

Explosion at 0742 AKST on January 28, 2006

The explosions at 0742 AKST (1642 UTC) on January 28, was smallest of the four explosive eruptions of this day in terms of the acoustic and seismic amplitudes (Petersen and others, 2006; McNutt and others, this volume). The duration (see fig. 21) was similar to the 0242 AKST (1104 UTC) event and was much longer than the earlier 2337 AKST (0837 UTC) event. This explosion began with a weak phase at 0742 AKST (1642 UTC), followed by a stronger phase starting at 0748 AKST (1648 UTC). We did not see the enhanced radiation

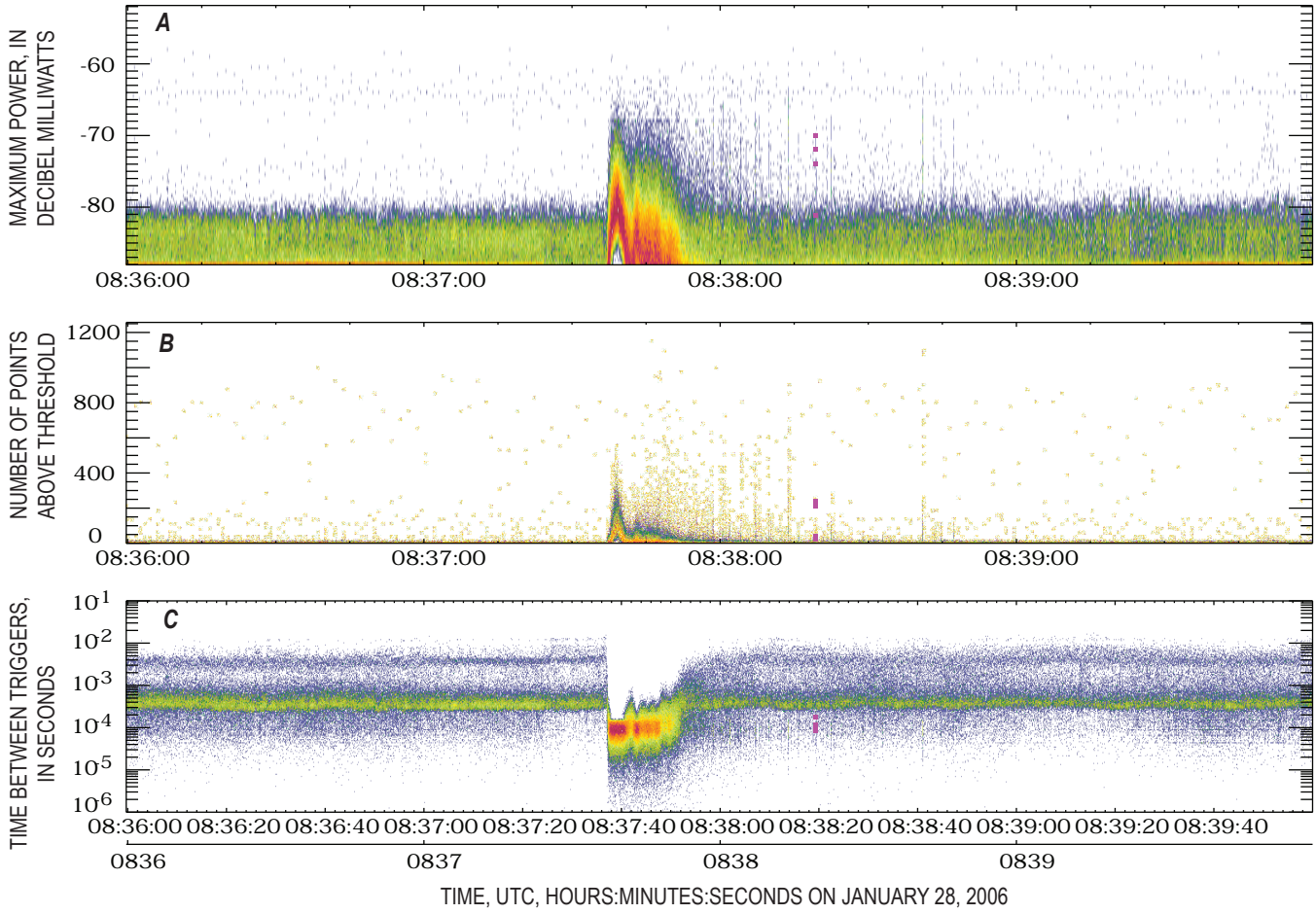

Figure 18. Data from Augustine Volcano's explosion at 2337 AKST on January 27 (0837 UTC on January 28), 2006. Because the background is small (easiest to see in panel *B*) both before and after the explosion, the vertical lines of signal points are probably small lightning flashes. See the captions of figures 6 and 7 for details. The dates and times in this plot are in universal time (UTC).

from electrical activity at the vent, but there were 6 small lightning flashes with correlated points. Most of the lightning occurs just before the major seismic event; this suggests it is near-vent lightning caused by the initial 0742 AKST (1642 UTC) event. It also implies that the large phase at 0748 AKST (1648 UTC) may have been mostly gas with little tephra. Figure 22 shows that all the flashes were very small and of short duration, similar to the near-vent lightning flashes associated with the other three explosions on January 28, 2006.

Lightning and Vent Discharges during the Continuous Phase on January 29 and 30, 2006

The explosive phase of the eruption ended with the event on January 28 at 0742 AKST (1642 UTC). This was followed by a transitional event that began at 1430 AKST (2330 UTC)

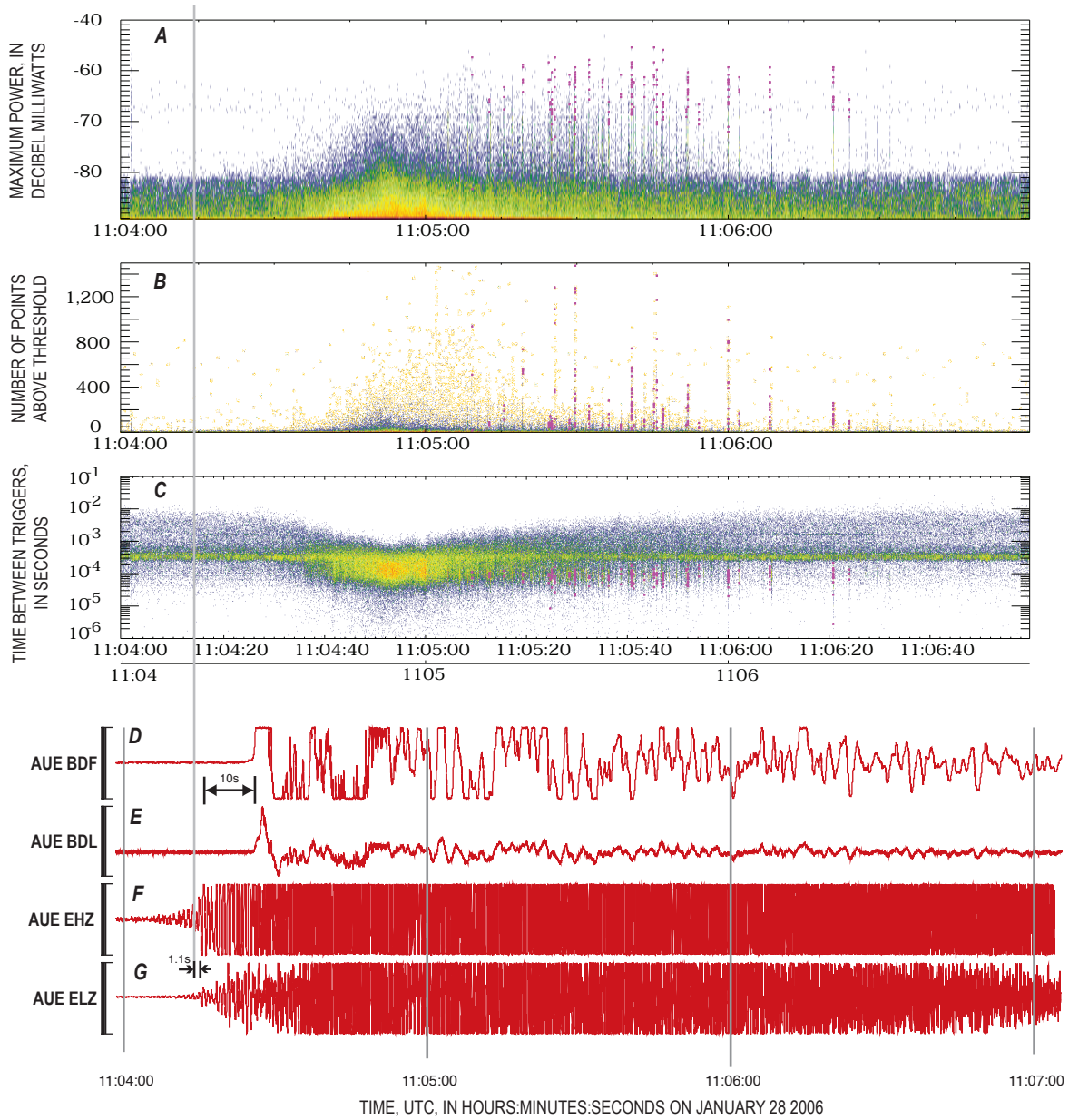

Figure 19. Data from Augustine Volcano's explosion at 0204 AKST (1104 UTC) on January 28, 2006. Panels *A* through *C* show electrical data, *D* and *E* acoustic data, and *F* and *G* seismic data. See figure 11 caption for details. Units for acoustic and seismic data in parts *D*, *E*, *F*, and *G* are the same as shown in figure 17. The dates and times in this plot are in universal time (UTC).

on January 28 (McNutt and others, this volume) and signaled the beginning of the continuous phase. The continuous phase was characterized by many small explosions that occurred a few minutes apart, so that ash was in the air continuously for several days. During this continuous phase, several larger explosions occurred. These were smaller than all 13 of the numbered explosive events (Petersen and others, 2006) but were larger than the small events that occurred every few minutes. Lightning was associated with several of these moderately large explosions.

Between 1540 and 1600 AKST on January 28 (0040 UTC and 0100 UTC on January 29), we saw electrical signals from about 28 lightning discharges (fig. 23). These occurred late during the transitional explosive event that began at 1530 AKST on January 27 (2330 UTC on January 28). This event had a seismic and acoustic duration of about 1 hr 45 min, and moderate amplitudes (McNutt and others, this volume). The lightning rate is much smaller here than in the previous events. Many of these flashes are as large as those in the big explosion at 2031 AKST on January 27 (0531 UTC on January 28), with 6 flashes lasting between 20 and 80 ms each (fig. 24). Several

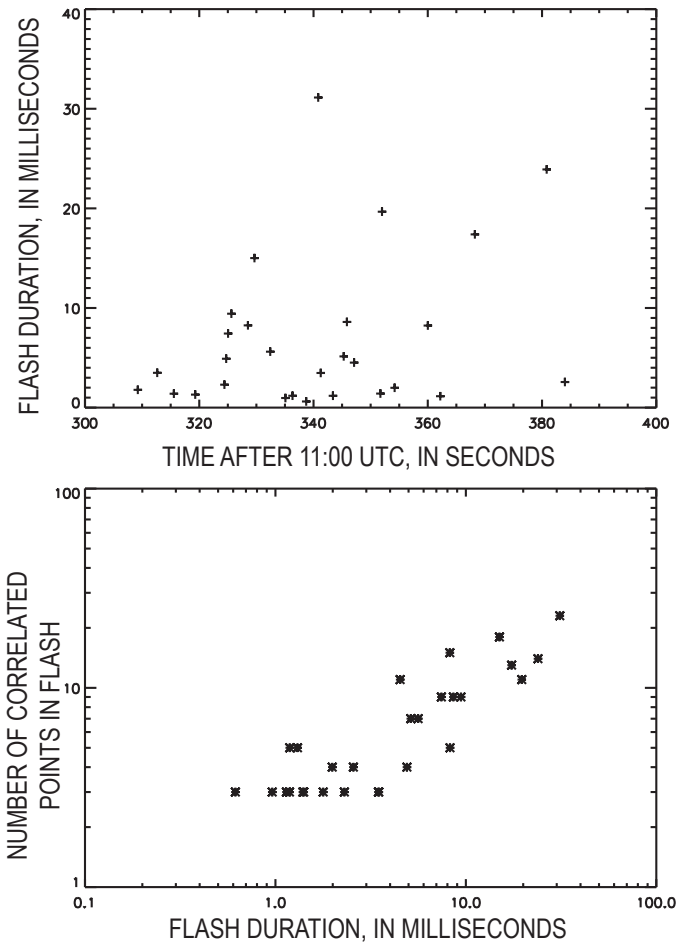

Figure 20. Durations of flashes during the 0204 AKST (1104 UTC) explosion of Augustine Volcano on January 28, 2006. The dates and times in this plot are in universal time (UTC).

of these show interference patterns and altitude analysis may be possible. Thus, we interpret the lightning to be composed of upward propagating near-vent flashes. The total number of flashes was small presumably because the amount of tephra and height of the ash column were smaller than the 2031 AKST, January 27 (0531 UTC, January 28), explosion. Radar data indicate that the ash plume height was about 3.8 km during this event (Schneider and others, 2006).

On January 29 between 11:19:30 and 12:21:18 AKST (20:19:30 and 21:21:18 UTC) (fig. 25) there was an increased electrical background signal similar to that seen during the explosive eruptions. At the same time a large increase was seen in the radar reflectivity at 7.2 km, indicating an impulse of ash injected into the atmosphere (Schneider and others, 2006). Seismic and acoustic data indicate that a moderately strong explosive event began at 11:17:54 AKST (20:17:54 UTC) and lasted 340 s. The signals were strongest from 1119 to 1121 AKST (2019 to 2021 UTC), corresponding to the time of the continuous electrical signal. Two flashes of near-vent lightning occurred 2 minutes after the start of the continuous electrical signal. These were both short duration flashes. No plume lightning was observed.

On January 30 between 0128 and 0130 AKST (1228 and 1230 UTC) (fig. 26) there was an increased electrical background signal due to vent discharges, similar to that seen during the explosive eruptions. Seismic and acoustic data indicate an explosion starting at 1:25:18 AKST (12:25:18 UTC), strongest from 1:28:40 to 1:29:10 AKST (12:28:40 to 12:29:10 UTC), and lasting 340 s total. At the same time an increase was seen in the radar reflectivity at 7.2 km indicating an impulse of ash injected into the atmosphere (see Schneider and others, 2006). No near-vent or plume lightning occurred in association with this explosion.

On January 30 between 6:22:25 and 6:22:50 AKST (15:22:25 and 15:22:50 UTC) (fig. 27) there was another increased background signal similar to that seen during the explosive eruptions. Seismic and acoustic data show a moderate explosion beginning at 6:19:42 AKST (15:19:42 UTC) and lasting 290 s, strongest from 6:21:20 to 6:23:50 AKST (15:21:20 to 15:23:50 UTC). This event was less than half the amplitude of the 0128 (1228 UTC) event. At the same time an increase was seen in the radar reflectivity at 7.2 km indicating an impulse of ash injected into the atmosphere (Schneider and others, 2006). Two flashes of near-vent lightning occurred just after the continuous signal ended (table 2). No plume lightning was associated with this explosion.

Electrical Events in March 2006

During the dome building phase in March we had the two additional stations operating, one on West Island and one at Oil Point (fig. 1). During this time we found 6 periods where there were signals from two stations that were correlated. Almost all the correlations were between signals received at the Homer station and Oil Point. Figure 28 shows the possible

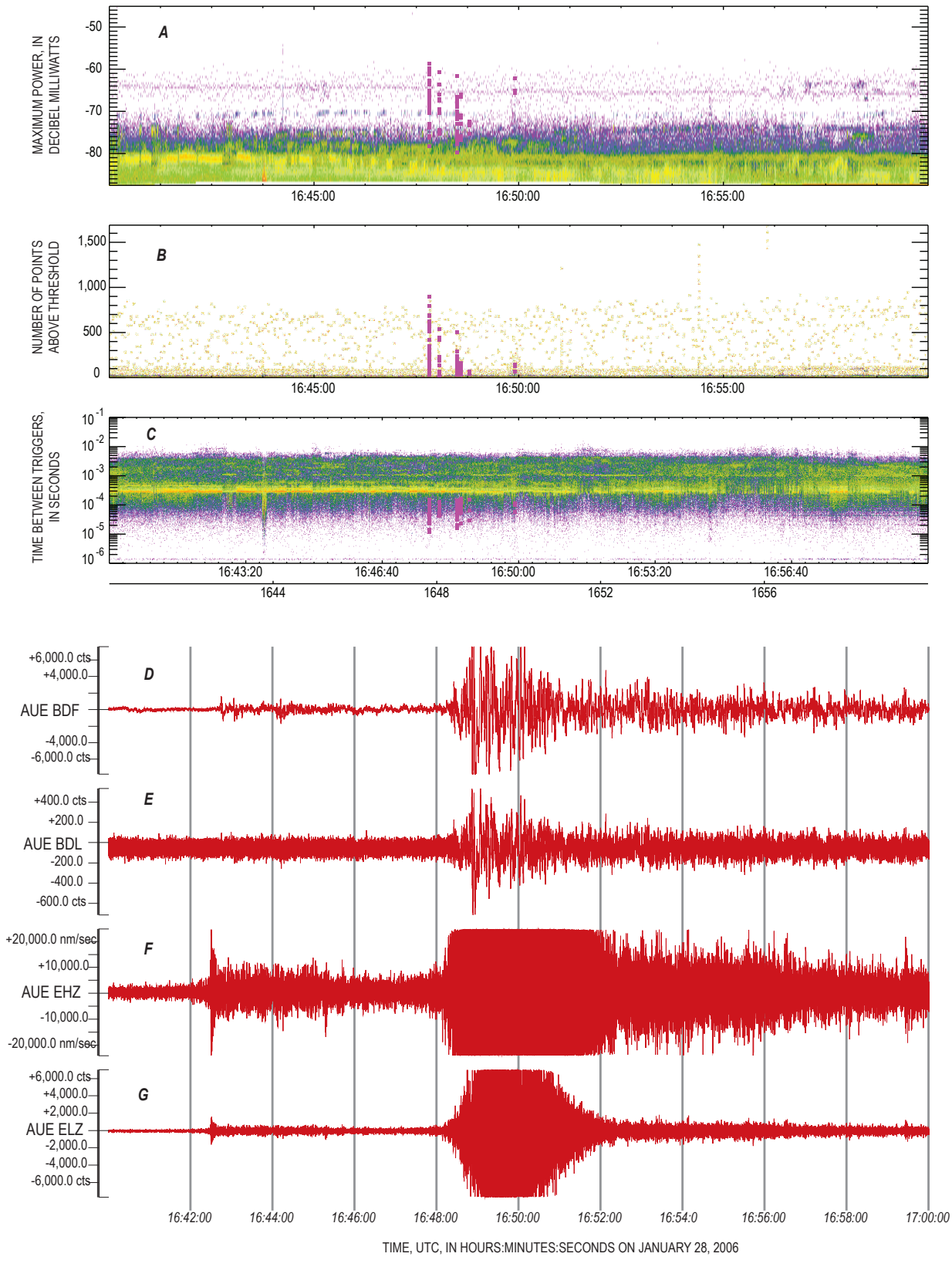

Figure 21. Data from Augustine Volcano's explosion at 0742 AKST (1642 UTC) on January 28, 2006. Panels *A* through *C* show electrical data, *D* and *E* acoustic data, and *F* and *G* seismic data. See figure 11 caption for details. The dates and times in this plot are in universal time (UTC).

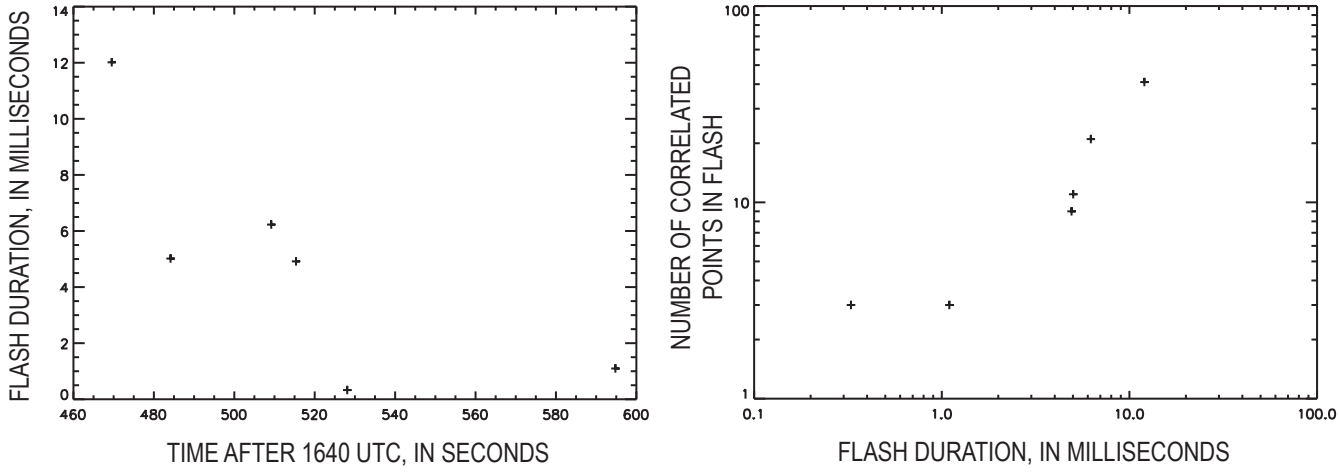

Figure 22. Durations of flashes during the 0742 AKST (1642 UTC) explosion of the Augustine Volcano on January 28, 2006. The dates and times in this plot are in universal time (UTC).

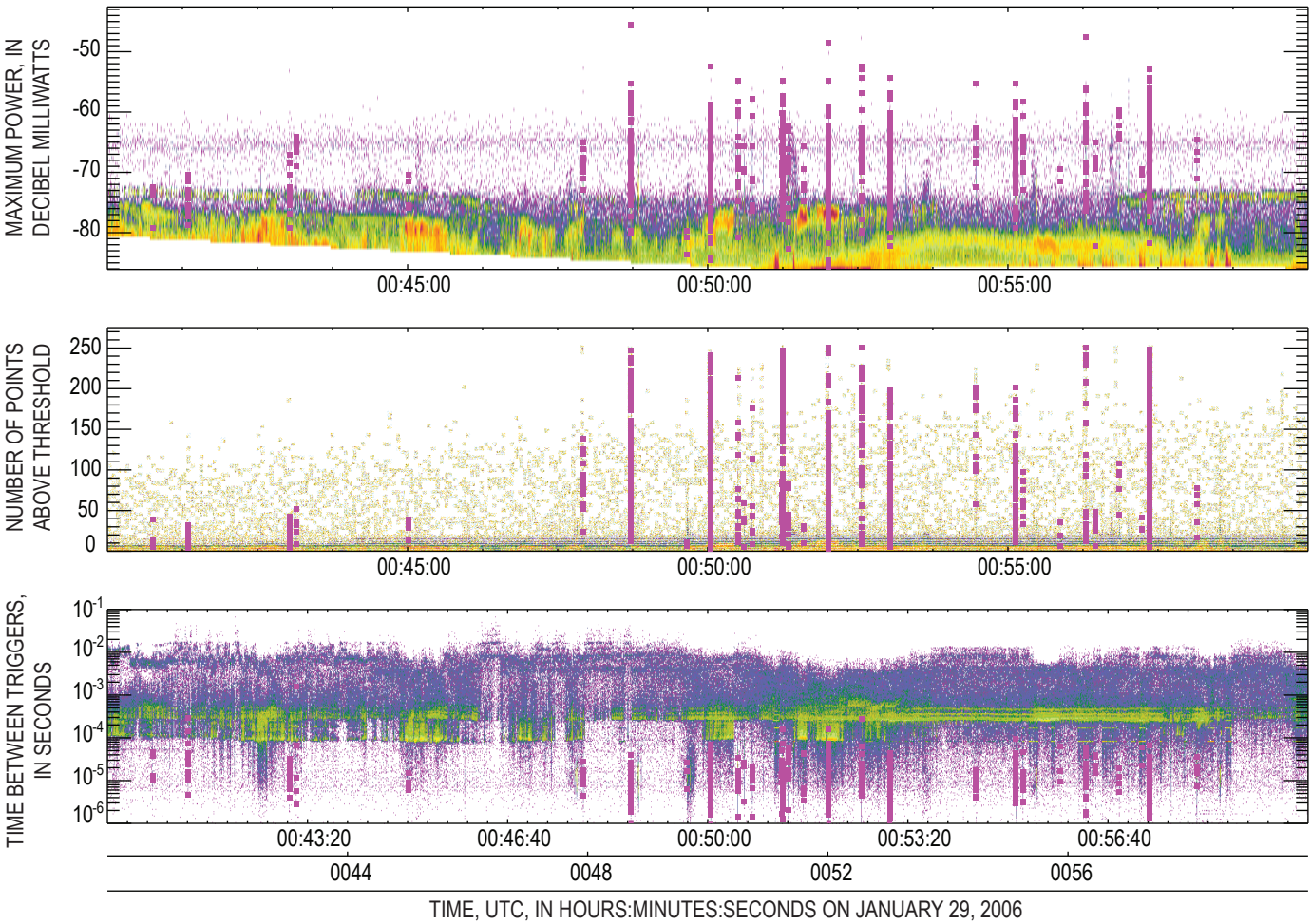

Figure 23. Lightning during Augustine Volcano's continuous eruptive phase, 1540 to 1600 AKST on January 28 (0040 to 0100 UTC on January 29). See the captions of figures 6 and 7 for details. The dates and times in this plot are in universal time (UTC).

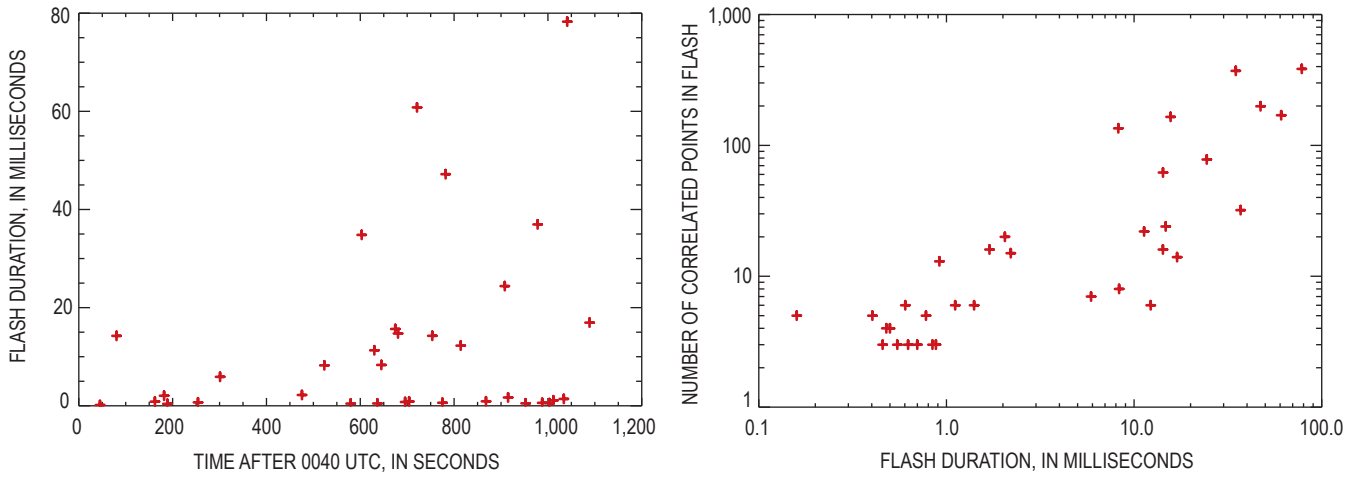

Figure 24. Durations of flashes between 1540 and 1600 AKST during Augustine Volcano's eruption on January 28 (0040 and 0100 UTC on January 29, 2006). The dates and times in this plot are in universal time (UTC).

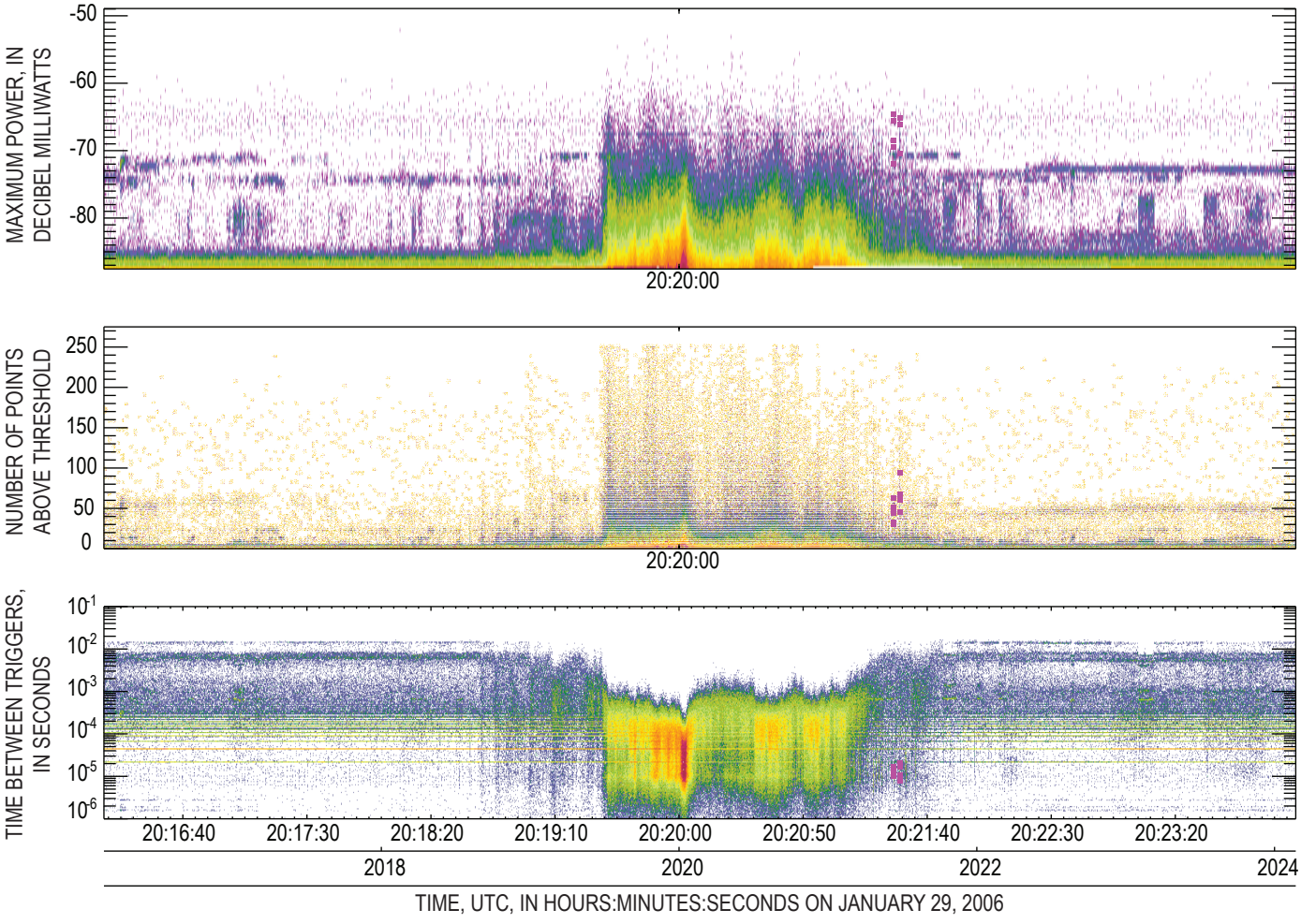

Figure 25. Lightning and electrical signals during Augustine Volcano's eruptive pulse at 1120 AKST (2020 UTC) on January 29, 2006. See the captions of figures 6 and 7 for details. The dates and times in this plot are in universal time (UTC).

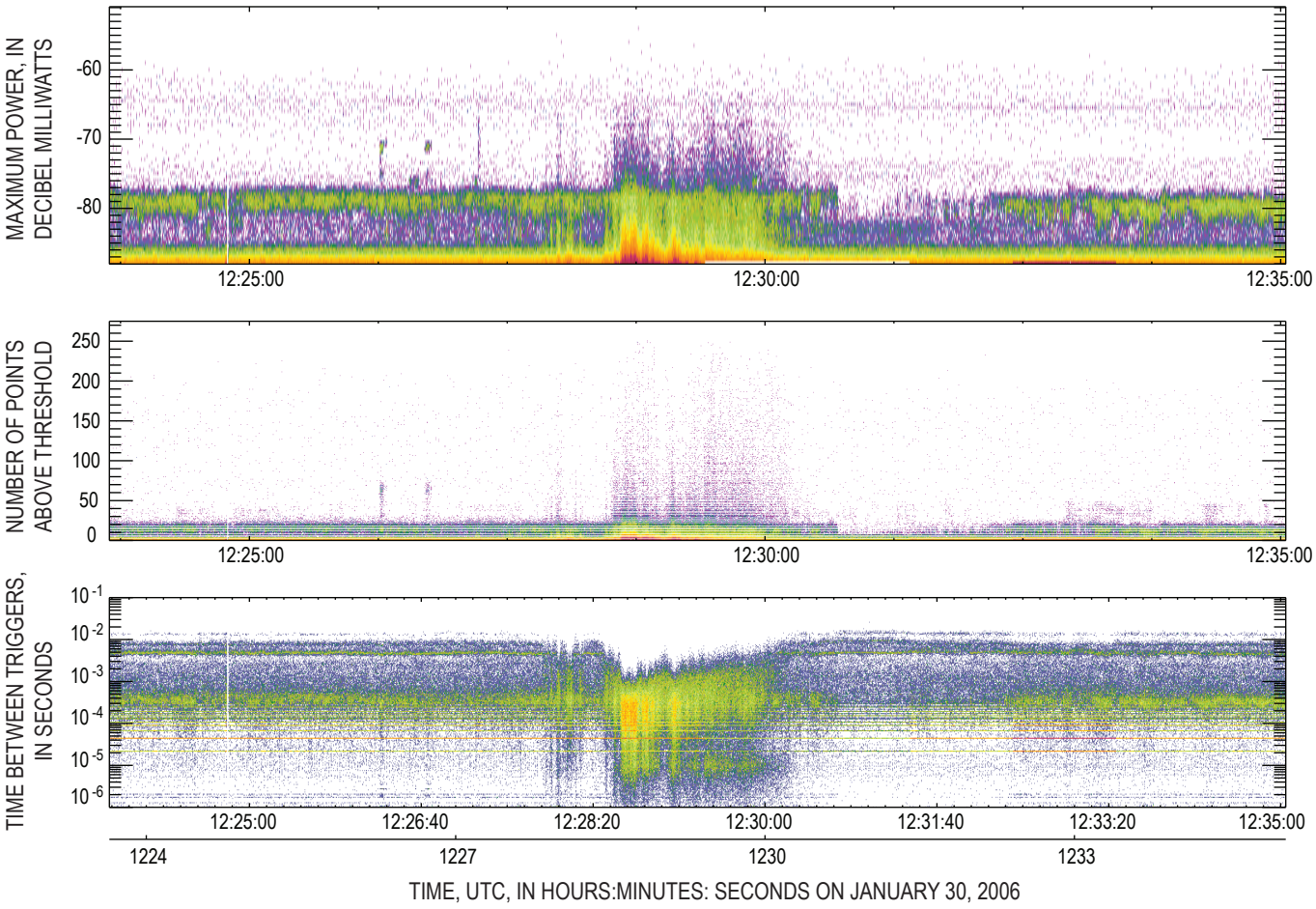

Figure 26. Lightning and electrical signals during Augustine Volcano's eruptive pulse at 0328 AKST (1228 UTC) on January 30, 2006. See the captions of figures 6 and 7 for details. The dates and times in this plot are in universal time (UTC).

location of sources for different time of arrival differences. Table 3 shows the time differences for the 6 periods. Because the signals were weak and coming from close to the volcano we would not expect to receive them at Anchor Point. The station at Oil Point was in a good location to observe signals arising from lava and pyroclastic flows on the north and east sides of Augustine. Because the station on West Island was very close (5 km), we expected to see many correlations in its data. However, we found correlations only during one period (table 3). There are two possible reasons for this. First we found a defective part in the antenna that could have intermittently blocked the signals, but we don't know when the part failed. Second, most of the other correlated signals seemed to come from the east side of Augustine Volcano and not visible to the station. Most of the ash and lava flows were also on the east side of the volcano (Coombs and others, this volume).

All these electrical emission are thought to be the result of charging of ash or gas during extrusion and flow of lava and pyroclastic materials. The breakup of material during pyroclastic flows can cause particles to become charged by fracto-emission (Hoblitt, 1994; Miura and others, 1996) (this mechanism will be discussed below). Additionally the interaction of hot volcanic material and water has been observed to produce charged particles (Vogfjörd and others, 2005).

For the event on March 5 there were several thousand correlated points received by the stations at Homer and Oil Point between 10:08:50 and 10:09:40 AKST (19:08:50 and 19:09:40 UTC). Their time difference were within a few tenths of a micro second of 240.0 μs. Figure 28 shows that these electrical signals came from the northeast side of Augustine Volcano along lava and ash flows. Neither the seismic data nor acoustic data give an indication that anything unusual occurred to give the electrical signals. Thus, it is likely they were associated with some sort of gravitationally driven flow event. Although the time difference could be due to events on the volcano's southwest side, neither station could have seen events occuring in this location.

On March 7 there was an event that produced a small number of correlated points between the Homer and West Island stations, with a duration of about 15 seconds. As this

signal ended there were 10 seconds of correlated points between Homer and Oil Point. There were no points from Homer that correlated with both Oil Point and West Island. A possible explanation for this could be that initially the flow or eruptive material was near the summit and visible from both the east and the west but not the north. As the material came down the north east side it became visible from the north but not the west. This event was the only one which produced correlation between the West Island station and one of the other stations that we found. The locations of the events giving rise to these signals are close to the intersection of the 240 μs and 327 μs lines on figure 28.

Several more events were seen on March 9, 10, and 11 (see table 3). The time differences of 237.2 μs to 238.5 μs indicate that they came from the west or south faces of Augustine. The south face can be excluded as it would not be visible from Oil Point to the north. The most likely source is the avalanche channel on the northeast face.

Discussion and Conclusions

The electrical activity measured during the eruption of Augustine Volcano has given us a wealth of new information on volcanic lightning. We have classified the lightning and smaller discharges into two phases and three types. The phases are the explosive phase and the plume phase, and the types are (1) small and very short vent discharges, (2) small near-vent lightning, and (3) thunderstorm-like plume lightning. A continuous variation of phenomena spanning these three classifications is very likely. The three types are shown as simple drawings in figure 29.

The nearly continuous signals from the vent discharges do not consist of a continuous radio signal but of impulses that occur about every 10 to 100 μs. A developing lightning channel could emit a similar series of impulses, but the impulses would form a long channel in the process. The vent discharges appear to remain localized at the vent. If they went much

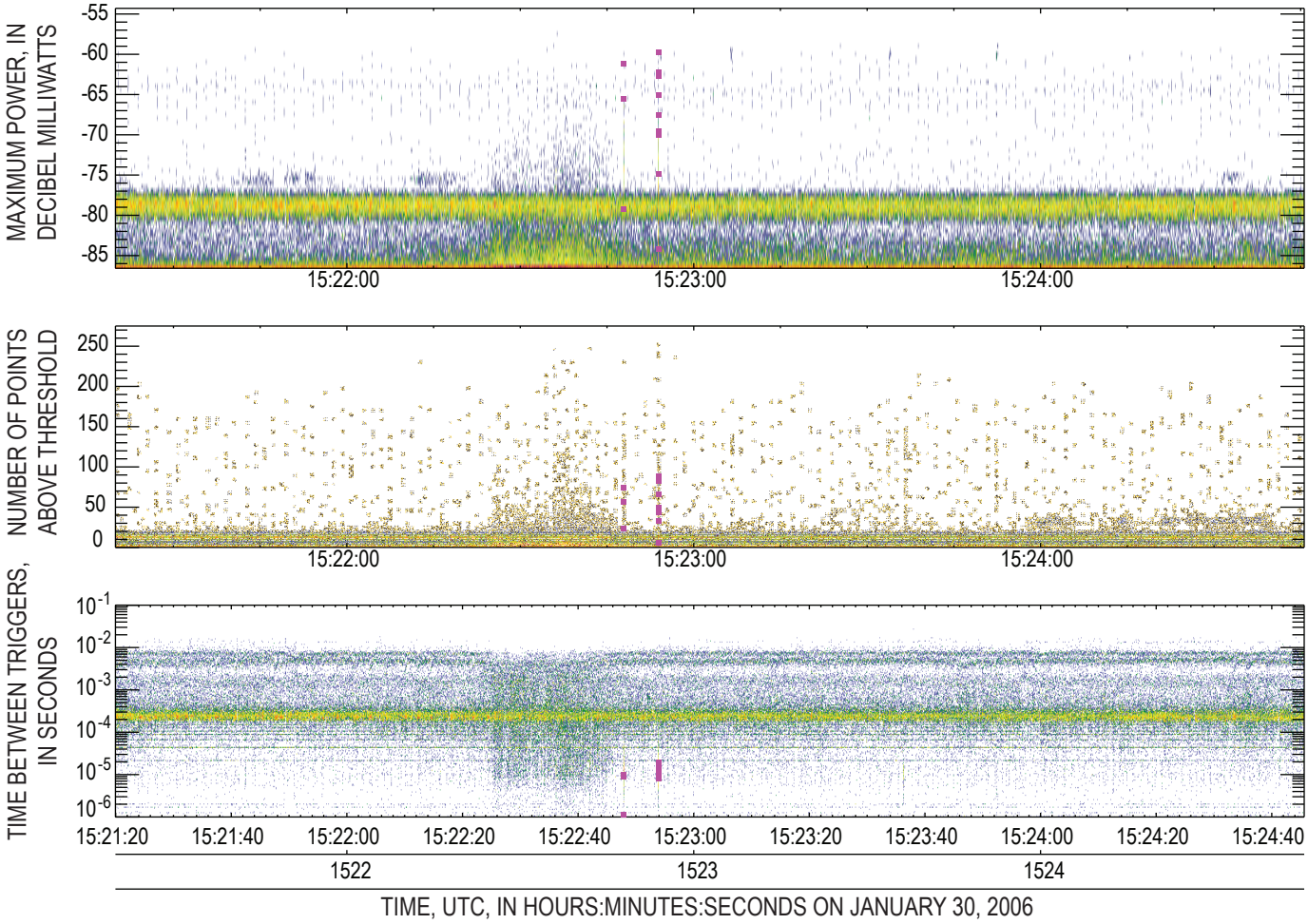

Figure 27. Lightning and electrical signals during Augustine Volcano's eruptive pulse at 0622 AKST (1522 UTC) on January 30, 2006. See the captions of figures 6 and 7 for details. The dates and times in this plot are in universal time (UTC).

Table 3. Electrical activity at Augustine Volcano detected during March 2006.

Date UTC	Time UTC	Homer-Oil Point Δt (arrival time difference) (μs)	Δt spread half-width (μs)	Duration (s)	Comments
March 5	1909	240.0	0.3	50	This correlation has the most points, also a suggestion of a Homer-Anchor Point correlation at 15.4 μs.
March 7	1241	240.0	0.3	10	Also a good 15 s of Homer-West Island correlations at 327.0 μs (0.3 μs wide).
March 9	2212	238.5	1.0	60	
March 10	0058	237.65	0.25	50	
	0059	237.7	0.1	10	
	0840	237.7	0.2	30	
March 11	0311	237.4	0.6	50	Time difference progressed from 237.8 to 237.2 μs.

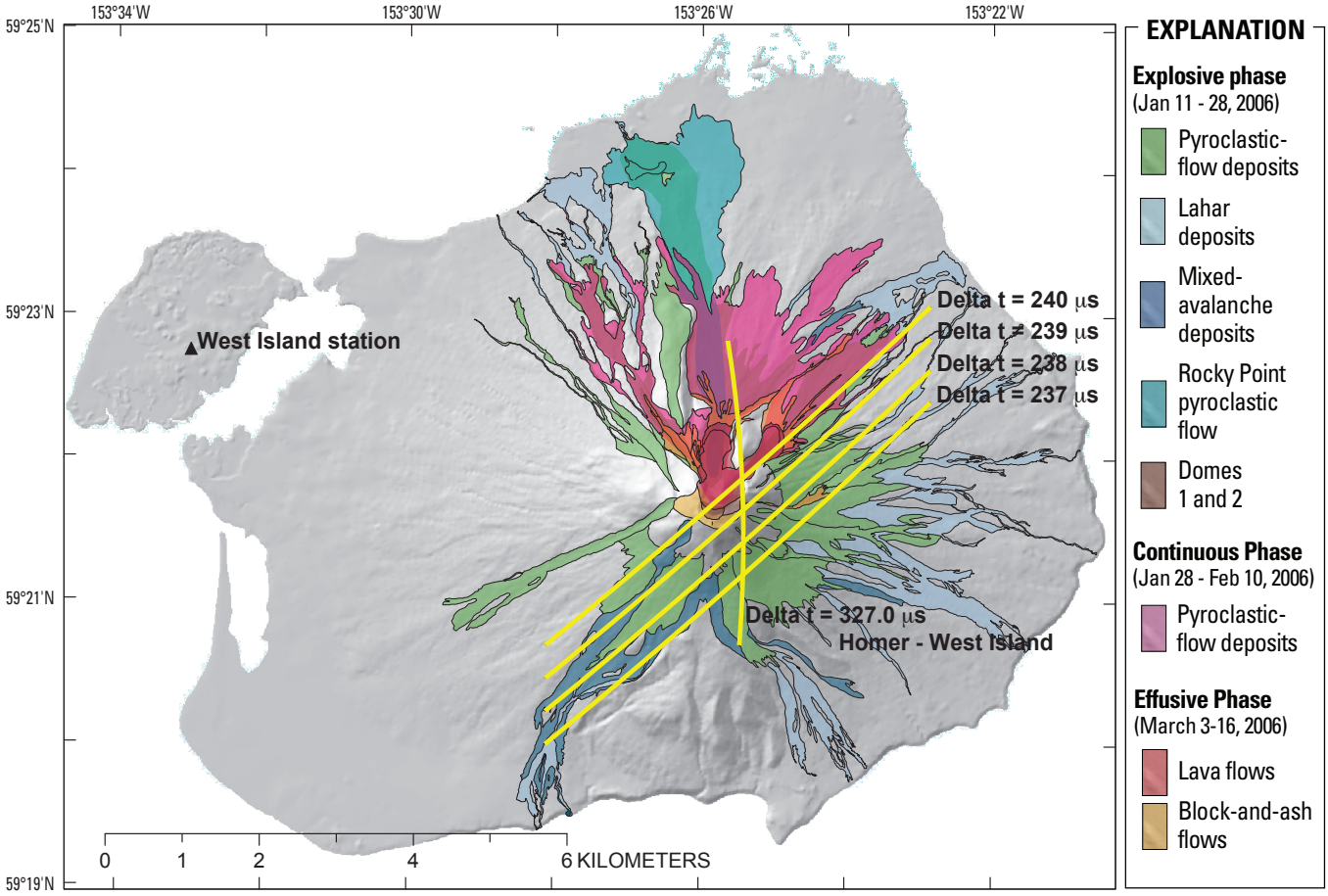

Figure 28. Simplified geologic map of Augustine Volcano deposits from the 2006 eruption with arrival time difference hyperbolas for March 2006. The time differences of 237 to 240 μs are for a combination of the Homer and Oil Point stations. Signal correlations were seen between Homer and West Island stations with a time difference of 327 μs. Base map courtesy of M.L. Coombs.

above the vent they would have been detected by the station at Anchor Point. In the large explosion on January 27 at 2031 AKST (January 28 at 0531 UTC) these impulses continued for 3 minutes. The discharges appear to be disconnected and independent. The RF power emitted by the impulses during vent lightning events is similar in magnitude to the power emitted during the formation of leader channels in thunderstorms (Thomas and others, 2001). This indicates that the sizes of the discharges that produce the RF are about the same as the steps during leader formation, about 10 to 100 m. The onset of the discharges coincided with the onset of the explosion indicating that the particle charging is due to processes associated with the explosion itself, rather than a delayed process such as particle interactions in a developing plume.

The charge is probably generated as the magma expands and fractures into ash particles in the volcanic conduit. The micro-physical properties of the ash and the other particles in the conduit will determine the sign of the charge transfer. This type of process is referred to as fracto-emission and leads to charged particles and emission of light in laboratory experiments. It was proposed by Lane and Gilbert (1992) as the mechanism charging ash rich plumes at Sakurajima Volcano in Japan. James and others (2000) conducted laboratory experiments fracturing pumice samples and found that charged particles were generated. Once the charged particles are generated in the conduit the positive and negative charge must be separated to produce the high electric field and discharges. In the upper part of the plume, as in thunderstorms, gravitational separation divides the particles by size and weight; however, in the conduit, jet flow dynamics could separate the particles. The observed vent discharges may be between different regions in the ejecta or between the ejecta and the vent of the volcano. Our observations of the upward development of the near-vent lightning indicate that the developing plume has a net positive charge. This indicates that much of the negative charge remains attached to the vent or is on large particles that fall back almost immediately. These vent discharges may be similar to the lightning photographed during Strombolian eruptions, such as those at Sakura-jima or Tavurvur. During the Augustine eruption there was probably much more ash, and these new-vent discharges could have been obscured by the ash cloud and would not have been visible even with good weather conditions.

During the explosions there were small near-vent lightning flashes that developed upward for several kilometers into the erupting column. These were observed as organized sets of impulses correlated between the Homer and Anchor Point stations. We were able to determine the altitude development of one of these near-vent discharges from the interference between the direct RF signal and the signal reflected from the sea surface received at the Homer station. Thunderstorm lightning that strikes the ground almost always begins in the cloud with a downward propagating leader channel forming a conducting path to ground, followed by a high current return stroke back up the channel. This return current pulse produces the bright flash as well as a low frequency electromagnetic pulse that can be used to locate the ground strike point by a network like the one operated by the BLM in Alaska. Occasionally lightning begins with a leader channel that develops from a tall tower and propagates upward into the thundercloud, with no associated return stroke. We suspect that most of the near-vent flashes begin at the summit and propagate upward into the developing column. This is consistent with the fact that no return strokes were detected by the BLM network during the explosions we observed. The near-vent lightning began 25 to 300 seconds after the onset of the explosion, during which time period an eruptive column formed (see table 2). The near-vent

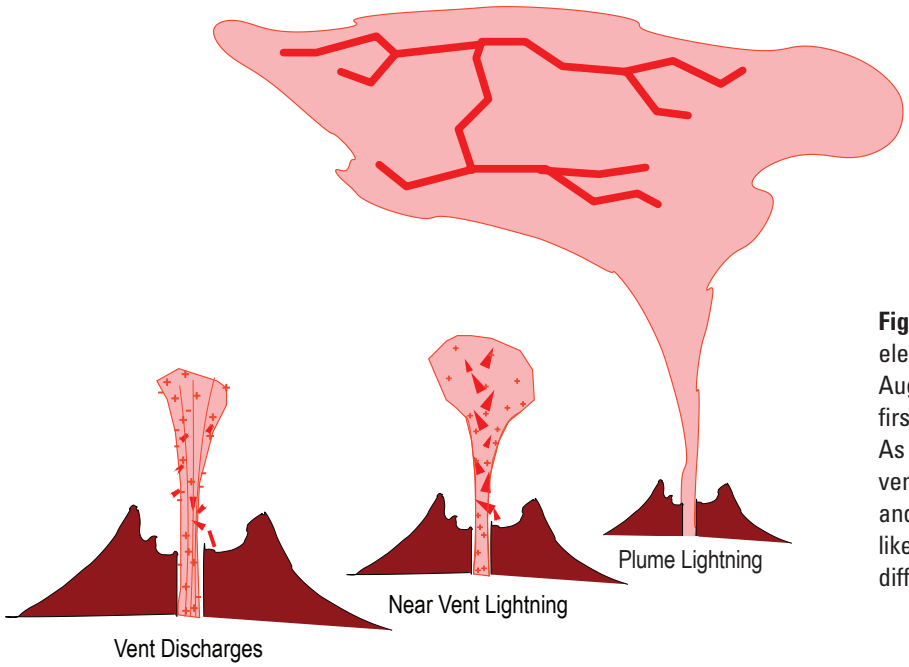

Figure 29. The three types of lightning or electrical discharges seen in the 2006 eruption of Augustine Volcano. The vent discharges are seen first, occurring as soon as the explosion begins. As the eruptive column develops upward near-vent lightning begins. After the plume develops and some charge separation occurs, thunderstorm like lightning begins; it is probably between two different charge regions at different altitudes.

lightning discharges ended several minutes after the end of the explosion. Charge generated by fracture in the conduit can account for these discharges. In other eruptions we would expect to see similar lightning discharges in or very close to the erupting column. The vent discharges indicate the electric field is the largest at the vent and this is where the near vent lightning would start and develop up into the plume.

One clear sequence of plume lightning was observed after the large explosion at 2031 AKST on January 27 (0531 UTC on January 28). The lightning began about 4 minutes after the onset of the large explosion and a minute after the explosion stopped. All the lightning during this period was intracloud (IC) lightning or upward lightning from the summit. There were no CG flashes detected by the BLM network. Data from the NEXRAD radars indicated that the plume extended to an altitude of 10.5 km (a typical height for thunderstorms) and drifted to the south east. It is very likely that the volcano injected a large volume of hot moist air into the cold winter atmosphere, producing conditions similar to those that exist in a small summertime thunderstorm (Williams and McNutt, 2004). As the buoyant air rises and mixes with surrounding air and cools, water droplets and ice are formed, that fall back through the rising air. This is the basis of the mechanism that is thought to produce charge separation in thunderstorms (Williams, 1985). A natural thunderstorm will typically last longer than this volcanic plume as it will have a much longer lasting source of rising warm moist air. A rough estimate of the amount of water injected into the atmosphere during the main explosion on January 28, 2006, can be made assuming that each cubic meter of magma had 100 kg of water (Williams and McNutt, 2005). About 17×10^6 m^3 of magma was erupted (Coombs and others, this volume). Thus there was about 1.7×10^9 kg of water vapor was injected into the atmosphere. Simulation of a small thunderstorm required about 10^9 kg (T. Mansell, oral commun., 2009). Thus all the components that generate and separate charge in a thunderstorm seem to be present in this plume.

After the ash, tephra, and gases have been injected into the plume by the initial velocity and buoyancy, the larger particles will settle out faster than the light ones. Cooled by entrained air, the particles will serve as condensation nuclei and the large quantities of water vapor will become coated with water or ice. The different sized particles falling at different speeds will collide, exchange charge, and separate. Because many of the particles are ice or water coated charge will be separated as in a thunderstorm. Volcanic plumes may have charge separation mechanisms not present in thunderstorms, because of collisions between different sizes and types of ash particles in the plume or collisions between ash particles and water droplets. If the large particles fall at 5 m s^{-1}, a plume could produce lightning for as long as 20 minutes as the particles fell 6 km.

Many of the particles were electrically charged during the ejection process (as evidenced by the vent discharges). If enough of these particles charged by fracturing in the conduit were not neutralized by the vent discharges and reach high altitudes and if the positive and negative charge were on different sized particles, subsequent settling could separate the charge and lead to lightning discharges. Lane and Gilbert (1992) proposed that electric fields (no lightning) observed during ash eruptions at Sakurajima were the result of this fracto-emission in the volcanic conduit and that the particles were charged negative and the positive charge was on gas. Our observations verify their idea that charged particles are generated in the explosion before they leave the vent of the volcano.

We can estimate the amount of charge needed if this mechanism was responsible for plume lightning we observed. A typical IC lightning flash discharges 10 to 40 C of charge. There were about 150 big flashes in the 10 minute sequence that would require 1,500 to 6,000 C. This implies a current of 2.5 to 10 A. The charging current produced by the settling of one type of charge particle is the charge density times the fall speed times the plume area. An 100 km^3 area (a square 10 km on a side) and a fall rate of 5 m s^{-1} indicates a charge density of 5 to 20 C km^{-3}. In thunderstorms charge densities are several C km^{-3} with a maximum of 10 C km^{-3} (MacGorman and Rust, 1998). Although this mechanism seems possible it is hard to understand why there was not charge separation and lightning during the period that the plume was forming.

It seems unlikely that gravitational separation of the different sized ash particles charged during the explosion could separate a sufficient amount of charge to produce the series of lightning flashes. Continued charge generation by a process such as the thunderstorm ice mechanism is needed for all but a brief series of flashes. More observations are needed to determine the roll of each charging mechanism in volcanic plumes.

Acknowledgments

We acknowledge important contributions by Nicholas O'Connor and Sandra Kieft in preparing for and conducting the field studies. This work was supported by the National Science Foundation under grants ATM-0536950 and ATM-0354218. Partial support was also provided by the Alaska Volcano Observatory, the University of Alaska Geophysical Institute, the U.S. Geological Survey, the State of Alaska, and NSF grant ATM-053831.

References Cited

Anderson, R., Bjornsson, S., Blanchard, D., Gathman, S., Hughes, J., Jonasson, S., Moore, C.B., Survilas, H.J., Vonnegut, B., 1965, Electricity in volcanic clouds: Science, v. 148, p. 1179–1189.

Behnke, S.A., Thomas, R.J., Krehbiel, P.R., and Rison, W., 2005, Initial leader velocities during intracloud lightning—possible evidence for a runaway breakdown effect: Journal Geophysical Research, v. 110, D10207, doi:10.1029/2004JD005312.

Bolton, J. G., and Slee, O.B., 1953, Galactic radiation at radio frequencies—V., The Sea Interferometer: Australian Journal of Physics, v. 6, p. 420–433.

Brook, M., Moore, C.B., and Sigurgeirsson, T. 1974, Lightning in volcanic clouds: Journal. Geophysical Research, v. 79, p. 472–475, Correction: Journal. Geophysical Research, v. 79, p. 3102.

Coombs, M.L., Bull, K.F., Vallance, J.W., Schneider, D.J., Thoms, E.E., Wessels, R.L., McGimsey, R.G., 2010, Timing, distribution, and volume of proximal products of the 2006 eruption of Augustine Volcano, Alaska, *in* Power, J., Coombs, M.L., and Freymueller, J.T., eds., The 2006 eruptions of Augustine Volcano, Alaska: U.S. Geological Survey Professional Paper 1769 (this volune).

Cummins, K.L., Murphy, M.J., Bardo, E.A., Hiscox, W.L., Pyle, R.B., and Pifer, A.E., 1998, A combined TOA/MDF technology upgrade of the U.S. National Lightning Detection Network: Journal Geophysical Research, v.103, p. 9035–9044.

Grunewald, O., 2007, Visions of earth (photograph of Tavurvur Volcano): National Geographic, v. 212, p. 14–15, September 2007.

Hoblitt, R.P., 1994, An experiment to detect and locate lightning associated with eruptions of Redoubt Volcano: Journal Volcanology and Geothermal Research, v. 62, p. 499–517.

James, M.R., Lane, S.J., and Gilbert, J.S., 2000, Volcanic plume electrification—experimental investigation of a fracture-charging mechanism: Journal Geophysical Research, v. 105, p. 16641–16649.

Lane, S.J., and Gilbert, J.S., 1992, Electric potential gradient changes during explosive activity at Sakurajima volcano, Japan: Bulletin of Volcanology, v. 54, p. 590–594.

McNutt, S.R., and Davis C.M., 2000, Lightning associated with the 1992 eruptions of Crater Peak Mount Spurr Volcano, Alaska: Journal Volcanology and Geothermal Research, v. 102, p. 45–65.

McNutt, S.R., Tytgat, G., Estes, S.A., and Stihler, S.D., 2010, A parametric study of the January 2006 explosive eruptions of Augustine Volcano, using seismic, infrasonic, and lightning data, *in* Power, J.A., Coombs, M.L., and Freymueller, J.T., eds., The 2006 eruption of Augustine Volcano, Alaska: U.S. Geological Survey Professional Paper 1769 (this volume).

Mather, T.A., and Harrison, R.G., 2006, Electrification of volcanic plumes: Surveys Geophysics, v. 27 p. 387–432, DOI 10.1007/s10712-006-9007-2.

Miura, T., Koyaguchi, T., and Yoshikazu, T., 1996, Atmospheric electric potential gradient measurements of ash clouds generated by pyroclastic flows at Unzen: Geophysical Research Letters, v. 23, p. 1789–1792.

MacGorman, D.R., and Rust, W.D., 1998, The electrical nature of storms: Oxford University Press.

Petersen, T., De Angelis, S., Tytgat, G., and McNutt, S.R., 2006, Local infrasound observations of large ash explosions at Augustine Volcano, Alaska, during January 11-28, 2006: Geophysical Research Letters, v. 33, L12303, doi:10.1029/2006GL026491.

Rison, W., Thomas, R.J., Krehbiel, P.R., Hamlin, T., and Harlin, J., 1999, A GPS-based three-dimensional lightning mapping system—initial observations: Geophysical Research Letters, v. 26, p. 3573–3576.

Schneider, D.J., Scott, C., Wood J., and Hall T., 2006, NEXRAD weather radar observations of the 2006 Augustine volcanic eruption clouds: Eos (American Geophysical Union Transactions), v. 87, abs. V51C-1686.

Thomas, R.J., Krehbiel, P.R., Rison, W., Edens, H.E., Aulich, G.D., Winn, W.P., McNutt, S.R., Tytgat, G., and Clark, E., 2007, Electrical activity during the 2006 Mount St. Augustine volcanic eruptions: Science, v. 315, p. 1097, doi: 10.1126/science.1136091.

Thomas R.J., Krehbiel, P.R., Rison, W., Hamlin, T., Harlin, J., and Shown, D., 2001, Observations of VHF source powers radiated by lightning: Geophysical Research Letters, v. 28, p. 143–146.

Thomas, R.J., Krehbiel, P.R., Rison, W., Hunyady, S.J., Winn, W.P., Hamlin, T., and Harlin, J., 2004, Accuracy of the lightning mapping array: Journal Geophysical Research, v. 109, no. D14, D14207, doi: 10.1029/2004JD004549.

Vogfjörd, K.S., Jakobsdóttir, S.S., Gudmundsson, G.B., Roberts, M.J., Ágústsson, K., Arason, T., Geirsson, H., Karlsdóttir, S., Hjaltadóttir, S., Ólafsdóttir, U., Thorbjarnardóttir, B., Skaftadóttir, T., Sturkell, E., Jónasdóttir, E.B., Hafsteinsson, G., Sveinbjörnsson, H., Stefánsson, R., and Jónsson, T.V., 2005, Forecasting and monitoring a subglacial eruption in Iceland: Eos (American Geophysical Union Transactions), v. 86, p. 245–248

Williams, E.R., 1985, Large scale charge separation in thunderclouds: Journal Geophysical Research v. 90, p. 6013–6025.

Williams E.R., and McNutt S.R., 2004, Are large volcanic eruptions just dirty thunderstorms?: Eos (American Geophysical Union Transactions), v. 85, Fall meeting. supp., Abstract AE23A-0842.

Williams, E.R., and McNutt, S.R., 2005, Total water contents in volcanic eruption clouds and implications for electrification and lightning, *in* Pontikis, Constantin, ed., Recent progress in lightning physics: Kerala, L\India, Research Signpost, p. 81–94.

The 2006 Eruption of Augustine Volcano, Alaska
Power, J.A., Coombs, M.L., and Freymueller, J.T., editors
U.S. Geological Survey Professional Paper 1769

Chapter 26

Emission of SO_2, CO_2, and H_2S from Augustine Volcano, 2002–2008

By Kenneth A. McGee[1], Michael P. Doukas[1], Robert G. McGimsey[2], Christina A. Neal[2], and Rick L. Wessels[2]

Abstract

Airborne surveillance of gas emissions from Augustine Volcano and other Cook Inlet volcanoes began in 1990 to identify baseline emission levels during noneruptive conditions. Gas measurements at Augustine for SO_2, CO_2, and H_2S showed essentially no evidence of anomalous degassing through spring 2005. Neither did a measurement on May 10, 2005, right after the onset of low level seismicity and inflation. The following measurement, on December 20, 2005, showed Augustine to be degassing about 600 metric tons per day (t/d) of SO_2, and by January 4, 2006, only 7 days before the first explosive event, SO_2 emissions had climbed to ten times that amount. Maximum emission rates measured during the subsequent eruption were: 8,930 t/d SO_2 (February 24, 2006), 1,800 t/d CO_2 (March 9, 2006), and 4.3 t/d H_2S (January 19, 2006). In total, 45 measurements for SO_2 were made from December 2005 through the end of 2008, with 19 each for CO_2 and H_2S during the same period. Molar CO_2/SO_2 ratios averaged about 1.6. In general, SO_2 emissions appeared to increase during inflation of the volcanic edifice, whereas CO_2 emissions were at their highest during the period of deflation associated with the vigorous effusive phase of the eruption in March. High SO_2 was probably associated with degassing of shallow magma, whereas high CO_2 likely reflected deep (>4 km) magma recharge of the sub-volcanic plumbing system, For the 2005–6 period, the volcano released a total of about 1.5×10^6 tons of CO_2 to the atmosphere, a level similar to the annual output of a medium-sized natural-gas-fired powerplant. Augustine also emitted about 8×10^5 tons of SO_2, similar to that produced by the 1976 and 1986 eruptions of the volcano.

[1]Cascades Volcano Observatory, U.S. Geological Survey, 1300 SE Cardinal Court, Vancouver, WA 98683.

[2]Alaska Volcano Observatory, U.S. Geological Survey, 4210 University Drive, Anchorage, AK 99508.

Introduction

Augustine Volcano is located on an uninhabited island in the lower Cook Inlet of Alaska (fig. 1). It lies about 100 km west of Homer and 280 km southwest of Anchorage. The site of frequent explosive eruptions, Augustine Volcano is a young 1,250-m-high convergent plate boundary stratovolcano, lying about 100 km above the Benioff zone in the eastern portion of the Aleutian arc. It has had at least four periods of significant activity in the twentieth century in 1935, 1964–65, 1976, and 1986 before the most recent eruption in 2006 (Miller and others, 1998) and erupts mostly andesitic and dacitic lavas (Kienle and Swanson, 1983). Augustine Volcano consists of a broad apron of pyroclastic and debris-avalanche deposits surrounding a central vent and dome complex (Swanson and Kienle, 1988; Waitt and and Begét, 2009). When Augustine erupts, a number of volcanic hazards have the potential to threaten communities in south central Alaska and aviation, industrial facilities, petroleum and natural gas production, shipping, and other activities (Waythomas and Waitt, 1998).

Airborne gas measurements at Augustine Volcano are part of a systematic program to monitor baseline gas emissions at Cook Inlet volcanoes in order to recognize the beginning of unrest and to identify baseline values of gas emissions to which future measurements could be compared in the event of unrest (Doukas, 1995). In 1990, 4 years after the 1986 eruption, annual measurements were begun and have continued through 2008. This paper reports gas measurements made from 2002 to 2008 with special emphasis on precursory and eruptive activity during 2005–6.

Data from two earlier eruptions of Augustine allow comparisons with peak SO_2 emission rates measured during 2006. From February 8 through 18 during the 1976 eruption, Stith and others (1978) made a series of measurements using a Meloy flame photometric detector to determine total gaseous sulfur, which was assumed, by smell, to be all SO_2. They

measured a peak value of 25,900 t/d of SO_2 on February 9, 1976, followed by 8,600 t/d on February 11, 13, and 18. Their lowest measured SO_2 emission rate was 173 t/d on February 12, 16, and 17. A little more than a year after the eruption, they returned to Augustine for an additional measurement and recorded a value of 26 t/d on April 22, 1977. Using a scrubber system attached to their instrument, they were also able to remove SO_2 and estimate an emission rate for H_2S of 3.5 t/d for the 1977 measurement. They estimated that Augustine emitted about 1×10^5 tons of SO_2 during the 1-year period surrounding the 1976 eruption. As this estimate neglects the paroxysmal emissions of April 1976, it is only a minimum value. They point out that a significant portion of the SO_2 emitted during the paroxysmal eruptions was attached to the surfaces of ash particles and fell out of the plume after a short time.

During the March–April 1986 eruption of Augustine, Rose and others (1988) successfully made airborne ultraviolet spectroscopic (COSPEC) plume measurements on April 3, 1986, and calculated a SO_2 emission rate of 24,000 t/d during active ash emission and under high wind conditions; gas emission rates were likely higher during the peak of the eruptive activity from March 27 to April 3. More than a year after the end of the eruption, additional measurements of 380 t/d (July 24, 1986) and 45 t/d (May 24, 1987) were made during a period of post-eruptive passive degassing (Symonds and others, 1990). Rose and others (1988) used ash leachate and emission data along with seismic information and other observations to scale up their SO_2 measurement of April 3, 1986, to an emission rate of 3.75×10^4 t/d that was likely achieved on more than one day during the peak phase of the eruption.

Before the 2005–6 eruption, fumarolic activity at Augustine was confined to scattered areas near the summit dome complex (fig. 2). As early as the summers of 1986 and 1987, Symonds and others (1990) observed that the 1986 lava dome produced >90 percent of the gas emitted from Augustine. Other sources were the solfataras located west of the 1986 dome along the high ridge between the remnants of the 1935 and 1964 lava domes and in unconsolidated pyroclastic flow deposits near the northern base of the volcano's dome complex. In 1987, at least one fumarole on the dome was as hot as 870°C, but by 1989 it

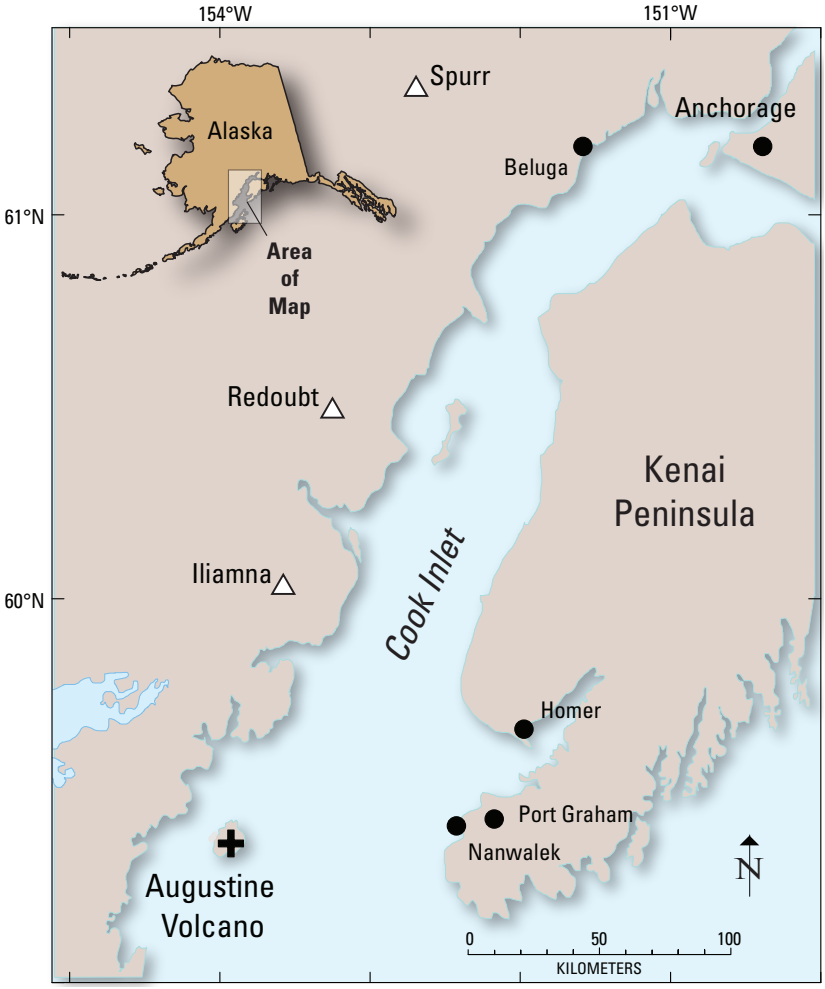

Figure 1. Location map for Augustine Volcano. Plus sign (+), Augustine Volcano; Open triangles, other volcanoes of Cook Inlet; Filled circles, cities and towns near Cook Inlet. Inset map of Alaska.

was only 640°C (Symonds and others, 1990). By 1992, fumarole temperatures had declined to about 97°C, boiling point for the summit elevation (Symonds and others, 2003).

Methods

Instrumentation

In this study, we used an instrument platform developed over the past 15 years at the Cascades Volcano Observatory (CVO). The platform is mounted on board an aircraft for transport to volcanic centers, usually in remote settings, and is capable of measuring volcanic CO_2, SO_2, and H_2S (Gerlach and others, 2008). For airborne emission measurements of the Augustine plume, a LI-COR Model LI-6252 nondispersive infrared analyzer and a Model LI-670 flow control unit were used to determine volcanic CO_2 (Gerlach and others, 1997; Gerlach and others, 1999). An Interscan Model 4170 analyzer with a 0 to 1 ppm range and an Interscan Model 4240 analyzer with a 0 to 2 ppm range were used for direct measurements of H_2S and SO_2 in the plume, respectively. These instruments consist of an electrochemical voltametric sensor coupled to a 1 -liter-per-minute sample-draw pump. The calibrated analog output of the instruments record gas concentrations as described in detail by McGee and others (2001) and Werner and others (2006).

The airborne instrument package also included a COSPEC for measuring SO_2 column abundance (units of parts per million-meter, or ppm·m) and a type-T thermocouple shielded from wind and direct sunlight for measuring ambient air temperature. Atmospheric pressure was measured in the unpressurized aircraft cabin by a pressure transducer mounted within the LI-COR analyzer. A GPS receiver was used to tag the precise latitude, longitude, and altitude of each measurement. Data from all of the instruments were recorded on a common 1/s time base. All gas readings were corrected for the actual pressure and temperature at the altitude at which the measurements were taken.

Procedure

Two different instrument configurations were used for the airborne measurements between 1995 and 2006 owing to funding limitations and instrumentation availability. In one configuration (24 of the 45 campaigns reported in table 1), only a COSPEC V and a Model 60CSX GPS were used to determine SO_2 emission rates. Typically, four to six traverses were flown under the downwind plume perpendicular to the direction of plume travel with the upward-looking COSPEC to determine an average column abundance of SO_2. GPS-registered wind circles (positions logged once per second) at the elevation of the plume were then flown in order to calculate the velocity of plume travel so that a SO_2 emission rate could

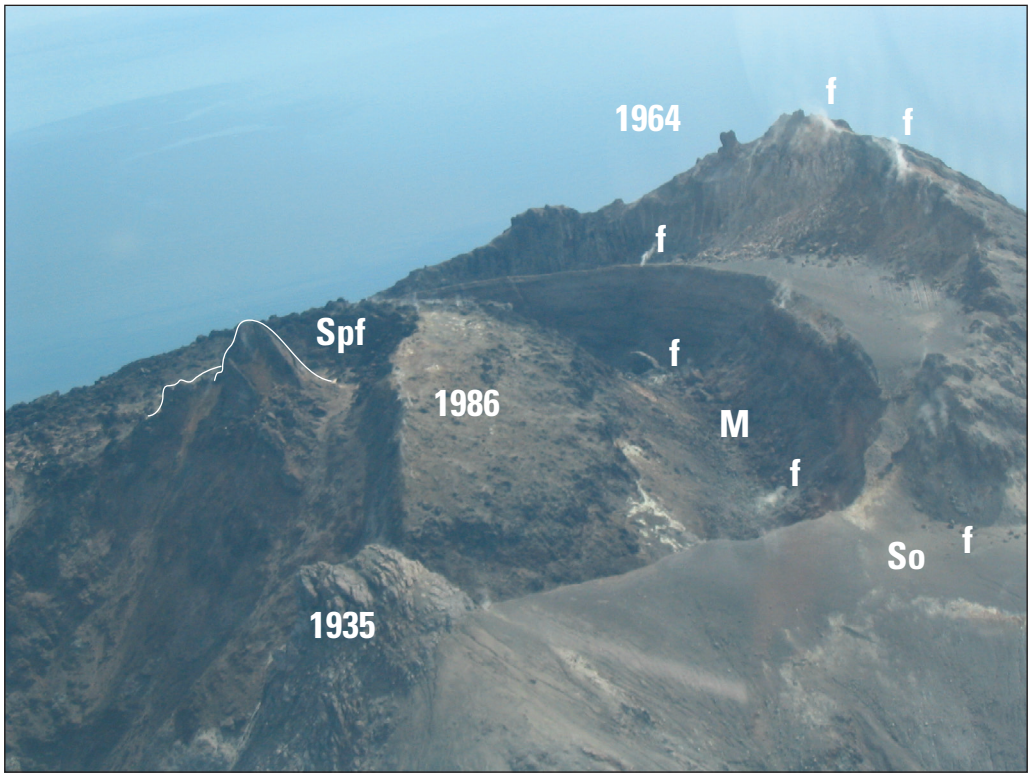

Figure 2. View of 2004 preeruptive summit of Augustine Volcano, as seen from the west. 1986, lava dome surrounded by moat (M) formed during the 1986 eruption. Spf, Spine fumarole located near base of spine (faint outline) (Symonds, and others, 1990). 1964, lava dome remnant forms collar on south summit. 1935, lava dome remnant lies north of the solfatara area (So). f, locations in 2004 wispy boiling-point fumaroles plumes (not sampled). Photo by M. Doukas.

be computed (Doukas, 2002). In the other configuration (21 of the 45 campaigns reported in table 1), the full instrument package for measuring CO_2, SO_2, and H_2S (LICOR, COSPEC, and Interscan) was mounted in a twin-engine aircraft configured for open-flow sampling of external air upstream of engine exhaust as described in Gerlach and others (1997) and Gerlach and others (1999). In addition to the traverses flown under the plume for the COSPEC measurements described above, a series of additional traverses were flown top to bottom through the plume at the same distance downwind of the vent in order to describe a vertical cross section of the plume.

To illustrate data collection techniques, figure 3 shows the reconstructed flight path from GPS data for a typical flight between 1400 and 1500 Alaska Standard Time (AKST) on January 19, 2006, with the full instrumentation package. Five traverses were made underneath the plume for the COSPEC measurements. Then, a series of 12 additional plume profile traverses were flown through the plume ranging from a top traverse at an altitude of 1,700 m above mean sea level (amsl) down to a bottom traverse of 780 m amsl based on aircraft altimeter readings and with an average vertical spacing of 80 m. Winds measured just after the flight by the wind circle method indicated winds out of the west-northwest at an average speed of 6.1 m/s. The plume from Augustine on this day was detected on all but the top and bottom traverses, and the characteristic smell of both H_2S and SO_2 was noticed by the aircrew on all of the traverses through the plume. Atmospheric pressure and temperature were nearly constant inside and outside the plume on each traverse and averaged 88.04 kPa and −9.8°C. No temperature anomaly was detected in the volcanic plume on any of the traverses.

Two representative COSPEC traverses from the January 19, 2006, example are presented in figure 4. The COSPEC SO_2 signal is processed in Peakfit v. 4.0 (AISN Software, Inc.) to determine the area under the signal curve in kilometers×ppm·m. The average ppm·m is then determined by dividing the area by the width in kilometers. The average signal is then reduced by the ratio of the calibration cells used during the flight. The reduction equation gives the SO_2 emission rate (E) in units of t/d:

$$E_{cospec}=0.00023(S_W \times Plume\ width \times Ave\ ppm{\cdot}m) \quad (1)$$

Where S_W is the average wind speed (m/s), Plume width in meters and *Ave ppm·m* is the resultant average ppm·m of the plume traverse. The constant reduces the concentration of the cross section to t/d.

Figure 5 shows a time-series plot of the January 19 CO_2, SO_2, and H_2S data series. The ambient CO_2 background measured on each traverse on either side of the CO_2 anomaly was fit using routines in PeakFit v. 4.0 (AISN Software, Inc.) and subtracted from each peak and zeroed to obtain the volcanic CO_2 gas signal. The resulting CO_2 plume anomaly on January 19, 2006, has a maximum concentration of nearly 5 ppm. A similar procedure was used for H_2S and SO_2 from the Interscan measurements, although no H_2S and SO_2 were present in the ambient

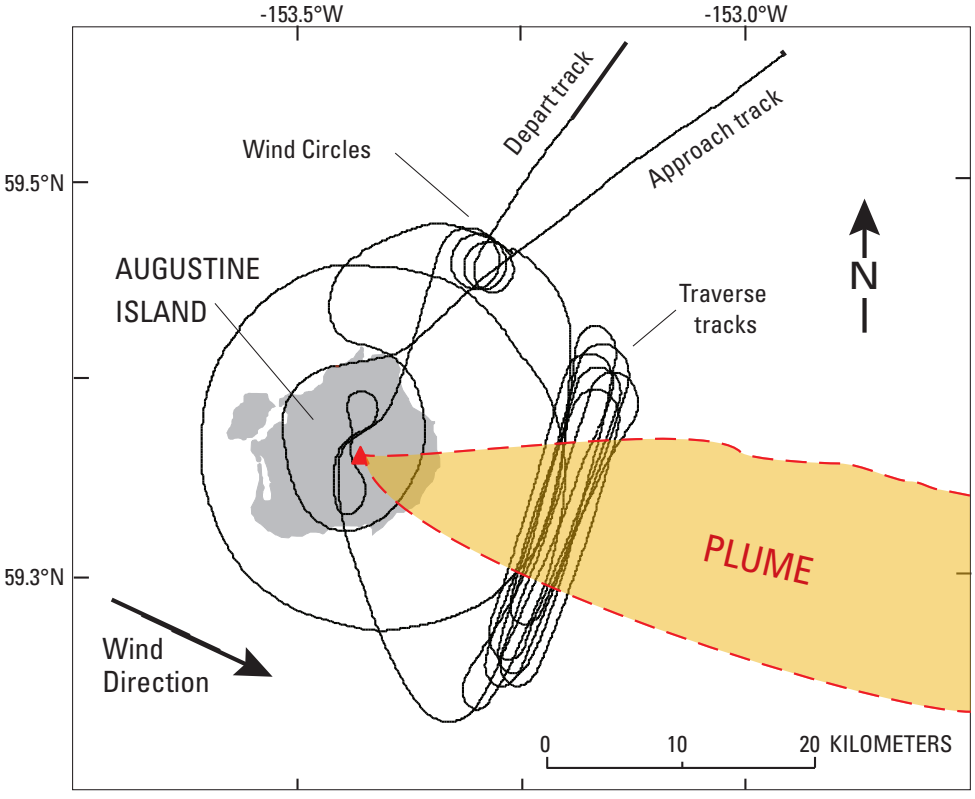

Figure 3. Map showing recorded GPS flight-track positions during the airborne survey at Augustine Volcano, Alaska, on January 19, 2006. Arrow shows determined wind direction, and the cluster of flights lines to the east of Augustine shows the NNE-SSW gas measurement traverses under and intersecting the volcanic plume downwind of the volcano. Red triangle locates the summit of the volcano. Flight tracks for wind circles to determine wind speed are shown northeast of Augustine and were flown at the altitude of the plume core.

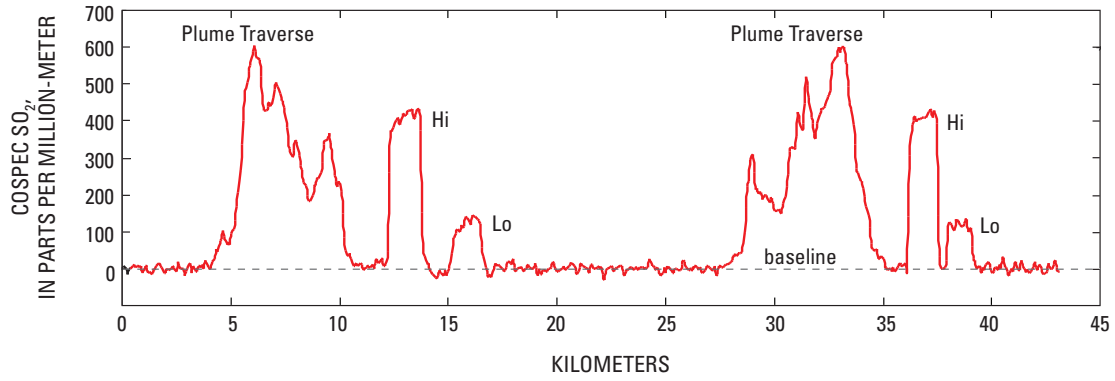

Figure 4. Data series from two of the five COSPEC traverses flown beneath the Augustine plume on January 19, 2006. High and low calibration-cell signals are labeled Hi and Lo and occur after the SO_2 peaks. The horizontal x-axis shows the cumulative flight distance for the two traverses in kilometers. Y-axis units are in parts per million-meter. Note the asymmetry of the SO_2 plume a result of flying in opposite directions.

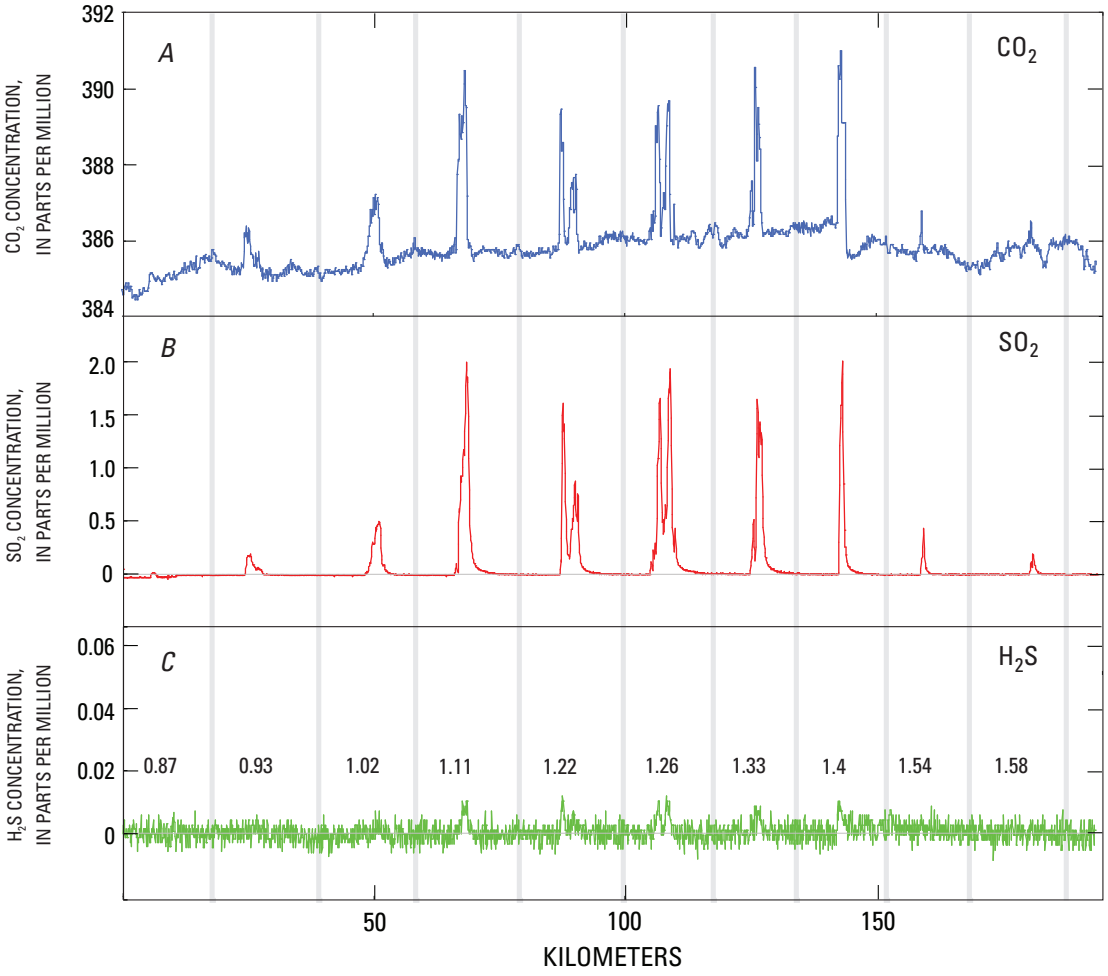

Figure 5. Time-series plots of concentration data (in ppm) for CO_2 (blue), SO_2 (red), and H_2S (green) during the series of traverses flown through the plume at Augustine Volcano on January 19, 2006. The horizontal x-axis is the cumulative flight distance during the traverses (kilometers). Elevation of each traverse indicated in kilometers in the H_2S box. Vertical gray lines locate turn-around point during flight.

(background) air. For the example shown, the maximum plume concentration was about 2 ppm for SO_2 and 0.01 ppm for H_2S.

The conventional airborne method for measuring CO_2 emission rates from passively degassing volcanoes is based on analysis of air sampled through the volcanic plume normal to wind direction. The emission rate is then calculated from the average plume pressure and temperature, wind speed, and the volcanic CO_2 concentration anomaly in cross section (Gerlach and others, 1997). This method was adapted further by using the location of H_2S peaks, when present, as a guide to resolving the boundary between volcanic CO_2 and ambient CO_2 (McGee and others, 2001). Further, anomalous CO_2 signals appear during flying maneuvers (fig. 5, between altitudes 1.26 and 1.33 km, CO_2 time series), but the absence of SO_2 and H_2S peaks confirmed the nonvolcanic nature of the gas. Because the measurement traverses at Augustine were flown in a back-and-forth fashion through the plume, every other traverse was inverted before processing so that all traverses start from a common latitude and longitude and extend in the same direction across the plume. This eliminates introducing potential offsets between traverses due to the travel time of gas in the sample tubing from intake to analyzer when importing the data into contouring and mapping software.

Equation (1) from Gerlach and others (1997) gives the CO_2 emission rate (E) in units of t/d:

$$E=0.457329\ (A\times S_W\times P_{CO_2})/\mathrm{T} \qquad (2)$$

where A is the area of plume cross-section (m^2), S_W is the average wind speed (m/s), P_{CO_2} is the partial pressure of CO_2 (Pa) in the plume calculated from the product of average barometric pressure and the average molar concentration of CO_2 in the plume, and T is the average air temperature in the plume (K). The constant includes the formula weight of CO_2, the universal gas constant, and the number of seconds in a day. Average concentration of CO_2 in plume cross section was determined with kriging models for gridding and contouring the concentration measurements. A similar approach was used for computing emission rates for H_2S (constant = 0.354141) and SO_2 (constant = 0.665665).

Figure 6 shows resultant vertical plume cross sections for each of the three gases measured from the plume profile traverses on January 19, 2006, using contouring and mapping software (Surfer v. 8, Golden Software, Inc.). The cross-section for H_2S appears to show a smaller plume than those for CO_2 and SO_2 due to the very low concentration of H_2S and an Interscan detection limit of ~4 ppb for this type of measurement.

Standard deviation (s.d., table 1) for each day's COSPEC SO_2 emission rate calculation are based on the number of traverses flown and therefore represent the natural variation of the volcanic plume's SO_2. To decrease the standard deviation of the mean of our measurements by a factor of two would require that we acquire four times as many observations in our daily measurements. The distance to and from the volcano and aircraft fuel capacity limits time at the volcano and thus the number of traverses made.

With the full instrument configuration, comparison of COSPEC results and Interscan SO_2 emission rates (table 1) were not always in agreement. Variability of environmental conditions during measurement was usually the cause. For example, clouds at the summit or opaque (perhaps ash bearing) plumes may prevent traverses through the whole plume, resulting in higher COSPEC SO_2 emissions compared with Interscan contoured results. A higher concentration section of a plume may lie between traverses. For internal consistency, only the COSPEC results are used in this report.

2005–2006 Eruption Chronology and Gas Data

Before the onset of volcanic unrest in 2005, airborne measurements were usually made once per year. Flight frequency increased once the unrest started but varied considerably over the course of the eruption. From July 2002 through the end of 2008, 45 successful COSPEC measurements of SO_2 and 21 measurements of CO_2 and H_2S were made using the full instrument package.

Emission rates from airborne measurements for CO_2, SO_2, and H_2S at Augustine Volcano from 2002 through 2008 are given in table 1 (Doukas and McGee, 2007) and are shown plotted with other eruption parameters and eruptive phases in figure 7. CO_2 or SO_2 were not detected at Augustine from 2002 through May 2005 with the exception of a very small amount of CO_2 in May 1997. H_2S measurements were not begun until 2001, and no H_2S was detected through 2005. Not until December 20, 2005, was SO_2 detected during a COSPEC flight. CO_2 measurements were not attempted until January 16, 2006. Note that some data from the 2006 time period have been revised from those published in McGee and others (2008), owing to reprocessing using the contouring technique.

Precursory Phase (April 30, 2005–January 11, 2006)

The precursory phase (fig. 7) began with an increase in the number of microearthquakes in late April 2005 (fig. 8; Power and Lalla, this volume). The first airborne gas measurement during the unrest on May 10, 2005, detected no CO_2, SO_2, or H_2S. In mid-summer 2005, geodetic baselines began to lengthen suggesting inflation of the edifice throughout the last half of 2005 (Cervelli and others, this volume). The increasing seismicity continued until early December 2005 when a number of small phreatic explosions were recorded on seismometers (fig. 8; Power and Lalla, this volume). Sulfur smells had been reported in Nanwalek and Port Graham (fig. 1) on December 11,

2005, suggesting the arrival of significant sulfur-bearing gas at the surface at least by early December. On December 12, 2005, a vigorous gas and minor ash plume from the summit area was noted in MODIS satellite imagery and by observers, representing the most energetic of precursory phreatic explosions (fig. 9). The next measurement, for SO_2 only, was made on December 20, 2005, during the period of phreatic activity and showed a modest amount of SO_2 (660 t/d) in the plume. The emission rate was considered a minimum value owing to high wind speeds that pushed the plume to the ground, preventing the aircraft from flying below the plume (fig. 10). From early December 2005 through early January 2006, increased surface heating and snowmelt, phreatic explosions, and the energetic venting of gas and steam were recorded by the seismic network and observed on overflights (Power and Lalla, this volume; Power and others, 2006; Wessels and others, this volume). The following three measurements, taken on January 4, 9, and 10 near the end of the precursory phase, and just days prior to the first violent Vulcanian explosions, showed a significant rise in SO_2 emissions (6,700, 2,800, and 5,500 t/d, respectively; table 1; fig. 7).

Explosive Phase (January 11–28, 2006)

The explosive phase began with a vigorous swarm of volcano-tectonic (VT) earthquakes early on January 11, followed by two brief (1:18 and 3:18 minutes), ash-poor explosions (fig. 7; Power and Lalla, this volume). Additional explosions reamed a vent through the southern margin of the 1986 lava dome on January 13, 14, and 17. Ash clouds from these events deposited trace amounts of fine ash on communities to the northwest and east and disrupted air traffic (Wallace and others, this volume; Neal and others, this volume). Seismicity characteristic of lava effusion was recognized on January 12, 2006, (Power and others, 2006) and a small new lava dome was observed during a gas flight on January 16, 2006. Lava formed a second lava lobe between January 17 and 27, followed by more explosive events (Coombs and others, this volume).

Three gas-measurement flights with the full instrument package were conducted during the explosive phase (January 16, 19, and 24; table 1, fig. 7*A*). Sulfur dioxide emission rates were high (2,800, 3,000, and 730 t/d) but down somewhat

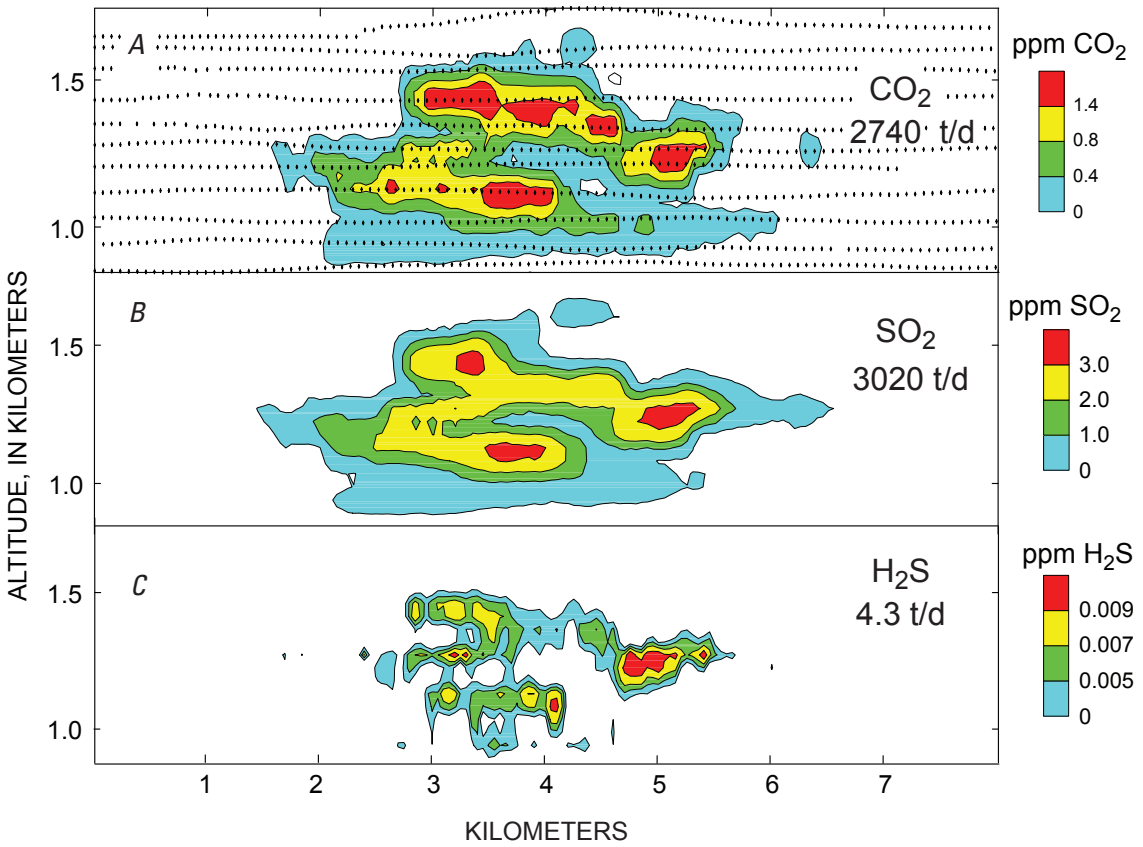

Figure 6. Concentration in a vertical cross-section for the CO_2 (*A*), SO_2 (*B*), and H_2S (*C*) components of the Augustine plume 5 km downwind from summit vent on January 19, 2006. View is upwind toward volcano. The x-axis is the flight distance during the traverses. Contours show concentration of each gas above background with color scale bars to the right. The CO_2 cross-section contains each data point of the traverses used to construct the contours (same points not shown in the SO_2 and H_2S contours). Cross-section of the 4 km-wide plume was constructed with contouring software (Surfer v.8) using exponential kriging models based on variograms fit to the concentration data for the plume. For the example shown, calculated emission rates are 2740 t/d of CO_2, 3,020 t/d of SO_2 and 4.3 t/d of H_2S.

Table 1. Augustine volcanic gas emission rates 2002 to 2008 (data from Doukas and McGee, 2007 and this report).

[Dates of eruption phases separate dates of measurements. Uncertainty derived primarily from wind speed measurements is estimated at plus or minus 19 percent (Doukas, 2002). n=number of traverses, s.d.=standard deviation, nm = not measured, tr = trace, below detection limit, nd = not determined m = minimum result]

Date	COSEC SO_2 t/d	n	s.d.	Interscan SO_2 t/d	LiCor CO_2 t/d	Interscan H_2S t/d	Molar ratio CO_2/SO_2	Distance Downwind km	Wind Speed m/s	Wind Error %	Wind Direction Degrees	T °C	P kpa	Plume Width km
07-01-02	0	5	0	0	0	0	0.0	3	8.8	6%	220	10.2	89.22	0
07-02-02	0	2	0	0	0	0	0.0	2	6.2	x	270	11.5	87.88	0
09-10-02	0	1	0	0	0	nm	0.0	2	nm	nd	180/270	1.4	85.64	0
09-10-02	0	7	0	0	0	nm	0.0	2	nm	nd		3.4	87.21	0
08-03-03	0	4	0	0	0	0	0.0	2	2.7	10%	270	7	88.02	0
08-07-04	0	2	0	0	0	0	0.0	2	3.4	38%	170	16.6	89.82	0
April 30, 2005			Precursory Phase											
05-10-05	0	5	0	0	0	0	0.0	1.5	4.6	26%	120	1.7	87.7	0
12-20-05[m]	660	4	190	nm	nm	nm	nd	4.5	8.7	nd	90	nm	nm	2.1
01-04-06	6,700	4	790	nm	nm	nm	nd	4.5	13.4	nd	100	nm	nm	9.6
01-09-06	2,800	7	520	nm	nm	nm	nd	1.6	6.2	nd	90	nm	nm	3
01-10-06	5,500	2	200	nm	nm	nm	nd	13	10	19%	60	nm	nm	22
January 11, 2006			Explosive Phase											
01-16-06	2,800	4	500	836	1,470	tr	0.8	7	14.5	10%	0	0.9	96.08	2.6
01-19-06	3,000	5	620	1,516	2,700	4.3	1.3	15	6.1	31%	250	-9.8	88.04	7.5
01-24-06	730	5	80	280	500	1	1.0	15	2	80%	300	-21	80.1	8
January 28, 2006			Continuous Phase											
02-08-06	4,000	3	820	nm	nm	nm	nd	7	16.5	19%	110	nm	nm	10
02-13-06	3,400	3	700	nm	nm	nm	nd	8	5.3	28%	300	nm	nm	13.5
02-16-06	7,800	5	990	nm	nm	nm	nd	7	13	nd	230	nm	nm	4.1
February 24, 2006			Hiatus											
02-24-06	8,930	5	630	nm	nm	nm	nd	4.5	6.5	15%	320	nm	nm	2.3
03-01-06	8,650	8	1,130	nm	nm	nm	nd	4.5	5.6	18%	310	nm	nm	2
March 3, 2006			Effusive Phase											
03-09-06	1,130	4	200	340	1,800	0	2.3	13	17.3	4%	350	-12	89.78	2.8
03-10-06	3,200	4	430	390	1,200	0	0.5	10	7	.17%	30	-7.5	82.64	5.1
03-16-06	3,050	5	400	nm	nm	nm	nd	8	9.6	42%	80	nm	nm	8.2
March 16, 2006			Post-eruption Phase											
03-22-06	1,070	6	190	nm	nm	nm	nd	6.3	5.6	nd	50	nm	nm	2.5
03-29-06	1,270	6	190	nm	nm	nm	nd	10	5.5	11%	320	nm	nm	3.2
04-06-06	1,970	6	160	nm	nm	nm	nd	8	6	nd	45	nm	nm	3.9
04-11-06	1,220	5	90	nm	nm	nm	nd	5.8	7.7	13.7%	140	nm	nm	3
04-19-06	1,440	5	180	nm	nm	nm	nd	3.4	3.6	nd	220	nm	nm	5.2
04-27-06	750	5	210	860	660	1.3	1.3	10	18.6	2%	20	1.4	95.28	2.4
05-12-06	400	7	50	nm	nm	nm	nd	6	2.6	nd	40	nm	nm	6.3
05-23-06	230	5	30	nm	nm	nm	nd	11	7	21%	45	nm	nm	3.3
06-02-06	430	6	80	nm	nm	nm	nd	2.6	4.6	14%	330	nm	nm	1.8
07-12-06	500	7	90	nm	nm	nm	nd	4	7.3	3%	25	nm	nm	1.9
08-23-06	530	6	30	nm	nm	nm	nd	3.6	3.3	15%	330	nm	nm	5.4
09-24-06	250	3	56	180	280	1.3	1.6	6.5	4	13%	330	1.25	86.55	5.3
09-25-06	280	5	50	nd	nd	0	nd	7.1	7.8	12%	110	6.54	95.8	5
10-12-06	1,100	2	56	nm	nm	nm	nd	5	10.6	5%	120	nm	nm	7.65
10-23-06	100	2	3	nm	nm	nm	nd	4	16	nd	280	nm	nm	3.6
11-04-06	190	2	15	nm	nm	nm	nd	7.2	4.1	7%	280	nm	nm	4
11-16-06	170	2	43	0	0	0	nd	6.3	13	7%	45	-15.7	80.15	1.8
11-17-06	100	1	0	0	0	0	nd	5	4.3	6%	40	-9.3	84.5	2.8
11-18-06	220	1	0	0	0	0	nd	3	7.3	9%	40	-7.4	88.83	1.5
02-22-07	50	4	8	nm	nm	nm	nd	1.3	4.8	15%	280	nm	nm	1.3
05-18-07	30	4	6	80	94	0.0	4.3	2.8	3.7	8%	90	-4.9	85.88	2
03-14-08	Tr	4	14	nm	180	0		3	3.8	2%	270	-7	88.79	4.2
07-17-08	120	3	17	tr	tr	0	nd	2	5.4	18%	280	9.8	94.1	2.3

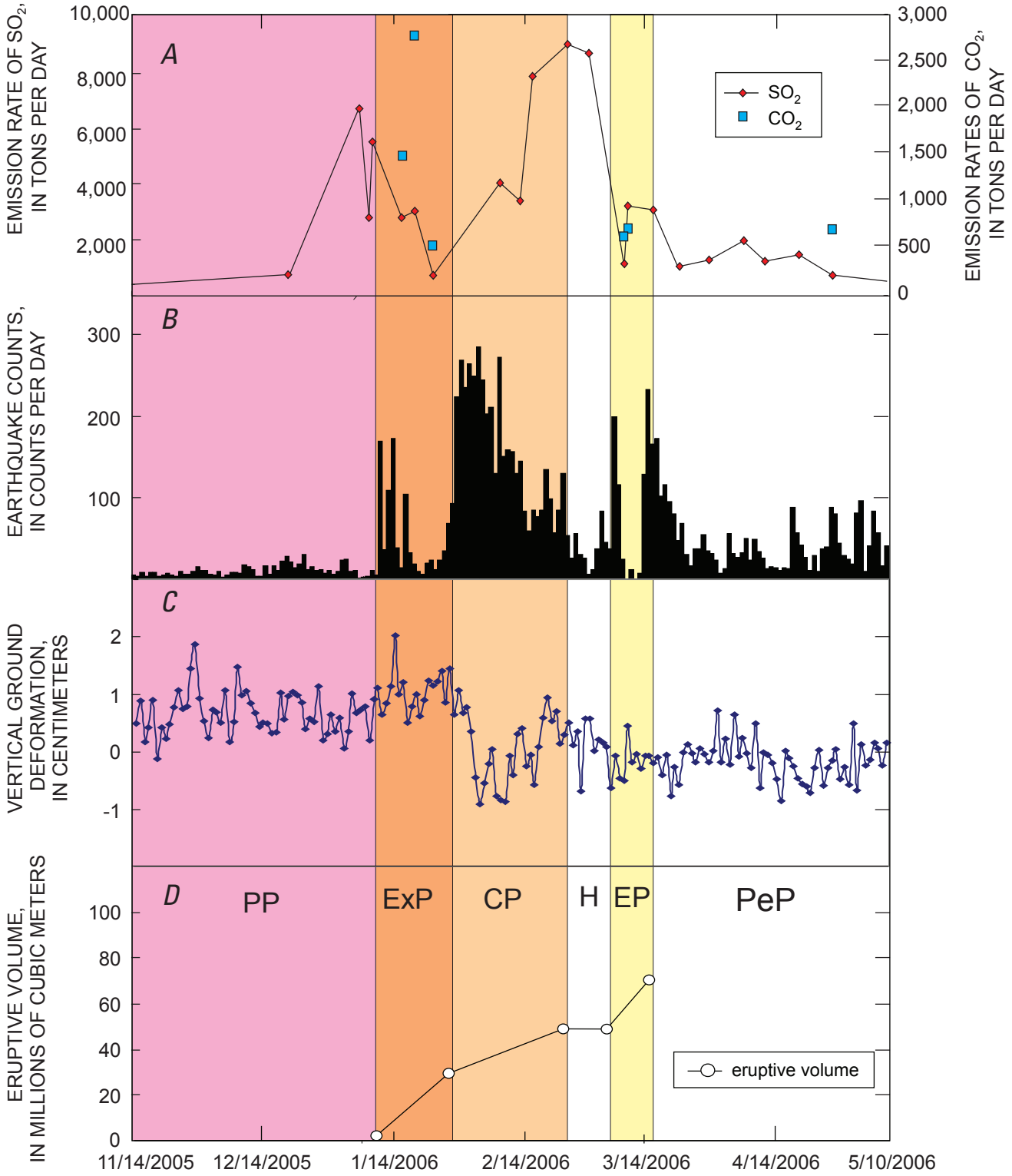

Figure 7. Time series from November 14, 2005, through May 10, 2006, showing: *A*, the measured SO_2 and CO_2 emission rates in tons per day, red diamonds are SO_2 and blue squares are CO_2; *B*, located earthquake counts per day (Power and others, this volume); *C*, the displacement in centimeters measured between CGPS stations A59 and AV02 (Cervelli and others, this volume), *D*, the erupted volume as determined by Coombs and others (this volume). Vertical colored segments in figure represent phases of the 2006 eruption (pre-November data not included). PP, precursory phase beginning April 30, 2005, to January 11, 2006; ExP, explosive phase January 11–28, 2006; CP, continuous phase January 28 to February 10, 2006; H, hiatus February 10 to March 3, 2006; EP, effusive phase March 3–16, 2006; PeP, post-eruption phase March 16, 2006 to July 17, 2008.

from the levels recorded during the precursory phase. CO_2 was measured for the first time since the beginning of the unrest (1,466, 2,740, and 500 t/d). The highest emission rate of H_2S during the eruption, 4.3 t/d, was recorded on January 19. We have no measurements of gas emissions during any of the 13 explosions that occurred between January 11 and 28.

Radar data and pilot reports suggest Augustine injected gases and ash into the stratosphere on as many as four different days during this period (January 11, 13, 17, and 27 (Collins, and others, 2007; Schneider and others, 2006). We estimate from meteorological data (NOAA, Air Resources Laboratory, www.arl.noaa.gov/ready.php, last accessed April 1, 2010) that the tropopause was at about 8.5 to 9.0 km asl above Augustine during this time period.

Infrared based Atmospheric Infrared Sounder (AIRS) satellite detected the SO_2 clouds during January 28 and 29, 2006. Prada (2006) reported that .0025 to .0041 Tg (2,500–4,100 t/d) were ejected into the atmosphere during the explosive events on these days. Early satellite measurements showed SO_2 eruption clouds represented equal to or above quiescent SO_2 emission rates (fig. 11). The AIRS satellite detected SO_2 in the stratosphere, so the values reported are probably minimums due to the missed SO_2 below 8 to 9 km. The first satellite measurements suggest measurements of the quiescent plumes with emission near 3,000 t/d (fig. 11). Later, measurements may represent syneruptive SO_2 plumes. These clouds did not contain the syneruptive amounts of SO_2 typical of explosive eruptions.

Ozone Monitoring Instrument (OMI) satellite determinations of SO_2 were unavailable during this time interval (Simon Carn, oral communication, 2008) owing to low winter UV levels. Not until March and at lower latitudes (Nevada) were OMI satellite results available.

Continuous Phase (January 28–February 10, 2006)

A continuous eruption phase began on January 28 and was characterized by nearly constant, low-altitude tephra emission and rapid andesitic dome extrusion, high rates of shallow seismicity, and steady deflation of the edifice. Repeated collapses of the growing dome and overlapping lobes of lava extending to the north beyond the margin of the 1986 lava dome produced block-and-ash flows intermittently through February 10, 2006 (Vallance and others, this volume; Coombs and others, this volume). Gas and ash plumes during this phase penetrated the tropopause on at least two days (January 28 and 29; Bailey and others, this volume); however, most ash plumes remained below 6,000 m asl. A gas measurement on February 8 (table 1, fig. 7*A*) during the continuous phase yielded an emission of 3,960 t/d SO_2, a value similar to those calculated during the late precursory and early explosive phases. SO_2 was detected (but no value derived) in the eruption cloud from January 29–30 by satellite (Dean and others, 2006). We have no CO_2 data from the continuous phase.

Hiatus (February 10–March 3, 2006)

Careful analysis of photography and other observations reveal no evidence of significant additional accumulation of lava in the summit crater from February 10 through March 3 (Coombs and others, this volume). Low levels of seismicity also suggest that the eruption was in a pause during this interval (Power and Lalla, this volume). Interestingly, of the four gas measurements made during the hiatus, three recorded the highest SO_2 emission rates of the eruption (7,800, 7,930, and 8,650 t/d; table 1; fig. 7*A*).

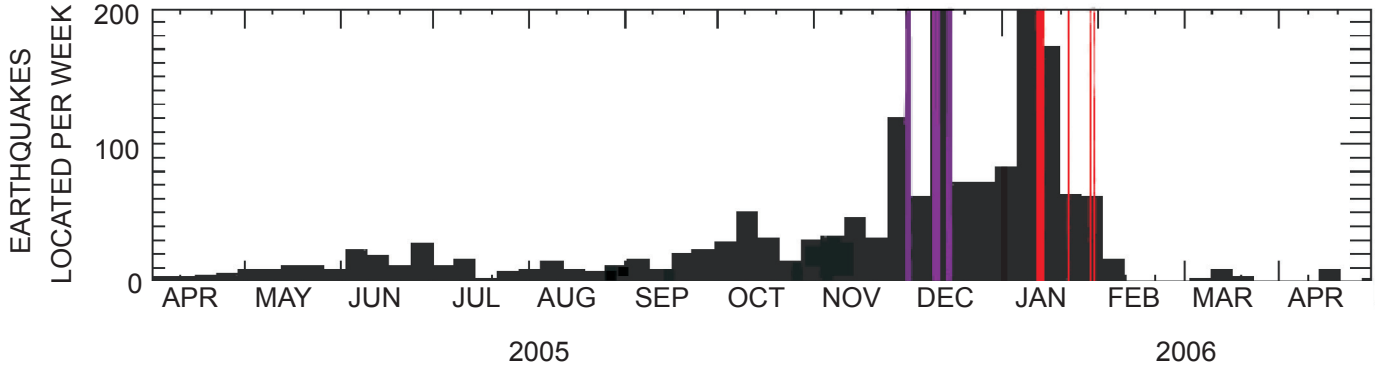

Figure 8. Earthquake counts from April 2005 through April 2006 showing the gradual increase of located earthquakes during 2005 (from Power and Lalla, this volume). Purple and red lines correspond to approximate times of phreatic and magmatic explosions, respectively (Power and Lalla, this volume).

Effusive Phase (March 3–16, 2006)

On March 3, increasingly frequent rockfall signals on seismometers suggested a return to active lava effusion and resulting instability of the dome as new material was added to the surface and lava flow fronts advanced. Over the next 2 weeks, more or less continuous eruption of lava from a single vent in the summit dome marked the final activity of the effusive phase of the eruption (EP, fig. 7*D*). The top of the growing dome eventually reached an elevation more than 100 m higher than the preeruption summit of the 1986 lava dome. Collapse of the fronts of two primary lava flow lobes produced block-and-ash flows down the north and northeast flank of Augustine especially during the early portion of the effusive phase. The end of the phase coincided with cessation of drumbeat earthquakes, which were recorded from March 7 to March 16 (Power and Lalla, this volume). Three SO_2 emission measurements during this period range from 1,130 t/d to 3,050 t/d, values in the low to moderate range for the eruption. Two emission rates for CO_2, however, were showing decline in the eruption sequence—590 and 680 t/d.

Post-eruption Phase (March 16, 2006–July 17, 2007)

Twenty-one additional gas measurement flights made from April 2006 to July 2008 show SO_2 emission rates declining from more 1000 t/d to less than or equal to 120 t/d (table 1). We define the end of the post-eruption phase as the date when SO_2 emissions reached levels of 50 t/d. A single helicopter-borne flight in July 2008 measured 120 t/d, revealing latent degassing was still possible at the volcano. These final low values of SO_2 emission are similar to those observed following the 1986 eruption of Augustine when, within 8 months of the end of the eruption, 45 t/d was measured (Symonds and others, 1990). Similarly, emission rates for CO_2 went from 660 t/d on April 27, 2006, to 94 t/d in May 2007. H_2S levels were typically very low (1.3 t/d) or not quantifiable through the last measurement in July 2008.

Discussion

Changing SO_2, CO_2, and H_2S emissions pre-, syn-, and post-eruption can be interpreted in the context of other monitoring and observational data to infer characteristics of changing magma supply and residence at shallow levels beneath and within the volcano (fig. 7). The following discussion is limited somewhat by the lack of equivalently detailed time series data for all three gas species, in addition to a paucity of gas output measurements by satellite or other means during individual explosive events.

Sulfur dioxide largely disappeared from the plume and fumarole gases of Augustine in the months following the 1986 eruption, indicating no further influx of fresh magma

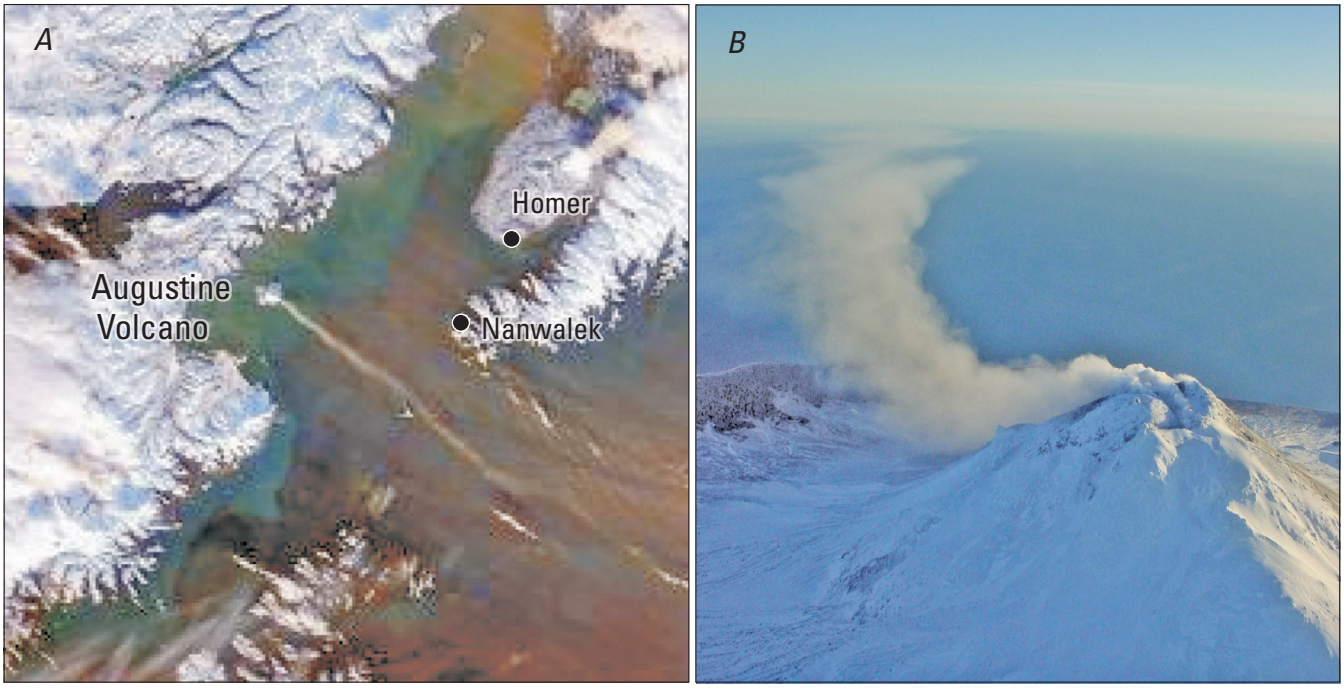

Figure 9. *A*, December 12, 2005, MODIS satellite view of lower Cook Inlet, Alaska, showing Augustine Volcano, as the source of a long narrow plume extending Southeast towards the southern portion of the Kenai Peninsula (image courtesy of the Geographic Information Network of Alaska (GINA)). *B*, December 12, 2005, photograph of an ashy plume extending from summit fumaroles to the southeast. Photo by R.G. McGimsey.

shallower than about 4 km below the summit (Doukas, 1995; Symonds and others, 1990; Symonds and others, 2003). Influx of water (both meteoric and seawater; Symonds and others, 1990) into the lower edifice likely consumed any residual SO_2 from the cooling 1986 magma by hydrolysis reactions. Indeed, annual airborne measurements at Augustine detected no SO_2 until December 2005, when precursory activity at Augustine was well advanced. It is notable that neither SO_2 nor CO_2 (CO_2 is a gas not easily scrubbed by water) were detected on a May 2005 flight during the earliest stage of the recent unrest. Cervelli and others (2006) suggest that a sea-level pressure source might have been present under the volcano by May 2005. If so, the lack of detected CO_2, which would have been significantly oversaturated in the magma at that shallow depth, suggests that the pressure source was not magmatic in origin but more likely resulted from an invigorated, expanding hydrothermal system being heated from below. Cervelli and others (this volume) conclude that this early deformation signal was not from a magma body. The corresponding lack of SO_2 is also consistent with no significant shallow (<4 km, sea level is approx 1.5 km) magma body at that time.

By late November 2005, magma likely rose to within several kilometers of the surface; shallow enough to degas SO_2 to the atmosphere and drive phreatic explosions. An airborne

Figure 10. Wind-depressed plume during the gas flight of December 20, 2005. Plumes from fumaroles were pushed down to the ground making COSPEC measurements difficult and minimizing the emission rate for that day. Photo by R.G. McGimsey.

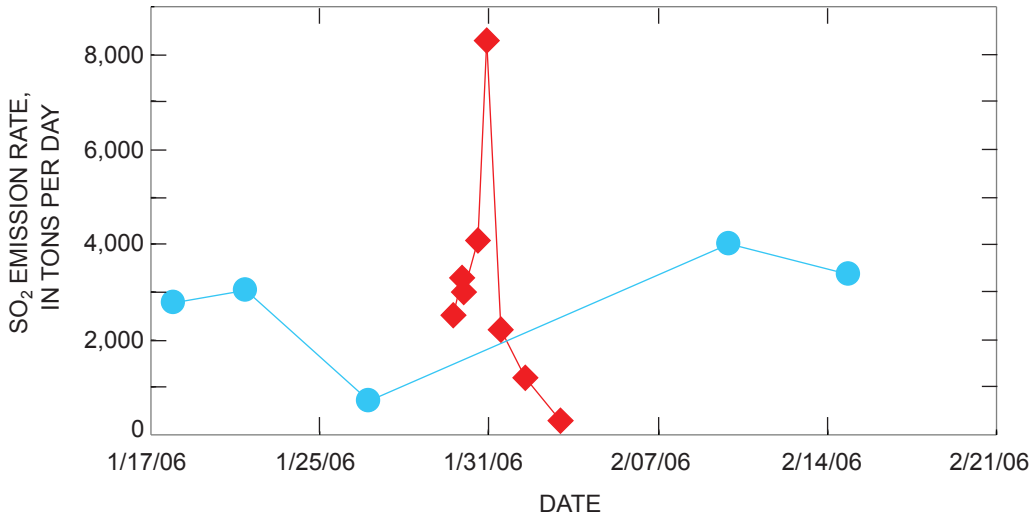

Figure 11. Airborne COSPEC emission rates (blue circles) and infrared AIRS satellite SO_2 determinations (red diamonds; F. Prada, written commun., 2009) during January 2006. AIRS satellite results are measurements of SO_2 in the stratosphere.

measurement on December 20, 2005, detected SO_2 at Augustine for the first time since 1987. A minimum emission rate of 660 t/d was measured on that flight (fig. 10, table 1; wind conditions prevented traverses completely beneath the plume, resulting in a minimum emission rate.). During December, observers also noted large white plumes that suggested the release of large amounts of water vapor from the volcano as it continued to heat up. ASTER thermal infrared (TIR) images of Augustine taken on December 20 showed a broad area of new snow-free ground and fumaroles at the summit, and forward-looking infrared (FLIR) surface-temperature measurements on December 22 indicated the temperature of a fumarole on the south flank was 210°C and the summit moat area at 80°C (Wessels and others, this volume). By January 4, 2006, the surface temperature of the moat area had increased to 390°C. Based on reports from residents in the village of Nanwalek on the lower Kenai Peninsula of strong "rotten egg" odors, it is likely that a significant portion of sulfur emissions from Augustine during the precursory stage were in the form of H_2S, consistent with earlier scrubbing of SO_2 by water and subsequent boiling of the fluid to create H_2S (Symonds and others, 2001). Further, during a FLIR flight on December 22, 2006, observers noted that fume emitted from a fumarole on the southeast base of the 1986 Augustine dome was distinctly pale yellow-green in color. We believe this was likely due to the transient presence of native sulfur in the plume produced by the reaction of H_2S and SO_2 (Symonds and others, 1994; Kodosky and others, 1991). Based on GPS measurements, dike propagation into the edifice started on November 17, 2005, a month earlier, and Cervelli and others (2006) conclude that magma was shallow enough by the time of the December 20, 2005, gas measurement to allow CO_2 and H_2S to escape, along with SO_2, and become incorporated into the plume. It is not possible, however, to confirm this because CO_2 and H_2S measurements were not made during this period.

By early January 2006, continued heating of the Augustine summit by the shallow magma had dried out the shallow hydrothermal system thereby limiting scrubbing effectiveness. The volcano was emitting SO_2 in large amounts with emission rates reaching 6,700 t/d (table 1; fig. 7*A*). On January 11, 2006, either the gas-filled dike tip arrived at the surface or a highly pressurized shallow hydrothermal system was breached, resulting in a series of explosions with little, if any, juvenile material ejected (Coombs and others, this volume; Wallace and others, this volume). SO_2 emission rates began to drop by more than half and finally to below 1,000 t/d near the end of the explosive period on January 28. This drop could reflect relative depletion in the volume of near-surface, SO_2-charged magma along with a temporary lack of replenishment. Similarly, CO_2 measurements during the explosive phase showed high CO_2 at the beginning (1,400–2,700 t/d) but dropping to 500 t/d by the end of the period. The continuing trend of inflation of the edifice throughout the explosive period (fig. 7*C*), however, suggests a net mass or pressure increase. An alternative explanation for the relatively low gas values during this time is a repetitive sealing of the shallow conduit system that prevented complete gas escape to the surface but contributed to pressurization seen as inflation.

Interestingly, on the gas-measurement flight of January 16, 2006, observers noticed a yellow-orange plume in the largely white vapor cloud enveloping the new lava dome within the summit crater (fig. 12). As noted earlier, the highest H_2S emission rate of the eruption was measured during this time (table 1). We believe the yellow-orange plume, like the colored plume observed on December 22, 2005, was native sulfur, produced at a single vent under just the right conditions of temperature and concentrations of gas streams rich in SO_2 and H_2S. This reaction possibly could reduce H_2S as seen in the trace amount measured that day. Production of native sulfur is achieved in industry using the Claus process ($2H_2S + O_2 \rightarrow S_2 + 2H_2O$) where gases rich in H_2S (>25%) at high temperatures burn to produce sulfur and water. An accompanying process with H_2S and SO_2 reacting together can reduce H_2S to native sulfur ($2H_2S + SO_2 \rightarrow 3S + 2H_2O$). The high-temperature fumarole at the base of the 1986 dome probably was a

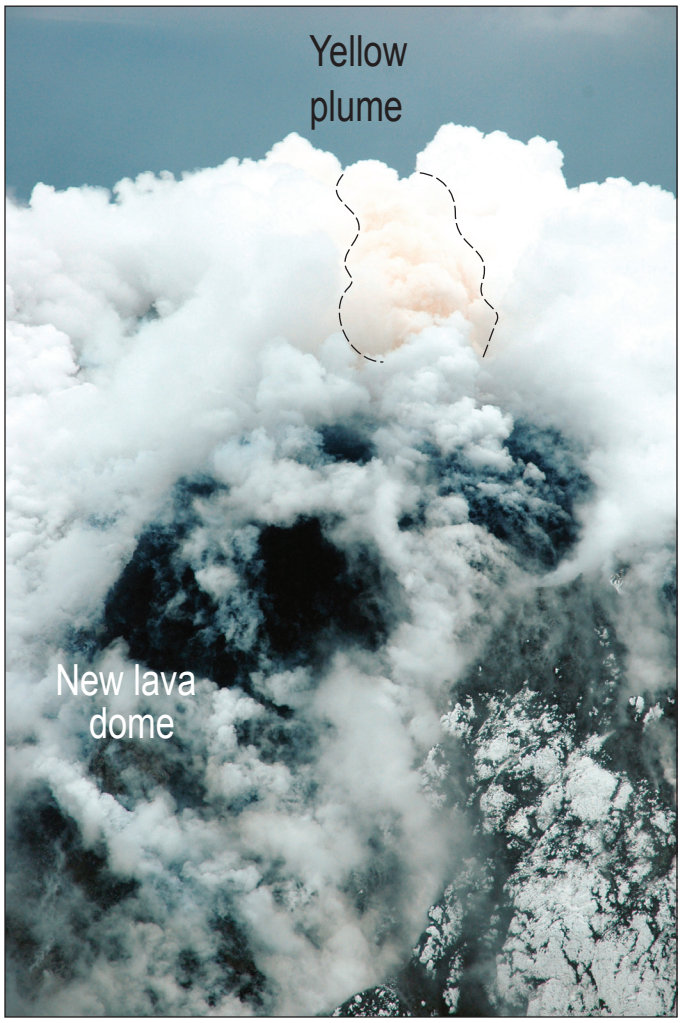

Figure 12. Yellow plume venting from summit of Augustine Volcano. View to the southwest. Dark mass below and left of yellow plume is first sighting of a lava dome mass (January 16, 2006). Dashed line outlines yellow part of plume. Photo by R.G. McGimsey.

source for this plume (Wessels and others, this volume). After January 19, 2006, H_2S emission rates declined and no further yellow plumes were observed during the eruption.

Moderate to high SO_2 emissions—similar in magnitude to those measured during the explosive phase—persisted during the continuous phase of the eruption and into the very early days of the hiatus as reflected in two airborne measurements on February 8 and 13 (table 1; fig. 7*A*). During the continuous phase, intense seismicity due to rapid extrusion and explosive disruption of blocky andesitic lava was accompanied by marked deflation of the volcano as magma was withdrawn to feed surface activity (Power and others, 2006; Coombs and others, this volume; Cervelli and others, this volume).

The onset of a hiatus in extrusion and a return to a very weak inflationary signal (Cervelli and others, this volume) on February 10 at first saw no significant change in SO_2 emission (fig. 7). However, SO_2 emission rates more than doubled on February 16 and remained high until the onset of rapid effusion (Coombs and others, this volume) and weak shallow deflation in early March (Cervelli and others, this volume). In fact, the highest SO_2 emission rates measured during the entire eruption occurred during this 3-week pause in extrusion, accompanied by low rates of seismicity and an overall weak inflationary trend (fig. 7). Several factors may have contributed to the high SO_2 during the hiatus. The high eruption rates and conduit drawdown of the continuous phase (fig. 7; Coombs and others, this volume) may have resulted in an open, hot, and dry pathway in the upper few kilometers of the conduit facilitating degassing of residual melt. Alternatively (or in addition), the inflationary signal during the hiatus may reflect recharge of the shallow conduit system with fresh, gas-rich melt that lacked sufficient time to reach the surface but was able to degas freely. Unfortunately, we have no CO_2 emission rate data for the hiatus.

The hiatus ceased on March 6 marked by the return of strong shallow seismicity and a deflationary signal as seen on GPS (fig. 7*C*). March 9 and 10 had relatively high CO_2 emission rates; at the same time, SO_2 emission rates were near the lower end of their range during the eruption. The plume was visually dramatic on these days (fig. 13). The high CO_2 probably reflected deep recharge of magma (see below) at depths below the SO_2 exsolution level. High CO_2 and heat flux could have been the response of the rapid extrusion of largely degassed lava in early March feeding the north and northeast lava flow lobes and associated block-and-ash flows (Coombs and others, this volume). The next measurement of CO_2 was at the end of April, by which time it had dropped to about 600 t/d, confirming that the influx of new magma had stopped.

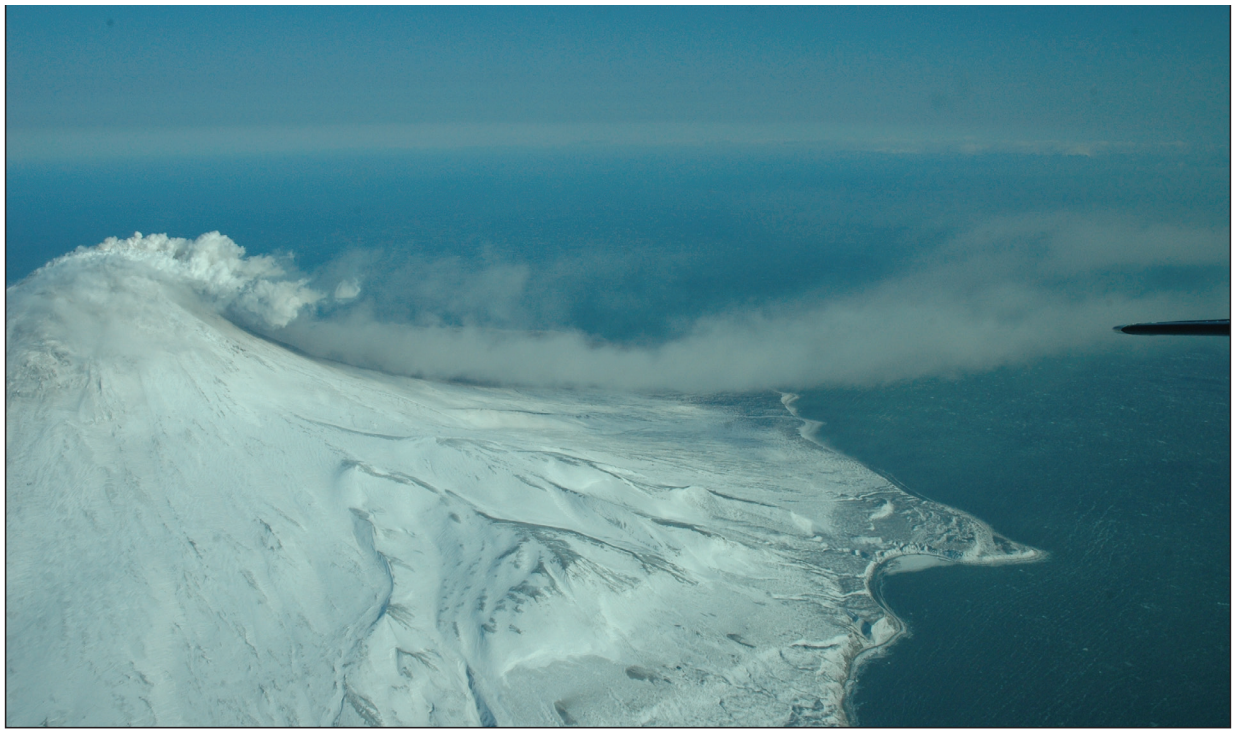

Figure 13. Gas plume from Augustine Volcano. White condensate plume is short lived, while gases and aerosols continue down wind. View to the east. Photo by R.G. McGimsey.

Evaluating CO_2/SO_2 Ratios

Seven instances of simultaneous airborne plume measurements of CO_2 and SO_2 during 2006 provide the opportunity to compute a CO_2/SO_2 ratio for those days (fig. 14). The mean molar ratio is 1.1 with a standard error of ±0.4.

The CO_2/SO_2 measured on March 9, 2006, (0.8 under a mean of 1.1) occurred during the effusive phase (EP), a period of intense seismicity that began in early March, increased to a nearly continuous signal by March 8, and lasted until March 14 (Power and others, this volume). This was also a period of weak deflation of the edifice (Cervelli and others, this volume) and partly reflects no new CO_2 or additional magma rising from depths up towards the surface to feed the eruption, and SO_2 being depleted from a shallower magma source. By May 2007 the molar ratio had climbed to 4.3, higher than the eruptive values (not used in the mean ratio calculation). Melting of the snow pack of winter 2006–7 added water to the shallow hydrothermal system in the summit, thus aiding in the scrubbing of residual sulfur gases and raising the ratio.

The mean molar CO_2/SO_2 value of 1.1 for Augustine during the eruption is not out of line with that of other active Cook Inlet volcanoes. Casadevall and others (1994) report an average CO_2/SO_2 of about 2 for the 1989–90 eruption of Redoubt Volcano. Molar CO_2/SO_2 values of 10 ranging to as great as 100 were noted for the gases produced by the 1992 eruption of Crater Peak, although the higher ratios were almost certainly due to the masking of SO_2 emissions by aqueous scrubbing (Doukas and Gerlach, 1995). During 1980–81 when CO_2 was measured at Mount St. Helens, CO_2/SO_2 ratios averaged about 8, while during 2004–5 the median CO_2/SO_2 was about 11; this difference was also attributed to scrubbing (Gerlach and others, 2008). In general, unless the magma is degassing through liquid or boiling water, it appears that CO_2/SO_2 values for convergent-plate volcanoes typically fall in the range 1 to 12 (Doukas and Gerlach, 1995; Marty and Le Cloarec, 1992; Williams and others, 1992).

SO_2 Emission Rates in Previous Augustine Eruptions

Two earlier eruptions of Augustine allow comparisons with peak SO_2 emission rates measured during 2006. Although the peak emission rates measured during the last three eruptions are different, other evidence suggests that the total SO_2 output for the Augustine eruptions in 1976, 1986, and 2006 were likely similar in magnitude.

During the 2006 unrest, the highest measured SO_2 emission rate was 8,930 t/d, only about one-third the peak values reported in 1976 and 1986. This could imply that the earlier eruptions were larger or more gas-rich events or simply reflect that during 2006 a measurement was not made on a day when SO_2 emissions were at their highest levels. Regardless, we believe total SO_2 emissions for the past three eruptions of Augustine are roughly similar. Eruptive volume estimates for the 1976, 1986, and 2005–6 eruptions of 0.39, 0.26, and 0.12×10^6 m^3, respectively (bulk volumes; Coombs and others, this volume) suggest that the recent event was smaller; however, limited gas data do not permit an in-depth comparison of total gas emissions from the three eruptions.

Comparison to Anthropogenic Emissions

Without quantitative emissions data it would be difficult to evaluate the volcanic contribution of greenhouse gases, such as CO_2, to the atmosphere. Augustine, even with its characteristically short interval between eruptions, illustrates that the volcanic contribution is likely not significant over time.

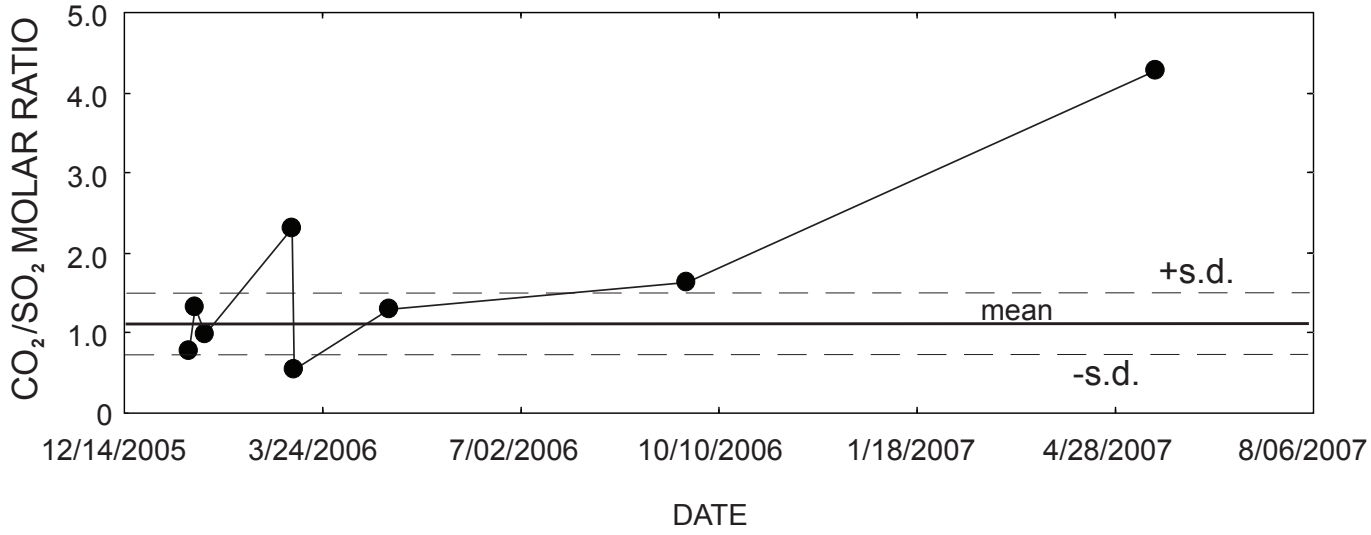

Figure 14. Molar CO_2/SO_2 for all the days when CO_2 and SO_2 were measured simultaneously. The mean molar ratio of the points (not counting the 4.3 ratio measured in 2007) is 1.3 (middle horizontal line) with a standard deviation of ±0.69.

Some volcanoes passively emit low levels of gases for decades or more (McGee, 2001). Others, like Augustine, become restless and emit gases for a few months and then become quiet again. In the case of Augustine, the repose periods between the five eruptions since the beginning of the twentieth century are 29, 11, 10, and 20 years. On the basis of CO_2 measurements reported here and using linear extrapolating to a full year, we estimate a total CO_2 output of 1.96×10^5 tons of CO_2 for Augustine in 2006, the year encompassing the majority of the most recent eruption. This is similar to the 1.2×10^6 tons of CO_2 emitted by the Beluga natural gas-fired powerplant on the west side of the Cook Inlet near Tyonek in 2004 (fig. 1) and significantly less than the output of most of the U.S. coal-fired power generation plants, some of which produce more than 20×10^6 million tons of CO_2 per year (U.S. Environmental Protection Agency, 2007). No CO_2 data exist for the earlier eruptions of Augustine. Even though Augustine erupts frequently, every 17.5 years on average since the beginning of the last century, it is clear that the greenhouse gas output of Augustine is negligible compared to the several hundred power plants of all fossil fuel types currently operating in the United States. Augustine's 2006 eruption might be considered a typical size for an average eruption worldwide (for example, volcanic explosivity index = 3, 0.01–0.1 km^3 of eruptive products; Simkin and Siebert, 1994). Using estimates from Casadevall and others (1994) for the total emission rate of SO_2 (1×10^6 tons) and the molar CO_2/SO_2 (~2) for the 1989–90 eruption of Redoubt Volcano, we can compute a total CO_2 emission rate of 1.4×10^6 tons for a similar-sized eruption of another Cook Inlet volcano.

From these data it is clear that even if several volcanoes like Augustine erupted continuously for a decade or even a century, they would still be negligible greenhouse gas contributors to the atmosphere compared to current anthropogenic sources of CO_2 emission. One of the largest continuous volcanic carbon dioxide sources on Earth is Kilauea Volcano, which emits about 9,000 tons of CO_2 a day (Gerlach and others, 2002). This amounts to 3.3×10^6 tons of CO_2 annually, still considerably less than the yearly output of a single large coal-fired powerplant (U.S. Environmental Protection Agency, 2007). Thus it appears that volcanoes are currently not significant contributors of greenhouse gases to the atmosphere compared to power generation plants.

We also estimate that Augustine emitted about 6.3×10^5 tons of SO_2 during 2006, slightly more than half the amount of CO_2 produced. Although not a greenhouse gas, SO_2 combines readily with water droplets to form aerosols and can fall as acid rain or cause cooling if injected into the upper atmosphere. The SO_2 output of Augustine during 2006 is equivalent to several coal-fired powerplants, but the short duration of the eruption insures that any impact from acid rain or acid-coated ash particles will be comparatively small. Further, given Augustine Volcano's island location and relatively low elevation, much of the gas from Augustine during 2006, with the exception of several days in January, was discharged at low elevation into the troposphere, and most of any resulting acid rain likely fell into the ocean or on sparsely inhabited land areas downwind. From early 2007 through the summer of 2008, the SO_2 output of Augustine was about 100 t/d and is expected to fall to near zero within several years as it has following the previous two eruptions.

Conclusions

1. The similar nature of recent Augustine eruptions points to generalizations regarding the timing and eruptive behavior of the volcano as well as to generalizations about the nature and magnitude of its gas emissions.

2. Geochemical surveillance of Augustine since the 1986 eruption indicates that degassing declines essentially to nil within 1 to 2 years after an eruption and does not resume to a measurable level until magma once again ascends toward the surface. This is likely due to abundant ground and hydrothermal waters available to scrub any acid gases released from remnant magma once the system cools down.

3. Although the number of plume measurements for SO_2 during the eruption is not large, the available evidence suggests that, in general, once magma is within hundreds of meters of the surface and an open pathway exists between magma and the surface, SO_2 emissions will increase. The measured SO_2 output decreased during the explosive and continuous phases but increased again during the hiatus phase of the activity prior to the final rapid effusion phase. The highest SO_2 emission rates were achieved during the early part of the hiatus, whereas the highest measured CO_2 emission rates were measured about 1 month earlier during inflation and explosive activity in January. This is in line with the idea that more SO_2 will be released as magma intrudes to shallow levels and lower pressures. High emission rates for CO_2 should be detected as deeper CO_2-rich magma moves toward the surface and discharges its load of CO_2 while still deep enough to inhibit SO_2 outgassing, although the scant CO_2 measurements do not conclusively illustrate this.

4. Emissions measurements yield an average molar CO_2/SO_2 value of about 1.3 ± 0.7 for the 2006 eruption of Augustine, similar to typical values of 1 to 12 reported for other convergent plate boundary volcanoes.

5. Augustine is not a significant contributor to the atmospheric load of greenhouse gases compared to anthropogenic sources. In 2006, Augustine released about 1.9×10^5 tons of CO_2, a level similar to the output of a medium-sized natural-gas-fired powerplant. Augustine also released about 8×10^5 tons of SO_2 during the 2006 eruption. Evidence from other investigators suggests that the sulfur dioxide output in the 1976 and 1986 eruptions was of similar magnitude to that measured in 2006.

Acknowledgments

We would like to acknowledge the skilled and dedicated pilots and staff of Security Aviation in Anchorage for providing safe and effective air support. Comments by Tobias Fischer, Cynthia Werner, Michelle Coombs, and William Scott were appreciated in improvement of the manuscript.

References Cited

Bailey, J.E., Dean, K.G., Dehn, J., and Webley, P.W., 2010, Integrated satellite observations of the 2006 eruption of Augustine Volcano, *in* Power, J.A., Coombs, M.L., and Freymueller, J.T., eds., The 2006 eruption of Augustine Volcano, Alaska: U.S. Geological Survey Professional Paper 1769 (this volume).

Casadevall, T.J., Doukas, M.P., Neal, C.A., McGimsey, R.G., and Gardner, C.A., 1994, Emission rates of sulfur dioxide and carbon dioxide from Redoubt Volcano, Alaska, during the 1989–1990 eruptions, *in* Miller, T.P., and Chouet, B.A., eds., The 1989–1990 Eruptions of Redoubt Volcano, Alaska: Journal of Volcanology and Geothermal Research, v. 62, p. 519–530.

Cervelli, P.F., Fournier, T.J., Freymueller, J.T., and Power, J.A., 2006, Ground deformation associated with the precursory unrest and early phases of the January 2006 eruption of Augustine volcano, Alaska: Geophysical Research Letters, v. 33, p. 1–5, L18304 , doi: 10.1029/2006GL027219.

Cervelli, P.F., Fournier, T.J., Freymueller, J.T., Power, J.A., Lisowski, M., and Pauk, B.A., 2010, Geodetic constraints on magma movement and withdrawal during the 2006 eruption of Augustine Volcano, *in* Power, J.A., Coombs, M.L., and Freymueller, J.T., eds., The 2006 eruption of Augustine Volcano, Alaska: U.S. Geological Survey Professional Paper 1769 (this volume).

Collins, R.L., Fochesatto, J., Sassen, K., Webley, P.W., Atkinson, D.E., Dean, K.G., Cahill, C.F., and Kohei, M., 2007, Predicting and validating the motion of an ash cloud during the 2006 eruption of Mount Augustine Volcano, Alaska, USA: Journal of the National Institute of Information and Communications Technology, v. 54, no. 1/2, p. 17–28.

Coombs, M.L., Bull, K.F., Vallance, J.W., Schneider, D.J., Thoms, E.E., Wessels, R.L., and McGimsey, R.G., 2010, Timing, distribution, and volume of proximal products of the 2006 eruption of Augustine Volcano, *in* Power, J.A., Coombs, M.L., and Freymueller, J.T., eds., The 2006 eruption of Augustine Volcano, Alaska: U.S. Geological Survey Professional Paper 1769 (this volume).

Dean, K.G., Dehn, J., Wallace, K.L., Prata, F., and Cahill, C.F., 2006, The distribution and movement of volcanic ash and SO_2 observed in satellite data from the eruption of Augustine volcano, 2006 [abs]: Eos (American Geophysical Union Transactions), v. 87, no. 52, Fall Meeting Supplement, abstract V41F-05.

Doukas, M.P., 1995, a compilation of sulfur dioxide and carbon dioxide emission-rate data from Cook Inlet volcanoes (Redoubt, Spurr, Iliamna, and Augustine), Alaska, during the period from 1990 to 1994: U. S. Geological Survey Open-File Report 95-55, 15 p.

Doukas, M.P., 2002, A new method for GPS-based wind speed determinations during airborne volcanic plume measurements: U.S. Geological Survey Open-File Report 02-395, 13 p.

Doukas, M.P., and Gerlach, T.M., 1995, Sulfur dioxide scrubbing during the 1992 eruptions of Crater Peak, Mount Spurr Volcano, Alaska, *in* Keith, T.E.C., ed., The 1992 Eruptions of Crater Peak Vent, Mount Spurr Volcano, Alaska: U.S. Geological Survey Bulletin 2139, 220 p.

Doukas, M.P. and McGee, K.A., 2007, A compilation of gas emission-rate data from volcanoes of the Cook Inlet (Spurr, Crater Peak, Redoubt, Iliamna, and Augustine) and the Alaska Peninsula (Douglas, Fourpeaked, Griggs, Mageik, Martin, Peulik, Ukinrek Maars, and Veniaminof), Alaska from 1995–2006: U.S. Geological Survey Open-File Report 2007-1400, 13 p.

Gerlach, T.M., Delgado, H., McGee, K.A., Doukas, M.P., Venegas, J J., and Cardenas, L., 1997, Application of the LI-COR CO_2 analyzer to volcanic plumes; A case study, Volcán Popocateptl, Mexico, June 7 and 10, 1995: Journal of Geophysical Research, v. 102, p. 8005–8019.

Gerlach, T.M., Doukas, M.P., McGee, K.A., and Kessler, R., 1999, Airborne detection of diffuse carbon dioxide at Mammoth Mountain, California: Geophysical Research Letters, v. 26, p. 3661–3664.

Gerlach, T.M., McGee, K.A., Elias, T., Sutton, A.J., and Doukas, M.P., 2002, Carbon dioxide emission rate of Kilauea Volcano—Implications for primary magma and the summit reservoir: Journal of Geophysical Research, v. 107, no. B9, 2189–2204, doi:10.1029/2001JB000407.

Gerlach, T.M., McGee, K.A., and Doukas, M.P., 2008, Emission rates of CO_2, SO_2, and H_2S, scrubbing, and preeruption excess volatiles at Mount St. Helens, 2004–2005, chap. 26 *in* Sherrod, D.R., Scott, W.E., and Stauffer, P.H., eds., A volcano rekindled; the renewed eruption of Mount St. Helens, 2004–2006: U.S. Geological Survey Professional Paper 1750, p. 543-571.

Kienle, J., and Swanson, S.E., 1983, Volcanism in the eastern Aleutian arc; Late Quaternary and Holocene centers, tectonic setting and petrology: Journal of Volcanology and Geothermal Research, v. 17, p. 393–432.

Kodosky, L.G., Motyka, R.J., and Symonds, R.B., 1991, Fumarolic emissions from Mount St. Augustine, Alaska; 1979–1984 degassing trends, volatile sources and their possible role in eruptive style: Bulletin of Volcanology, v. 53, p. 381–394.

Marty, B., and Le Cloarec, M.-.F, 1992, Helium-3 and CO_2 fluxes from subaerial volcanoes estimated from polonium-210 emissions: Journal of Volcanology and Geothermal Research, v. 53, p. 67–72.

McGee, K.A., Doukas, M.P., and Gerlach, T.M., 2001, Quiescent hydrogen sulfide and carbon dioxide degassing from Mount Baker, Washington: Geophysical Research Letters, v. 28, p. 4479–4482.

McGee, K.A., Doukas, M.P., McGimsey, R.G., Neal, C.A., and Wessels, R.L., 2008, Atmospheric contribution of gas emissions from Augustine volcano, Alaska during the 2006 eruption: Geophysical Research Letters, v. 35, L03306, doi: 10.1029/2007GL032301, 5 p.

Miller, T.P., McGimsey, R.G., Richter, D.H., Riehle, J.R., Nye, C.J., Yount, M.E., and Dumoulin, J.A., 1998, Catalog of historically active volcanoes of Alaska: U.S. Geological Survey Open-File Report 98-582, 104 p.

Neal, C.A., Murray, T.L., Power, J.A, Adleman, J.N., Whitmore, P.M., and Osiensky, J.M., 2010, Hazard information management, interagency coordination, and impacts of the 2005–2006 eruption of Augustine Volcano, *in* Power, J.A., Coombs, M.L., and Freymueller, J.T., eds., The 2006 eruption of Augustine Volcano, Alaska: U.S. Geological Survey Professional Paper 1769 (this volume).

Power, J.A., and Lalla, D.J., 2010, Seismic observations of Augustine Volcano, 1970–2007, *in* Power, J.A., Coombs, M.L., and Freymueller, J.T., eds., The 2006 eruption of Augustine Volcano, Alaska: U.S. Geological Survey Professional Paper 1769 (this volume).

Power, J.A., Nye, C.J., Coombs, M.L., Wessels, R.L., Cervelli, P.F., Dehn, J., Wallace, K.L., Freymueller, J.Y., and Doukas, M.P., 2006, The reawakening of Alaska's Augustine volcano: Eos (American Geophysical Union Transactions), v. 87, no. 37, p. 373–377.

Prada, F., 2006, Augustine: Bulletin of the Global Volcanism Network v. 31, issue 01.

Rose, W.I., Heiken, G., Wohletz, K., Eppler, D., Barr, S., Miller, T., Chuan, R.L., and Symonds, R.B., 1988, Direct rate measurements of eruption plumes at Augustine volcano: A problem of scaling and uncontrolled variables: Journal of Geophysical Research, v. 93, p. 4485–4499.

Schneider, D.J., Scott, C., Wood J., and Hall T., 2006, NEXRAD weather radar observations of the 2006 Augustine volcanic eruption clouds [abs.]: Eos (American Geophysical Union Transactions), v. 87, abstract V51C-1686.

Simkin, T., and Siebert, L., 1994, Volcanoes of the World (2nd ed.): Tucson, Arizona, Geoscience Press, Inc., 349 p.

Stith, J.L., Hobbs, P.V., and Radke, L.F., 1978, Airborne particle and gas measurements in the emissions from six volcanoes: Journal of Geophysical Research, v. 83, p. 4009–4017.

Swanson, S.E., and Kienle, J., 1988, The 1986 eruption of Mount St. Augustine; Field test of a hazard evaluation: Journal of Geophysical Research, v. 93, p. 4500–4520.

Symonds, R.B., Rose, W.I., Gerlach, T.M., Briggs, P.H., and Harmon, R.S., 1990, Evaluation of gases, condensates, and SO_2 emissions from Augustine volcano, Alaska; The degassing of a Cl-rich volcanic system: Bulletin of Volcanology, v. 52, p. 355–374.

Symonds, R.B., Rose, W.I., Bluth, G.J.S., and Gerlach, T.M., 1994, Volcanic-gas studies: methods, results, and applications, *in* Carroll, M.R., and Holloway, J.R., eds., Volatiles in magmas: Reviews in Mineralogy, V. 30, p. 1–66.

Symonds, R.B., Gerlach, T.M., and Reed, M.H., 2001, Magmatic gas scrubbing; Implications for volcano monitoring: Journal of Volcanology and Geothermal Research, v. 108, p. 303–341.

Symonds, R.B., Janik, C.J., Evans, W.C., Ritchie, B.E., Counce, D., Poreda, R.J., and Iven, M., 2003, Scrubbing masks magmatic degassing during repose at Cascade-Range and Aleutian-Arc volcanoes: U.S. Geological Survey Open-File Report 03-435, 22 p.

U.S. Environmental Protection Agency, 2007, Emissions and Generation Resource Integrated Database (eGrid2006, Version 2.1): [http://www.epa.gov/cleanenergy/egrid/index.htm; last accessed April 12, 2007].

Vallance, J.W., Bull, K.F., and Coombs, M.L., 2010, Pyroclastic flows, lahars, and mixed avalanches generated during the 2006 eruption of Augustine Volcano, *in* Power, J.A., Coombs, M.L., and Freymueller, J.T., eds., The 2006 eruption of Augustine Volcano, Alaska: U.S. Geological Survey Professional Paper 1769 (this volume).

Waitt, R.B., and Begét, J.E., 2009, Volcanic processes and geology of Augustine Volcano, Alaska: U.S. Geological Survey Professional Paper 1762, 90 p, 2 plates.

Wallace, K.L., Neal, C.A., and McGimsey, R.G., 2010, Timing, distribution, and character of tephra fall from the 2005–2006 eruption of Augustine Volcano, *in* Power, J.A., Coombs, M.L., and Freymueller, J.T., eds., The 2006 eruption of Augustine Volcano, Alaska: U.S. Geological Survey Professional Paper 1769 (this volume).

Waythomas, C.F., and Waitt, R.B., 1998, Preliminary volcano-hazard assessment for Augustine volcano, Alaska: U.S. Geological Survey Open-File Report 98-106, 39 p.

Werner, C.A., Christenson, B.W., Hagerty, M., and Britten, K., 2006, Variability of volcanic gas emissions during a crater lake heating cycle at Ruapehu Volcano, New Zealand: Journal of Volcanology and Geothermal Research, v. 154, p. 291–302.

Wessels, R.L., Coombs, M.L., Schneider, D.J., Dehn, J., and Ramsey, M.S., 2010, High-resolution satellite and airborne thermal infrared imaging of the 2006 eruption of Augustine Volcano, *in* Power, J.A., Coombs, M.L., and Freymueller, J.T., eds., The 2006 eruption of Augustine Volcano, Alaska: U.S. Geological Survey Professional Paper 1769 (this volume).

Williams, S.N., Schaefer, S.J., Calvache, M.L., and Lopez, D., 1992, Global carbon dioxide emission to the atmosphere by volcanoes: Geochimica et Cosmochimica Acta, v. 56, p. 1765–1770.